6-2010

Die separation strength for deep reactive ion etched wafers.

Daniel Allen Porter
University of Louisville

DIE SEPARATION STRENGTH FOR DEEP REACTIVE ION ETCHED WAFERS

By

Daniel Allen Porter
B.S., University of Louisville, 2007

A Thesis
Submitted to the Faculty of the
University of Louisville
J. B. Speed School of Engineering
as Partial Fulfillment of the Requirements
for the Professional Degree

MASTER OF ENGINEERING

Department of Mechanical Engineering

SUMMER 2010

SEPARATION METHODS FOR SILICON DIE AND THEIR IMPACT ON STRENGTH

Submitted by: _____
Daniel Allen Porter

A Thesis Approved on

06/28/2010
(Date)

By the Following Reading and Examination Committee:

_____
Thomas A. Berfield, Thesis Director

_____
Roger D. Bradshaw

_____
Shamus McNamara

ACKNOWLEDGMENTS

I would like to express my appreciation to my thesis advisor, Thomas Berfield, for his knowledge and guidance on my Master's thesis. His advice and mentoring has given me the motivation to pursue my dreams. Thanks to Mark Crain for his precious time and fabrication expertise that he has lent to me. Crain has given me the basic knowledge and precious tricks need to be successful in the microfabrication environment. Also, thanks to Scott Cambron, who spent his time and talents dicing my samples to absolute perfection. I would like to thank my family who has supported and encouraged the furthering of my education. Lastly, I would like to thank the members of my examination committee, Dr. Bradshaw and Dr. McNamara, who have given their time to review and grade my work.

ABSTRACT

In the electronic and microfabrication industry, die separation is one of the most critical steps in producing an undamaged, stand-alone micro-scale device. For silicon based devices, it is the predominant step governing resistance to die failure by mechanical fracture. Traditional separation methods include the use of dicing saws and/or backside grinding to dice-by-thinning. Excessive forces, vibrations, and surface contact involved with these methods can cause undesirable side-wall chipping and microcracking, which often translates to inoperable devices. Deep Reactive Ion Etching (DRIE) offers an alternative technique for die separation with less mechanical force. The DRIE process may be used to either introduce notches in one uniform step that allow for die separation via fracture in three-point bending, or to directly separate the dies by etching completely through the substrate.

This work presents an analysis of the stress concentrations due to DRIE etched notches and the bending stress required to achieve die separation. The defect rate and die strength associated with DRIE-based die separated is compared with traditional saw methods for a variety of notch depths. Results indicate that the DRIE-based separation technique offers modest advantages over the traditional methods, but can also greatly reduce strength if the protective mask is over etched. It will also show that shallow trenches formed by a mechanical dicing saw resulted in stronger die than deeper trenches.

TABLE OF CONTENTS

LIST OF TABLES

LIST OF FIGURES

I. Introduction

1.1 Overview of Research

The objective of this research is to investigate the strength of separating moderately thick silicon wafers using deep reactive ion etching (DRIE) in comparison to standard separation methods, such as dicing. The goal is to minimize losses due to the separation method, while fitting as many die on a wafer as possible by minimizing kerf width. Emphasis will be placed on the effects that different trench depths have on the bending stress required for die separation and also the corresponding failure stress for the individual silicon die.

After a fabrication run has been completed for a wafer containing multiple devices, it needs to be separated. Previous works indicate that the strength of these devices varies depending on the separation method. Additionally, the time and resources required to execute the die separation procedure can vary drastically with the method. This thesis will investigate the effect of DRIE and dicing saw separation methods on

separation stress, as well as test the corresponding effect on individual die fracture strength and flaw rates.

Specimens will be fabricated by notching grooves between dies at increasing depths. Separation method/notch depth combinations to be tested include: sawing a wafer all the way through; DRIE a wafer all the way through; saw a wafer to varying depths and then cleaving; DRIE a wafer to varying depths and then cleaving; and DRIE a wafer 25% on both sides. Cleaving of the wafers will be done in a 3 point bending test setup.

Notch geometry will be taken into account when analyzing separation stresses. Finite element modeling will be performed to determine the stress concentration factors associated with the different notching methods. All wafers tested will have the same crystal orientation and come from the same lot to keep results as comparable as possible.

The fracture strength of the die is expected to be proportional to the area of the sidewalls exposed during the trench formation process. Between the two methods to be tested, the DRIE produced die are predicted to create a less substantial damage zone and yield stronger die. The separation method expected to result in the strongest die is the 100% DRIE etch, as defects on the sidewall should be minimized using this approach. The weakest separation method is expected to be "the saw 25% then cleave" due to the large amount of defects it will produce. DRIE is also expected to give a larger stress concentration at edges due to its sharp filleting nature, while the dicing saw is expected to give lower stress concentrations coming from the rounded corners it produces. Stress concentration factors are expected to be low for the double sided DRIE wafer due to the neutral axis being closer to the stress gradient lines.

1.2 Background of Microfabrication

Most microscale devices fabricated in a clean-room environment are constructed in bulk on a wafer. A single wafer can hold anywhere from one to a few hundred devices. Individual or separated devices are called die. While there are many ways to build-up, or construct, a micro-device, eventually the individual devices, must be separated in some manner. A few common processes used to compose sensors, pre-concentrators, and other MEMS devices are photolithography, thin-film deposition, wet-etching, dry-etching, and anodic bonding.

Photolithography is the process of exposing an organic or non-organic resin to ultraviolet light that makes it either pseudo-chemically inert (negative resist), or not inert (positive resist), to a developer solution. The part that is non-inert is put into a developer solution and dissolved while the other part remains adhered to the substrate. This process is used to replicate patterns from a master mask onto the substrate (Jeager 2002). Generally the resin is termed 'photo-resist' and provides protection for the substrate so that patterns may be utilized in other fabrication processes (etching, deposition, etc.).

Thin-film deposition is used when a thin layer of a particular metal or ceramic needs to be adhered on the surface of a substrate. This process can leave films nanometer to micrometers thick and can be patterned using photolithography. The material can be deposited via sputtering using direct current or radio frequency oscillation methods. The common procedure of "lift-off" is a combination of photolithography and thin-film deposition in which the photo-resist is patterned to block some areas and has an

overhanging side wall profile. This allows the photo-resist to be removed afterward via a solvent like NMP (N-Methyl-2-pyrrolidone).

Wet-etching is the process of removing substrate material via a liquid chemical reaction. Usually a strong acid or base is used in wet-etching and tends to be isotropic. By eating away material along weaker crystal orientations at a higher rate, wet etching can form nearly perfect square bottom features with 54.74º sidewalls. Dry-etching is the process of removing substrate material via a plasma gas and can be very anisotropic. Etching is generally used to build 3-D structures in a substrate and is commonly done in multiple steps to achieve elaborate devices (Jaeger 2002).

Anodic bonding is the adhesion of two substrates using high temperatures or a high voltage. The extra energy given to the surfaces of the substrates causes them to become ionized and promotes anodic bonds. This process is used as a sealing technique or for creating a strong backing structure to increase the mechanical stability of a device (Jaeger 2002). Glass on silicon is a common combination used in anodic bonding.

The appeal of these methods is that they are processes that can be applied uniformly to an entire wafer. Thus, a batch of hundreds of devices can be fabricated on one wafer at once. Eliminating repetition of fabrication steps for each device saves time and money, but the devices still must be separated so that they can be used individually. Separation methods for wafer-based devices can be time-consuming and traditionally involve a mechanical grinding process that can lead to lowered die strength. As the microelectronics industry calls for smaller and smaller components, manufacturers are moving to use thinner wafers (less than 300μm in thickness) for their products. Thin wafers are desirable for electronics and MEMS due to their increased thermal dissipation

characteristics, mechanical flexibility, and lower silicon usage. However, thinner wafers are also more prone to failure due to their fragility (Kroninger 2006). A single induced crack or ample flaw during manufacturing can immediately yield a bad device, or lead to premature failure. Though not all manufacturers use thinned wafers due to the extra overhead of cost and time used to thin the silicon. Inexpensive solar cell manufacturers still used relatively thick silicon to fabricate photovoltaic devices.

The push towards thin wafers comes at a time when silicon is in high demand while production in the U.S. declines. As an example, the photovoltaic industry grows at a compounded annual rate of 40% per year from 2002 to 2007 (Mints 2008). As abundant as silicon is, it is expensive and complicated to manufacture into ingots. HSC, a silicon production company in Michigan, went from producing 14,000 metric tons of silicon in 2008 to 19,000 metric tons in 2009 (Bruno 2009). Therefore, companies based in the microfabrication area try to lower costs by decreasing the thickness of wafers and increasing yield.

Silicon based device manufacturing is one of the world's most technologically advanced businesses. To remain economical, manufacturing of silicon-based electrical and MEMS devices demands mass production, meaning a larger number of die must be fabricated on a larger diameter wafers. Fabrication facilities can increase throughput by doing single uniform fabrication processes, which take roughly the same amount of time per step on either small or large diameter wafers. While larger diameter wafers contain more devices, they can require an extensive amount of time to separate the die without damage. Any small increases in production yield or reliability, or decreases in the required separation time, can save manufacturers millions of dollars in the long run.

One market that has shown increasing demand for silicon usage is in the area of solar cell production. Figure 1-1 below shows the trend of installed photovoltaic devices since the turn of the century. The number of fabricated photovoltaic devices has soared since the turn of the century and everyday solar companies are looking for ways to decrease the cost of their products. One way to do this is to devise a way to separate crystalline solar cells cheaply that are grown using the silicon ribbon pulling method. Silicon ribbon pulling allows for inexpensive photovoltaic production because it minimizes the cost and time associated with substrate creation. Usually a rounded silicon wafer is grown in a cylindrical shaped structure called an ingot. This ingot needs to sawn into small wafers and is usually time consuming, expensive, and wasteful. Figure 1-2 below shows the expected trend for the next five years.

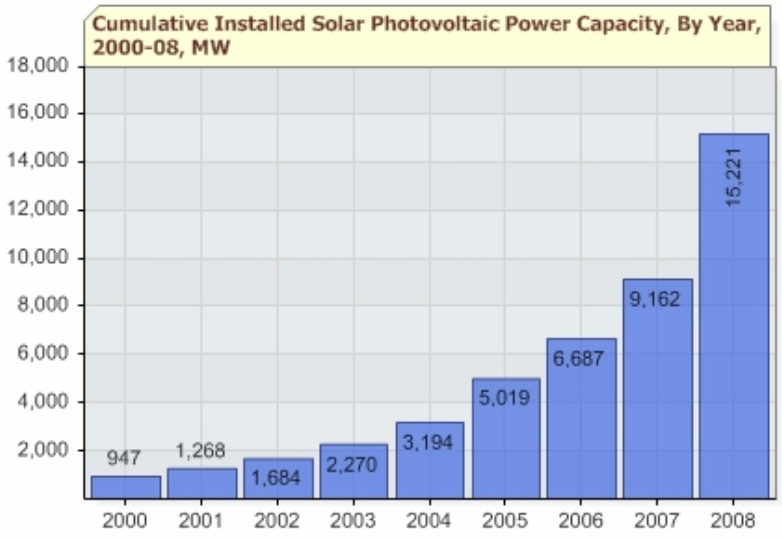

Figure 1-1. Cumulative installed photovoltaic power capacity since 2000 (GreenChipStock 2010).

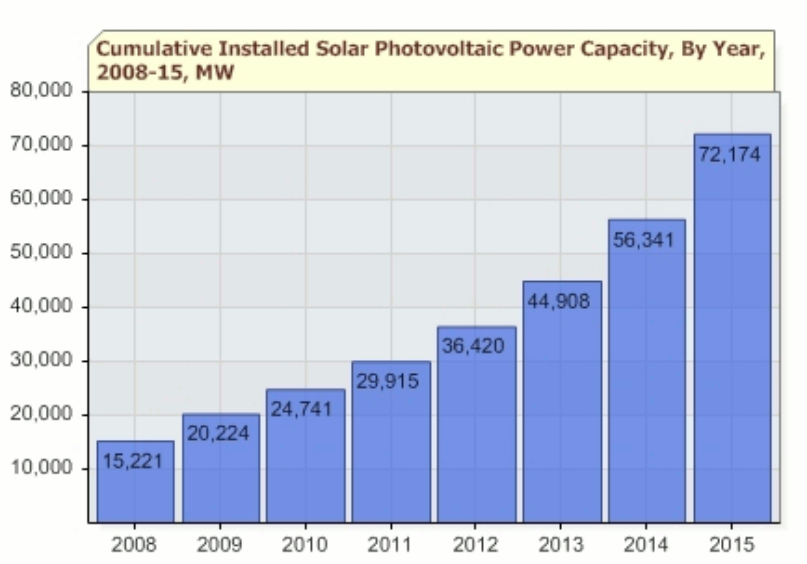

Figure 1-2. Expected trend for photovoltaic product product implementation over the next five years (GreenChipStock 2010).

1.3 Current Separation Methods

Currently, most manufacturers separate die by means of mechanical grinding via the use of a diamond saw or, more commonly, a "dicing saw." Problems that arise from use of a mechanical grinding technique include chipping and cracking on the top and bottom edges of the substrate near the sawn grooves (Kroninger 2006). To lower the amount of damage done to the wafer, diamond tipped saws usually traverse the material at a very slow rate (10 to 15 mm/s) (Cooke 2006). Figure 1-3 shows a typical dicing saw from Majelac Technologies (Majelac 2007). After completing all grooves along one direction, the wafer must be reoriented and the dicing saw must then repeat the process. Kerf widths, or the groove width dimension, for this type of separation technique are typically 20 to 50 μm for thin wafers (Cooke 2006).

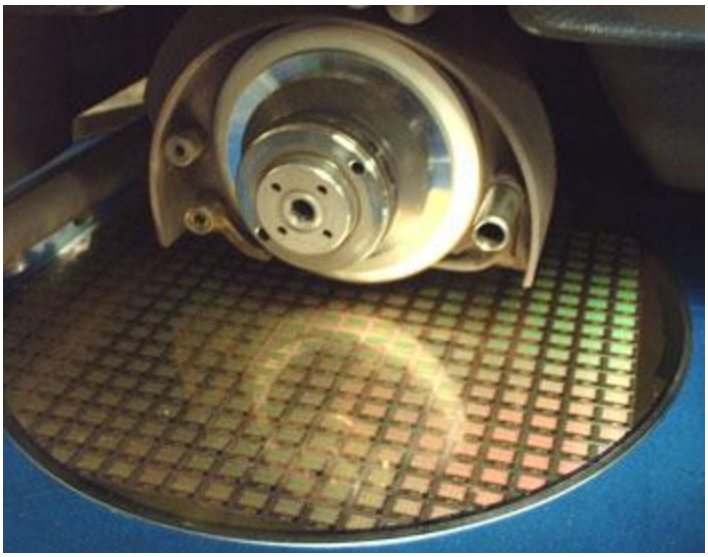

Figure 1-3. Typical dicing saw (Majelac 2007).

In addition to edge chipping and cracking, dicing saws can also leave residual stresses on the sidewalls that can cause failure at low stresses when undergoing thermal cycling. Another problematic issue with dicing saws is the high-pressure cooling water that is applied to prevent fast blade wear during the dicing process. The water stream can damage sensitive electrical devices via direct force or contaminate a device via diffusion. Usual steps taken to prevent this is a nitride or silicon oxide layer fabricated on top of sensitive devices.

Another separation method is the "Scribe and Break" method, which has its own benefits when compared to a dicing saw. The scribe and break method uses a sharp tool to scribe or scratch the surface of the wafer, creating a stress concentration at the grooved notch tip. There are multiple methods for creating a scribe line, including diamond tipped scribes, dicing saws, laser scribes, wet-chemical etching, dry etching, or high pressure water jet scribes. After scribing, the wafer is then constrained and bent so that tension is applied perpendicular to the scribe line, causing the wafer to fracture along the

stress concentration. The diamond scribing procedure produces one of the smallest kerf widths of all common wafer separation methods and has a typical cut depth of roughly 4µm. Scribe and break methods work best on thin silicon wafers and other hard materials (Acker 2001). Although scribe dicing is faster than a dicing saw, it is still a serial process in which every line must be scribed individually, as shown in Figure 1-4. Scribe and die separation methods can still leave large defects on the shear plane of the separated die, thus lowering the die strength.

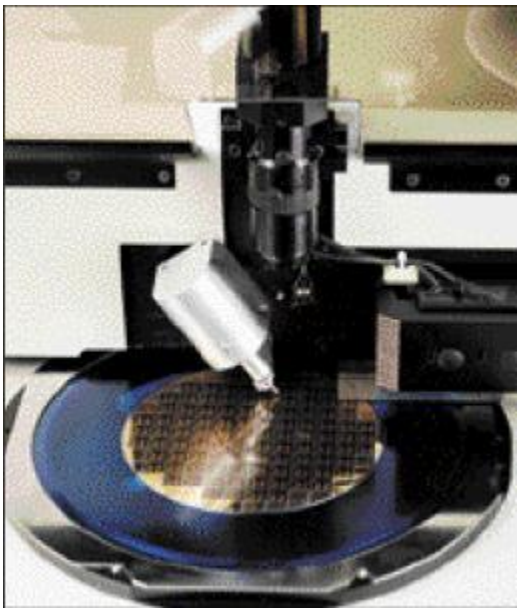

Figure 1-4. A typical wafer scribing system (Dynatex 2001).

Laser separation techniques are new to the wafer market and present unique benefits as well as some disadvantages to thin chip separation. Dry-laser cutting based techniques use high powered laser pulses to obliterate or sublimate substrate material from the surface in quick succession, which is called ablation. Scribing via a laser ablation process can cause thermal damage to appear in the lower silicon layers. This

thermal damage can alter doping profiles and induce built in stresses that can induce premature die failure. The kerfs resulting from this technology are typically around 25vμm, and kerf widths of 10vμm have been observed from dual-focused laser beams (Venkatakrishnan 2007). A range of laser light wavelengths can be used, depending on the substrate material. Generally, pulse widths in the range of 1-100 ns are used, delivering on average 11W of power (Venkatakrishnan 2007). Linear progression rates for laser cutting are typically fast, roughly 100-180vmm/s (Venkatakrishnan 2007). The downside to laser cutting is that ablated material tends to sputter on the die. These dust and debris particles tend to adhere to the substrate causing mechanical or electrical problems. Similar to water damage prevention, the additional step of covering a wafer with a nitride or oxide layer can usually protect fabricated devices from the effects of problems stated above.

A more advanced method of laser cutting that can prevent debris contamination is called wet-laser cutting. Wet-laser cutting uses a cooling liquid in conjunction with a cutting laser. Exposing some fabricated wafers to water can lead to ion contamination (Alballak 2007), though wet-laser cutting does leave a cleaner cut than traditional laser cutting. Figure 1-5 is a picture comparing die separated by dry-laser, wet-laser, and classical mechanical dicing procedures.

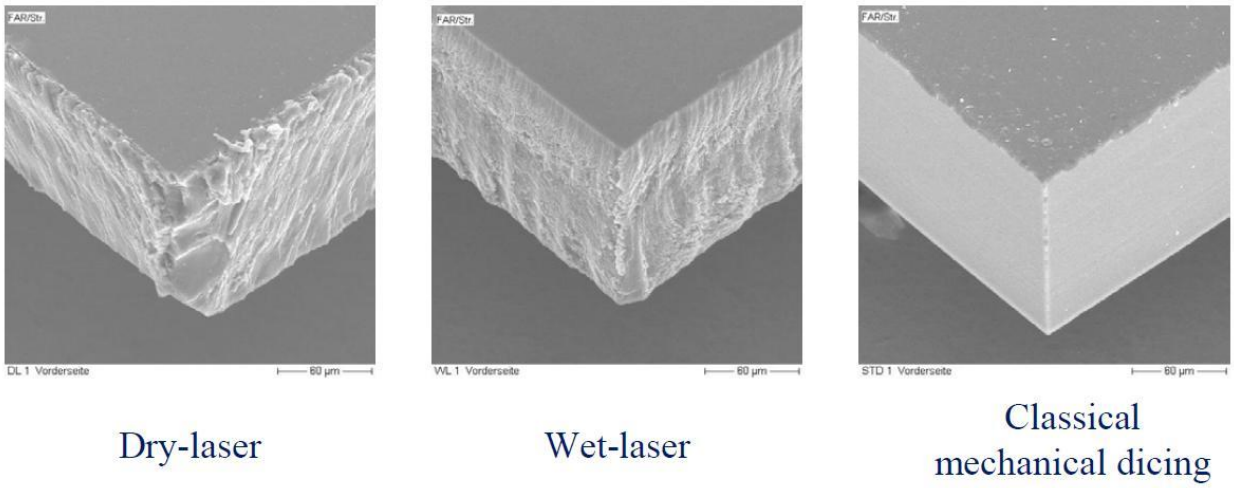

Figure 1-5. Side wall of die produce by various dicing methods (Kroninger 2006).

There are three components of die damage in mechanical dicing that effect die strength. These components are front-side chipping, back side chipping, and side wall damage (Kroninger 2006). Figure 1-6 shows the location of the three components of damage. The image on the right of Figure 1-6 shows the three layers by means of a sandwiched block. It can be seen that the side wall damage is well defined yet the top and bottom damage layer has a variable transition point. It is important to note that an additional damage layer will be present for the work of this thesis, the cleavage plane. This is the exposed wall from the throat of the notch after separation from three-point bending.

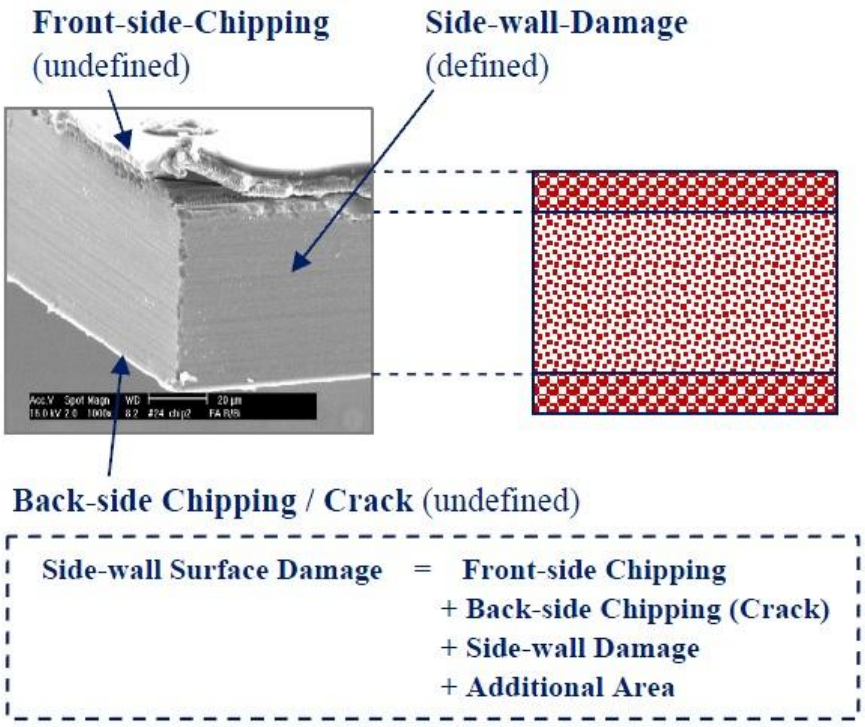

Figure 1-6. Three components of sidewall damage (Kroninger 2006).

A novel separation method called "Stealth Dicing" has evolved into a useful die singulation technique by the Hamamatsu company and is gaining interest in the fabrication industry (Hamamatsu 2010). This method focuses a laser midway through the substrate thickness, Figure 1-7. Internal thermal stresses build and induce localized internal cracking along a plane in the laser scanning direction, Figure 1-8. One advantage of this new technique is that it can dice wafers rapidly (300mm/s) without chipping (Hamamatsu 2005). The method also eliminates debris and contamination from laser ablation or saw blade kick up. After the stealth dicing procedure is done, minimal surface defects or marks are apparent.

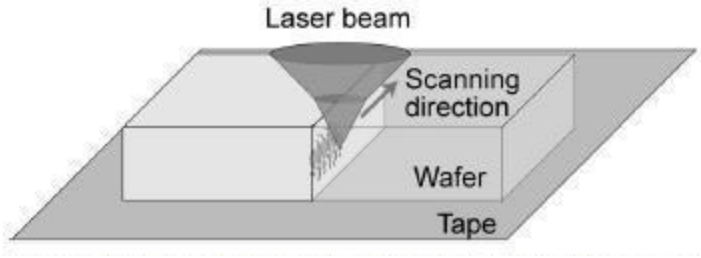

Figure 1-7. Stealth dicing focuses a laser in the center thickness of the wafer, scanning in one direction (Kumagai 2007).

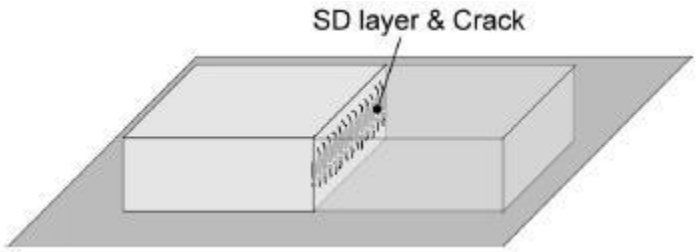

Figure 1-8. Resulting diced layer from the stealth dicing technique (Kumagai 2007).

The stealth dicing procedure is usually performed with the substrate adhered to dicing tape. After the laser cycle is complete, dicing tape is stretched using a mechanical stage. The tension created separates the diced wafer pieces, as shown schematically in Figure 1-9 below. Stealth dicing can potentially increase the number of devices per wafer and the kerf width is extremely small, on the order of 1 to 2 µm. The upper and lower edges of a stealth diced sample are smooth due to the presence of a shear plane, this makes them ideal for tensile and compressive bending because the maximum stress will be near the top and bottom of the wafer while the neutral axis (location with the majority of flaws) is at a lower stress. However, a major downside to stealth dicing is the high thermal loading that the material undergoes in order to propagate the cracks.

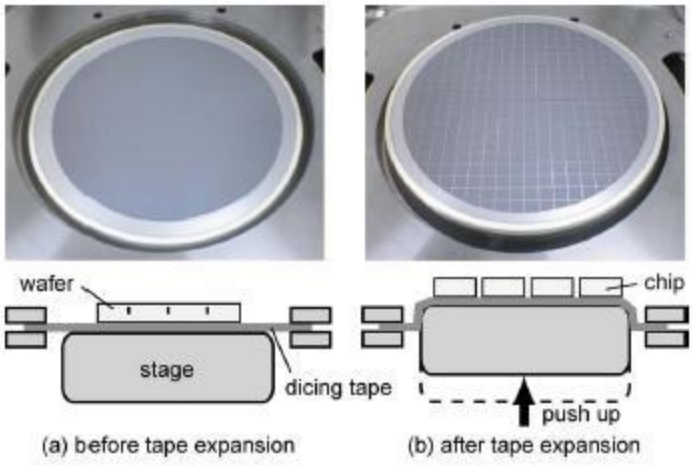

Figure 1-9. Stealth dicing separation process (Kumagai 2007).

An alternative separation method of recent interest is dry etching. Although generally more time consuming than dicing, dry etching may offer benefits in the other areas of concern. During dry etching, the semi-conductor material is removed through the bombardment of ions. In most cases, ions are supplied by a plasma of reactive gases. The gases are passed through a very high magnetic field alternating at a high frequency with a power of a few hundred watts. This effect causes the gas particles to rip apart, and thus becoming ionized (*i.e.* a plasma). The etch rate is dictated by the substrate material, the operating pressure, and the gas flow rates. Some common gases that are used for etching are CF_4, O_2, and Ar. Dry etching performed by ionized gases is almost always anisotropic and leaves very smooth surfaces. Reactive ion etching (RIE) is one form of dry etching in which plasma generated ions bombard a substrate that has been patterned with a photo-mask. Typical etch rates for RIE can vary from 1nm to 1μm per minute. Due to the anisotropic nature of RIE, extremely vertical sidewalls are very

difficult to achieve, which makes RIE best suited for short etch depths. Figure 1-10 shows a typical RIE setup (OpenLearn 2009).

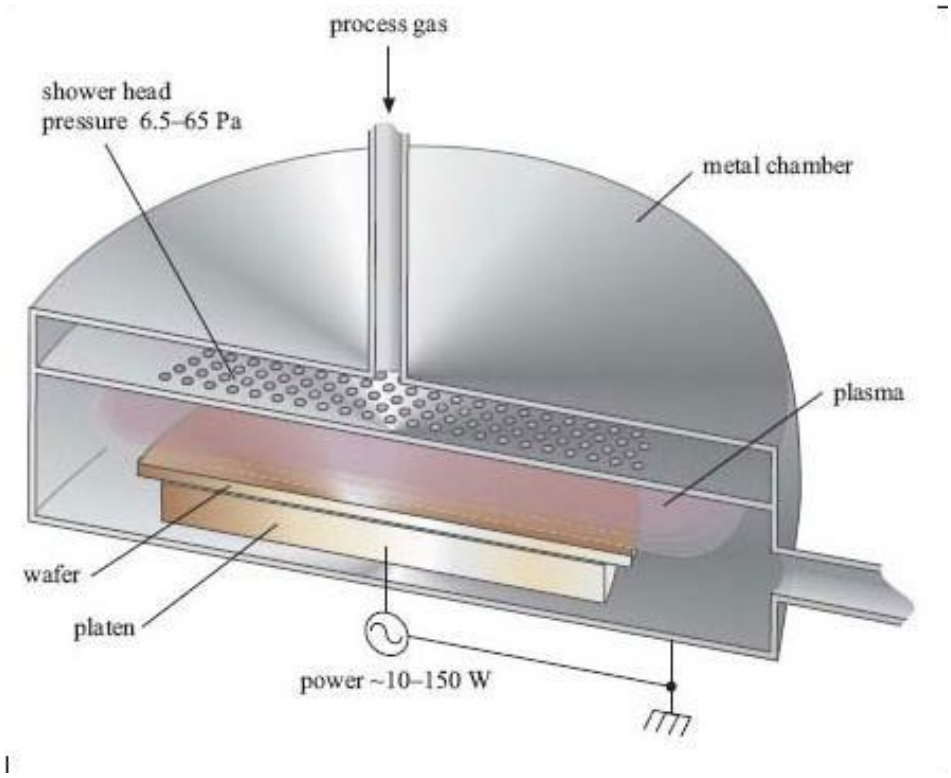

Figure 1-10. Reactive Ion Etch (RIE) chamber (OpenLearn 2009).

A more advanced dry etch is called deep reactive ion etching or DRIE. In this method the substrate is etched as normal reactive ion etching, but with alternating passivation cycles inserted into the process. In the first phase of the DRIE process, ions from plasma gas bombard the surface, bond with silicon, and release it from the surface (identical to the RIE procedure). During the second phase of the DRIE process, the side-walls and bottom of the notch are passivated with a polymer or oxide coating that prevents the etch cycle from cutting into the sidewalls. In the etching chamber, plasma ions are forced down in the vertical direction, causing the passivated bottom of the notch

to be etched faster than the sidewalls. The sidewall profile exhibits "scallops" which are concave structures as shown in Figure 1-11.

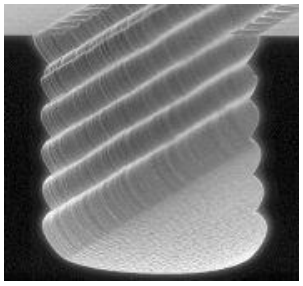

Figure 1-11. DRIE trench with large sidewall scallops formed by alternating etch and passivation cycles, no scale bar available (STS, 2009).

High aspect ratios (depth-to-width ratio of the etched feature) are what distinguish DRIE from scribing and RIE. Aspect ratios of around 25:1 are not uncommon for the DRIE process (Jaeger, 2002). Depending on the substrate, DRIE has etch rates of about 50 nm-24 μm per minute (Selbrede 2009). Etch rates also affect how smooth and vertical a trench can be fabricated, with faster rates usually giving a rougher surface. For silicon substrates using SF_6/O_2 (etching/passivation gas), etch rates up to 10 μm/min can be achieved (Laermer 1999). Another common passivation gas for DRIE is C_4F_8.

The need to construct vertical sidewall features in the MEMS area is critically important. Pivot plate resonators, as shown in Figure 1-12, are an example of 3-D geometry structures that require a vertical etch to achieve an appropriate mechanical function. Without these vertical sidewalls the resonant oscillation frequencies would be difficult to calculate. Instead one would have to use finite element analysis (FEA) to back out the resonant frequencies and this method would not give an equation of motion that would be more useful in understanding its operation. The ability to construct vertical sidewall features uniformly over large areas is a very attractive tool for the patterning and

manufacturing of MEMS devices. However, little is known about the effects of the passivation process on the sidewalls, the geometry effects of DRIE notches on die separation, and the overall effect on die strength.

Though these etching processes look nice and give great results in terms of edge defects, they are extremely expensive and time consuming. Uniformity of the DRIE with respect to wafer location is also subject to gas flow variations and exposed etching locations.

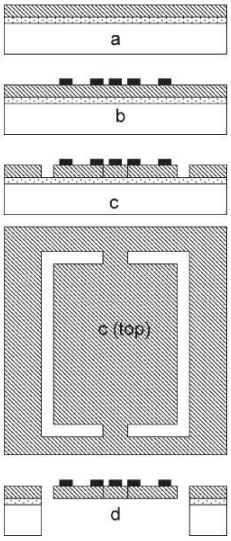

Figure 1-12. Pivot plate resonator fabrication step layout showing large DRIE backside etch (Manginell 2008).

1.4 Strength Testing

The fracture stress of silicon materials is difficult to determine using standard tensile testing, especially for thin processed silicon wafers. The primary issue is that securing the base tensile sample by each end often causes scratches and cracking on the

specimen, which is detrimental to the strength for brittle materials. Instead of a tensile test, most researchers tend to use beam and plate bending analyses to calculate stresses from applied bending moments.

Three-point bending tests are commonly used to test the strengths of materials when tensile testing is not feasible. In a three-point bending configuration, a load is applied to the middle on top of the beam while two bottom supports spaced symmetrically balance the top force. Both a shear stress and an axial bending stress are induced in the specimen between the supporting structures. Usually the three-point bending test causes specimen failure below the middle support, where the normal stress due to bending is at a maximum, Figure 1-13.

Four-point bending is another common test performed to determine material strength. For the material between the bottom edge support and the top edge support there is shear and normal axial stress in the beam, just like in the three-point bending case. The region between the two top supports, however, is theoretically in constant bending and has no shear component. In actual practice, finite element analysis (Schoenfelder 2007) have shown a slightly non-linear stress profile for this region, Figure 1-13, which arises due to non-linear force displacement behavior. The main difference between the tests is the length of the beam that experiences the maximum bending stress. Four-point bending tests a larger area for flaws than the three-point bending test.

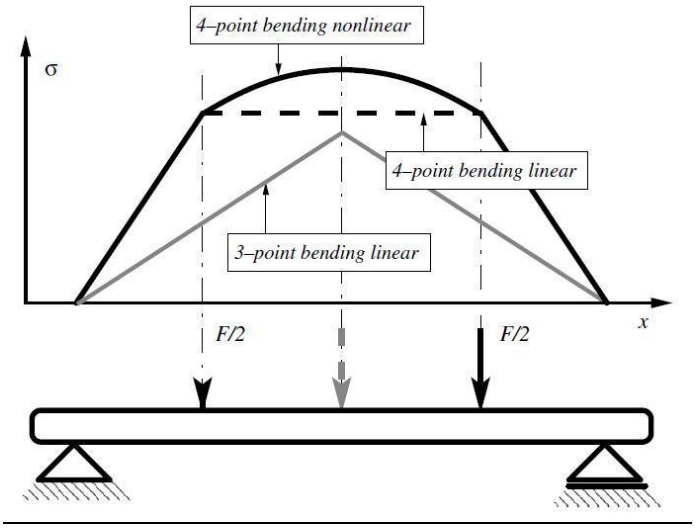

Figure 1-13. Axial stress profile for three and four-point bending (Schoenfelder 2007).

For brittle materials, both three and four-point bending techniques generally induce failure via cracks that emanate from edge or surface defects. Edge defects are chips or cracks that occur on the edge of a die the size and density of which are highly influenced by the separation method. Surface defects are considered to be on the top and bottom of the substrate and are dependent on the grinding and polishing methods used. Other strength testing methods generally only probe the effects of one type of flaw. For example, a ring-on-ring fixture tests for surface defects because the surface of the material is loaded with the highest stress. Another example is the ball-on-edge technique which tests the influence of edge flaws on die strength by applying maximum stress on the edge of a sample.

Parts with lateral geometry variations are subjected to stress concentration factors (SCF). These SCF come about from gradual or sudden changes in contour and amplify the nominal stress associated with the minimum throat cross section. Typical stress concentrations for designed components fall within the 1 to 3 range but can be much

larger if geometry allows. Figure 1-14 shows the effect of right angle and gradual fillets on a component loaded in uniaxial tension. Dense stress flow lines represent amplified stresses.

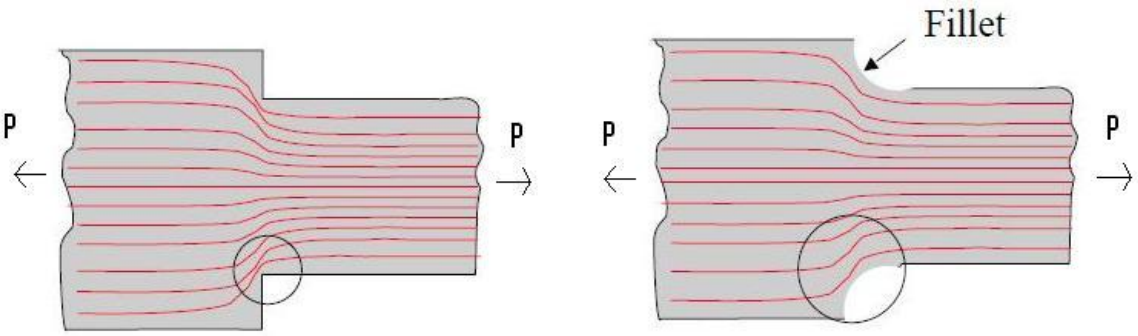

Figure 1-14. How force flows in structures (Haftka 2009).

SCF associated with common geometry cases have been studied extensively and have been reported in journals and fracture/fatigue handbooks (Peterson 1974). To obtain the SCF for a particular geometry, specimen dimensions must first be noted; then a SCF can be derived via a graph or an equation. When calculating stress concentration factors, it is important to note the range of valid input parameters. If the constraint ratios are ignored, then some assumptions may be violated and high errors can be expected for the predicted SCF values.

Troyani *et al,* (Troyani 2004) investigated the effect on SCF of varying low ratios of beam length (L) to plate thickness, (H). Often SCF graphs presented in books and journals do not include the "L/H" ratio because the graphs were either derived theoretically with the assumption that L was much larger than H, or derived empirically with specimens that had long L to H ratios. Troyani found from finite element analysiss that U-shaped notches in bars under bending loads, as shown in Figure 1-15, had

significantly higher stress concentration factors for L/H ratios of 1 and lower. Up to a 40% difference in the FEA calculated and derived SCF from engineering textbook graphs was found, Table 1-1 (TSCF is the theoretical stress concentration factor). The transition ratio is the ratio at which the stress concentration factor starts to deviate noticeably.

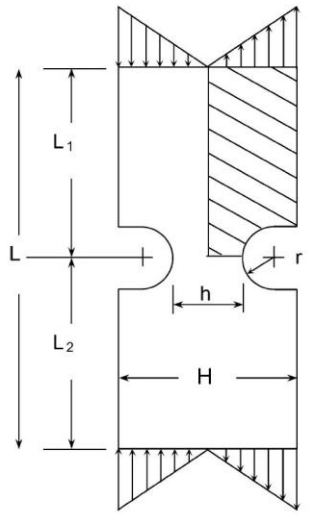

Figure 1-15. Beam with double notches (Troyani 2004).

Effect of length on various values of the TSCF for $r/h = 0.10$

L/H	$H/h = 1.2$		$H/h = 1.5$		$H/h = 2.0$	
	TSCF	% difference with respect to transition value	TSCF	% difference with respect to transition value	TSCF	% difference with respect to transition value
Transition	2.10	–	2.22	–	2.24	–
1.0	2.11	0.476	2.23	0.450	2.24	0.00
0.8	2.14	1.90	2.28	2.70	2.24	0.00
0.6	2.26	7.62	2.46	10.8	2.27	1.34
0.4	2.62	24.8	3.11	40.0	2.91	29.9

Table 1-1. Stress Concentration Factors for low L/H ratios (Troyani 2004).

Ikehara and Tsuchiya investigated the effects of anisotropic material properties on stress concentrations in single crystal silicon films (Ikehara 2009). Again, FEA was utilized to show that anisotropic properties can cause a difference in stress concentrations values of greater than 10% when compared to stress concentration factors calculated assuming isotropic material properties. This is a significant increase/decrease when designing MEMS structures. In this study the films were oriented on the (001) plane, while the loading setup and crystal axis tilt were varied. Additionally, the effect of changes in the notch radius for specimens loaded in tension and variation of the radius of the curved bars was investigated, as shown in Figure 1-16. Not only did the stress concentration values differ for the FEA models, but the location of the maximum stress also changed when the angle theta was a value other than 0, 45, or 90 degrees. When Ikehara *et al*, decreased notch radius in their analysis (models 1 and 2), the stress concentration value deviation also decreased. In this case the anisotropy effects are suppressed by the narrowing of the high stress area.

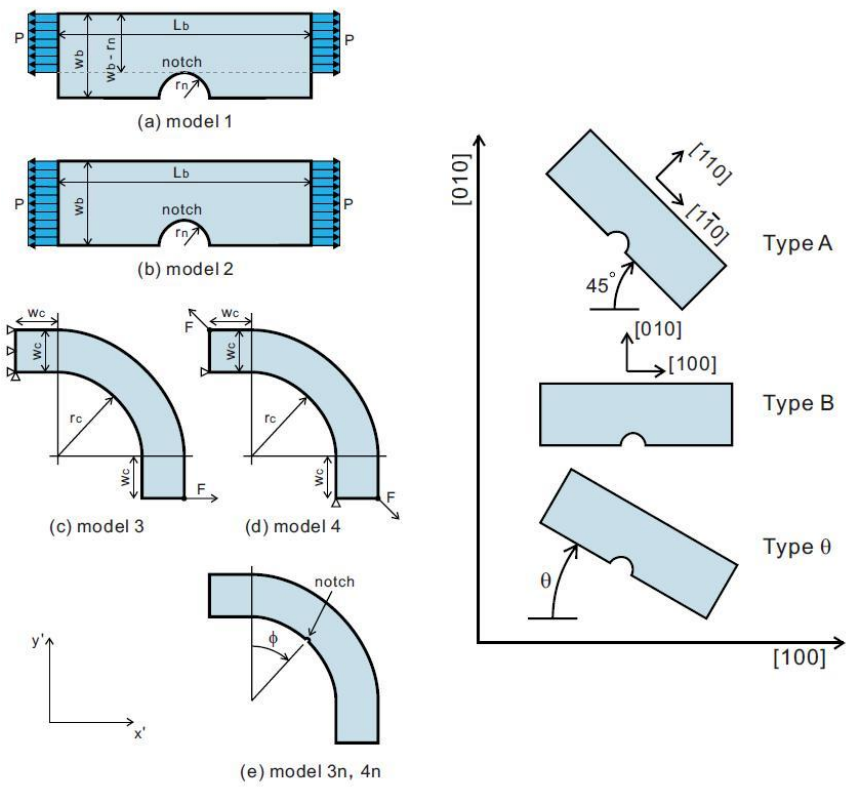

Figure 1-16. FEA model subjects and differing crystal orientations (Ikehara 2009).

1.5 Die Separation Strength

Previous studies have shown that number of factors influence die separation strength. Some of these include die thickness, post separation treatments, edge defects, surface defects, thermal cycling, edge geometry, and wafer processing history prior to separation. Separation techniques are one area that can be improved upon while thermal processing and other factors most likely have to remain constant due to fabrication restrictions.

Schoenfelder *et al* (Schoenfelder 2006) investigated the influence of different separation techniques on the failure strength of individual silicon chips. Three primary methods were used to separate the chips: sawing after thinning; sawn grooves followed by a "dice-by-thinning" (DbyT) procedure; and finally a deep reactive ion-etch (DRIE) followed by a DbyT procedure. Die sample sizes were in the range of 200 μm to 48 μm thick and were 5 mm by 1 mm. All samples were ground from the backside to remove material and had a wet-chemical spin-etch treatment applied to relieve stresses introduced by grinding.

Three-point bending was used to determine the fracture stress of each separated die, as shown in Figure 1-17. Non-linear behavior was observed for thin die during the three-point bending test, as large deflections caused the die to slide on the supports. A theoretical mechanical model of the bending system was devised consisting of a moment spring (allowed to transverse in the y direction), a beam, and a fixed support. The model was derived using a four-point bending setup, as shown in Figure 1-18, a schematic of the analytical model is shown in Figure 1-19.

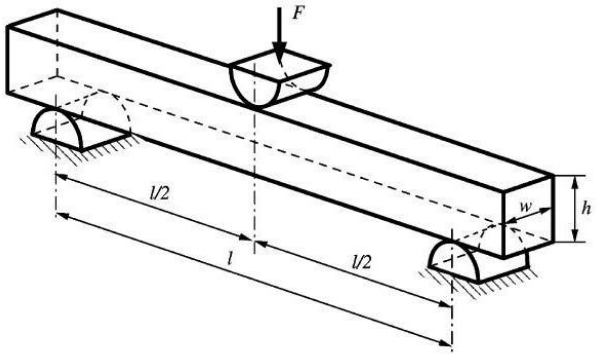

Figure 1-17. Typical 3-point bending setup (Schoenfelder 2006).

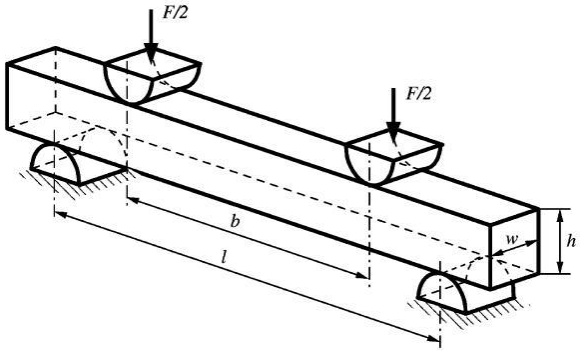

Figure 1-18. Typical 4-point bending setup (Schoenfelder 2006).

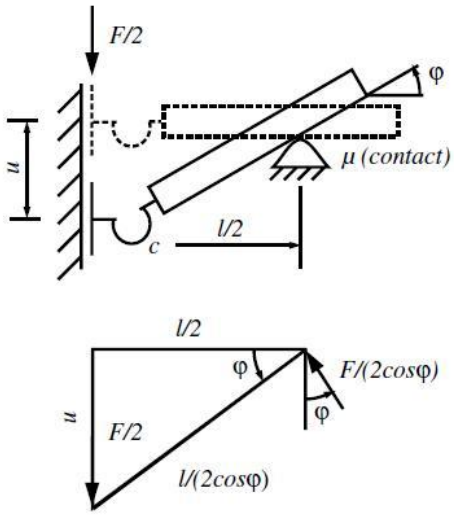

Figure 1-19. Theoretical model for 3-point bending (Schoenfelder 2006).

This model assumed that friction effects were negligible and that bending only happened close to the center of the die. The static model used by Schoenfelder did not include a reaction force near the base of the moment spring, but a reaction force was needed in order to balance forces. The equation relating force and displacement in the Schoenfelder' model for 3-point bending is

$$F(u) = 4\frac{cl}{4u^2+l^2} tan^{-1}\left(2\frac{u}{l}\right)$$ (Eq. 1-1, Schoenfelder 2006)

where u is the vertical displacement of the center of the die and l is half the length of the die. Equation 1-1 shows the non-linear behavior of the theoretical model, though Schoenfelder only plots b/l ratios against each other and not against actual experimental data. The plot for b/l=0 is a three-point bending test, since b is the width of the top two support arms (center span) of a four-point bending test. Figure 1-20 shows variations of b/l ratios and its effect on the needed force for a given displacement.

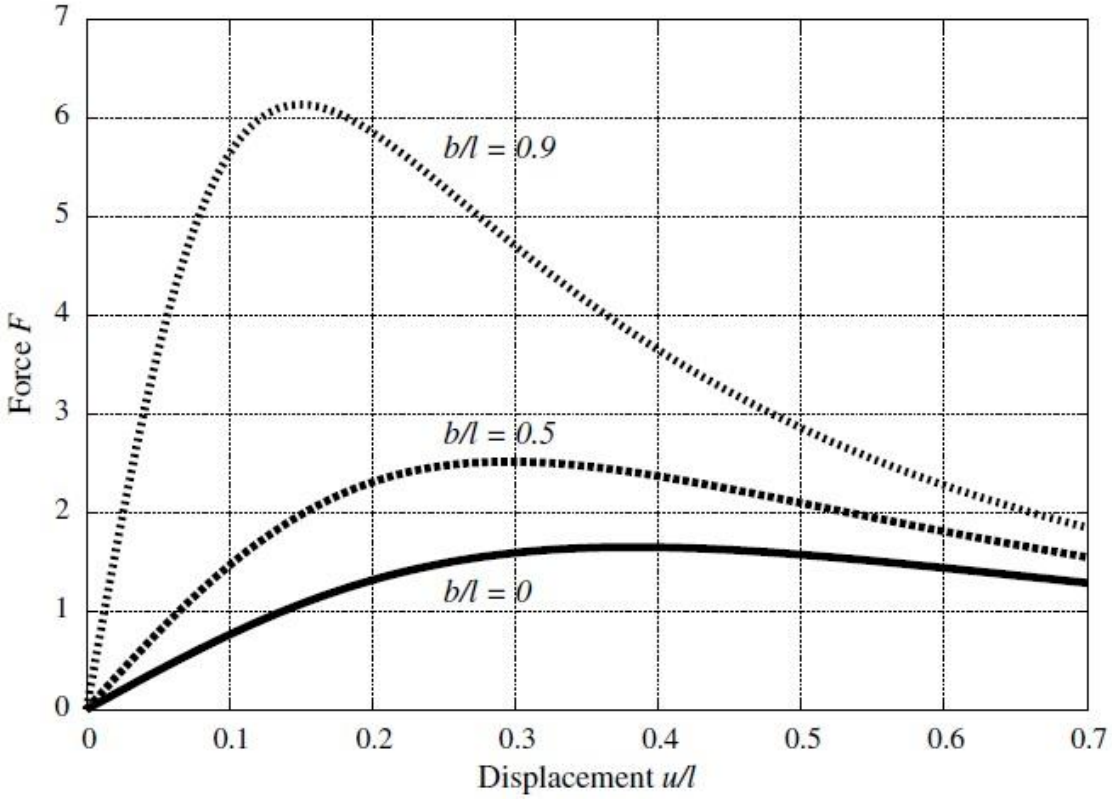

Figure 1-20. Variations in b/l ratios for Schoenfelders model (Schoenfelder 2006).

FEA was also done to verify that friction in the above model was negligible. Analyses with different coefficients of friction and without friction were performed and

showed little effect on the stress results, affirming a frictionless model was valid. Figure 1-21 below shows how a frictionless FEA model and experimental results compare; thus affirms the frictionless model for the scheme shown in Figure 1-19.

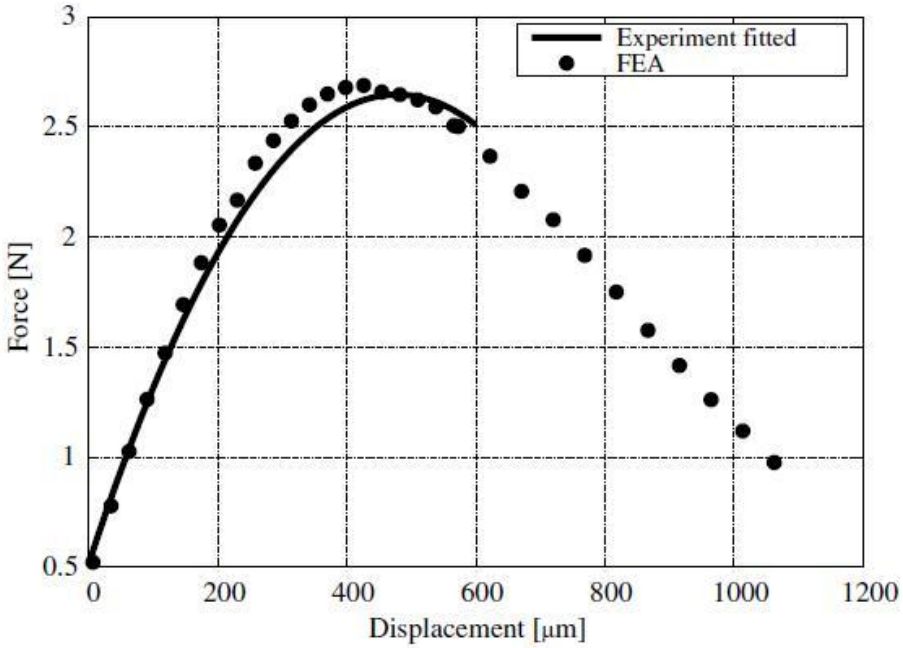

Figure 1-21. FEA versus experimental data for a three-point bend test on a DbyT dry-etch 48 μm silicon specimen (Schoenfelder 2006).

It was found that die strength of the DbyT method with a dry-etch failed at a much higher stress than the other separation methods. In this case the back side failed at a much higher stress than the front-side due to the rounding of the backside from dry-etching and also from the wet-etch treatment on the backside. Consistent with this result, the front-side of the die visually had more flaws than the back sides. Whichever side of the sample is in tension is considered the side being tested. Top and bottom chipping arising from separation methods, like in the case above, is an example of edge defects.

Figure 1-22 below shows a graph of Schoenfelder's results. These results indicate that die strength is strongly affected by edge flaws introduced by the different separation techniques (Schoenfelder 2006).

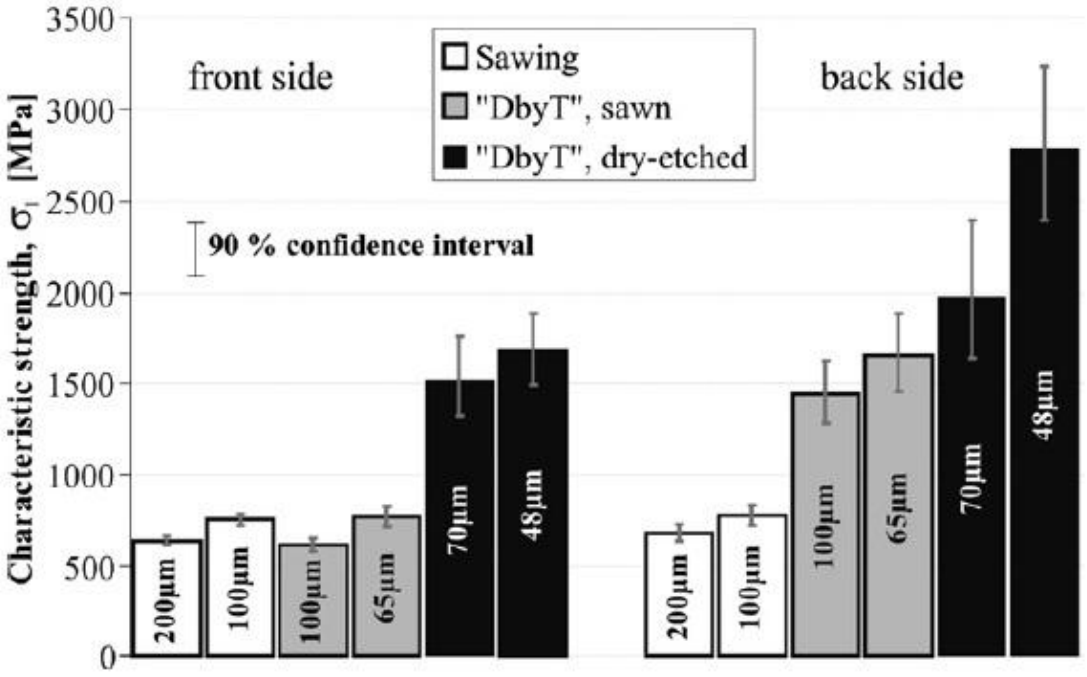

Figure 1-22. Stress results for Schoenfelders experiments (Schoenfelder 2006).

Desmond Chong *et al*,(Chong 2004) investigated crack and fracture failure for separated die using a three-point bending test. They tested dummy wafers with thicknesses varying from 150 µm to 394 µm. Lengths for the specimens did not mater since the span of the bending structure was kept at a constant 4 mm. However the widths of the samples were 6, 6.52, and 8 mm. The equation for maximum tensile stress due to pure bending comes from simple beam mechanics,

$$\sigma = \frac{Mc}{I} = \frac{3FL}{2wt^2} \qquad \text{(Eq 1-2, Beer 2006)}$$

where M is the maximum moment that the beam is experiencing, c is the distance from the center of the beam to the bottom (or half the thickness), I is the moment of inertia of the beams cross section, F is the force applied to the center of the beam, L is the length of the outer supports, w is the width of the beam, and t is the total thickness of the beam. Equation 1-2 is good for simple beam theory and gives reliable results as long as displacements remain small. Due to the large deflections associated with thinned die, Equation 1-2 only gives an estimate of σ for comparing the strengths of differently processed wafers qualitatively.

It was found that the dummy wafers from which Chong sampled fractured at an average stress of 544 MPa. Conversely, the actual processed wafers, which were excessively handled and thermally cycled, failed at roughly 300 MPa. These results show that devices that undergo physical processing and handling environment have a much greater chance of failing at a lower stress. Failure stresses in the experiment ranged from 300 to 1000 MPa and did not vary linearly with thickness, Figure 1-23.

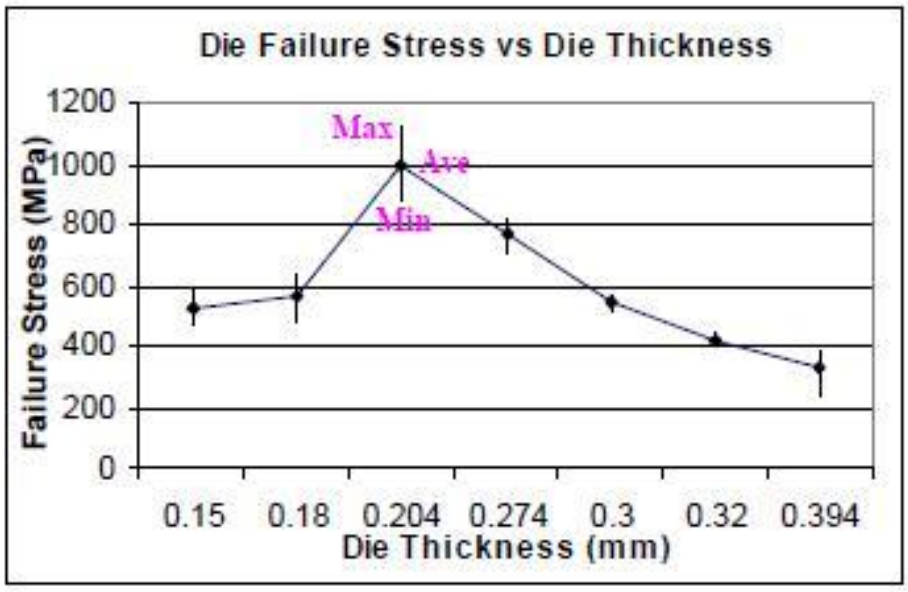

Figure 1-23. Stress data from dummy wafers in 3-point bending (Chong 2004).

From Figure 1-23, it is seen that the 204 μm lot had the maximum failure stress of 1000 MPa. The decreasing trend from the 204 μm thick die moving towards the 394 μm die is due to decreased flexibility from thicker specimens. When a die is flexible, some of the bending energy can go into deflecting the die without permanently deforming it.

Back grinding pattern tests were also reported in Chong's research. Sections from a wafer corresponding to different pattern orientations were examined and tested in a three-point bend. Sections that had back grinding patterns parallel to the bending axis failed at half the stress than sections with back grinding patterns perpendicular to the bending axis, Figure 1-24 .

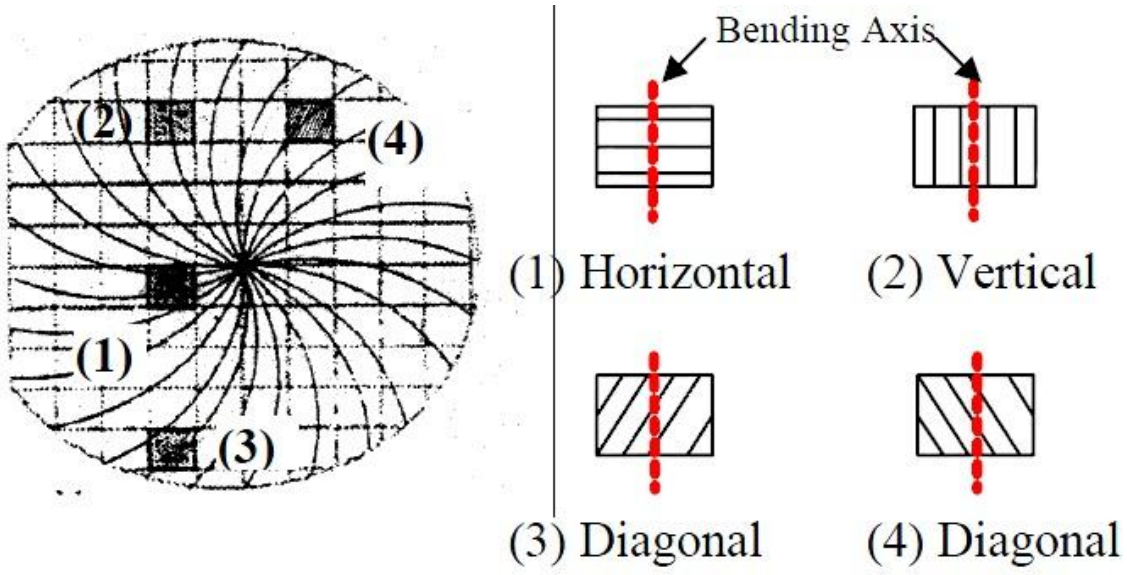

Figure 1-24. Backside grinding patterns correlating to bending tests (Chong 2004).

Bivragh Majeed *et al,* (Majeed 2006) performed experiments on 5 mm x 10 mm die samples in a three-point bending test to investigate the effects of thinning on different properties of silicon test die. Thicknesses for the various sample die ranged from 50 to 525 µm. Sample test die were fabricated with a diffused heater resistor and three temperature sensitive diodes all on the front surface. The backsides of the wafers were ground down to a desired thickness. Two types of separation techniques were used: mechanical dicing with a specialized diamond tipped blade (sawing) and a cost intensive laser dicing process, though laser dicing was only done on 50 µm samples. The thinning procedure varied due to different amount of wet spin etching on the ground side. After singulation, atomic force microscopy (AFM) was performed to determine surface roughness of each thinning procedure. Surface roughness was found to decrease as wafer thickness decreased. Fracture strength was calculated with equation 1-2. Majeed did not

measure the radius of curvature of die in the bending structure, instead he used the equation

$$R_{cur} = \frac{4\delta^2 + l^2}{8\delta} \qquad \text{(Eq 1-3, Majeed 2006)}$$

where δ is the vertical displacement at which the sample breaks and l is the gap between the supports. R_{cur} is a measure of flexibility and is expected to be high for very thick un-flexible die while very thin die will have a small radius of curvature.

After stress values where obtained from three-point bending, the theoretical flaw size for each sample was estimated based on silicon material properties. This "theoretical flaw size" is the size or depth of an initial flaw predicted to start the crack propagation that leads to complete die failure at the measured fracture stress. The equation for flaw size used by Majeed is the fracture toughness equation and defines the flaw length c by

$$\boldsymbol{c = \frac{1}{\pi}\left(\frac{K_{IC}}{1.12\sigma}\right)^2} \qquad \text{(Eq 1-4, Majeed 2006)}$$

where K_{IC} is the fracture toughness of the material and σ is the stress perpendicular to the flaw. The factor 1.12 in Equation 1-4 is related to orientation assumptions with respect to what type of flaw is being loaded. The factor K_{IC} for all of Majeeds experiments was a constant 0.9 MPa-$m^{1/2}$. Table 1-2 below shows a summary of Majeeds results. Laser cut samples were roughly 45% weaker than the dicing saw cut samples, likely due to pits and unsmooth surfaces created by the laser ablation process.

Sample ID	Load (N)	Extension at break (mm)	Fracture stress (MPa)	Radius of curvature (mm)	Average flaw size (μm)	Roughness Ra (nm)
525	-25.54 ± 8	-0.15 ± 0.05	223 ± 69	-55.20 ± 8	5.78 ± 1.65	154.21
250	-10.05 ± 4	-0.20 ± 0.07	386 ± 100	-44.05 ± 6	2.65 ± 0.65	3.43
100	-2.12 ± 0.49	-0.32 ± 0.06	509 ± 119	-25.42 ± 6	0.98 ± 0.32	1.22
50	-0.69 ± 0.08	-0.50 ± 0.10	666 ± 150	-17.77 ± 7	0.64 ± 0.1	1.05
50 LD[a]	-0.37 ± 0.10	-0.39 ± 0.10	354 ± 125	-21.25 ± 7	2.1 ± 0.9	

[a] Laser diced.

Table 1-2. Results from Majeed's experiments (Majeed 2006).

All broken samples were separated into three categories: low breaking force; average breaking force; and high breaking force. Samples that fractured at lower forces tended to shatter into a few larger pieces, samples that fractured at average forces tended to shatter into about 5 pieces, and high fracture force samples broke into many small silicon shards. The high fracture force samples shattered into many pieces at failure due to a large amount of strain energy being released. This large amount of energy caused multiple failure sites and propagation paths. All average and high force fracture types started off with a smooth mirror region fracture wall profile which is expected for a <111> plane fracture. The mirror region eventually merged into a much rougher "mist" region which is indicative of a stress change and shows "chevrons" that indicates the direction of fracture (Majeed 2006).

Landesberger *et al* (Landesberger 2001) also investigated the mechanical strength of ultra thin silicon die by means of a three-point bending test. The research dealt with 20 to 65 µm thick wafers fabricated using support wafers bonded to the substrates using temperature sensitive tapes. These tapes have one permanent bonding side and the other

side uses an adhesive, that when brought above a certain temperature, loses its adhesive property. Landesberger *et al* constructed three types of samples; the first used wafers that were diced after they had been thinned, the second were pre-diced trenches done by a dicing saw and then thinned using the DbyT process, and the last sample lot had DRIE trenches fabricated onto the substrates that were then separated by a DbyT process.

By use of the DbyT method, dies with smaller defects can be obtained. Trying to dice a thinned wafer can induce more damage if it is not rigidly supported. For the DRIE sample preparation standard photo-resist was used to pattern the grooves and SF_6 gas was used as the plasma etching source. All DRIE sample trench widths varied from 5 to 100 µm and every sample was etched 30 µm deep. After all samples were adhered to a support wafer, a backside grinding process was done followed by a spin-etch. Spin-etch depths varied from 0 to 80 µm. Samples were then put in a three-point bend test and loaded until fracture. A histogram for the diced wafers after thinning is shown in Figure 1-25 below.

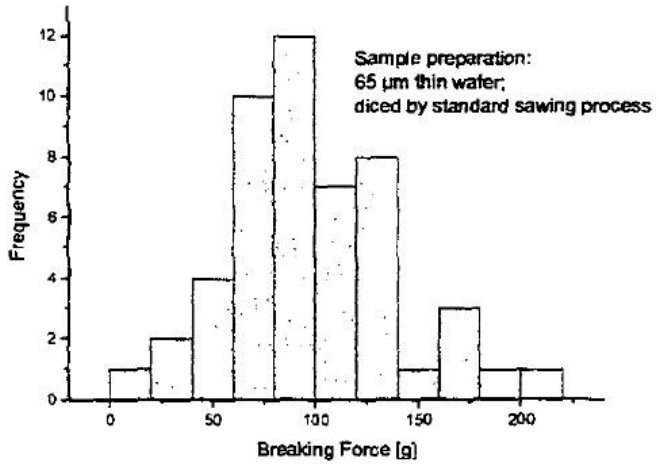

Figure 1-25. Frequency distribution for the diced after thinning samples. (Landesberger 2001).

Landesberger *et al* also investigated the effect of backside etching on grinding. Etching 15 µm after grinding gave a factor of two improvement on fracture strength, but etching anymore than that had no effect. Landesbergers graph of the effects of backside grinding is shown below Figure 1-26. Note that the standard deviation bars are quite large and can be an indication of low repeatability.

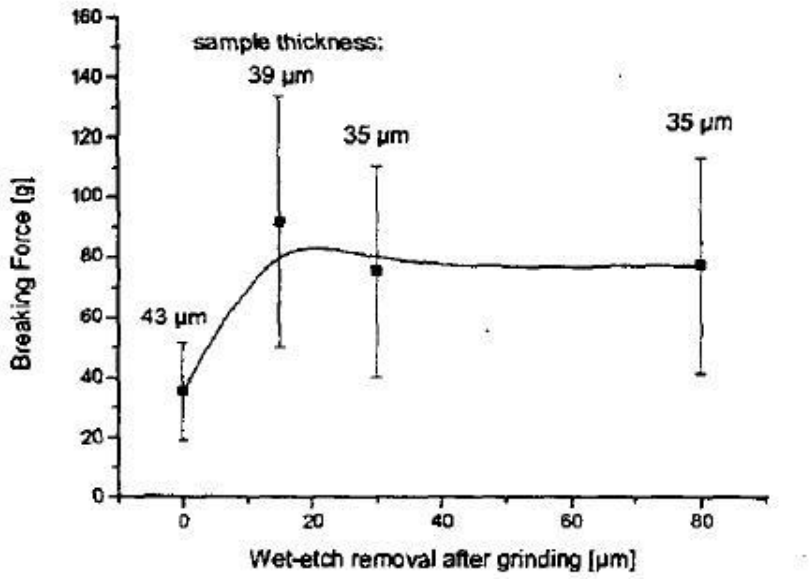

Figure 1-26. Effect of etching on backside grinding (Landesberger 2001).

Another test done by Landesberger was to compare dice by thinning samples to the standard sawing process. All of the DbyT samples came from the second sample preparation lot (diced trenches followed by the thinning procedure). It was noted that the standard 3-point bend distance of 16 mm was too large for most of the thinned samples because of flexibility, so the distance was decreased to 6 mm to reduce the radius of

curvature of the samples. Both sample lots had a wet spin-etch treatment of 30µm to relieve grinding stress. The DbyT samples were thinner yet broke at twice the force, Figure 1-27.

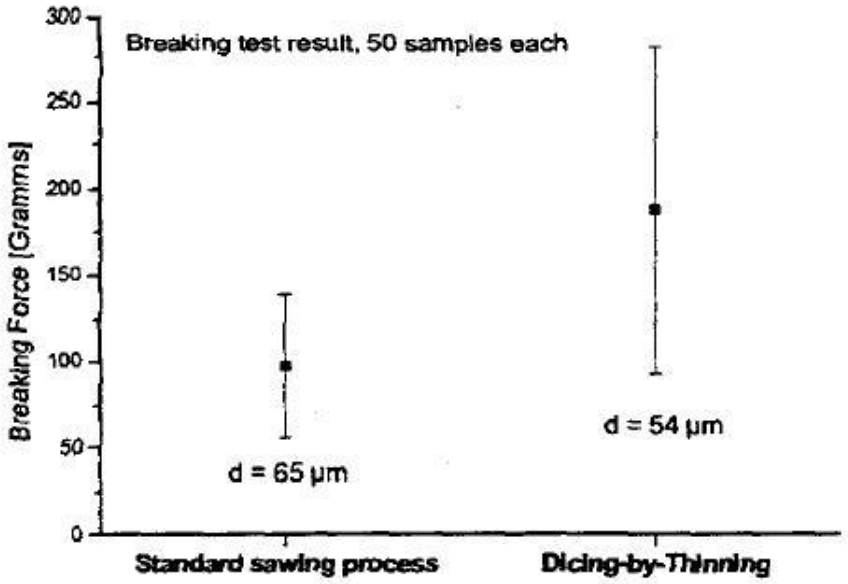

Figure 1-27. Dice by thinning process versus standard sawing process (Landesberger 2001).

The last experiment done by Landesberger *et al* was the breaking of 20 µm thick samples that were DbyT with DRIE grooves. Final thickness of the dies were 20 µm but only after 45, 30, and 15 µm of material was wet-etched from the backside. The results of this test showed that the mean fracture force of the thin chips increases with increased material removal on the backside. Some of the thin die could not be broken at all. Another interesting result is that there was no saturation behavior for the mean fracture force like there was in the thicker wafers. The author points out that damage induced by backside grinding could depend on wafer thickness. Results for the 3rd experiment results is shown in Table 1-3 below.

Etch removal [μm]	Number of samples	Chips not broken	Mean fracture force [g]	Std. dev. of force [%]
15	32	8	26	34
30	32	17	37	27
45	32	21	60	43

Table 1-3. Results of 20μm breaking tests (Landesberger 2001).

A number of important trends found from the literature review have relevance to the current work. A few of the most pertinent findings that were used to guide this current investigation are restated herein. In particular, it is noted that three-point bending tests are traditionally the standard method for testing fracture strength of silicon wafer specimens. Additionally, dry-etch procedures yielded higher fracture strength devices compared to traditional dicing saw separation methods. Samples produced via dice by thinning benefited from a stress relieving wet-etch to optimize die fracture strength and resulted in a higher average strength than standard sawing processes.

Other important findings that were considered include the effects that thermal processing and other fabrication methods can have on wafer strength, the effects of die thickness and defects on fracture strength, and the tendency for high energy die fractures to have numerous crack propagation paths. From past research it is expected that DRIE separated wafers will produce the highest fracture strength die due to the smooth edges it produces. To date, however, this has only been shown for very thin wafers.

II. Procedure

2.1 Preparation of Standard Dicing Saw Notched Samples

Materials:

a) Disco Dicing Saw (DAD321).

b) Dicing tape and dicing accessories.

c) 20 x (525 µm thick, 100 mm diameter) (100) orientation boron doped wafers (Engineering Wafer Company).

A Disco dicing saw was used to mechanically dice streets into the (100) silicon wafers, with streets aligned parallel and perpendicular to the <110> wafer flat. The wafers were first placed face down (polished side) on a hot plate while dicing tape was pulled over the back. The samples were rolled with a rubber tool to eliminate bubbles between the substrate and dicing tape. If bubbles are present then the dicing depth will change in certain areas of the cut. A metal ring was then placed over the tape so that the wafer, tape, and ring could be mounted on the dicing saw. Finally, the wafer package

was aligned on the dicing saw chuck. The chuck is a porous ceramic that pulls a vacuum holding the wafer in place as the dicing saw program is run. The dicing blade used for all cuts had a nominal width of 70 µm. For all dicing samples, five streets were cut aligned to the <110> wafer flat, followed by another five streets cut perpendicular to the <110> wafer flat. Each street was placed 17.07 mm apart giving a die size of 17 mm, with a total of 16 complete die obtained from each fully diced wafer. Dicing speed was performed at 1 mm/s for all diced specimens. The wafers were diced at depths of 25, 50, 75, or 100% of the total wafer thickness. Scott Cambron, a trained technician at the University of Louisville MNTC, operated the dicing saw for all diced samples used in this work. Figure 2-1 below shows the dicing routine for all diced wafers.

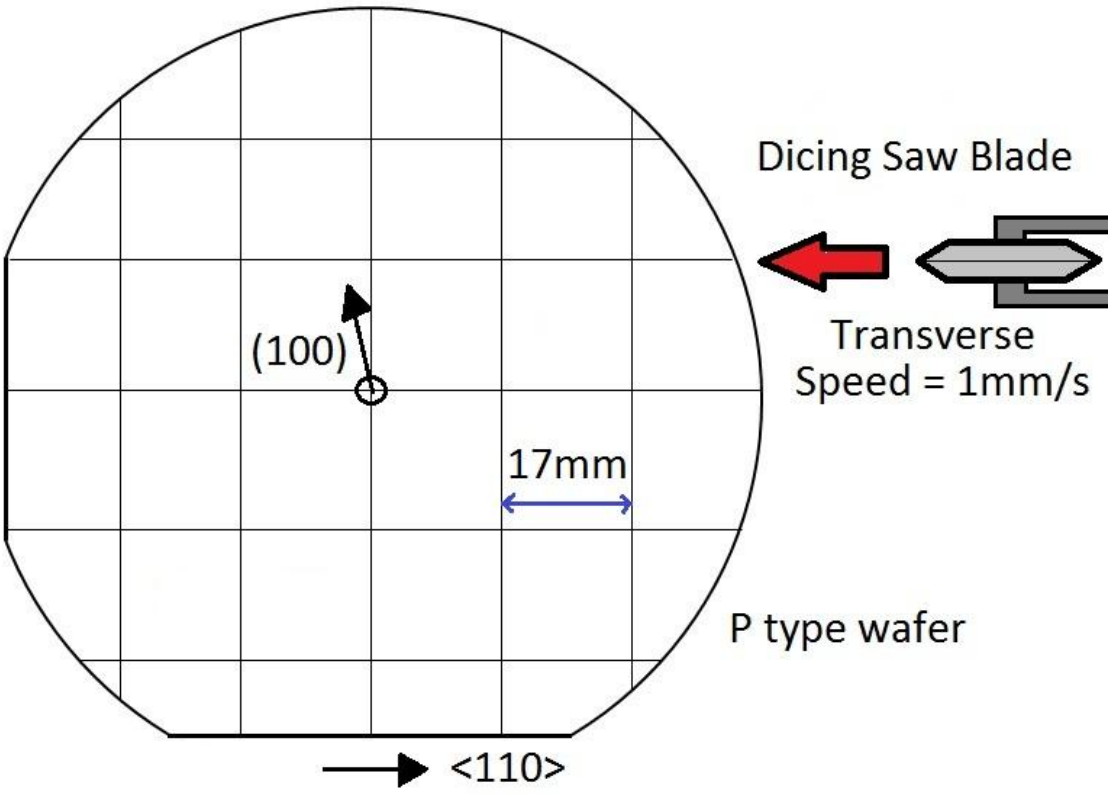

Figure 2-1. Dicing scheme for the diced samples.

After dicing, the wafer package was carefully removed from the vacuum chuck, and then the wafer and tape were cut apart from the metal ring. The dicing tape was then sheared at a 0 to 10º angle so that minimal normal force is applied to the wafer and prevent unintentional die separation. In the case of 100% cut wafers the dies were simply pulled from the tape. All samples were stored in a clear carrying container and handled with extreme care until they were ready for separation and/or the die fracture test.

Figure 2-2. Dicing tape removal scheme.

2.2 Preparation of DRIE Etched Samples

Materials:

a) STS (MSC) DRIE Multiplex machine, Figure 2-3 below.

b) Shipley 1827 positive photo resist.

c) Headway Spinner and hotplate bench.

d) SUSS Mask Aligner.

e) 23 x (525 µm thick, 100 mm diameter) (100) orientation boron doped wafers.

f) Acetone and N-Methyl-2-pyrrolidone (NMP).

g) Veeco Dektak 8M Profilometer, Figure 2-4 below.

h) Zeiss Axio Microscope, Figure 2-5 below.

Figure 2-3. STS DRIE machine at the University of Louisville.

Figure 2-4. Dektak Profilometer.

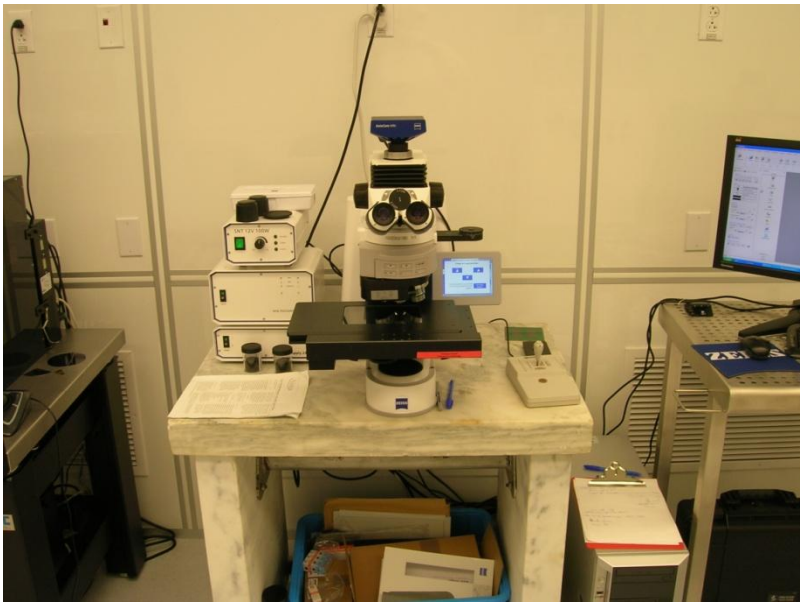

Figure 2-5. Zeiss Axio Microscope.

Prior to deposition of the photoresist masks needed for DRIE processes, the wafers were subject to a 5 minute prebake at 115ºC on a hotplate to evaporate any moisture that may be adhered to the surface. Shipley 1827 photoresist was then poured onto the wafer until it covered about one half of the surface. Two types of profiles were used for the DRIE etching process which defined the thickness of the photoresist. Because the resist mask is slowly depleted during etching, careful attention was paid to photoresist thickness. The deeper etch depths needed a thicker photoresist layer so that the entire masking layer survives the etching process. For the 25% and 50% etched samples, the spin profile used a ramp rate of 1000 rpm/s and a spin speed of 3000 rpm for 20 seconds. A soft bake at 115ºC for 1 minute was done afterward to evaporate the majority of the remaining solvents in the photo resist. The 75% and 100% etched samples' spin profile was nearly the same as the other profile, except that the spin speed used was 1800 rpm. A soft bake at 115ºC for 1 minute was done afterwards to evaporate

the majority of the remaining solvents. The thicker resist profile resulted in a slightly thicker photoresist bead around the edge of the wafer.

The first step in exposing the photoresist was to insert the photo mask into the SUSS aligner and lock it into place. The photo mask for the DRIE is shown in Figure 2-6 and Figure 2-7 below. Each die was 17 by 17 mm and each wafer held 16 individual die. A 70 μm street width was chosen for comparison with the 70 μm dicing saw specimen. The wafers with photoresist were put onto a vacuum chuck and locked into Suss aligner the machine for ultraviolet light exposure. Next the wafer is aligned and exposed for 40 seconds at roughly 20 mW/cm^2. The wafer was developed in a bath of Microposit MF-319 for 1 minute and dried using the nitrogen gun. The developed profile was inspected under a microscope to determine if there are any major flaws in the photoresist such as tears or undeveloped regions. A hard baking was done after inspection at 115ºC for 2 minutes to drive out the rest of the solvent in the photoresist. After the photoresist was done developing, the profile was measured using the Dektak Profilometer and the planar profile is measured using the Axio microscope, Figure 2-5. For a spin speed of 1800 rpm/s and 3000 rpm/s the photo resistance thickness was 3.2 μm and 4.25 μm, respectively.

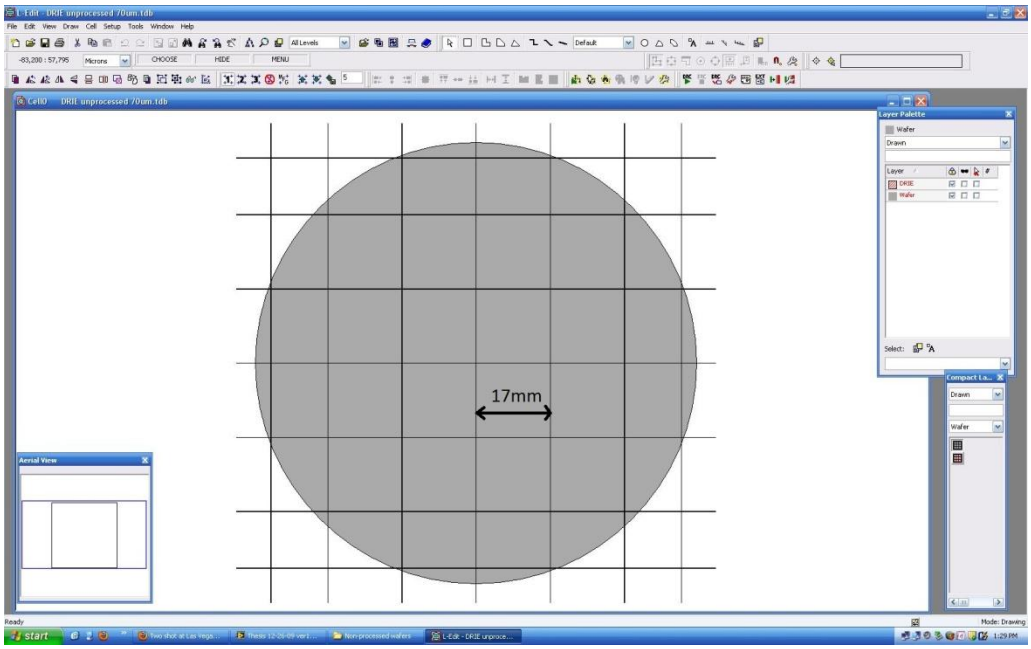

Figure 2-6. Photomask for DRIE etched samples designed in L-edit.

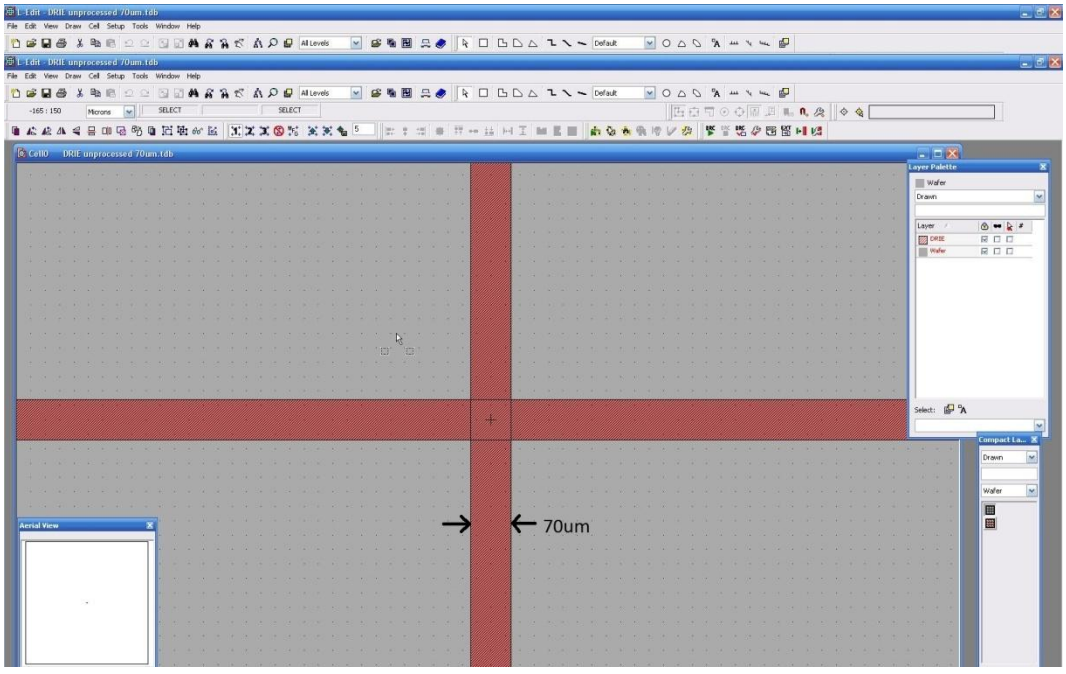

Figure 2-7. Enhanced view of the 70μm trenches.

Measuring the trenches on the photomask under a microscope revealed that they were nearly 70 μm as expected. There was a slight variation of the actual photo resist profile after development but none ever went more than ±3 μm from the optimal 70 μm trenches. Pictures of a 50% DRIE #3 wafer after development are shown in Figure 2-8, Figure 2-9, and Figure 2-10 below. Variations from the center, one square diagonal, and two squares diagonal from the center consistently did not vary more than 1μm.

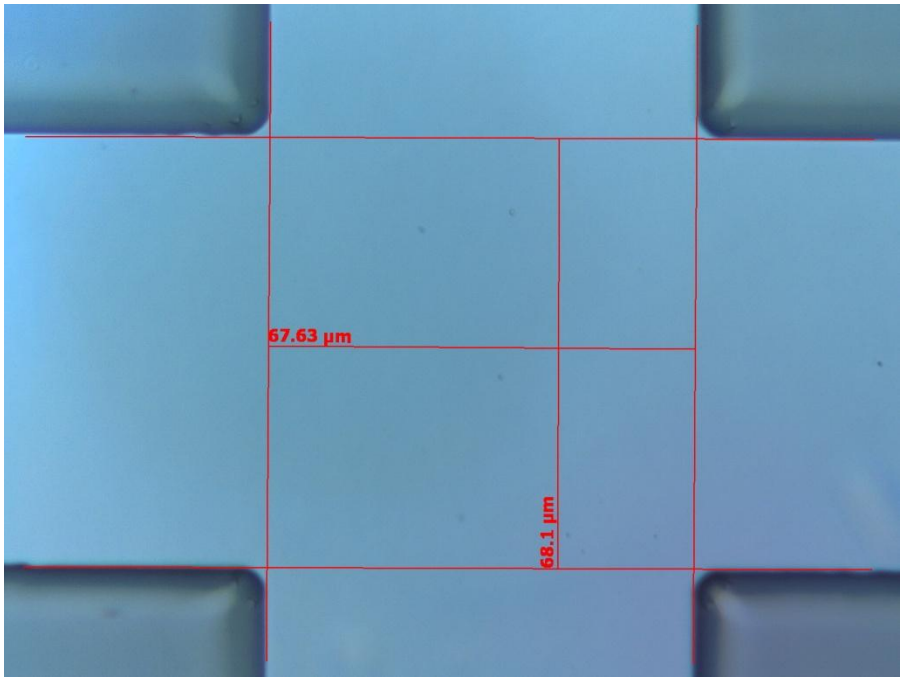

Figure 2-8. Axio picture of photoresist developed on a wafer. DRIE 50% wafer #3, center.

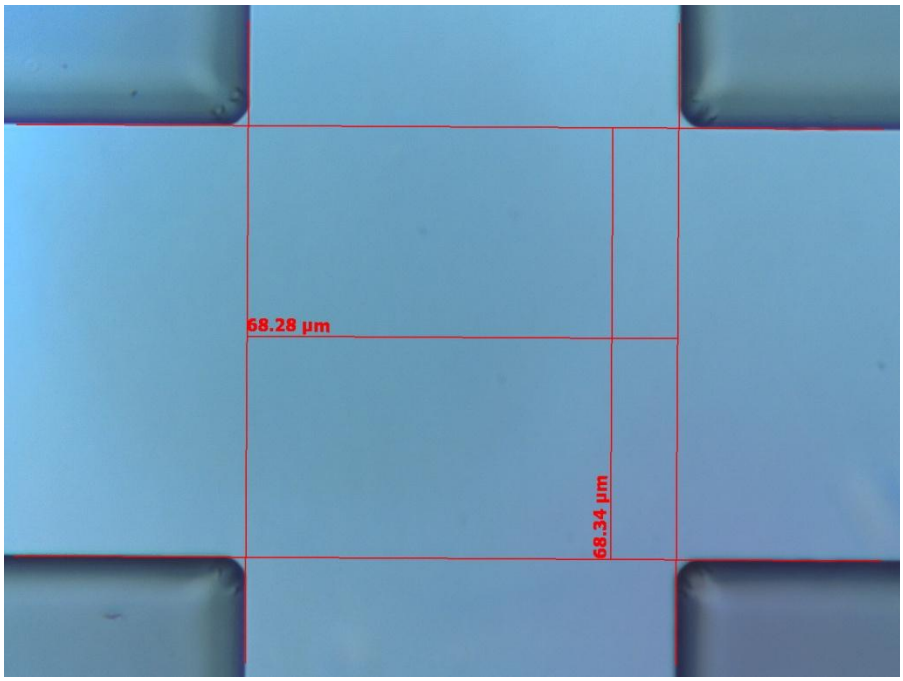

Figure 2-9. Axio picture of photoresist developed on a wafer. DRIE 50% wafer #3, one square diagonal from the center.

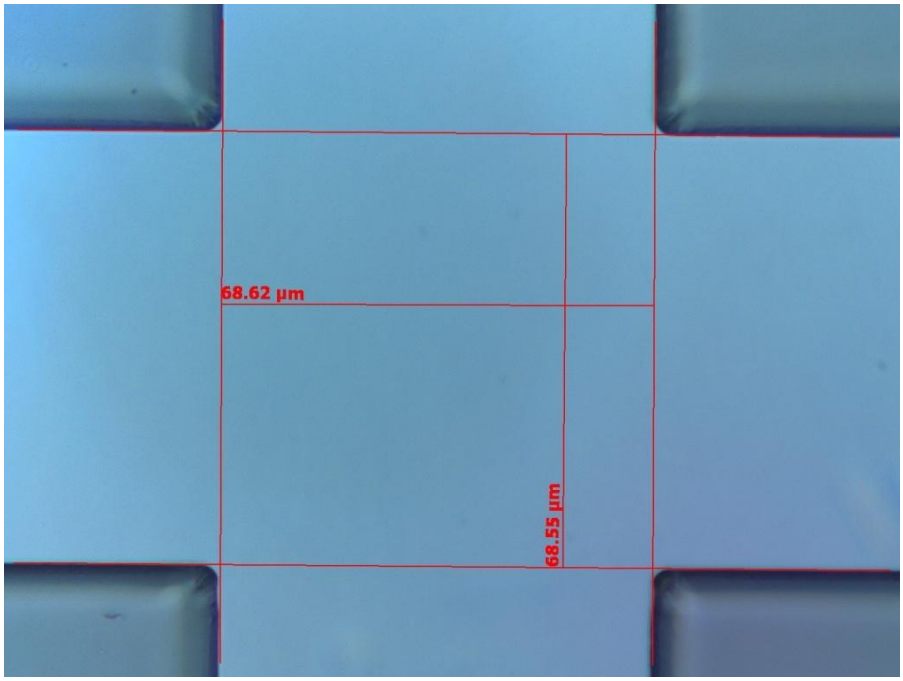

Figure 2-10. Axio picture of photoresist developed on a wafer. DRIE 50% wafer #3, two square diagonal from the center.

After etching in the DRIE was done, pictures were taken in the Axio so that the top of the trenches could be measured. About 3 μm of horizontal etching occured, which is shown in Figure 2-11, Figure 2-12, and Figure 2-13 below.

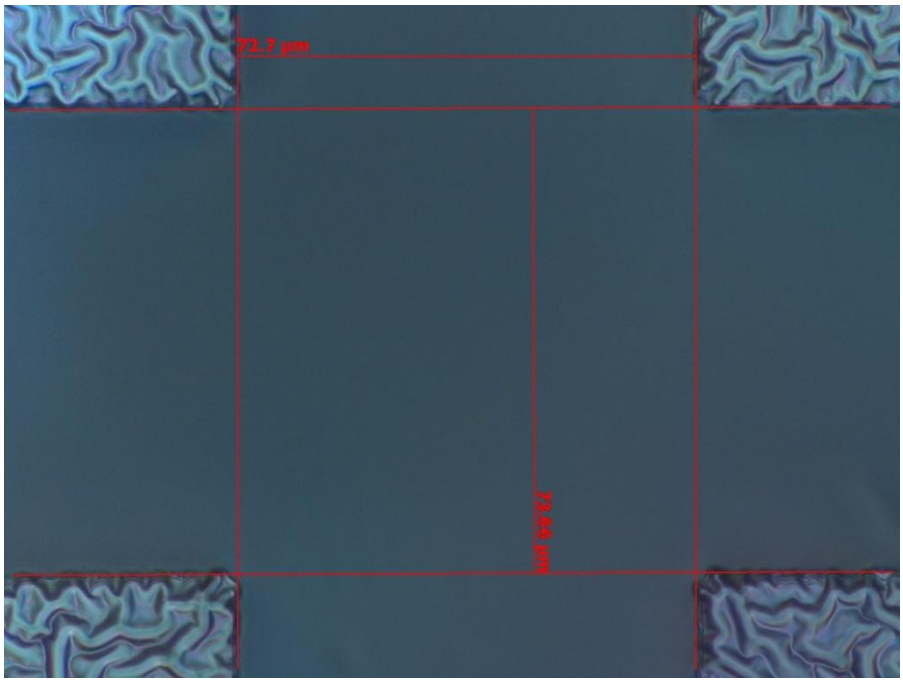

Figure 2-11. Axio picture of wafer after DRIE etching. DRIE 50% wafer #3, center.

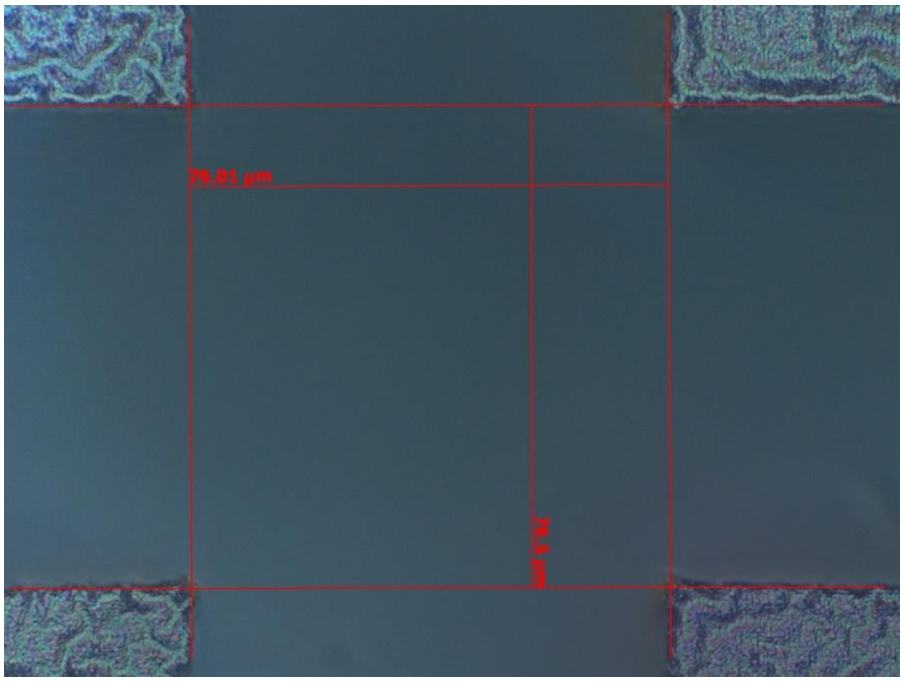

Figure 2-12. Axio picture of wafer after DRIE etching. DRIE 50% wafer #3, one square diagonal from center.

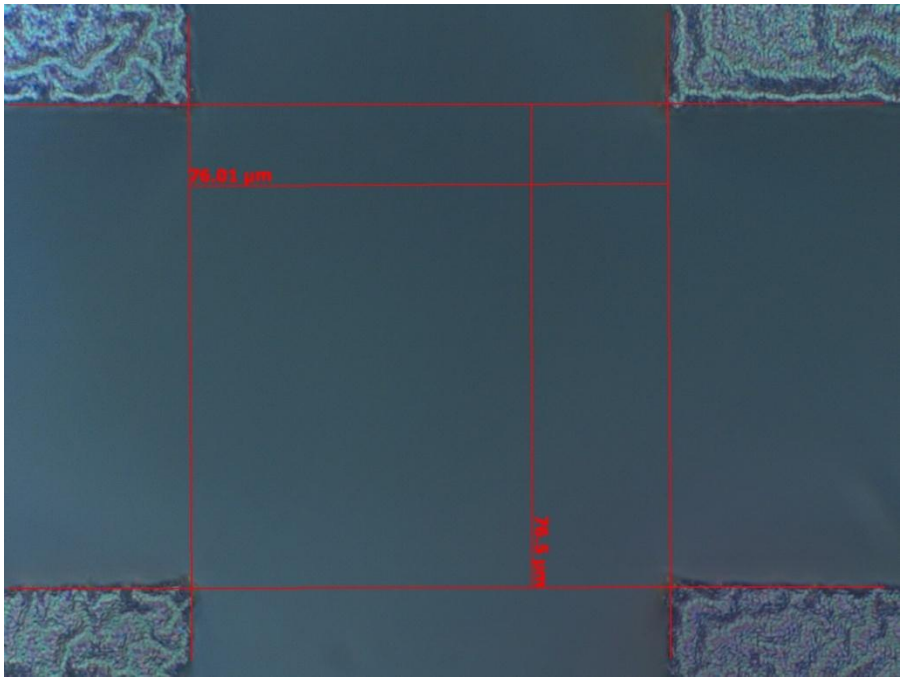

Figure 2-13. Axio picture of wafer after DRIE etching. DRIE 50% wafer #3, two square diagonal from center.

For all etching depths, initially, each wafer was put into the DRIE for 150 cycles. The STS DRIE machine has a standby pressure of about 0.4 mTorr. Etching settings used were as follows: Pump down for 20 seconds, etch to passivate time ratio is 9:6, base pressure 0.2 mTorr. The etching gas was 160 sccm SF_6, 13 sccm O_2 and the passivation gas was 75sccm C_4F_8. The STS chiller was set at a constant 15ºC. The only parameter that varied for the DRIE etching was the total number of cycles run, which changed the total etch depth. Figure 2-14 shows a wafer after the initial 150 cycles. Each cycles takes 15 seconds, so the initial 150 cycles took 37 minutes and 30 seconds to complete.

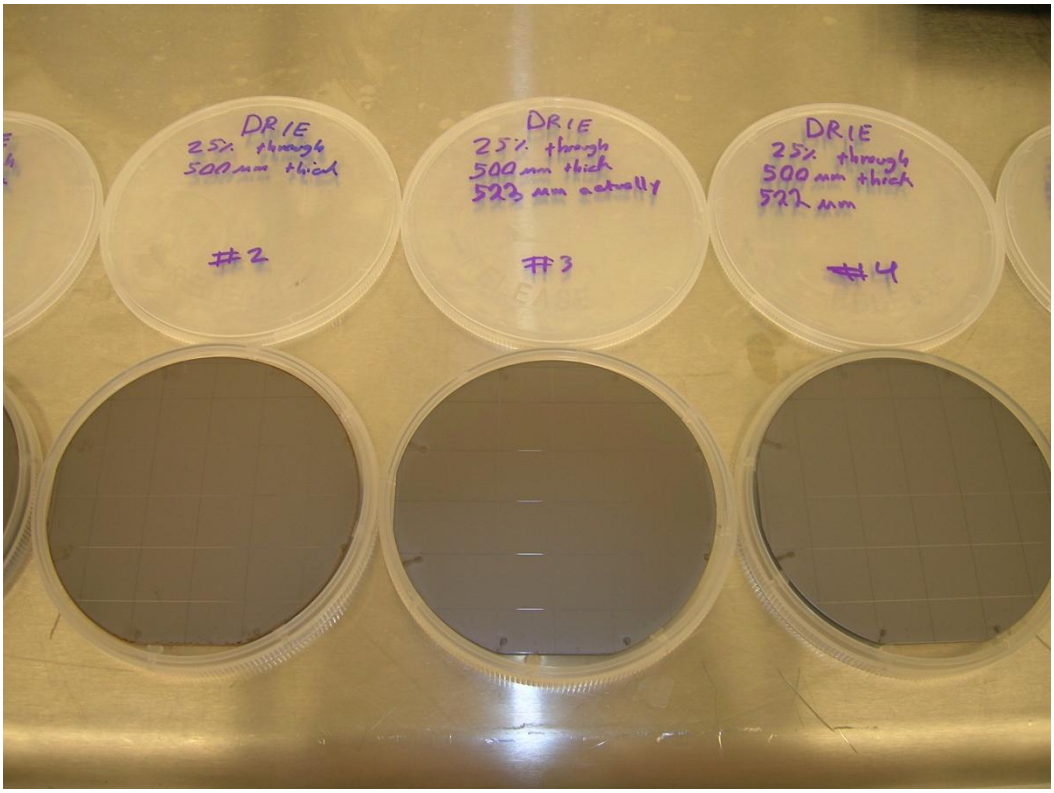

Figure 2-14. Wafers with photoresist after 150 cycles in the STS DRIE. Each wafer is 97.4mm wide.

To determine the number of cycles needed to etch to a certain depth, a set of trials was done using 150 cycle intervals and then measuring the etch depth using the Zeiss Axio. The Carl Zeiss Axio microscope was used to measure the trench depths and had lens focus step size of 25 nm, a reproducibility rate of ±75nm, and a mechanical stage step size of 0.1 µm with a reproducibility of ± 0.3 µm is used. Using planar focusing, the trench depth was found for each test wafer and then plotted versus the number of cycles. Both linear and polynomial fits were used to back out an equation describing trench depth and cycles. The results of the trial are shown below in Figures 2-5 and 2-6. Since the polynomial had the better R^2 value, it was used for determining the appropriate number of etch cycles to achieve our desired depths. The polynomial equation defining cycles given depth was

$$N = 0.0009 * (d^2) + 1.2385 * d + 25.28 \qquad \text{(Eq 2-1)}$$

where *N* is the number of cycles and *d* is the etched depth measured to the bottom of the trench.

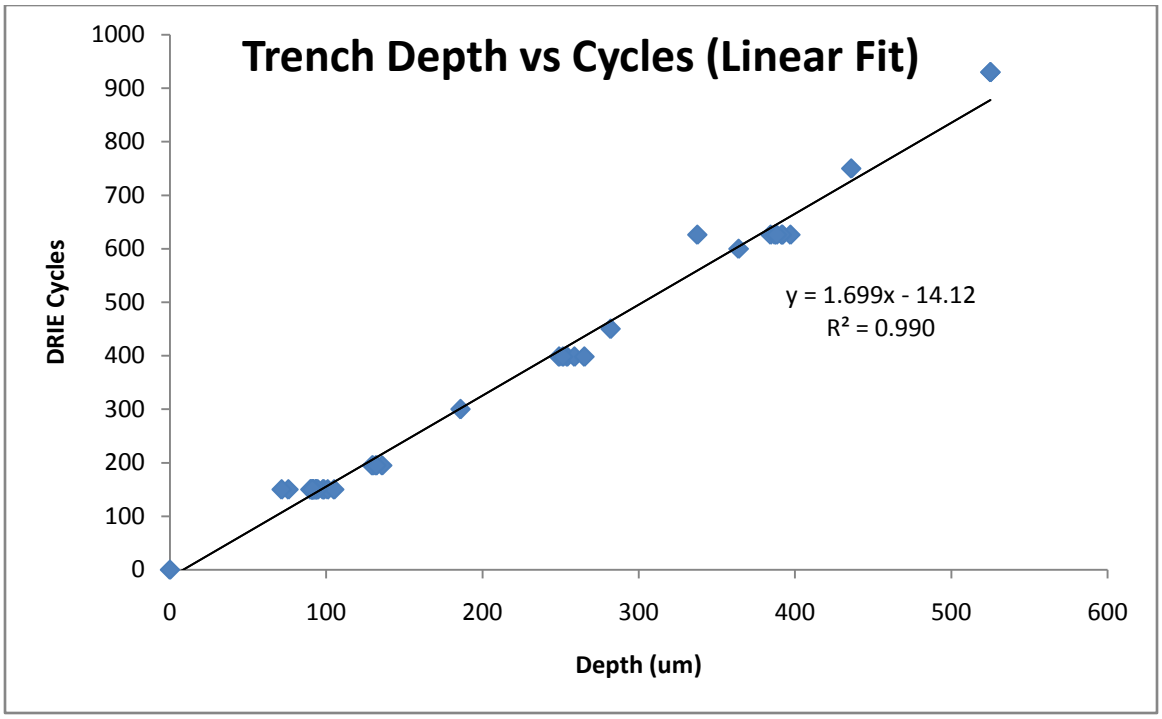

Figure 2-15. Linear profile for the etch rates.

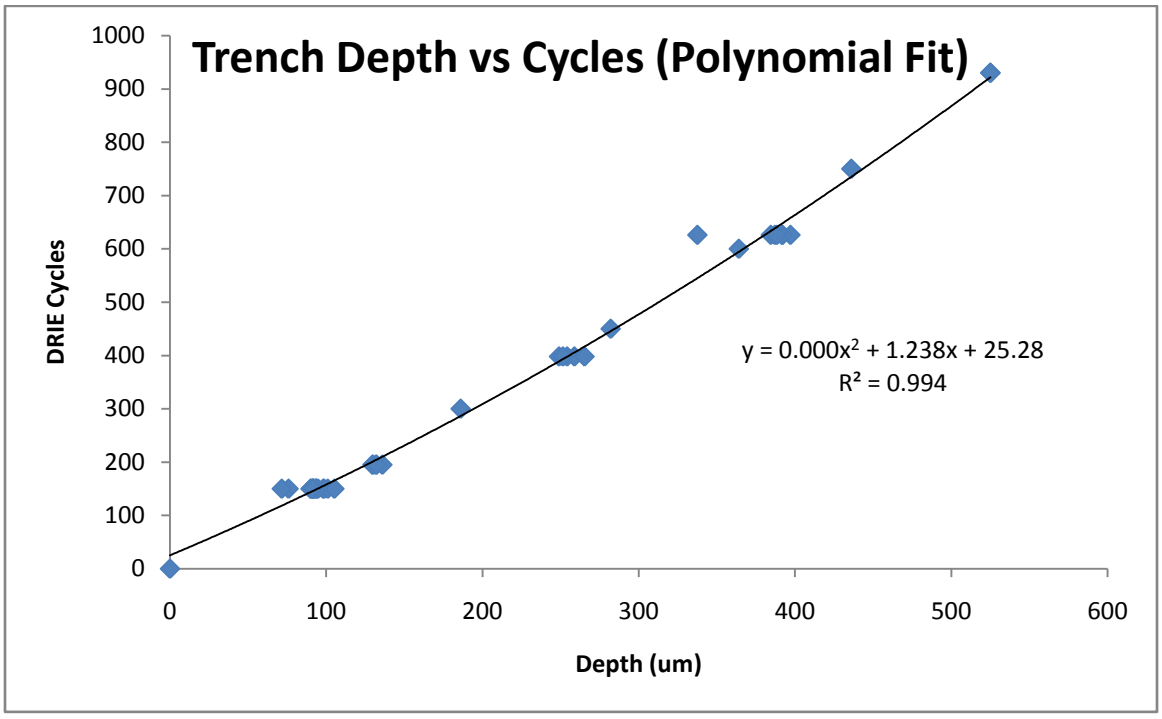

Figure 2-16. Polynomial profile for etch rates.

After the initial 150 cycles in the STS DRIE, the wafer with the remaining photo resist was baked on a hot plate at 115ºC. This additional bake hardens the photoresist and causes it to become more resilient to the etching process. A backing wafer was also put on the hot plate and brought to 115ºC so that the temperature sensitive adhesive, Crystal Bond, could be applied. The Crystal Bond was applied to about 75% of the wafer and spread out with a metal tool. Afterwards, the wafer that has already been etched 150 cycles was put on top of the backing wafer and then removed from the hotplate so that the Crystal Bond could cool and set. The sample wafer and backing wafer were then put into the DRIE machine and etched to the desired depth.

Once the sample wafer was done etching, it is put back on the hot plate at 115ºC and carefully removed from the backing wafer. The sample wafer was then cleaned with isopropyl alcohol to strip the remaining photoresist and then was rinsed with de-ionized water. A nitrogen gun was then utilized to dry the wafer while it was laid flat. Care must be taken during the cleaning and drying process so as not to break the sample. The etched sample was then loaded into a carrier and brought back to the lab to be cleaved with the three-point bending structure.

To prepare the double sided wafers, a 25% etch was done on one side just like the previous DRIE wafers. Then dicing tape was put on the etched side so that photoresist could be spun onto the backside. After exposure and development a 150 cycle DRIE etch was done followed by a 2 minute 115ºC bake and then the rest of the etch cycles were done to reach 25% depth.

2.3 Separation of Samples Using a Three-Point Bending Structure

Materials:

a) National Instruments Data Acquisition System (NI PXI-1033).

b) Honeywell Model 11 (25 lb_f) Subminiature Load Cell.

c) Lebow 200 lb_f load cell.

d) National Instruments Labview 9.0.

e) 3-Point Bending Structure.

f) 2" Encoded Travel Max Stage (LNR50), Stepper Motor Actuator (DRV014), and APT Stepper Motor Controller (BSC101)

g) Non-drying model clay.

h) National Instruments SCC-SG24 Full Bridge 100x amplifier.

A convertible fixture for either three-point or four-point bending tests was designed using Solid Edge and then was machined in the University of Louisville's prototyping lab. Parts for the bending structure and the assembled bending structure are shown in Figure 2-18 and Figure 2-8 below, respectively. The fixture also has an adjustable span so that it can be modified if needed.

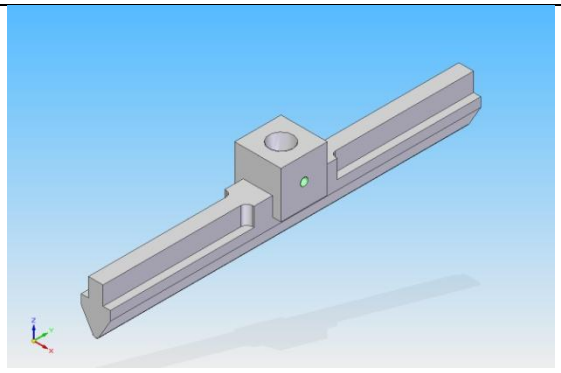

a) 3-Point Bending Head

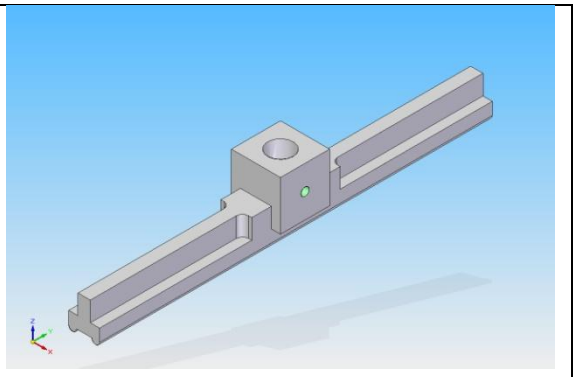

b) 4-Point Bending Head

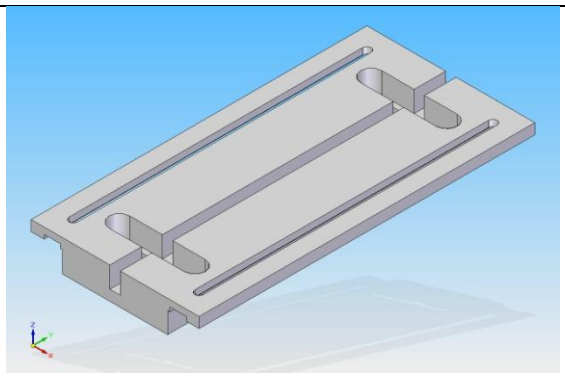

c) Base Plate

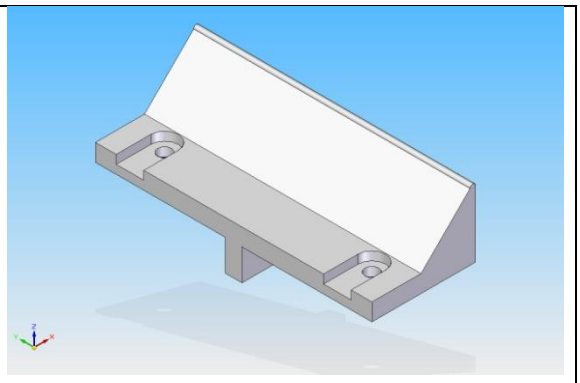

d) Bending Support

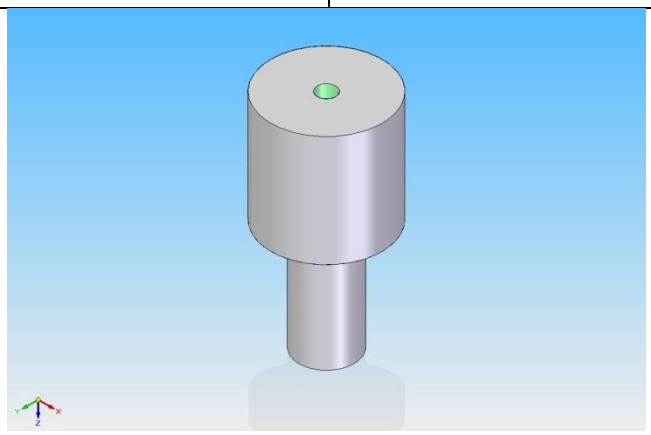

e) Bending Head to Load Cell Adapter

Figure 3-17. Bending structure parts.

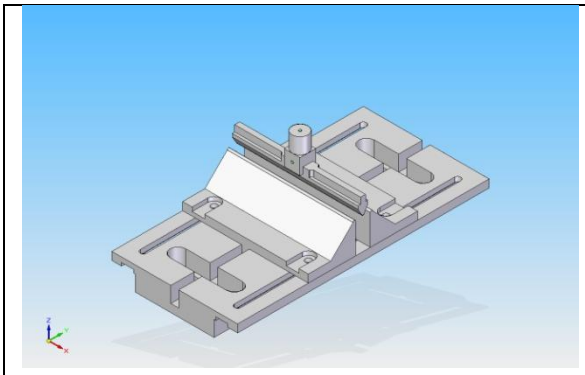

a) 3-point bending structure isotropic view

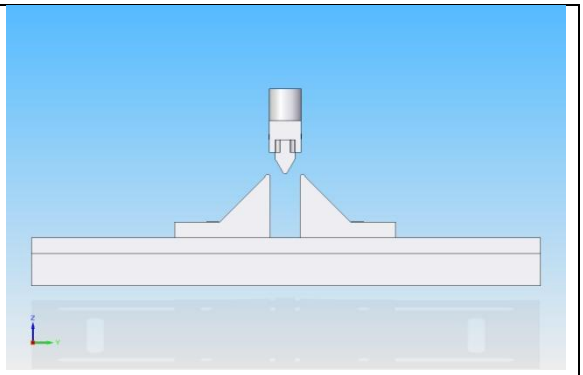

b) 3-point bending structure side view with a 15mm span

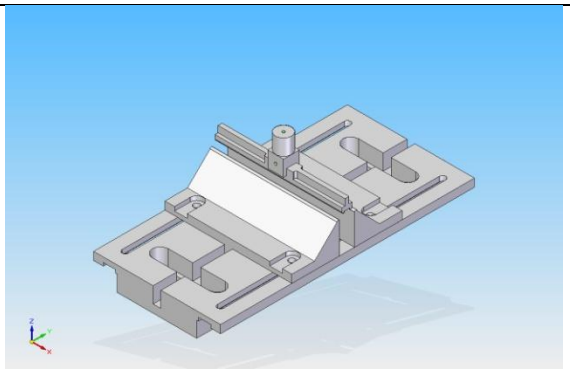

c) 4-point bending strucutre isotropic view

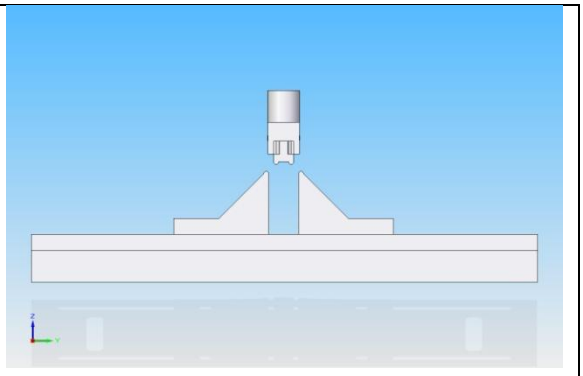

d) 4-point bending structure side view

Figure 2-18. The assembled bending structure.

To measure the exerted force on the samples, a 25 lb_f and a 200 lb_f load cell were used. The load cells exhibit a small change in resistance with strain, therefore a 100x amplifier was used to boost the signal. The boosted signal was read from a National Instruments data acquisition system and recorded with Labview. Figure 2-19 shows the load cell, actuator, and bending structure assembly, while Figure 2-20 shows the Thorlabs controller, and NI-DAQ system with amplifier.

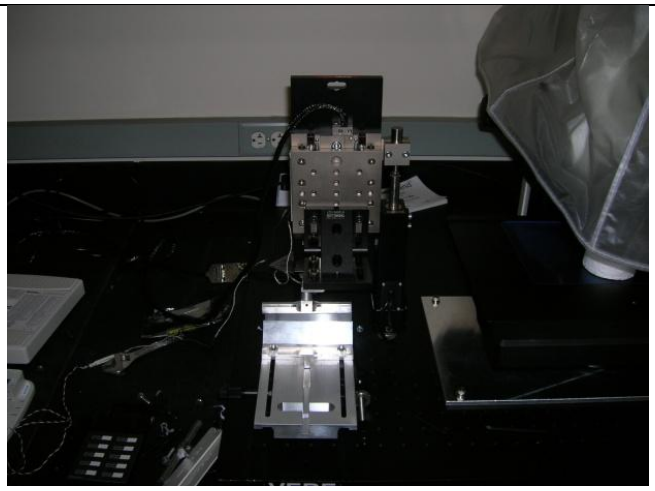

Figure 2-19. Actuator, load cell, and bending structure.

Figure 2-20. Actuator controller, data acquisition system, and amplifier.

Labview 9.0 was utilized to record and organize data. The program was written by the student and was made to simplify the data logging task. Figure 2-21 below shows the front panel of the program. Not only was the raw data for the load cells and stage displacement recorded, but there was an averaged and formatted file that did calculations to simplify data analysis. Some of the formatting included calculating the baseline load before the bending head touches the wafer, using input parameters to calculate maximum three-point bending stress, and trimming/formatting the data so that the Microsoft's Excel file reports displacement versus force .

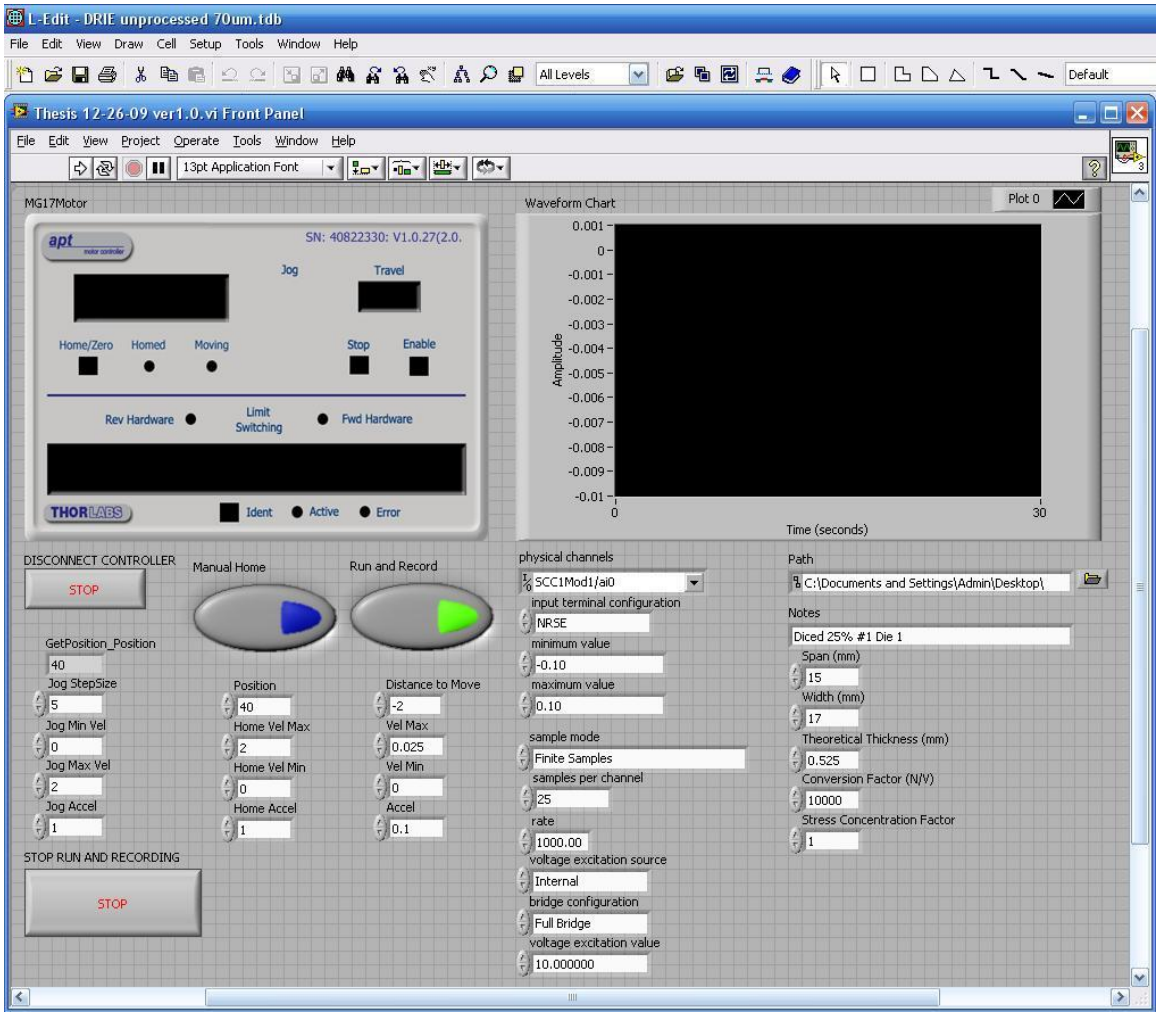

Figure 2-21. LabVIEW program used to log data.

To calibrate the output voltage of the load cells to a force, a known set of weights was applied to the load cells and the voltage was be measured. A graph was then plotted and a slope was derived so that a change in voltage can be related to a change in force. The R^2 value of this graph show how linear the load cells are within a given range. Figure 2-22 below shows output voltage versus mass for the 25 lb_f load cell while Figure 2-23 shows output voltage versus mass for the 25 lb_f load cell. As seen from Figure 2-23 a 0.01 change in μV is equivalent to a 1 Newton change for the 25 lb_f load cell.

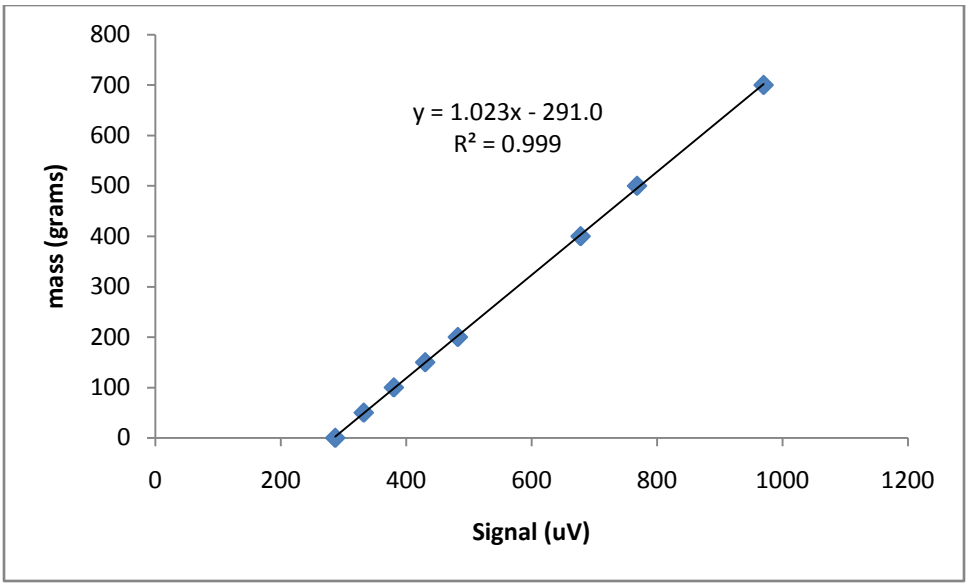

Figure 2-22. Mass versus voltage for the 25 lb_f load cell.

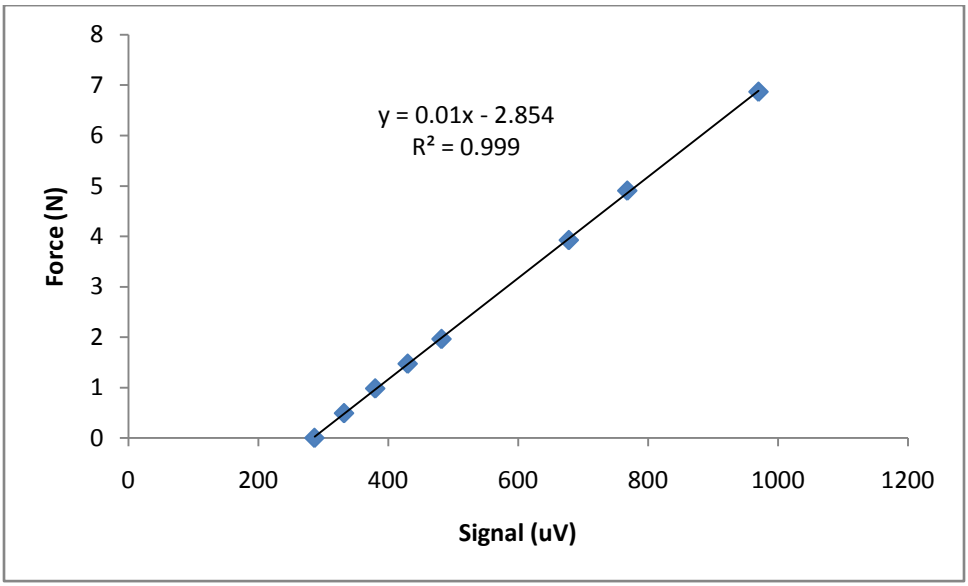

Figure 2-23. Force versus voltage for the 25 lb_f load cell.

Clay was put around the bending structure to dampen the fall of remaining samples that separate during the cleaving process. For every wafer, dies were numbered in the same way so that die performance from every lot could be compared based on

location. The numbers were put on the top polished side of the wafer. Figure 2-24 shows the numbering scheme for each die.

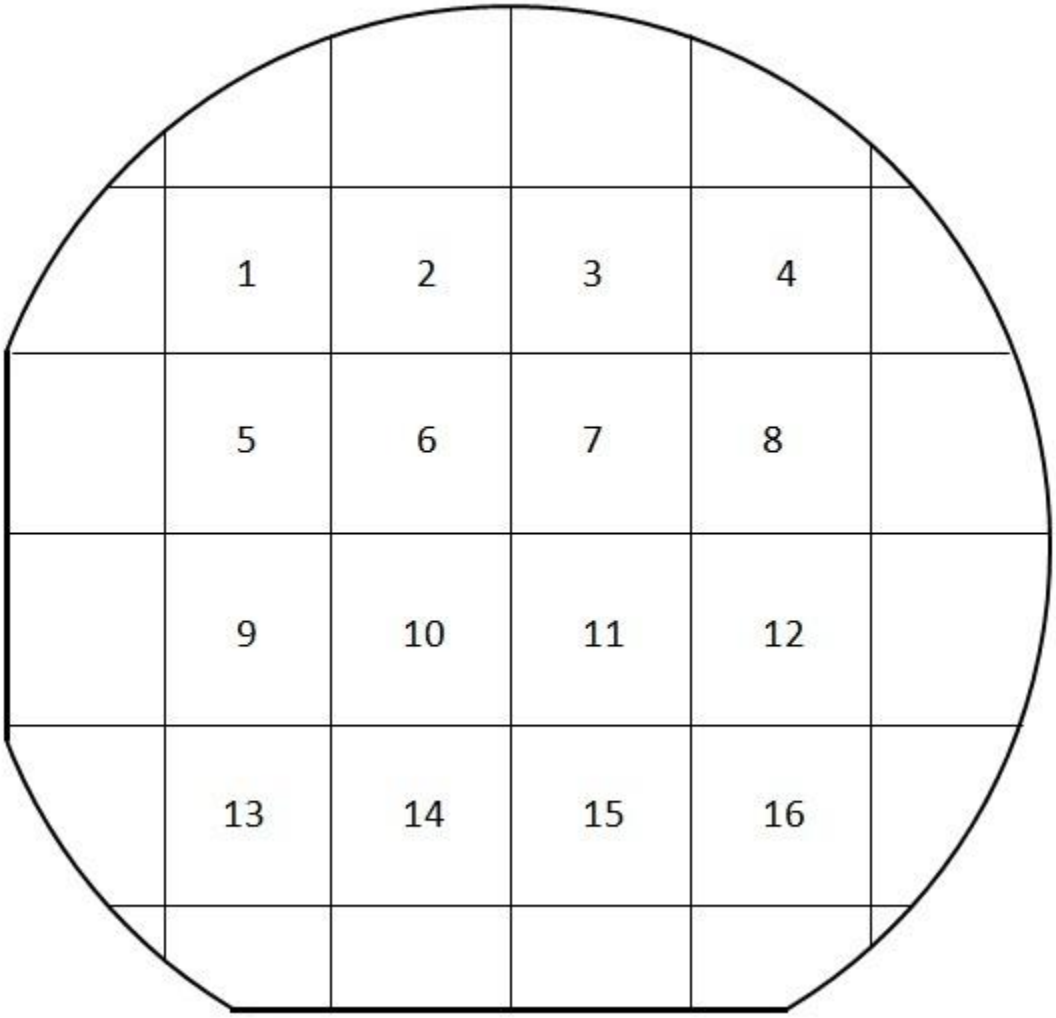

Figure 2-24. Die labeling scheme for each wafer.

Each sample wafer was cleaved in a consistent manner and order. The polished side with the notch was placed face down so that the moving middle support of the three-point bending structure was in contact with the rough back side of the wafer. The breaking order is shown in Figure 2-25 below and was followed for each wafer. Figure 2-25 a) shows the initial breaking runs that were performed for each wafer. During

"Break 1" the specimen has a width of 97.4mm, for "Break 2" and "Break 3" it has a width of 94mm, and for "Break 4" and "Break 5" it has a width of 72.7mm. Figure 2-25 b) shows the order of the remaining "Break" runs for which all samples have a width of 17mm.

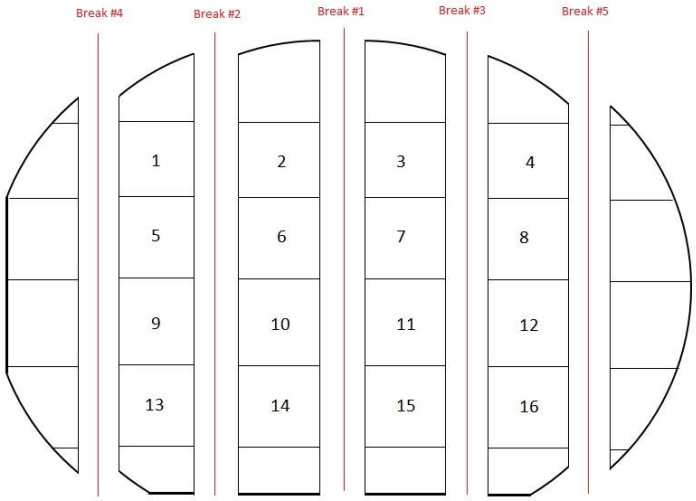

a) Separation testing order (initial breaks).

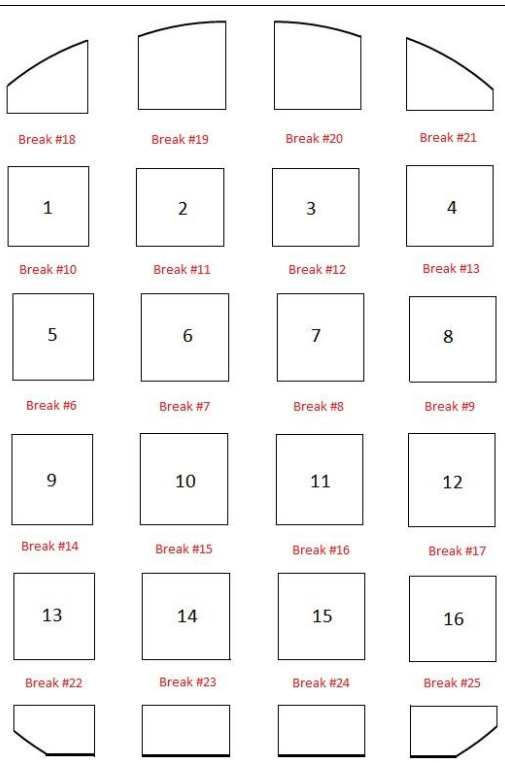

b) Remaining separation runs

Figure 2-25. Breaking scheme for separation.

During the testing routine, the bending structure head was brought within 1mm of the sample and the sample notch was aligned visually with the help of a highlighting marker. Yellow highlight marker will be placed on the back of the wafer so that the notch can be placed directly in line (parallel) with the bending head. The data acquisition rate for the National Instruments hardware was 1000 Hz and 25 samples per channel were grabbed. (using 1 channel). The stage transition speed was set to the absolute minimum (0.04 mm/s) to negate time dependant strain effects.

2.4 Strength Testing of Die Using a Three-Point Bending Structure

Materials:

a) National Instruments Data Acquisition System (NI PXI-1033).

b) Honeywell Model 11 (25 lb_f) Subminiature Load Cell.

c) Lebow 200 lb_f load cell.

d) National Instruments Labview 9.0.

e) 3-Pt and 4-Pt Bending Structure.

f) 2" Encoded Travel Max Stage (LNR50), Stepper Motor Actuator (DRV014), and APT Stepper Motor Controller (BSC101)

g) Non-drying model clay.

h) National Instruments SCC-SG24 Full Bridge 100x amplifier.

To test the strength of each separated die, the three-point bending structure was used with the same parameters as it was for the separation routine. There are two types of die breaking scheme: (a) one with each die being broken polished side in tension and the highlight marker numbers parallel to the bending supports and three-point bending head; and (b) the other with the highlight marker numbers perpendicular to the three-point bending head. This bending scheme is shown in Figure 2-26.

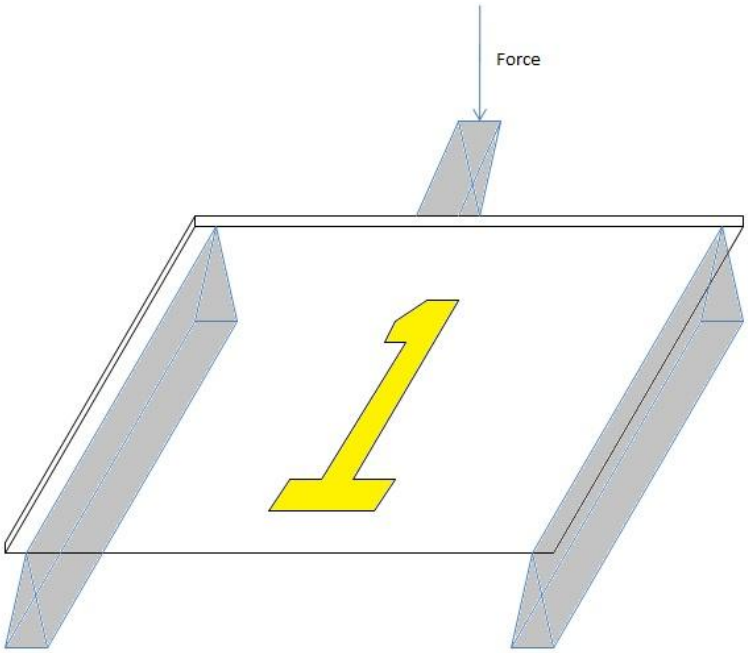

Figure 2-26. Parallel bending scheme.

Figure 2-26 show the middle top support and the two bottom supports. When possible, shards of the broken samples were collected for analysis. The bending support spam for all samples is 15 mm which is exactly the same as the separation bending tests.

III. Results and Discussion

3.1 Stress Concentration Derivation

To derive the theoretical stress concentration factors for the bending separations, ANSYS 12 and Solid Edge were utilized. Prior to beginning the modeling work, cross section profiles of the notch geometries formed by the DRIE and dicing saw were visually inspected using both a scanning electron microscope (SEM) and optical microscopy. The notch geometries associated with the two methods vary significantly due to the vastly different physical mechanism by which they are formed.

Dicing saw trenches had the same bottom radius and side wall slope for all trench depths. To back out the features for the dicing saw, pictures were taken of the notch cross section and then measured graphically with the known wafer thickness (525 μm). Figure 3-1 shows profile images of diced samples taken with a Retiga 4000R monochrome camera (QImaging) and a 20x and 50x objective lens.

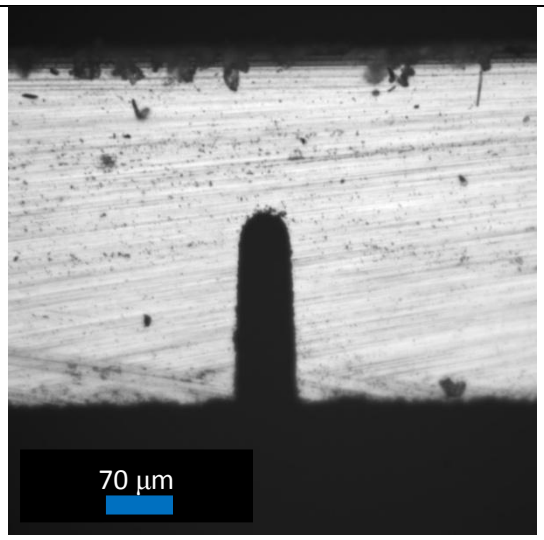

a) Diced 50% at 20x.

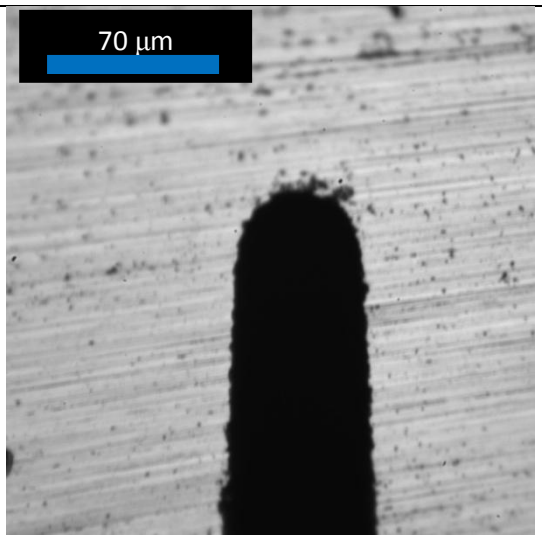

b) Diced 50% at 50x.

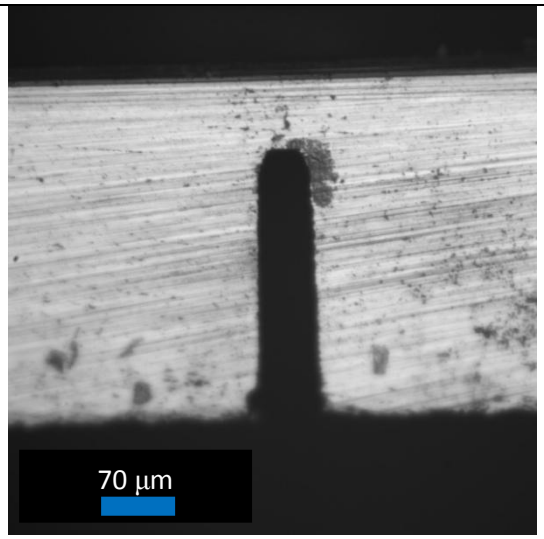

c) Diced 75% at 50x.

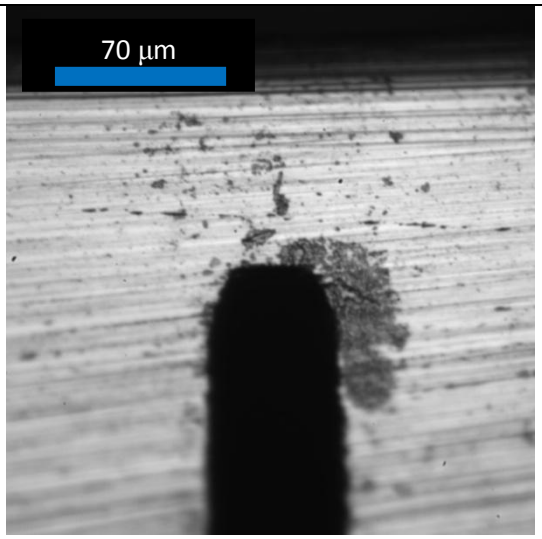

d) Diced 75% at 50x.

Figure 3-1. Dicing saw samples under an optical microscope.

Diced samples were viewed and measured in a SEM as a check of the optical microscope measurements. A circle was used to fit the notch geometry at each depth, giving a radius of curvature that was used in the FEA model, Figure 3-2 below.

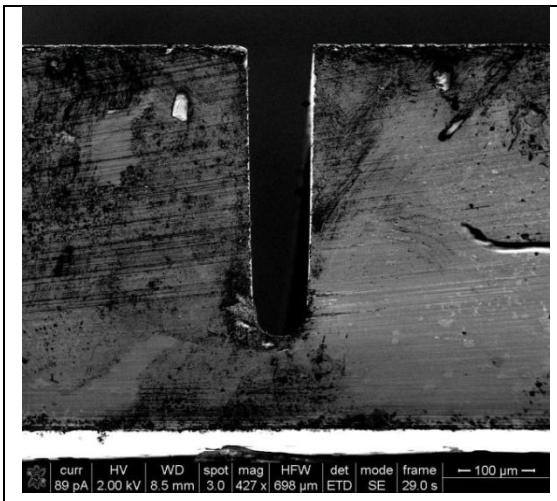

a) Diced 75% sample.

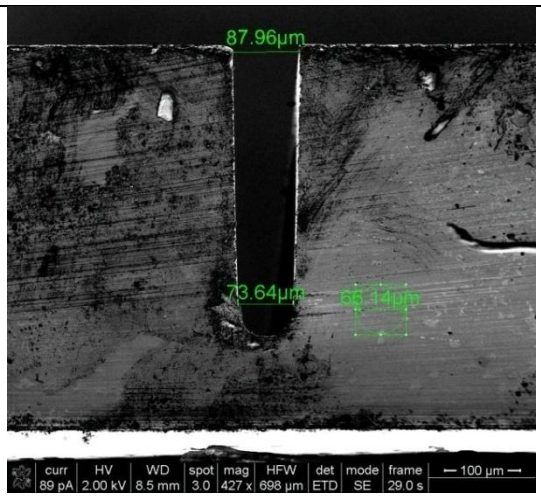

b) Diced 75% sample top and bottom neck width measurements.

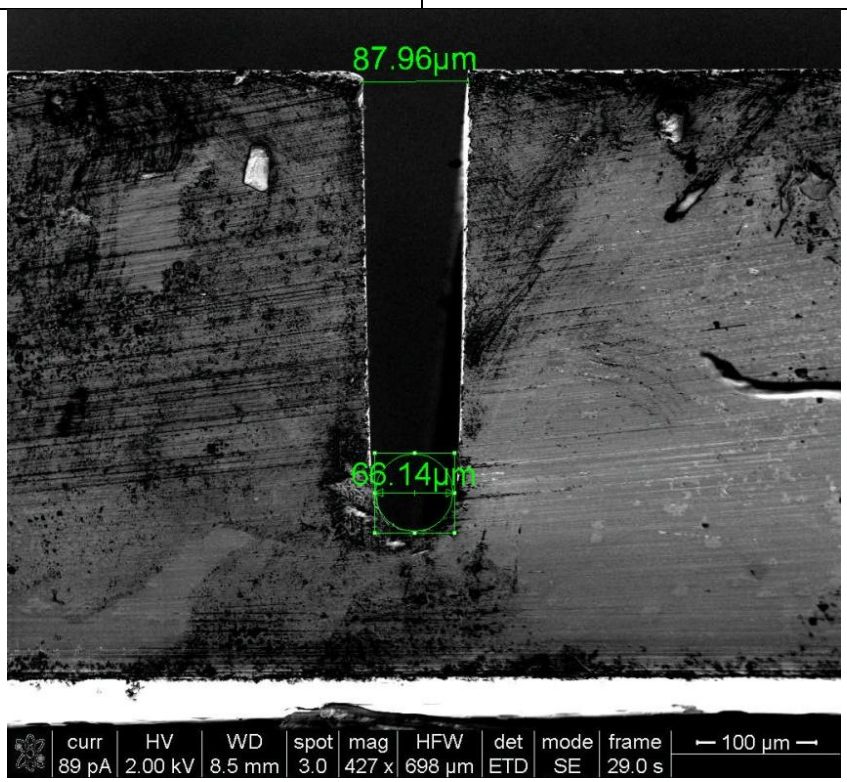

c) Diced 75% sample bottom radius measurements.

Figure 3-2. SEM pictures of diced samples.

To derive the notch side-wall slope of the profile needed in the FEA model, the depth, width, and radius of each sample was measured and recorded. Table 3-1 below shows the measured radius of four random diced samples while Table 3-2 shows the measured attributes of the four random diced samples.

	#1	#2	#3	#4	Average	Average Rounded
Radius (μm)	35.79	35.30	36.02	36.73	35.96	36.00

Table 3-1. Measured radius of four random diced samples.

The slope of the diced specimen was first found from deriving dimensions X (defined as the base of a right triangle) and Y (defined as the height of the triangle). An equation for X is

$$\boldsymbol{X} = \frac{\boldsymbol{w-2*r}}{\boldsymbol{2}} \qquad \text{(Eq 3-1)}$$

Where *w* is the width and *r* is the radius. The equation for Y is

$$Y = d - r \qquad \text{(Eq 3-2)}$$

where *d* is the depth of the notch and *r* is the radius. A physical representation of X and Y are shown in Figure 3-3 below. Note the dimensions of the right triangle in Figure 3-3 are exaggerated.

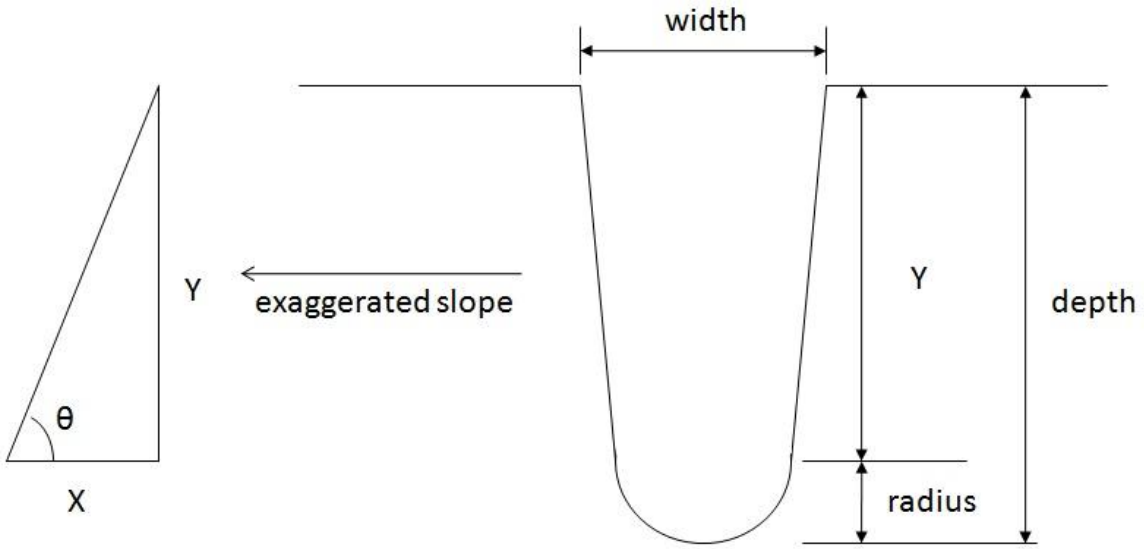

Figure 3-3. X and Y shown with the right triangle.

To find the slope of the triangle the formula is

$$\boldsymbol{\theta = tan^{-1}\frac{Y}{X}} \qquad \text{(Eq 3-3)}$$

Depth (μm)	Width (μm)	Y (μm)	X (μm)	Theta (rad)	Theta (deg)
267.92	88.87	231.92	8.435	1.534	87.917
276.62	88.59	240.62	8.295	1.536	88.026
403.4	95.94	367.4	11.97	1.538	88.134
393.74	94.93	357.74	11.465	1.539	88.164

Table 3-2. Slope derivation data.

The average slope rounded for all diced notch depths was found to be 88.0 degrees. Figure 3-4 shows the 10% sawn depth profile created in Solid Edge. The model was exported as an IGES file for calculation of principal stresses near the notch under three-point bending.

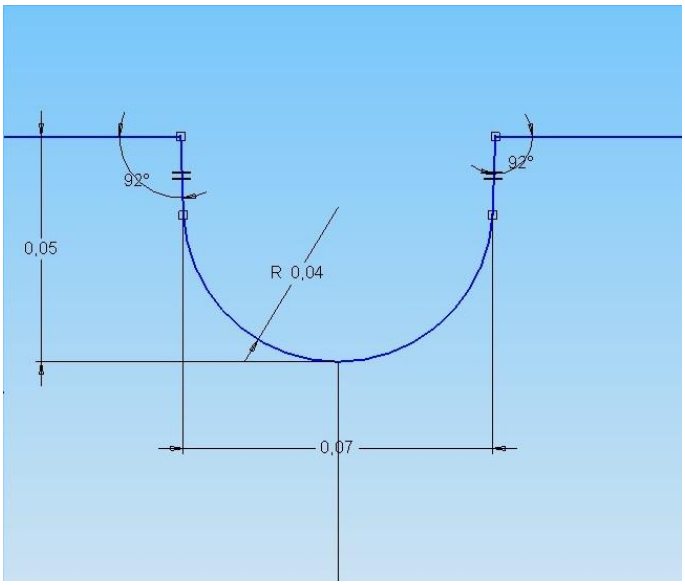

Figure 3-4. Solid Edge model of the 10% dicing saw model.

In the DRIE process, the material removal rate depends on the gas flow and heat transfer about the specimen, causing the trench geometry to vary with depth. Shallow trenches have a much flatter base than the deep etched trenches, due to a more uniform flow pattern of fresh ionized etching gas. Deeper trenches start to become more rounded due to the difficulty of the ionized gas to remain uniform, becoming more like flow going through a pipe rather over a free surface.

Cross-section images showed that the DRIE produced deep trench and shallow trenches had roughly the same radius of curvature connecting the trench wall and the base. It was assumed for the finite element analysis modeling (FEA) modeling that the trenches are etched highly anisotropically, with nearly vertical trench walls for all depths tested in this work. This assumption was consistent with SEM images of the DRIE trench profiles (included later in Figure 3-5 and Figure 3-6).

The DRIE profile modeled from SEM pictures is shown in Figure 3-6 below. The fillet radius between the trench walls and bottom radius of the etches was a constant 5 µm and was independent of etch depth. The bottom radius changed slightly with depth, starting very large at shallow etches (nearly flat, radius on order of millimeters), and reached a maximum of 90 µm for etch depths just beyond 25% of the wafer thickness. Figure 3-5, below, shows a large radius notch bottom profile for a shallow DRIE trench. Figure 3-6 shows the 90 µm radius that is seen for trenches deeper than 20%.

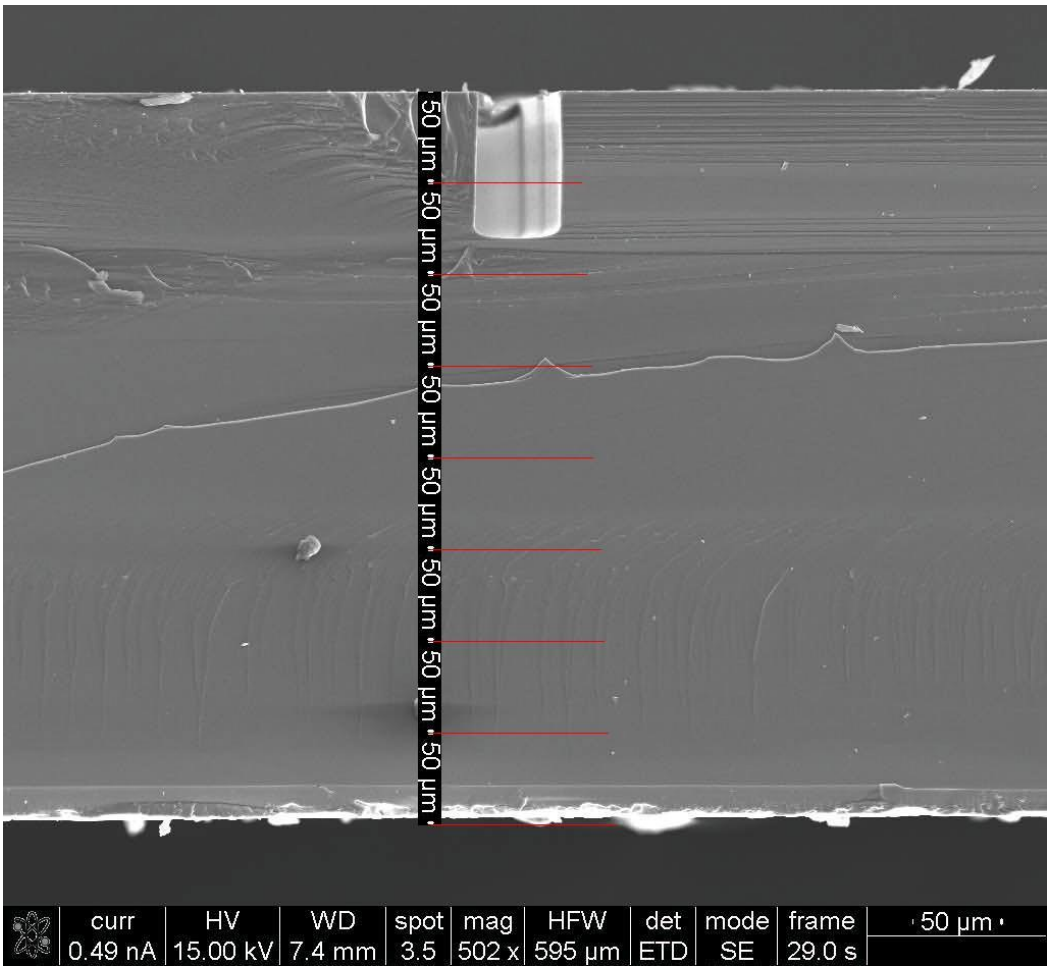

Figure 3-5. 80µm etch showing large radius bottom profile.

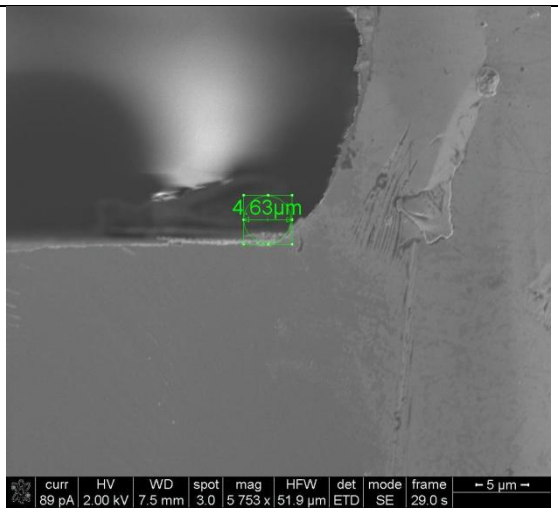

a) Side fillet radius fit.

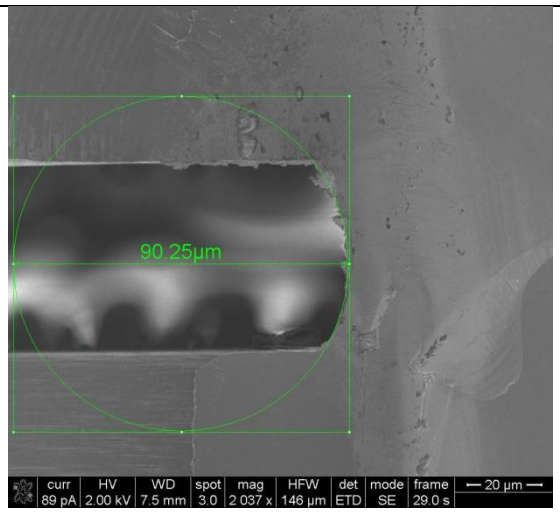

b) Notch bottom radius fit.

Figure 3-6. DRIE etch at 50% depth taken with SEM.

The model used in ANSYS is shown schematically below in Figure 3-7. In the figure, W is the width of the trench, α is the sidewall angle, ρ is the bottom trench radius, d is the etch depth, and r is the fillet between the sidewall and bottom of the trench.

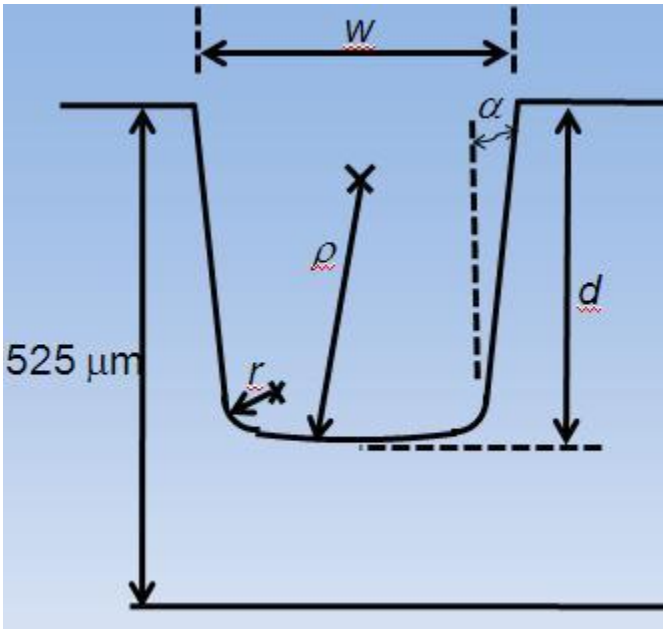

Figure 3-7. Derived DRIE profile used in FEA modeling.

Using ANSYS 12 and the models of each notch geometry made in Solid Edge, stress concentration factors were derived for various depths while keeping the loading conditions, stiffness matrix, and loading magnitudes constant. Silicon is an anisotropic material with a 6x6 stiffness matrix [C_{jj}]. The relationship between stress and strain is described by Hooke's law and is expressed as

$$\begin{bmatrix} \sigma_x \\ \sigma_y \\ \sigma_z \\ \tau_{yz} \\ \tau_{xz} \\ \tau_{xy} \end{bmatrix} = \begin{bmatrix} c_{11} & c_{12} & c_{12} & 0 & 0 & 0 \\ c_{12} & c_{11} & c_{12} & 0 & 0 & 0 \\ c_{12} & c_{12} & c_{11} & 0 & 0 & 0 \\ 0 & 0 & 0 & c_{44} & 0 & 0 \\ 0 & 0 & 0 & 0 & c_{44} & 0 \\ 0 & 0 & 0 & 0 & 0 & c_{44} \end{bmatrix} \begin{bmatrix} \varepsilon_x \\ \varepsilon_y \\ \varepsilon_z \\ \gamma_{yz} \\ \gamma_{xz} \\ \gamma_{xy} \end{bmatrix} \quad \text{(Eq 3-4, Ikehara 2009)}$$

where σ, τ, and ε are normal stress, sheer stress and strain respectively. The values of [C] are c_{11}=167.4 GPa, c_{12}=65.23 GPa, c_{44}=79.57 GPa [Ikehara 2009, Kaajakari 2008].

Parameters used in the ANSYS analysis are shown in Table 3-3 below. Once the IGES model created in SolidEdge was imported and meshed, the mesh was refined around the etch profile to increase the accuracy of the solution and to ensure convergence. It was assumed that the stress through the width of the wafer was negligible so plane stress was used. A width was given to the model so that the stress units would be MN per m^2, or MPa.

All analysis done with ANSYS use the X-Y plane, where X is the horizontal axis and Y is the vertical axis. The Z axis is out of the pictures and since plane stress was assumed, the stress in the Z direction is zero. Loading was done using 3 vectors, the middle one having a magnitude of 1 Newton's and the two beside it have a magnitude of

0.5 Newton's. This was done to distribute the load so that all the force was not concentrated on one node.

ANSYS Parameters	
Beam Loading Type	3-Pt Bending
Beam Support Type	Simply Supported
Load	2 Newtons
Element Type	Solid 8 node 183
Element Behavior	Plane Stress w/ Thickness
Element Shape	Quad
Element Edge Length	0.1

Table 3-3. ANSYS parameters used in stress concentration factor analysis.

The FEA loading constraints, mesh, X component of stress, Y component of stress, XY shear, Von Mises stress, and 1st principal stress for the 70% dicing saw trench are shown in Figure 3-8, Figure 3-9, Figure 3-10, Figure 3-11, Figure 3-12, Figure 3-13, and Figure 3-14, respectively. For the U-notch, dicing saw produced geometry the maximum 1st principal stress was located at the very bottom of the notch.

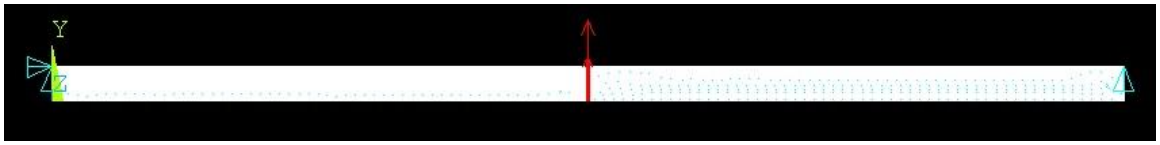

Figure 3-8. Constraints for 70% dicing saw FEA model.

(a)

(b)

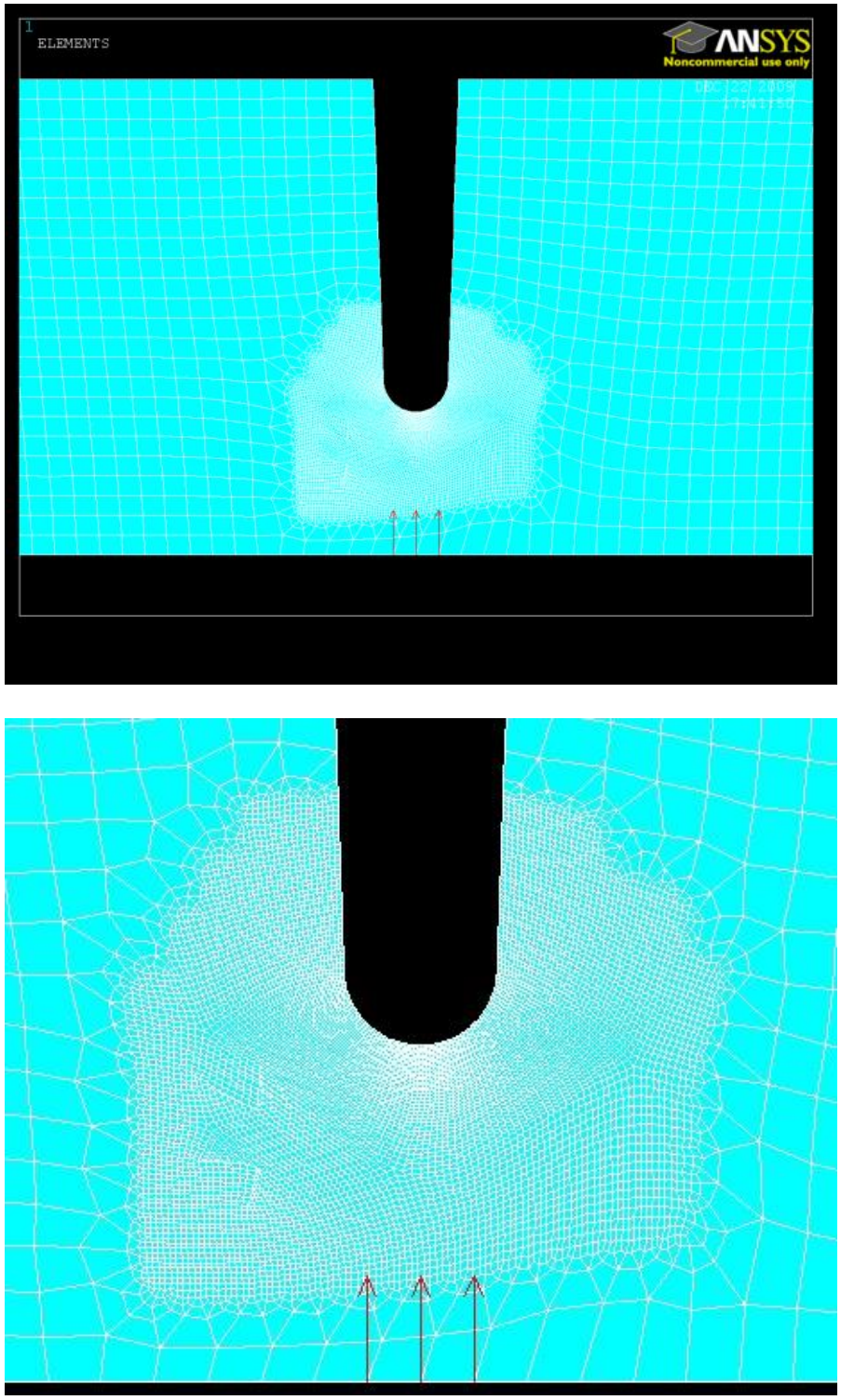

Figure 3-9. FEA modeled notch geometry for the 70% dicing saw (a), and zoomed region showing refined mesh around notch region (b).

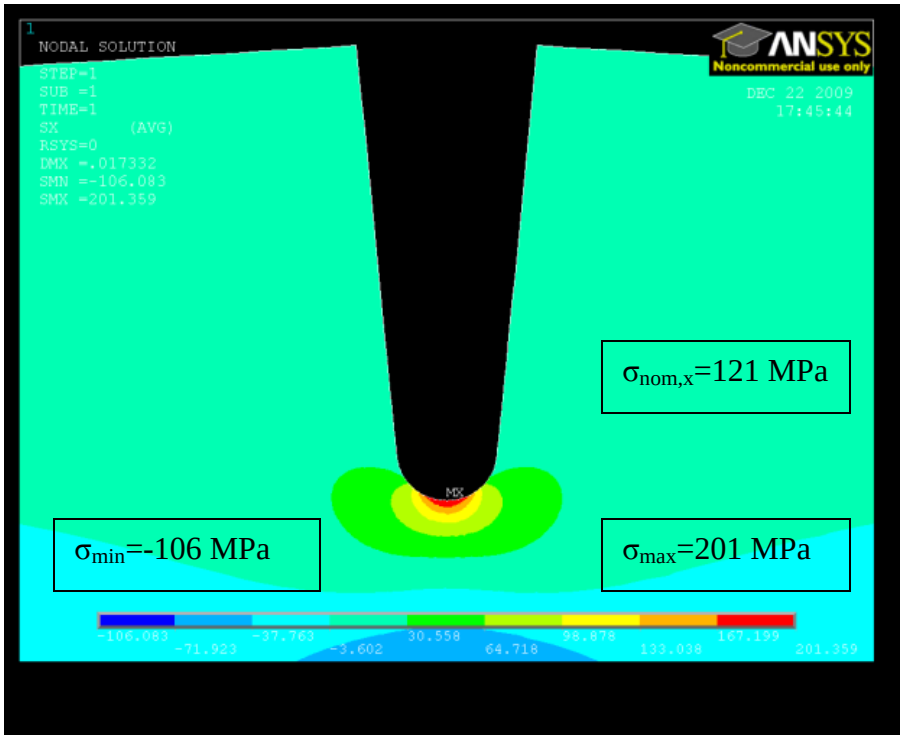

Figure 3-10. Stress in X direction (horizontal orientation) from the 70% dicing saw FEA.

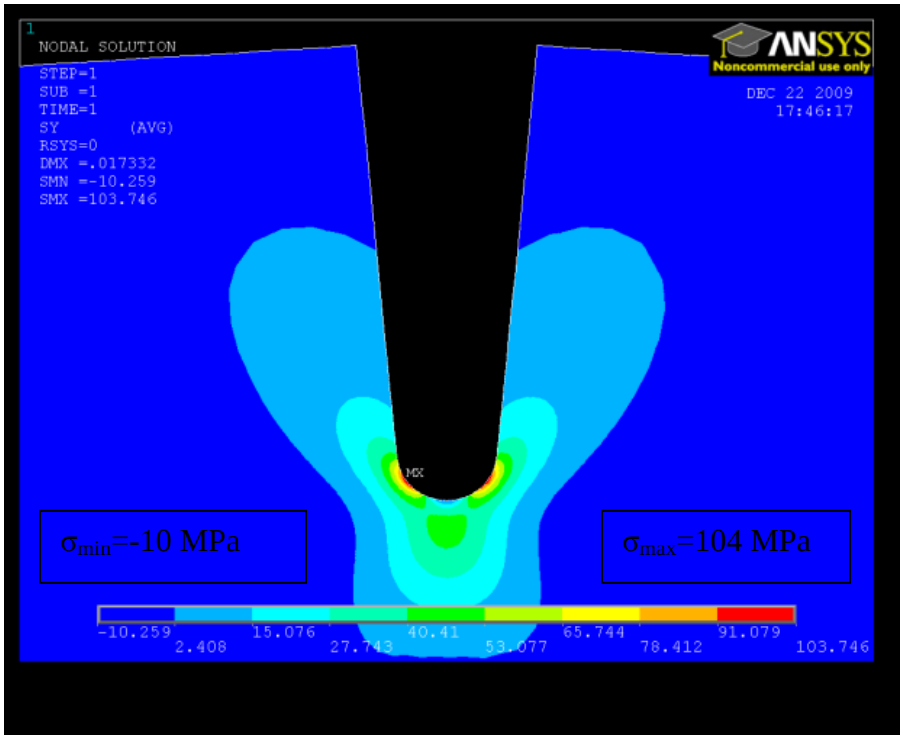

Figure 3-11. Stress in Y direction (vertical orientation) from the 70% dicing saw FEA.

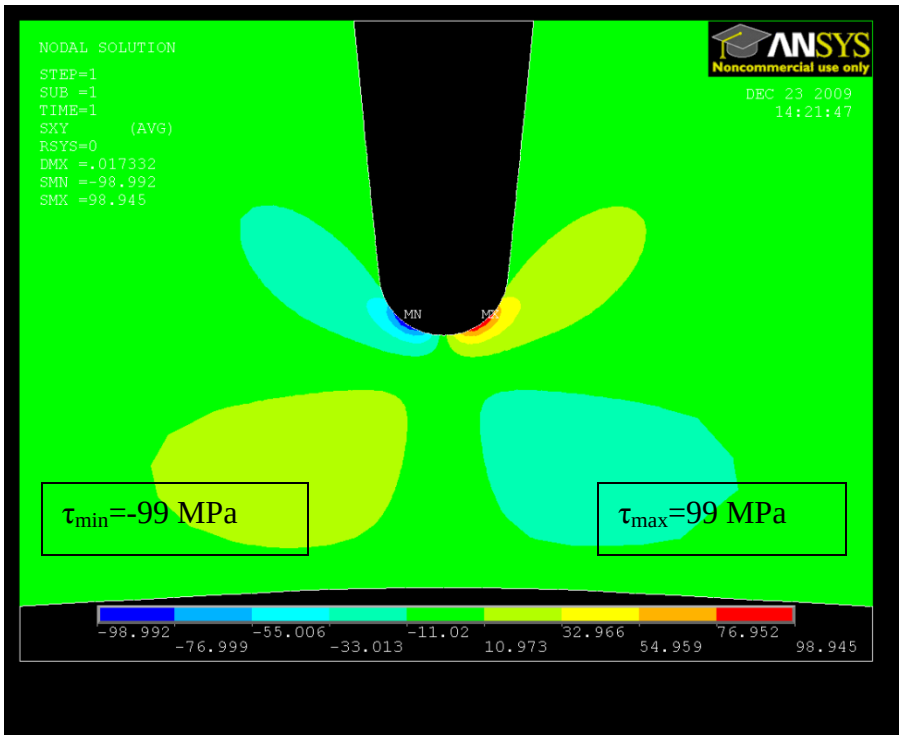

Figure 3-12. Stress in XY direction from the 70% dicing saw FEA.

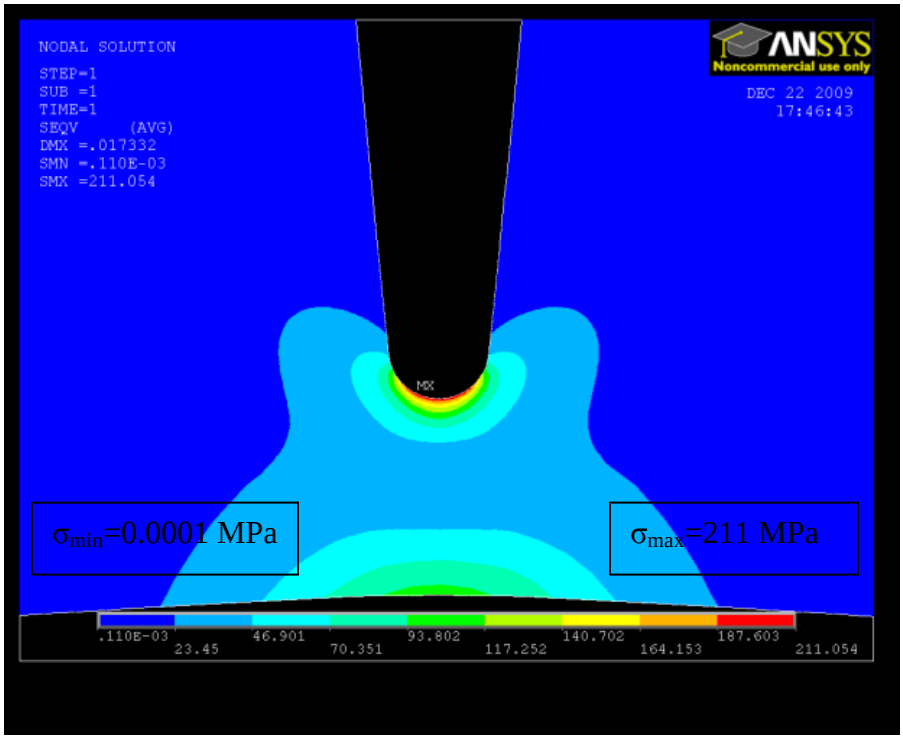

Figure 3-13. Von Mises stress magnitude from the 70% dicing saw FEA.

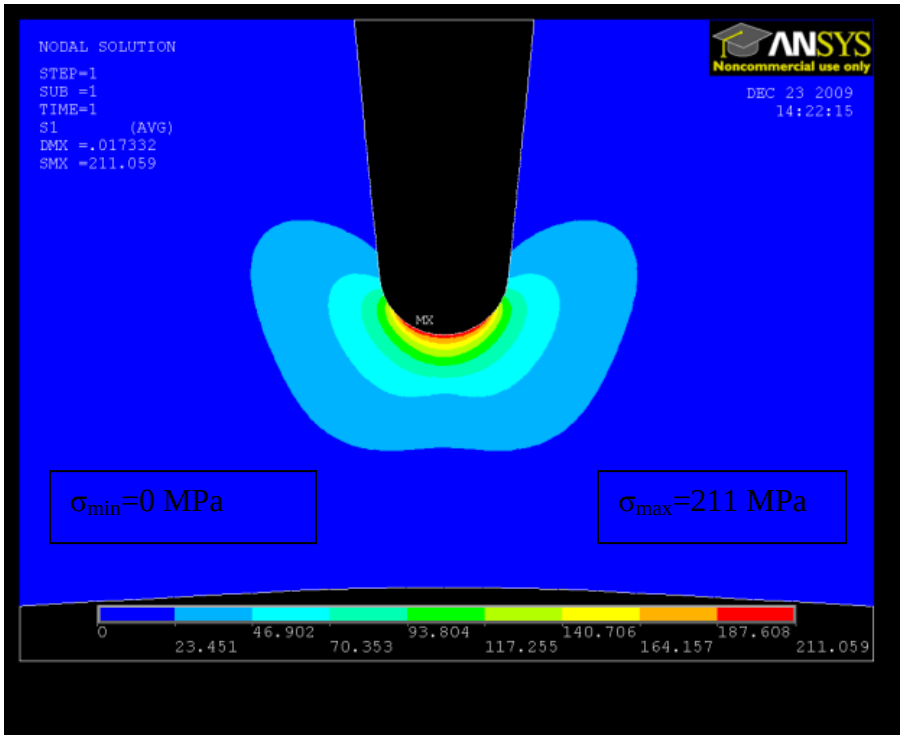

Figure 3-14. 1st principal stress magnitude from the 70% dicing saw FEA.

Similarly, FEA modeling of the DRIE notch geometries was performed in ANSYS using identical loading conditions and constraints, Figure 3-15. Results showing the X direction of stress, Y direction of stress, XY shear, Von Mises stress, and 1st

principal stress for a 70% DRIE etch are shown in Figure 3-16, Figure 3-17, Figure 3-18,

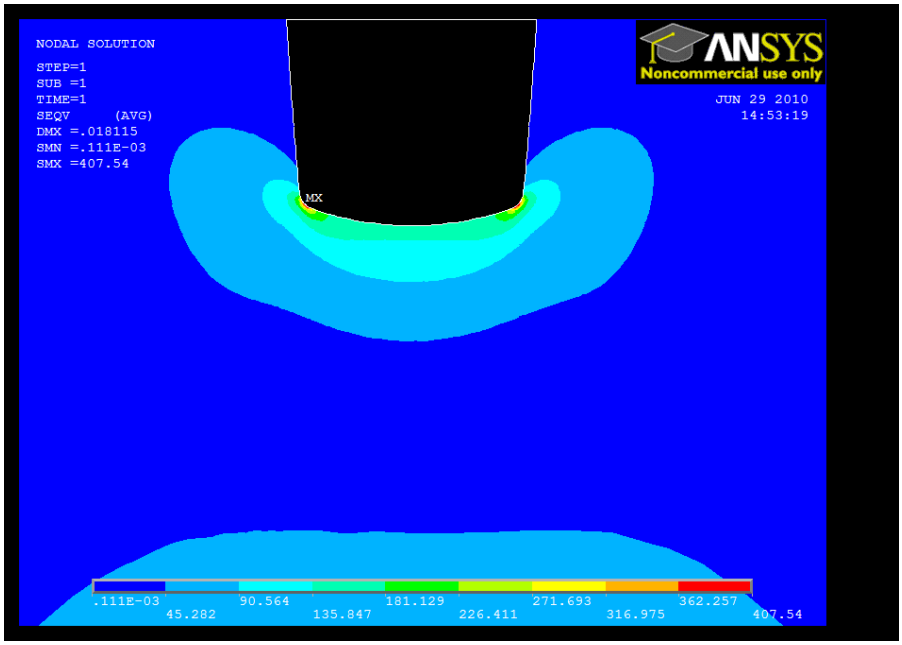

Figure *3-19*, Figure 3-20 below, respectively. The maximum principal stress for these etching profiles was located around the 5μm side fillets.

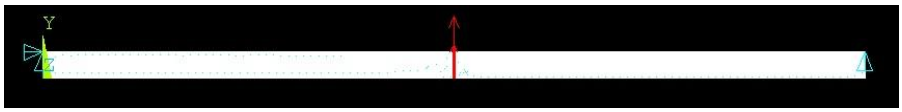

Figure 3-15. Constraints for the 70% DRIE FEA modeling.

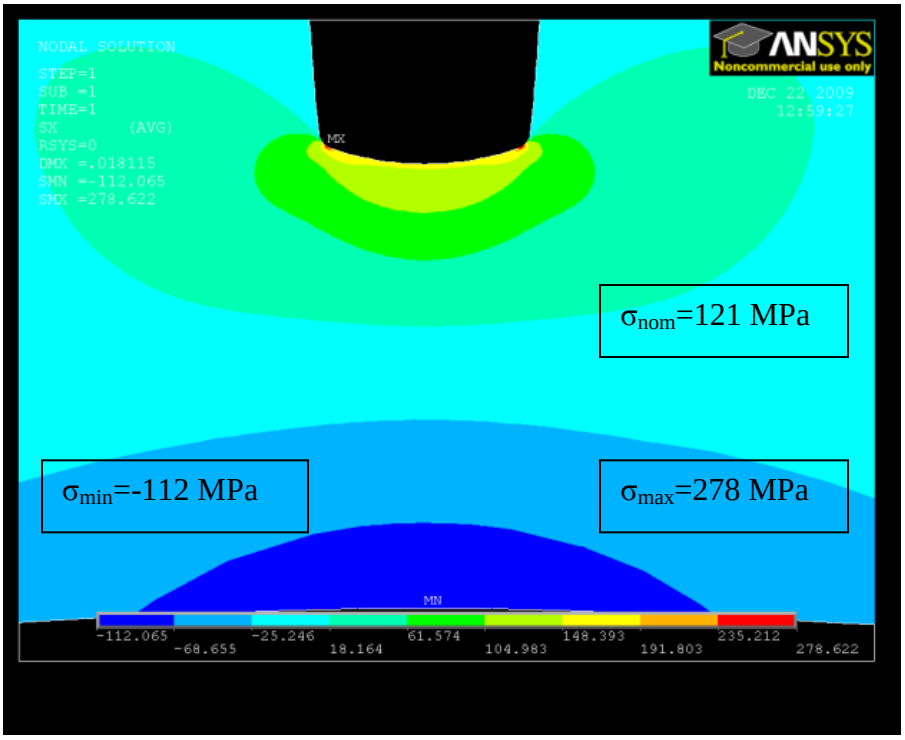

Figure 3-16. Stress in X direction (horizontal orientation) from the 70% DRIE FEA.

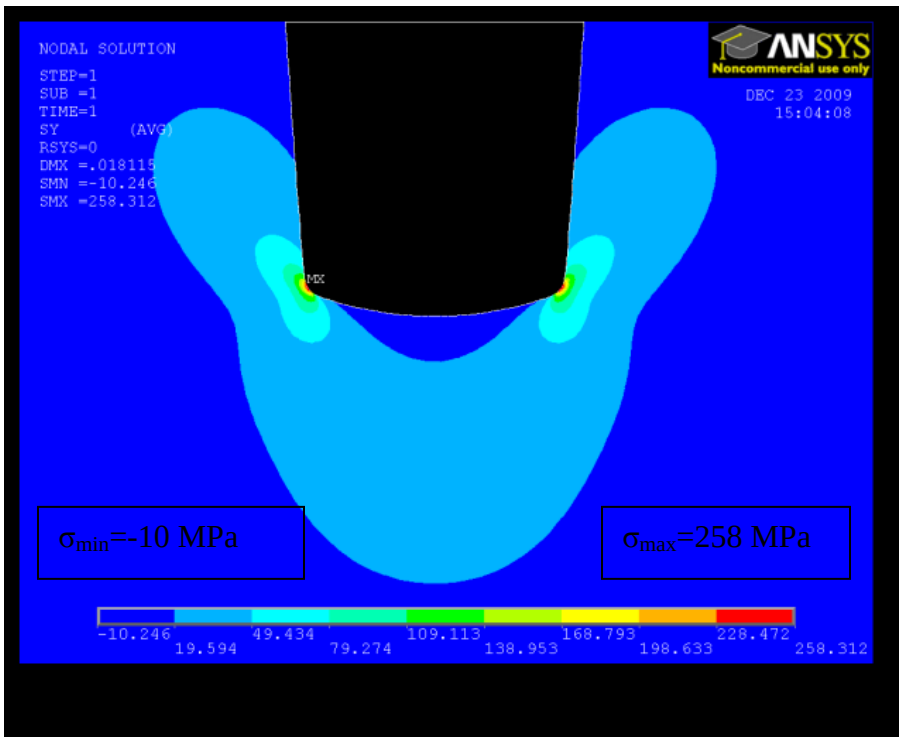

Figure 3-17. Stress in Y direction (vertical orientation) from the 70% DRIE FEA.

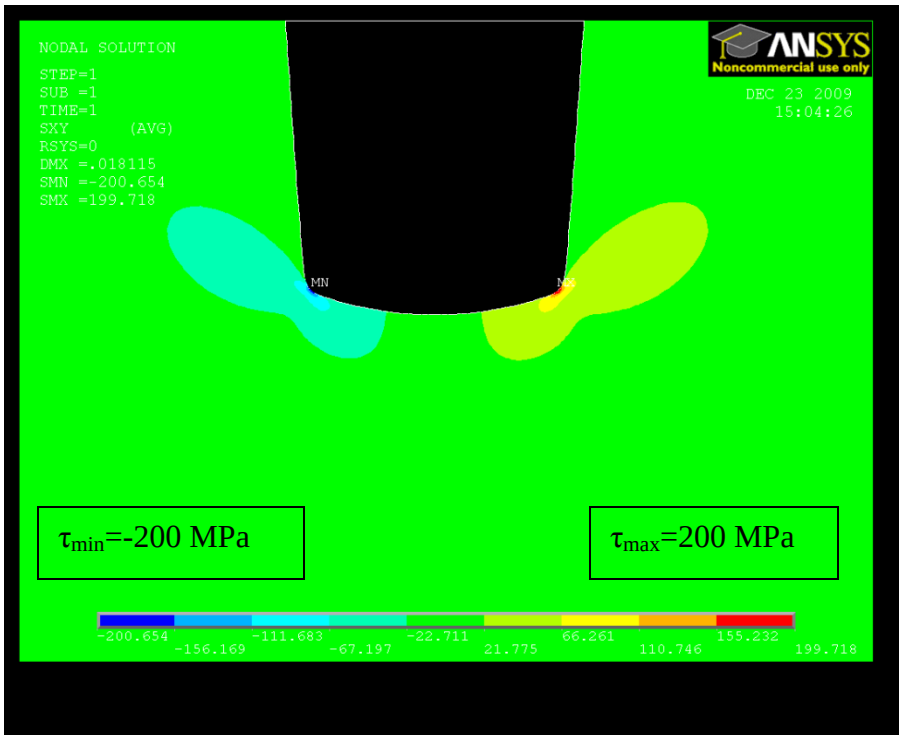

Figure 3-18. Stress in XY direction from the 70% DRIE FEA.

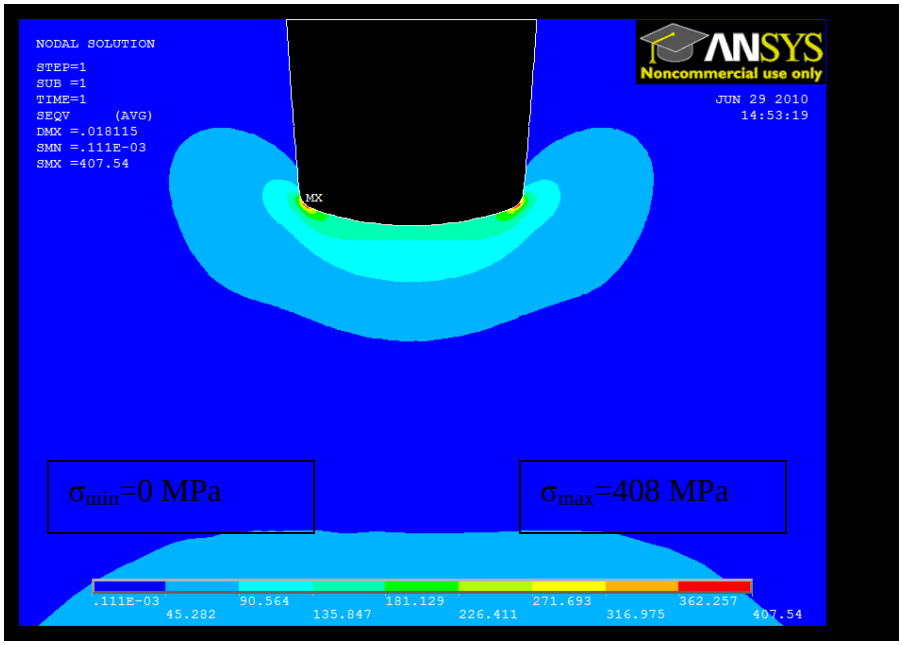

Figure 3-19. Von Mises stress magnitude from the 70% DRIE FEA.

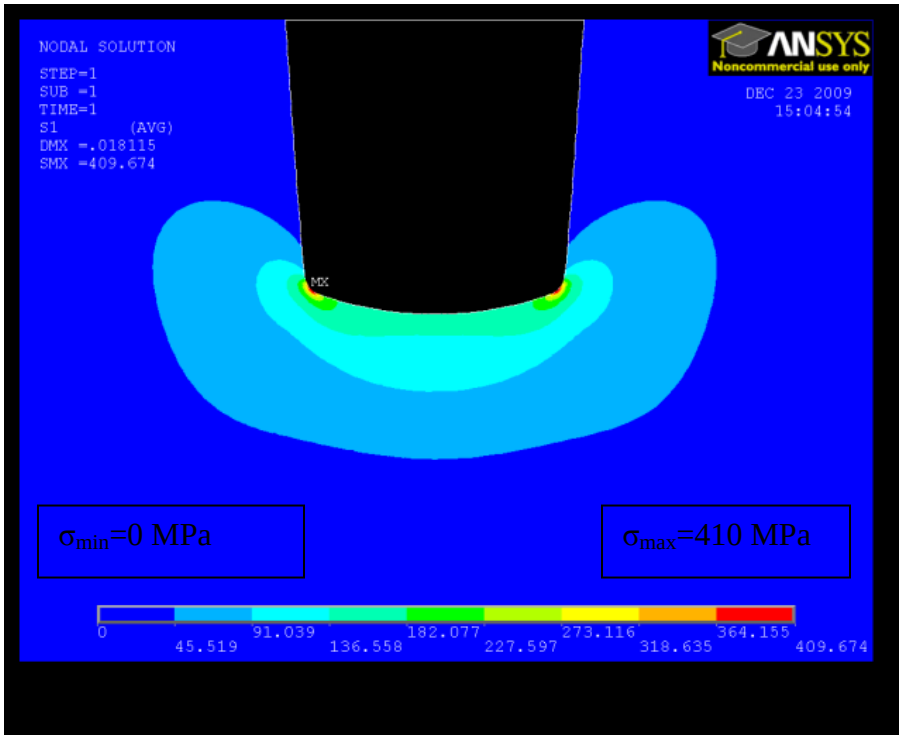

Figure 3-20. 1st principal stress magnitude from the 70% DRIE FEA.

For the double-sided DRIE wafer, an FEA model mimicking the DRIE profile 150 μm deep on the top side and 145 μm on the backside was made. The maximum stress from this model was located in the 5 μm fillet just like the previous DRIE FEA results. Loading conditions, mesh, 1st principal stress, and a close up of the 1st principal stress for the DRIE 25% double-sided etch model are shown in Figure 3-21, Figure 3-22, Figure 3-23, Figure 3-24 below, respectively. Loading for the double sided DRIE was done using 4 force vectors with 0.5 Newton magnitudes.

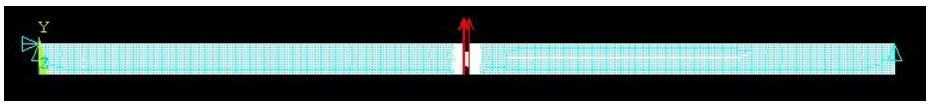

Figure 3-21. Loading conditions for the 25% doubl- sided FEA model.

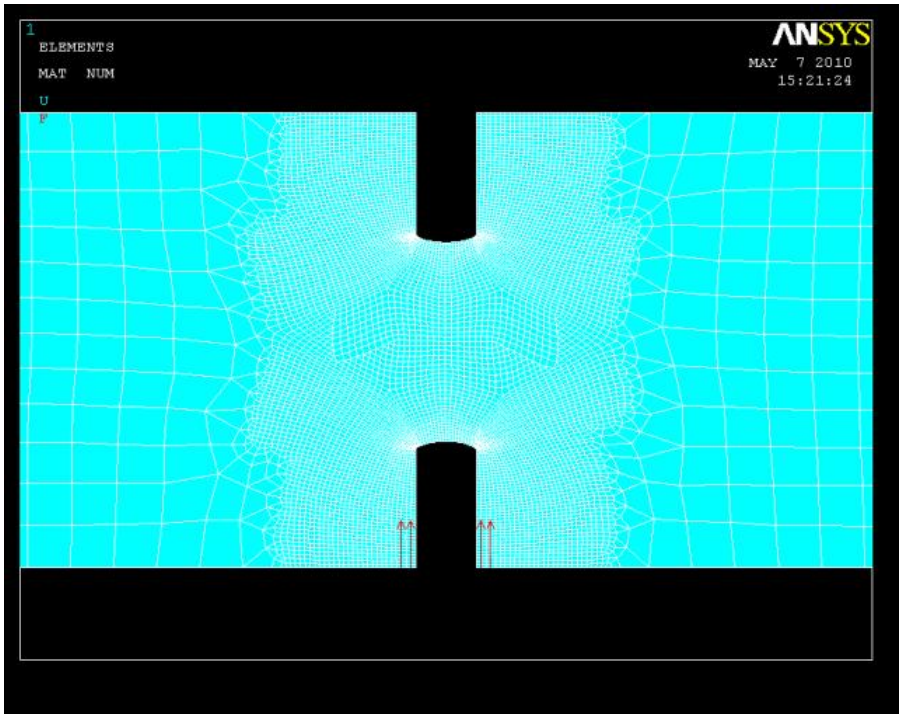

Figure 3-22. Close up of notch for DRIE 25% double sided etch FEA model.

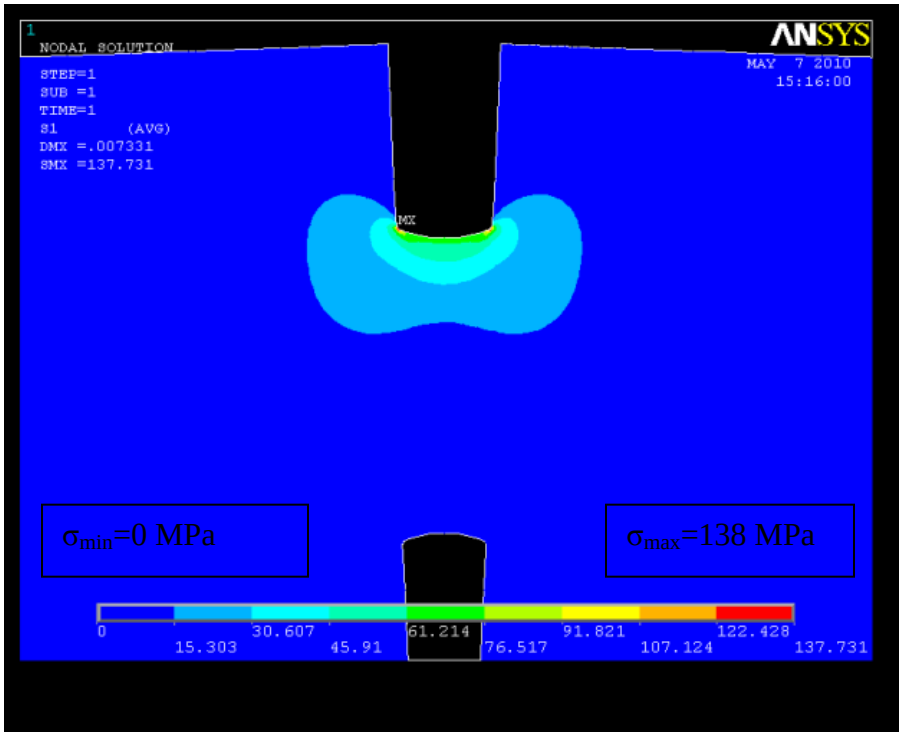

Figure 3-23. 1st principal stress for DRIE 25% double-sided etch FEA. (Contoured such that compressive stress not shown).

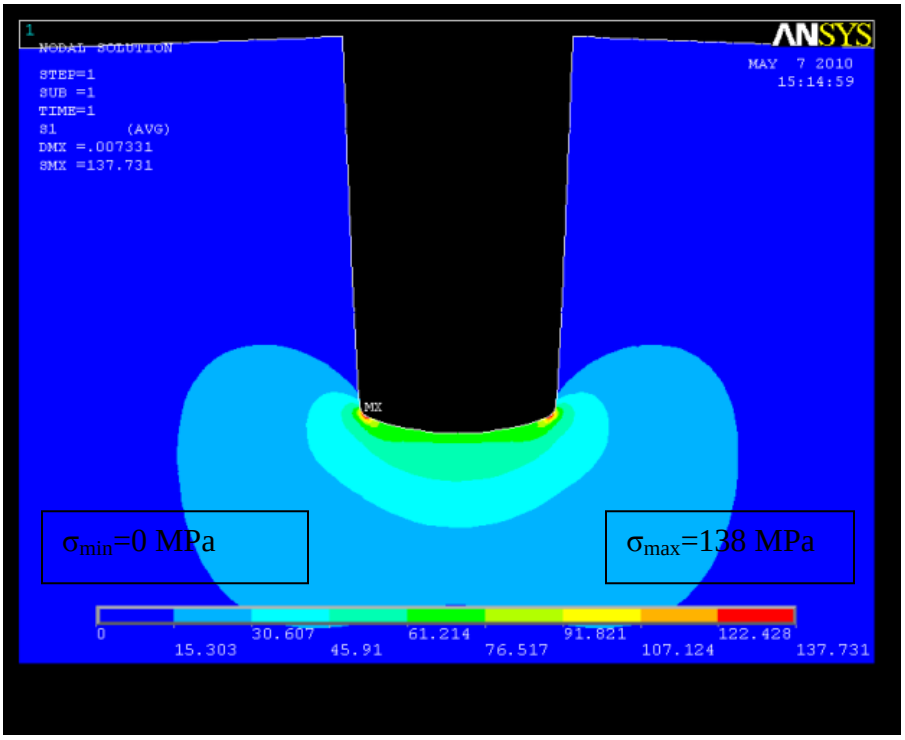

Figure 3-24. Close up of 1st principal stress for DRIE double-sided etch FEA (Contoured such that compressive stress not shown).

.

For the purposes of this study, the stress concentration factor is defined as

$$SCF = \frac{1st\ Principal\ Stress}{Nominal\ Stress} \qquad \text{(Eq 3-5)}$$

where the 1st principal stress is defined as the maximum tensile stress in the XY-plane due to the X, Y, and shear stresses. The definition of nominal stress is the bending stress resulting from the applied moment and calculated in the reduced cross-section below the notch. Figure 3-25 below shows the nominal throat area.

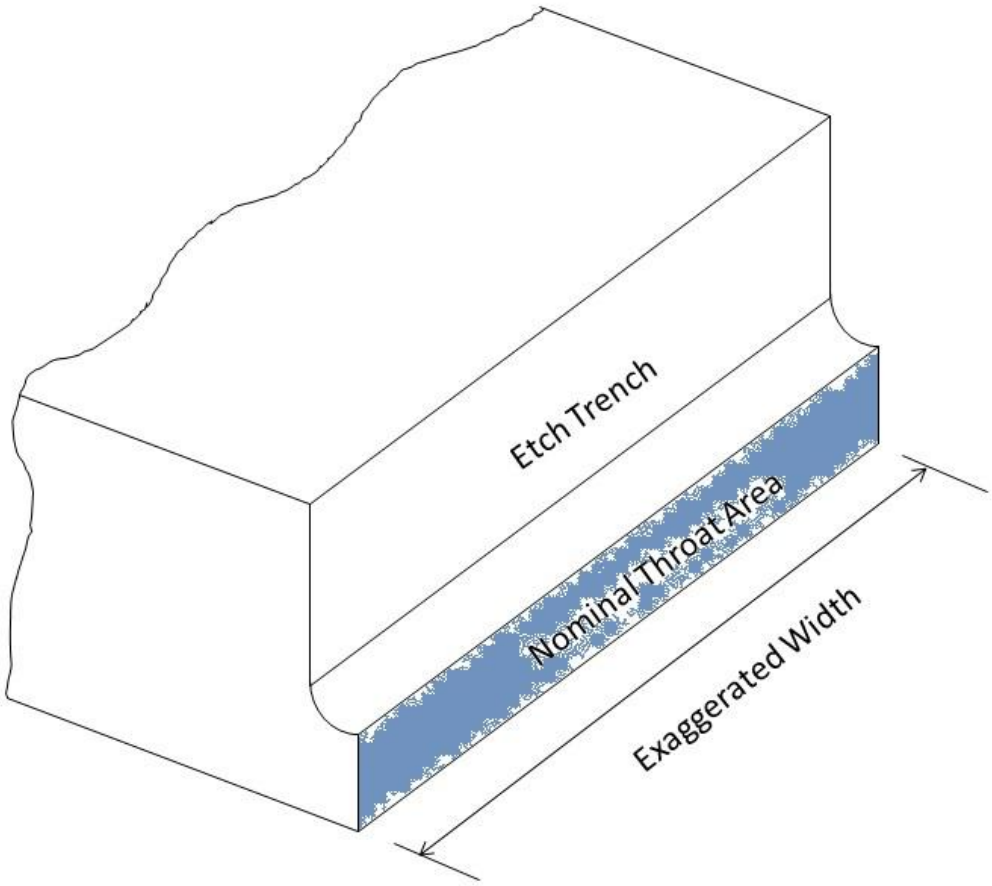

Figure 3-25. Reduced cross section below notch.

Results from the dicing saw FEA analysis and SCF are shown in Table 3-4 and Table 3-5 below respectively. The theoretical nominal stress in the X direction is

$$\sigma = \frac{Mc}{I} = \frac{\frac{1}{2}P\frac{1}{2}L\frac{1}{2}t}{\frac{1}{12}wt^3} = \frac{3PL}{2wt^2} \qquad \text{(Eq 3-6, Beer 2006, pg 309)}$$

where P is 2.0 Newtons, L is 17 mm, w is 17 mm, and t is the nominal thickness of the reduced cross section. Figure 3-26 shows the SCF for the dicing saw plotted versus dicing depth.

		Maximum Stress (MPa)					
Depth Percent (of 1)	Depth (mm)	Nominal Theoretical X	FEA X	FEA Y	FEA Von Mises	FEA XY	1st Principal
0	0.525	10.88	10.78	0	11.49	0	10.78
0.1	0.4725	13.44	31.84	10.42	31.84	12.75	31.84
0.2	0.42	17.01	41.74	17.08	42.21	18.56	42.21
0.3	0.3675	22.21	52.54	24.17	54.09	24.65	54.09
0.4	0.315	30.23	67.02	33.22	70.03	32.58	70.02
0.5	0.2625	43.54	89.01	45.98	93.84	44.12	93.83
0.6	0.21	68.03	126.53	66.29	133.58	62.91	133.58
0.7	0.1575	120.94	201.36	103.75	211.05	98.95	211.06
0.8	0.105	272.11	395.34	190.10	404.75	185.68	405.27
0.9	0.0525	1088.44	1332	517.85	1333	557.83	1332

Table 3-4. FEA results for the dicing saw analysis.

Depth Percent (of 1)	Depth (mm)	SCF (1st)
0	0.525	0.991
0.1	0.4725	2.370
0.2	0.42	2.482
0.3	0.3675	2.435
0.4	0.315	2.316
0.5	0.2625	2.155
0.6	0.21	1.964
0.7	0.1575	1.745
0.8	0.105	1.489
0.9	0.0525	1.224

Table 3-5. Stress concentration factors for dicing saw depth.

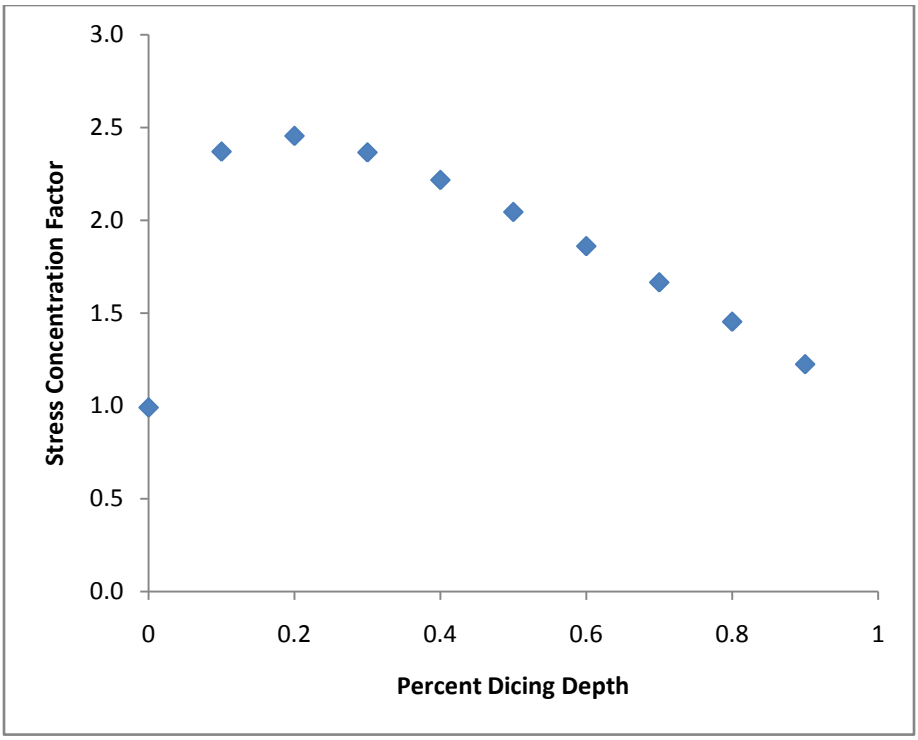

Figure 3-26. Stress concentration factor for diced trenches.

As a comparison to the FEA, "Roarks Formulas For Stress and Strain" give a SCF of 2.851 for a V-notch with geometry equal to a diced 20% sample (Young 2002). This is a 14.9% difference from the 20% diced FEA solution. The anisotropic properties of silicon could account for these differences.

Single-side etched DRIE notch stress results are shown in Table 3-6 below. The SCF's for the DRIE trenches are shown in Table 3-7 while the graph of the DRIE SCF versus depth are shown in Figure 3-27. For all DRIE cases, the applied load and other constraint factors were identical to those used for the diced sample analysis. For the double-sided DRIE case, the maximum stress magnitude was 137.73 MPa and the corresponding nominal stress for the throat area of the double sided DRIE wafer was 50.565 MPa, giving a SCF of 2.724.

		Maximum Stress (MPa)					
Depth Percent (of 1)	Depth (mm)	Nominal Theoretical X	FEA X	FEA Y	FEA Von Mises	FEA XY	1st Principal Stress
0	0.525	10.88	10.78	0.00	11.49	0.00	10.782
0.1	0.4725	13.44	32.53	24.21	44.18	21.20	44.783
0.2	0.42	17.01	50.02	41.09	70.19	33.75	70.880
0.3	0.3675	22.21	66.82	58.93	95.72	43.02	94.789
0.4	0.315	30.23	89.65	81.20	129.65	63.37	131.012
0.5	0.2625	43.54	123.37	114.04	180.56	86.61	182.002
0.6	0.21	68.03	176.77	165.35	259.24	126.61	261.449
0.7	0.1575	120.94	278.62	258.31	405.58	199.72	409.674
0.8	0.105	272.11	523.00	479.13	768.96	368.22	774.360
0.9	0.0525	1088.44	1555.00	1319.00	2211.00	1085.00	2220.000

Table 3-6. FEA results for the DRIE FEA analysis.

Percent (of 1)	Depth (mm)	Stress Conc (1st)
0	0.525	0.991
0.1	0.4725	3.333
0.2	0.42	4.168
0.3	0.3675	4.267
0.4	0.315	4.333
0.5	0.2625	4.180
0.6	0.21	3.843
0.7	0.1575	3.387
0.8	0.105	2.846
0.9	0.0525	2.040

Table 3-7. Stress concentration factors for DRIE etch depths.

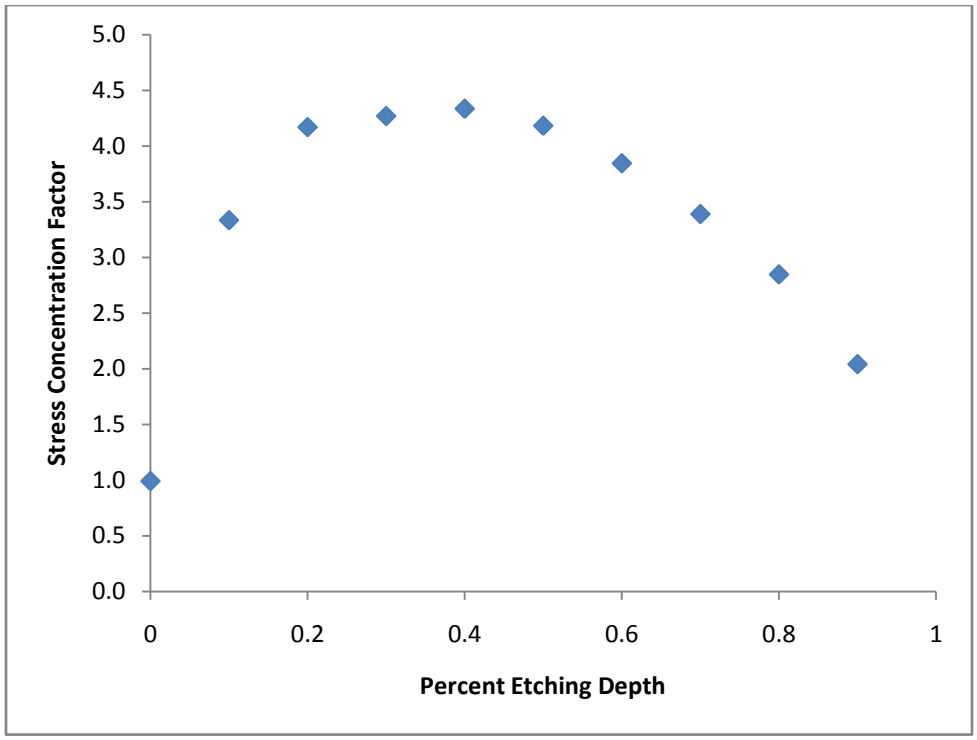

Figure 3-27. Stress concentration factor for etched trenches.

3.2 Diced and DRIE Depth Measurements

Notches on each wafer were measured in three different locations and then averaged to give a single depth measurement. The first measurement was performed in the center of the wafer while the other two were taken at one square diagonal and two square diagonals away. Measurement locations are schematically shown in Figure 3-28 below. Measured depth results all of the sample wafers are shown in Table 3-8 and Table 3-9 below.

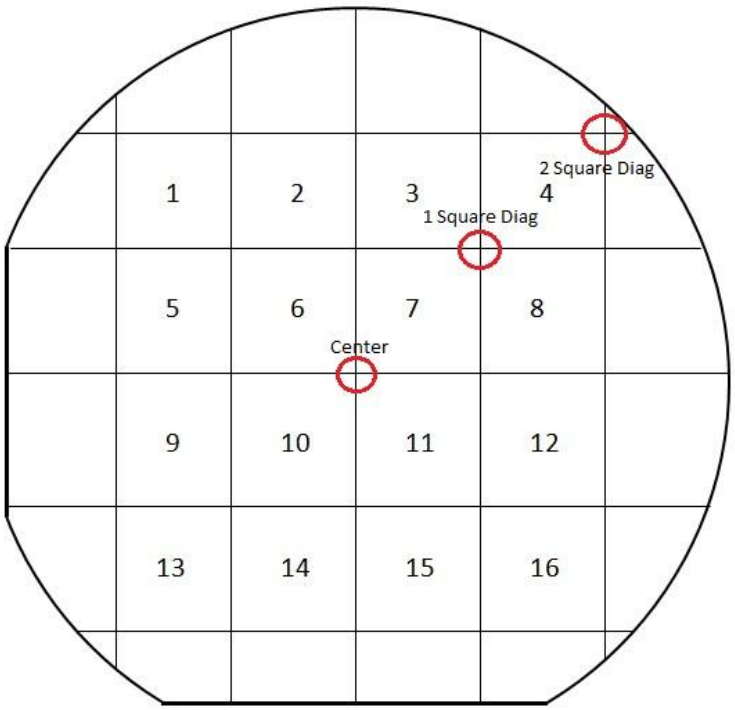

Figure 3-28. Trench depth measurement locations.

	Diced 25% Etch Depth (µm)			
Wafer #	Center	1SqD	2SqD	Average
1	134.85	134.85	135.8	135.17
2	134.9	136.15	136.5	135.85
3	132.4	135.5	136.1	134.67
4	133.13	134.28	134.45	133.95
5	133.45	133.53	136.3	134.43
	Diced 50% Etch Depth (µm)			
Wafer #	Center	1SqD	2SqD	Average
1	255.55	259.55	258.03	257.71
2	256.63	258.2	258.7	257.84
3	257.43	258.65	257.35	257.81
4	261.55	262.9	264.15	262.87
5	261.2	262.68	263.95	262.61
	Diced 75% Etch Depth (µm)			
Wafer #	Center	1SqD	2SqD	Average
1	379.53	380.05	379.83	379.80
2	380.93	381.83	382.8	381.85
3	381.6	382.8	382.8	382.40

4	380.28	380.95	381.25	380.83
5	381.38	382.83	382.93	382.38

Table 3-8. Diced wafer trench depth measurements.

	DRIE 25% Etch Depth (µm)			
Wafer #	Center	1SqD	2SqD	Average
1	131.72	132.58	139.78	134.69
2	129.9	128.53	133.75	130.73
3	135.9	133.55	142.55	137.33
4	129.55	126.7	130	128.75
5	132.15	130.98	136.2	133.11
	DRIE 50% Etch Depth (µm)			
Wafer #	Center	1SqD	2SqD	Average
1	254.13	251.1	262.93	256.05
2	248.95	249.43	256.88	251.75
3	258.8	258.28	266.15	261.08
4	251.45	251.88	262.45	255.26
5	265.27	263.28	270.88	266.48
	DRIE 75% Etch Depth (µm)			
Wafer #	Center	1SqD	2SqD	Average
1	392.02	393.1	400	395.04
2	397.05	399.2	N/A	398.13
3	384.48	383.5	391.9	386.63
6	399.85	397.68	N/A	398.77
7	388.38	386.18	N/A	387.28

Table 3-9. DRIE wafer trench depth measurements.

The double sided DRIE wafer etch depths are shown in Table 3-10 below. A cleaved cross section of the double sided DRIE wafer is shown in Figure 3-29 below.

	DRIE Both Sides (µm)			
	Center	1SqD	2SqD	Average
Polished	149.68	147.70	153.50	150.29
Back	143.95	142.30	151.38	145.88

Table 3-10. Double sided DRIE wafer depth measurements.

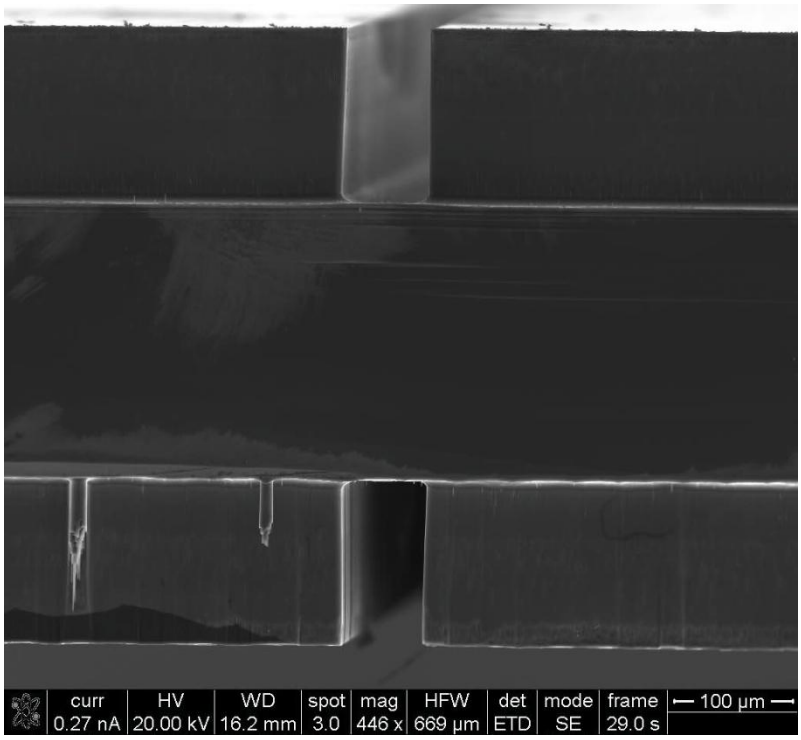

Figure 3-29. Double sided DRIE wafer cleaved cross section.

3.3 The Weibull Distribution

All samples were broken and fit to a Weibull distribution since literature shows a skewing probability with brittle materials (Bohm 2004). A Weibull function allows for skewing of the statistical function instead of forcing symmetry distribution as in a normal distribution. In silicon fracture studies, the Weibull is used most often [Greek 1996, Bohm 2004, Schoenfelder 2006, Tsuchiya 1998, Kroninger 2006]. One of the parameters for the Weibull distribution is call the shape parameter β and the other is called the scale parameter α. The two parameter Weibull distribution fit was used and correlated with the data very well. Deriving the two parameters is a very involved task and can be used with a rank regression on Y. A rank regression on Y reduces the failure data deviation in the

Y axis. First the data is sorted from lowest to highest values then labeled from *i*=1 to the highest number of samples, N. Next the median rank is found from

$$\boldsymbol{F(T_i) = \frac{i-0.3}{N+0.4}} \qquad \text{(Eq 3-7, Weibull.com 2009)}$$

where *i* is the numbered rank of the data, *N* is the total number samples, and *T* is the stress value of rank *i*. The variables *x* and *y* are used in the least squares parameter estimation method and are defined as

$$\boldsymbol{x_i = ln(T_i)} \qquad \text{(Eq 3-8, Weibull.com 2009)}$$

$$\boldsymbol{y_i = ln(-ln\{1 - F(T_i)\})} \qquad \text{(Eq 3-9, Weibull.com 2009)}$$

Another set of variables, *a* and *b*, which are the coefficients of the linear equation fit are found from the equations

$$\boldsymbol{b = \frac{\sum_{i=1}^{N} x_i y_i - \frac{\sum_{i=1}^{N} x_i \sum_{i=1}^{N} y_i}{N}}{\sum_{i=1}^{N} x_i^2 - \frac{\left(\sum_{i=1}^{N} x_i\right)^2}{N}}} \qquad \text{(Eq 3-10, Weibull.com 2009)}$$

$$\boldsymbol{a = \frac{\sum_{i=1}^{N} y_i}{N} - b\frac{\sum_{i=1}^{N} x_i}{N}} \qquad \text{(Eq 3-11, Weibull.com 2009)}$$

With the coefficients determined, the two Weibull parameters can be found. The parameter β is simply

$$\boldsymbol{\beta = b} \qquad \text{(Eq 3-12, Weibull.com 2009)}$$

and the value of α comes from

$$\boldsymbol{\alpha = e^{-\frac{a}{b}}} \qquad \text{(Eq 3-13, Weibull.com 2009)}$$

To assess how well the distribution fits the data, the correlation coefficient is defined as

$$\boldsymbol{\rho = \frac{\sum_{i=1}^{N}(x_i-\bar{x})(y_i-\bar{y})}{\sqrt{\sum_{i=1}^{N}(x_i-\bar{x})^2 * \sum_{i=1}^{N}(y_i-\bar{y})^2}}} \qquad \text{(Eq 3-14, Weibull.com 2009)}$$

where $\bar{x}$ is the average of the x column and $\bar{y}$ is the average of the y column.

With these two parameters, a cumulative distribution function and probability density function can be applied to the data while deriving the mean and standard deviation. The Weibull cumulative distribution function is

$$\boldsymbol{CDF(T) = 1 - e^{-\left(\frac{T}{\alpha}\right)^{\beta}}} \qquad \text{(Eq 3-15, Weibull.com 2009)}$$

while the probability density function is

$$\boldsymbol{PDF(T) = \frac{\beta}{\alpha}\left(\frac{T}{\alpha}\right)^{\beta-1} e^{-\left(\frac{T}{\alpha}\right)^{\beta}}} \qquad \text{(Eq 3-16, Weibull.com 2009)}$$

To find the mean the equation is

$$\boldsymbol{m = \alpha * \Gamma\left(1 + \frac{1}{\beta}\right)} \qquad \text{(Eq 3-17, Weibull 1951)}$$

where $\Gamma\left(1 + \frac{1}{\beta}\right)$ is the gamma function evaluated at $\left(1 + \frac{1}{\beta}\right)$. The gamma function is defined as

$$\boldsymbol{\Gamma(z) = \int_0^\infty z^{(z-1)} e^{-t} dt} \qquad \text{(Eq 3-18, Kreyszig 1997)}$$

The standard deviation for the Weibull function is defined as

$$\boldsymbol{\sigma_{StdDev} = \alpha \sqrt{\Gamma\left(\frac{2}{\beta} + 1\right) - \Gamma\left(\frac{1}{\beta} + 1\right)^2}} \qquad \text{(Eq 3-19, Weibull 1951)}$$

3.4 Single-Side Notched Wafer Separation and Die Strength Results

All samples were separated and each die was tested for failure strength according to Figure 3-28 above. Side profiles of the separated die are shown in Figure 3-30, Figure 3-33 below. Notice that failure in the DRIE samples initiates at the maximum stress concentration locations, and then finds a new plane to fracture along. Both of these crack paths correspond to the (110) planes and appear to occur on the majority of DRIE samples. The SCF modified stress versus displacement data for a DRIE separation sample is shown in Figure 3-31 and Figure 3-32 below. Notice the slight change in slope at roughly 55 μm into the loading of the silicon wafer.

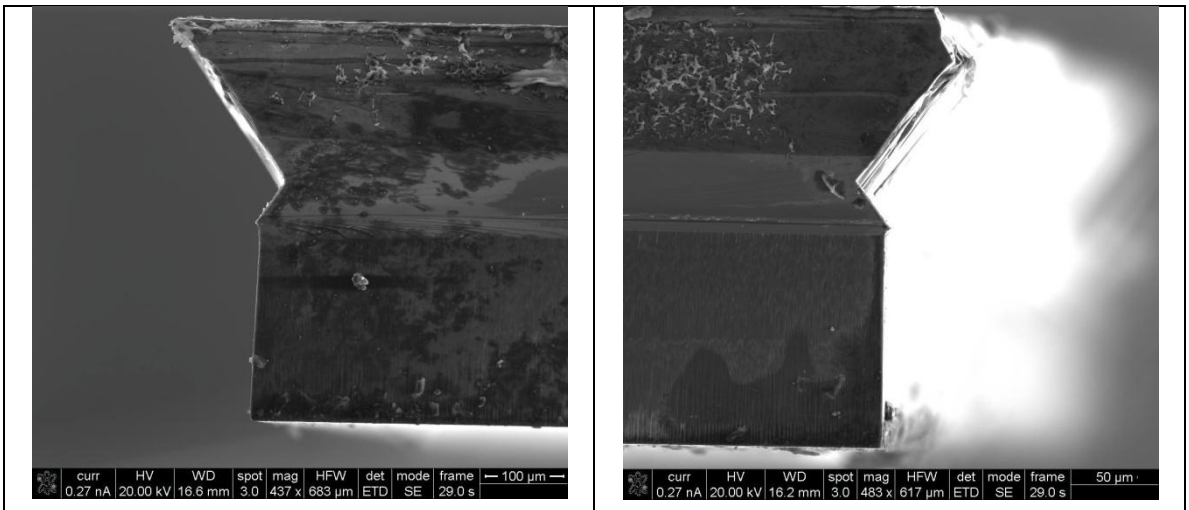

a) Top side die, separation 7

b) Bottom side of die, separation 11

Figure 3-30. 50% DRIE wafer 5 separated die #6. <110> flat facing out of page.

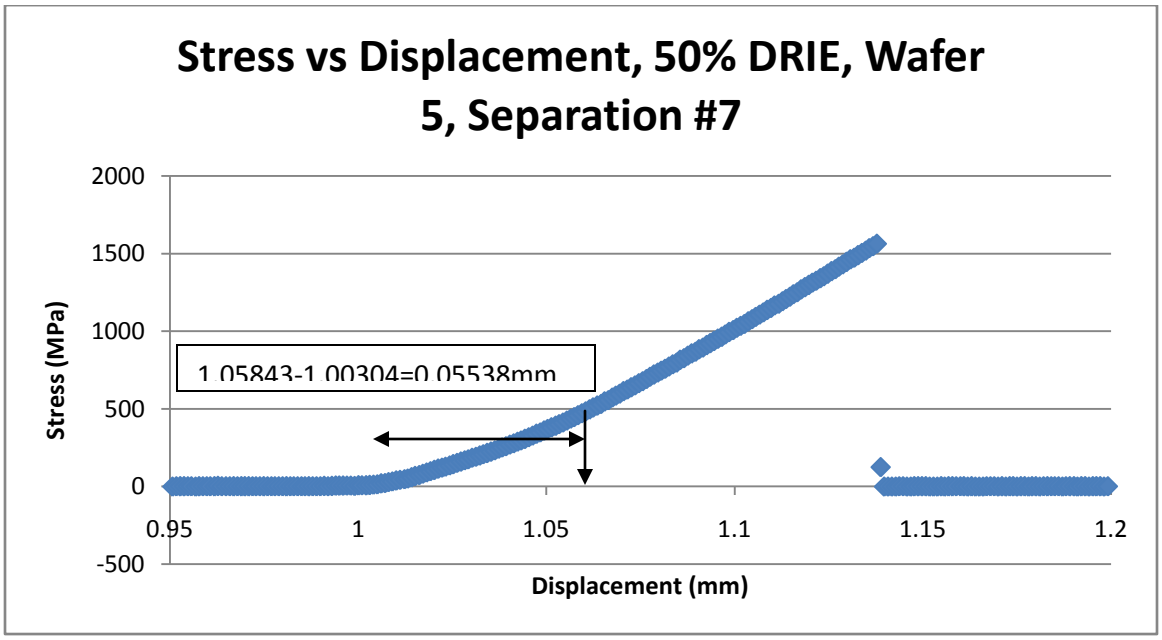

Figure 3-31. SCF corrected stress versus displacement for 50% DRIE wafer 5, separation #7.

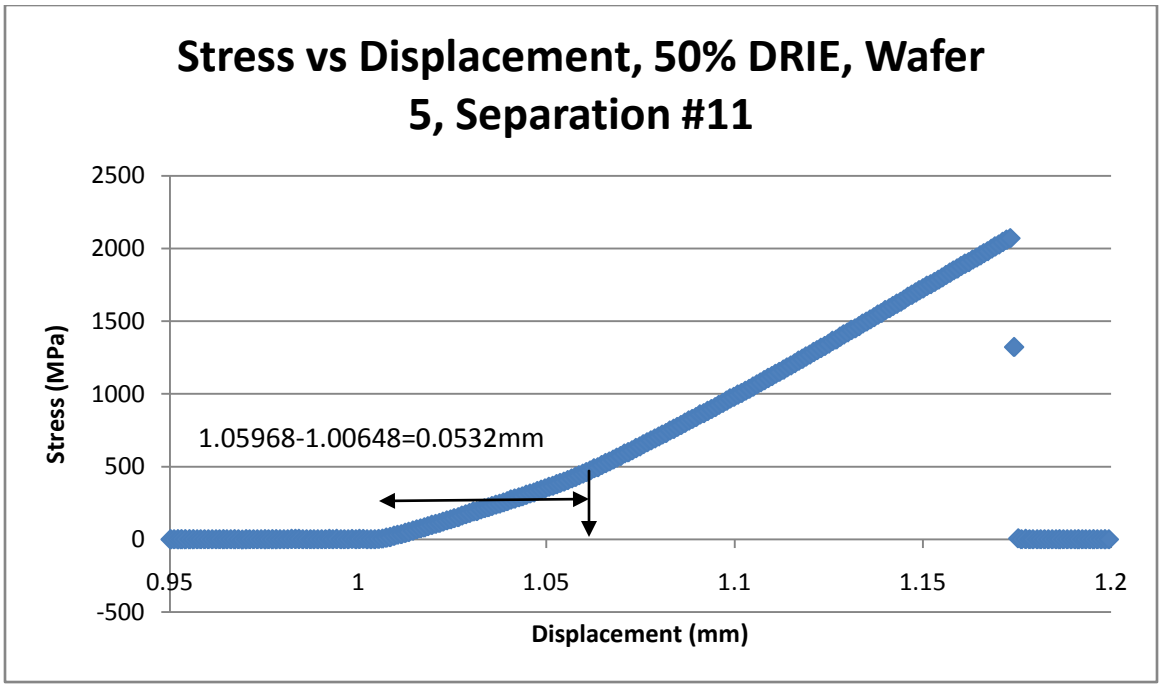

Figure 3-32. SCF corrected stress versus displacement for 50% DRIE wafer 5, separation #11.

Diced separation profiles shown in Figure 3-33 show that fracture occurs at the connection point between the round saw edge and the linear taper of the blade and not at the middle point of the saw tip as was expected.

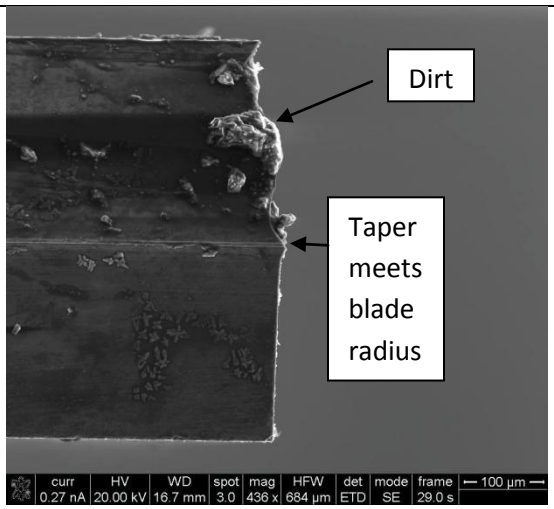

a) Top side die, separation 7

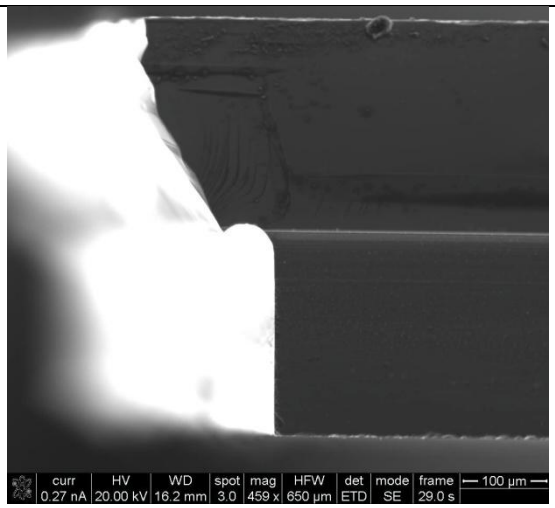

b) Bottom side die, separation 11

Figure 3-33. 50% Diced wafer 4 separated die #6. <100> flat facing out of page.

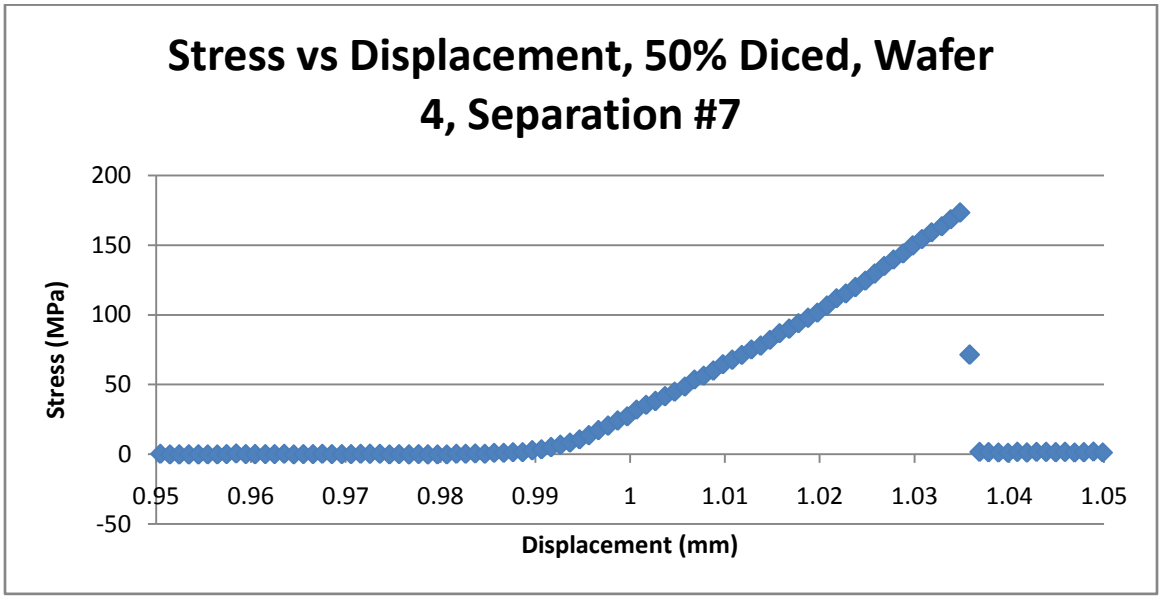

Figure 3-34. SCF corrected stress versus displacement for 50% diced wafer 4, separation #7.

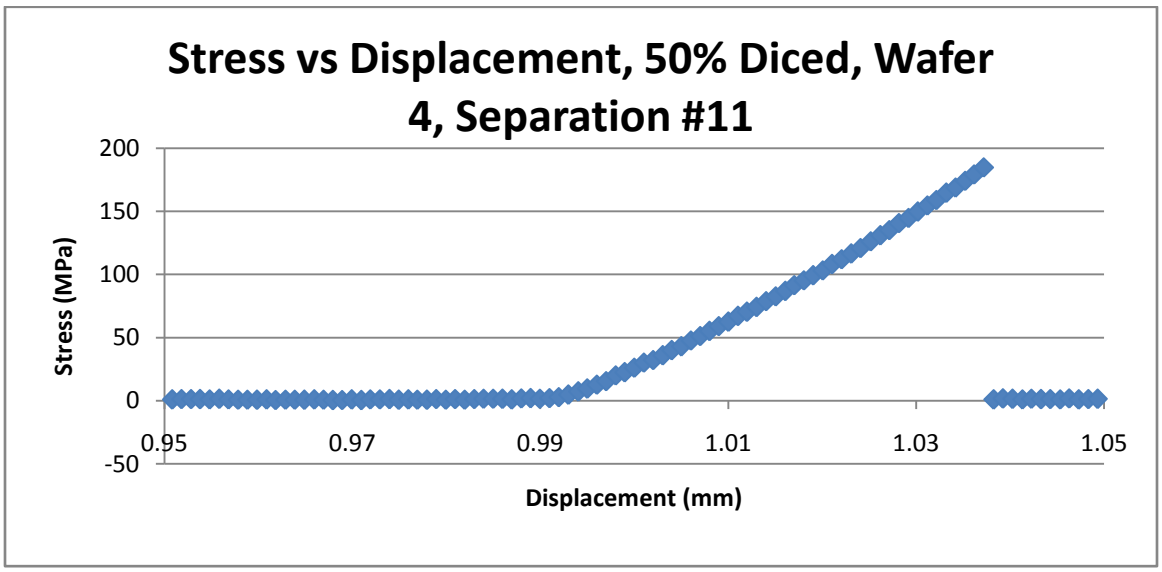

Figure 3-35. SCF corrected stress versus displacement for 50% diced wafer 4, separation #11.

Separation and fracture stress data for the 50% diced and 50% DRIE samples is shown below while, all others are shown fully in the appendix (A1). The Weibull fit was effective at predicting cleaving stress for the samples. The Weibull parameters for the 50% diced separation (cleaving) stress data were α=188.4 MPa and β=3.701. Figure 3-36, Figure 3-37, and Figure 3-38 show the cumulative distribution (CDF), probability distribution function (PDF), and the frequency versus separation stress respectively. Separation stress for the 50% diced samples when fitted with the Weibull distribution had a correlation coefficient of 0.9229. The closer a correlation coefficient is to 1 the better the fit.

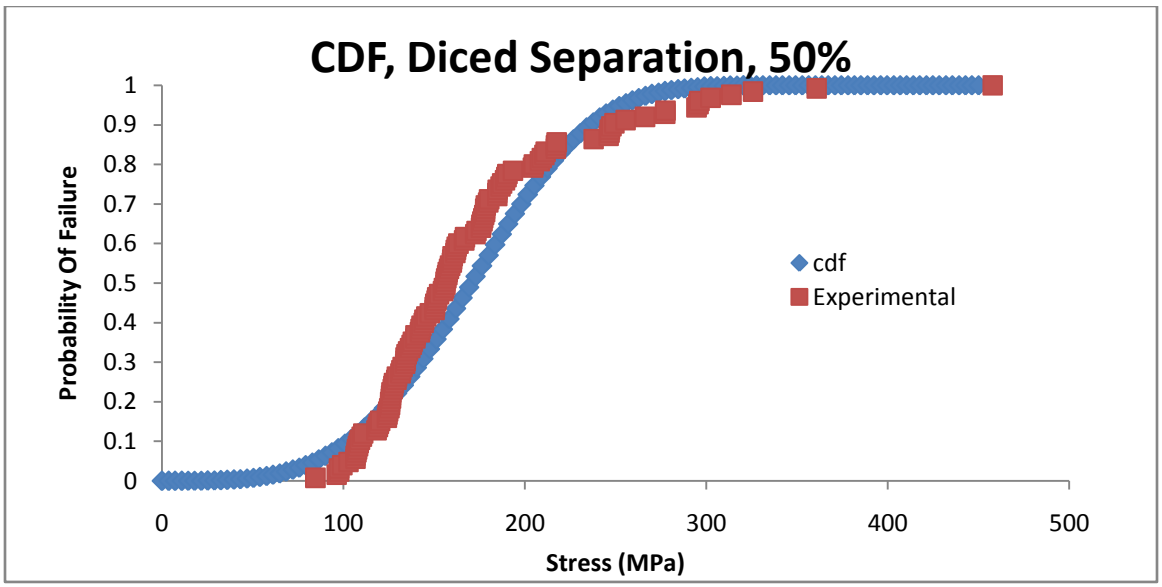

Figure 3-36. Cumulative distribution function and experimental stress for the separation of all the diced 50% samples.

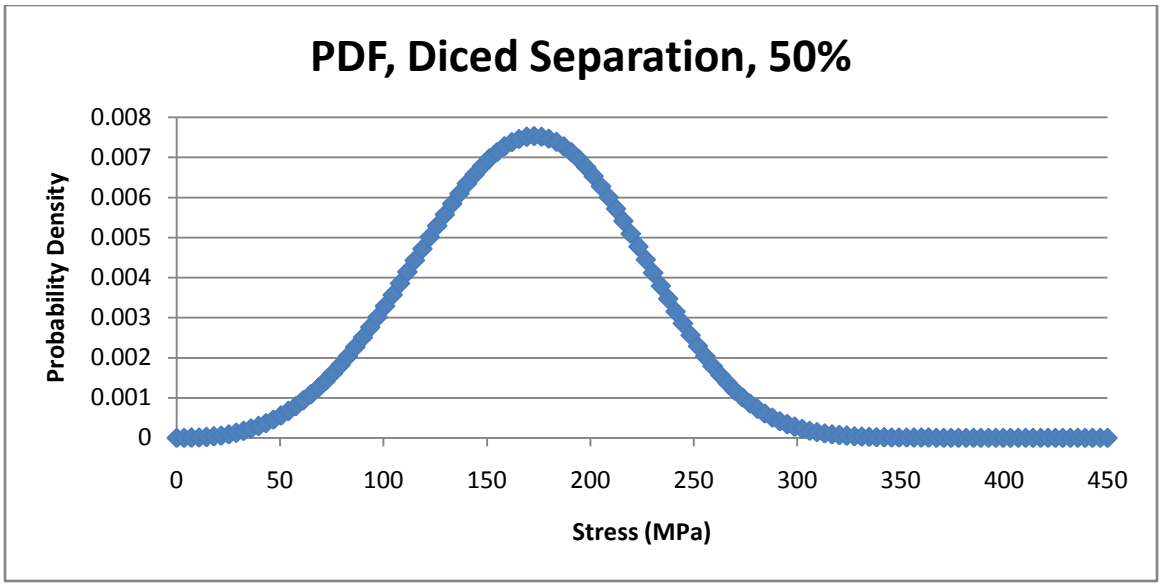

Figure 3-37. Probability density function for the separation of all the diced 50% samples.

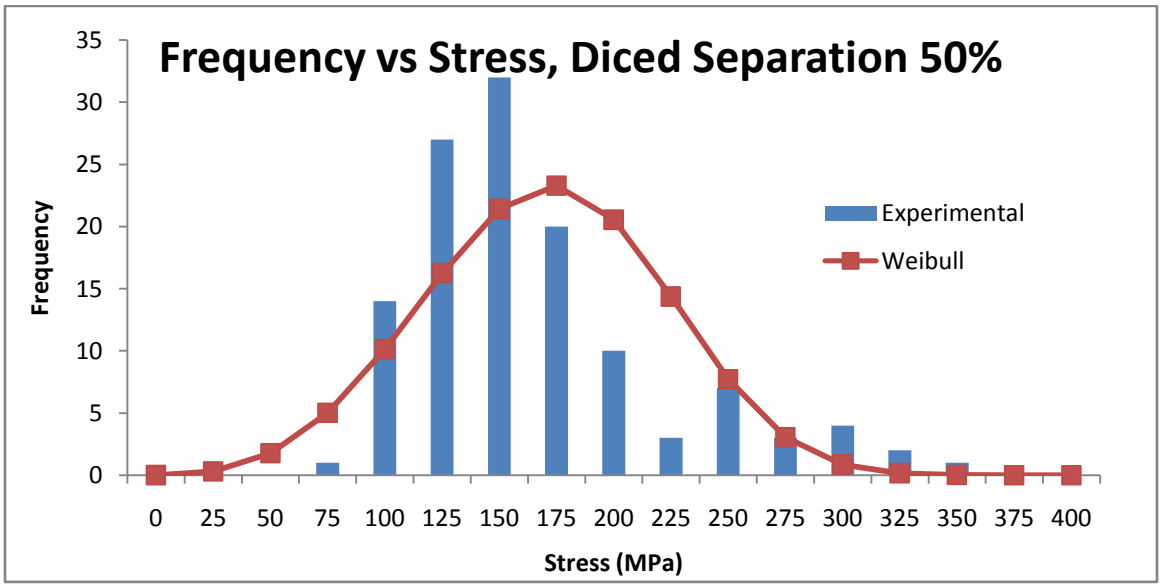

Figure 3-38. Frequency versus stress for the experimental data and the Weibull fit for the separation of the diced 50% samples. Total number of samples is 125.

After separation, the individual dies were broken and the stress was recorded.

Figure 3-39, Figure 3-40, and Figure 3-41 show the cumulative density function, the

probability density function, and the frequency versus stress for the diced die fracture 50% test. The shape factor (β) and scale factor (α) for the 50% die set was 6.160 and 527.89 MPa, respectively. The correlation coefficient for the diced die break at 50% was 0.9265.

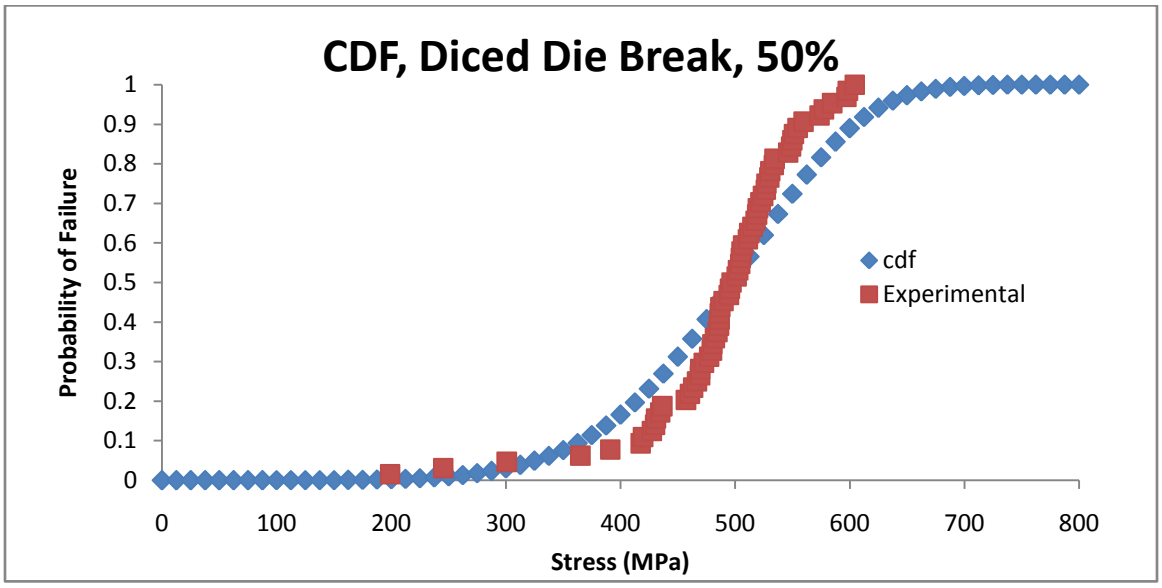

Figure 3-39. Cumulative distribution function and experimental stress for the die break of all the diced 50% samples.

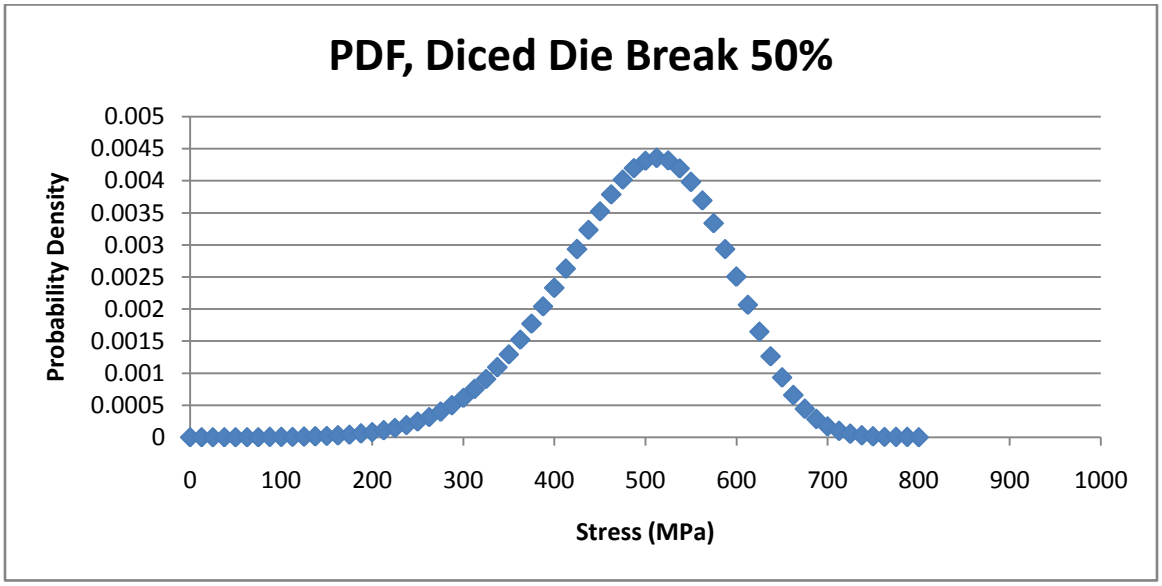

Figure 3-40. Probability density function for the die break of all the diced 50% samples.

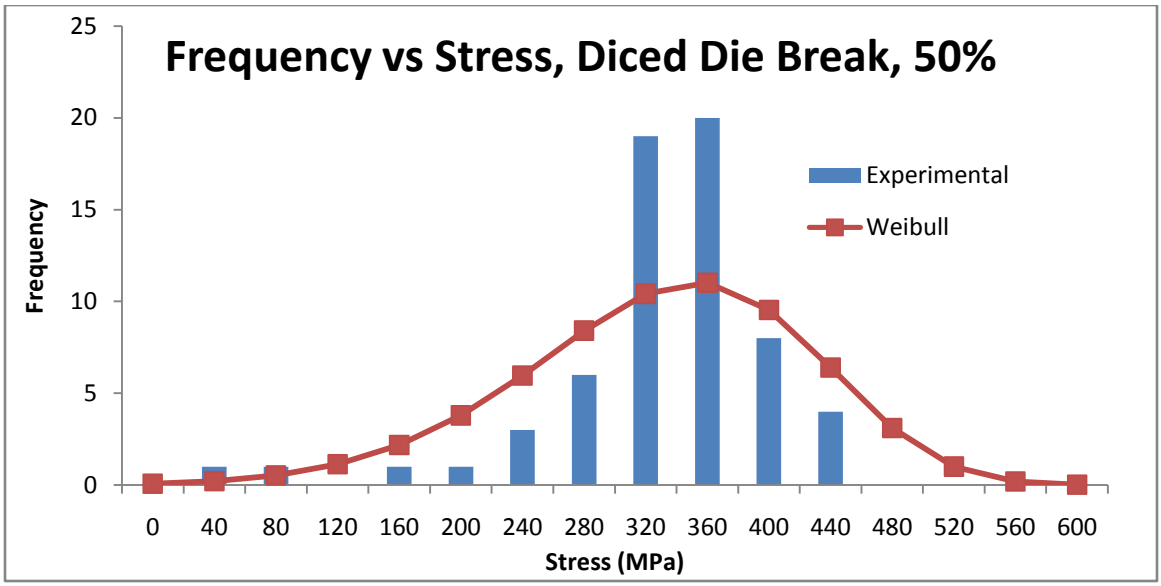

Figure 3-41. Frequency versus stress for the experimental data and the Weibull fit for the die break of the diced 50% samples. The total number of samples is 64.

Cumulative density function, probability density function and frequency versus stress results for the 50% DRIE separation samples are shown in Figure 3-42, Figure 3-43, and Figure 3-44 below respectively. The shape factor (β) and scale factor (α) for the 50% die set was 1.524 and 1241.6 MPa, respectively. The correlation coefficient for the 50% DRIE separation data below is 0.969.

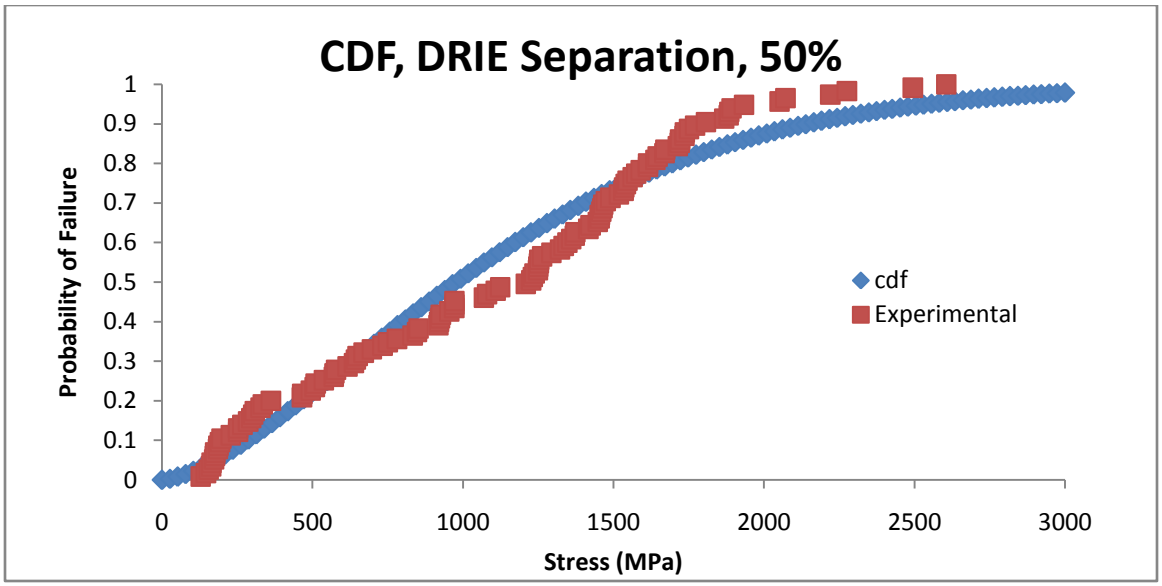

Figure 3-42. Cumulative distribution function and experimental stress for the separation of all the DRIE 50% samples.

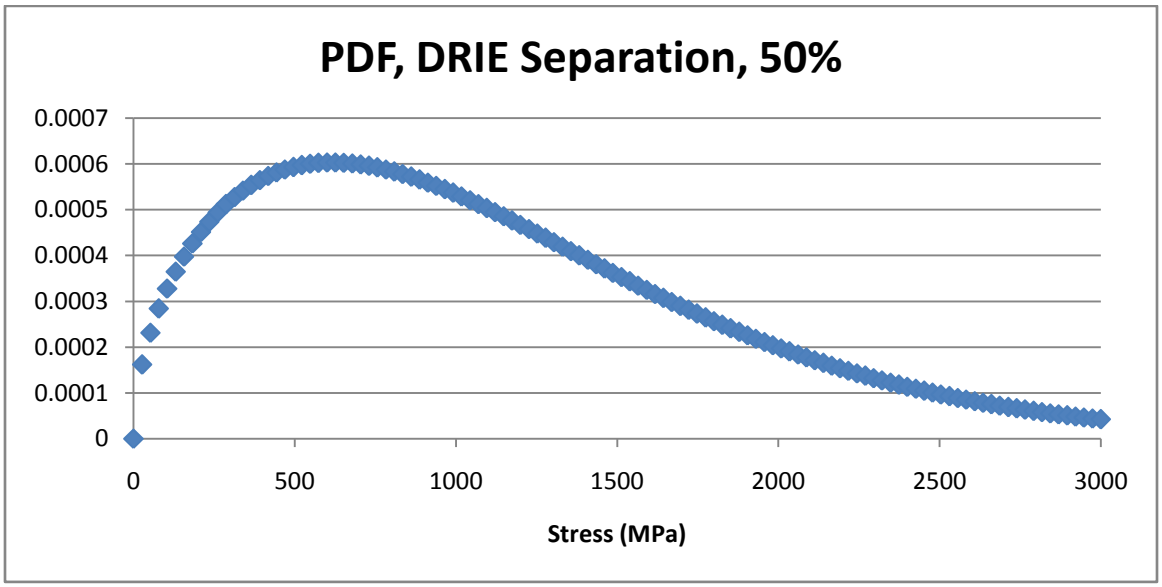

Figure 3-43. Probability density function for the separation of all the DRIE 50% samples.

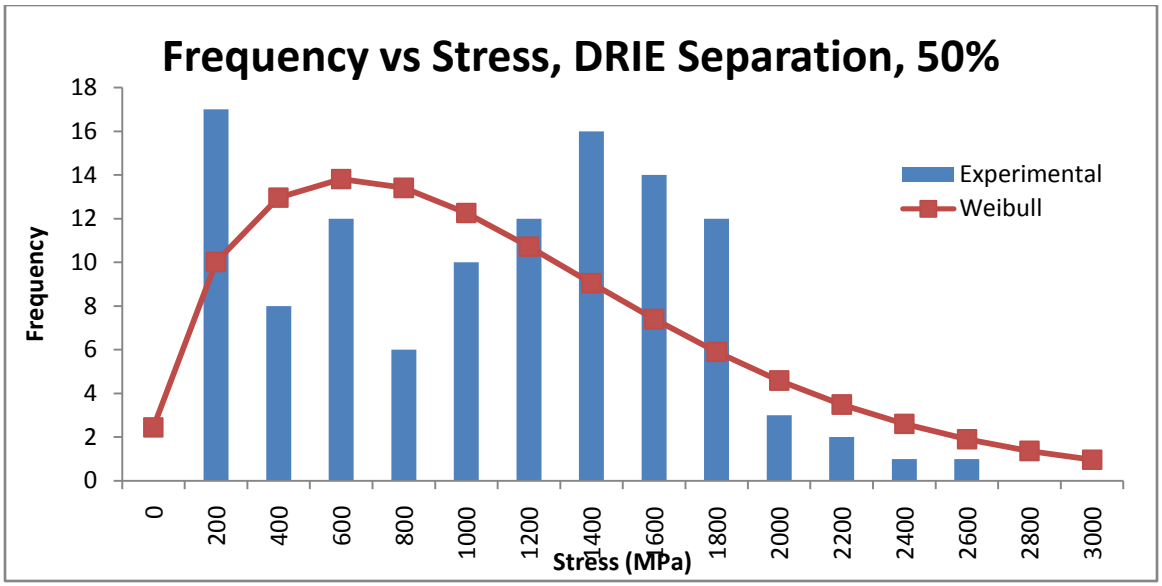

Figure 3-44. Frequency versus stress for the experimental data and the Weibull fit for the separation of the diced 25% samples. Total number of samples is 115.

Cumulative density function, probability density function and frequency versus stress results for the 50% DRIE break samples are shown in Figure 3-45, Figure 3-46, and Figure 3-47 below respectively. The shape factor (β) and scale factor (α) for the 50% die set was 3.456 and 530.45 MPa, respectively. The correlation coefficient for the 50% DRIE break data below is 0.989.

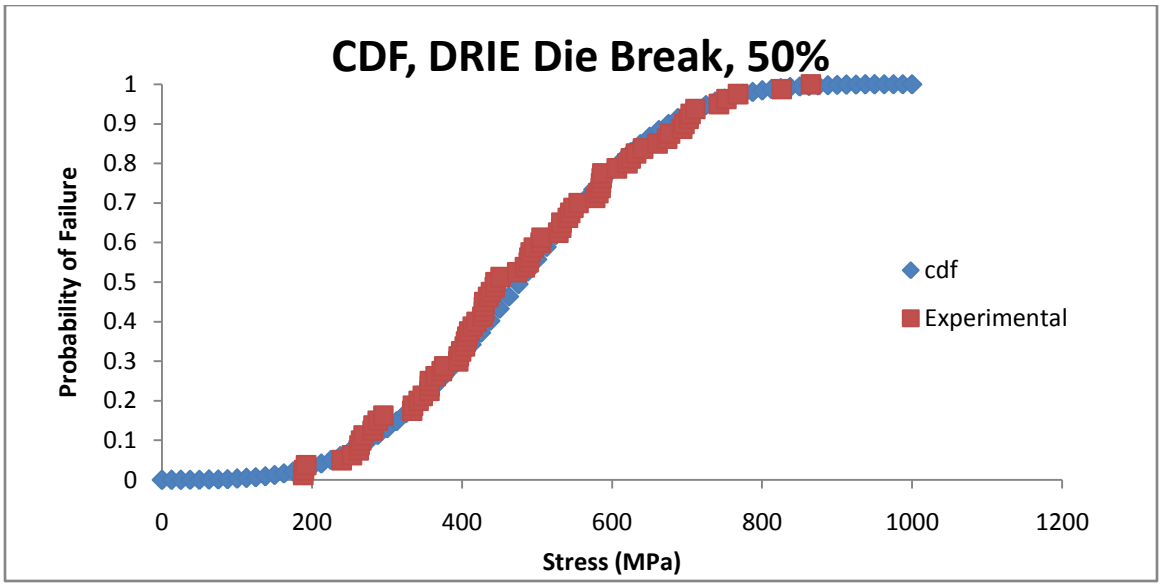

Figure 3-45. Cumulative distribution function and experimental stress for the die break of all the DRIE 50% samples.

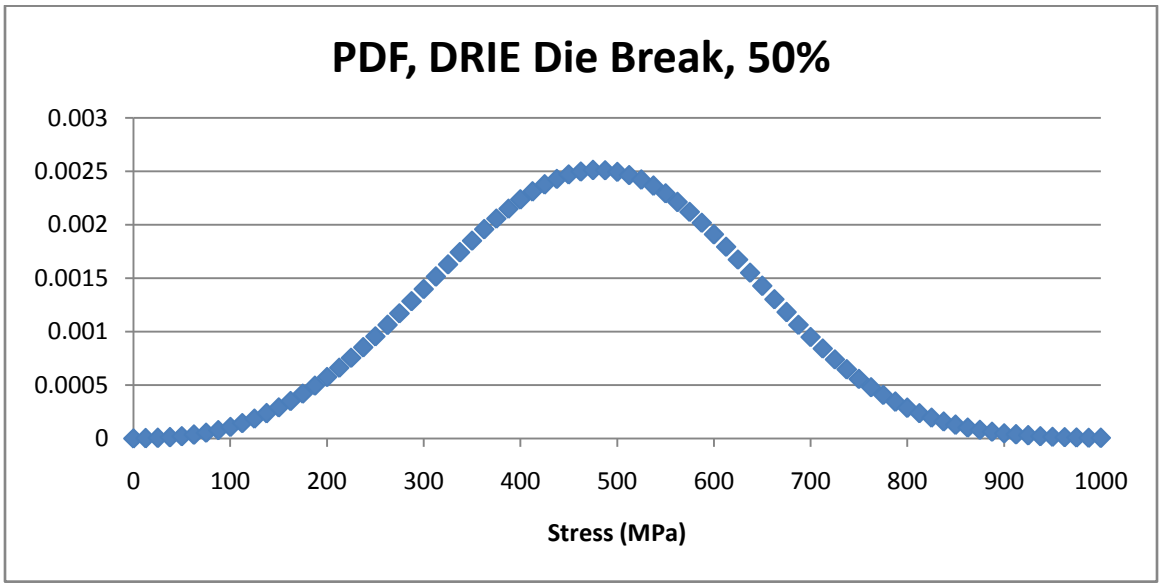

Figure 3-46. Probability density function for the die break of all the DRIE 50% samples.

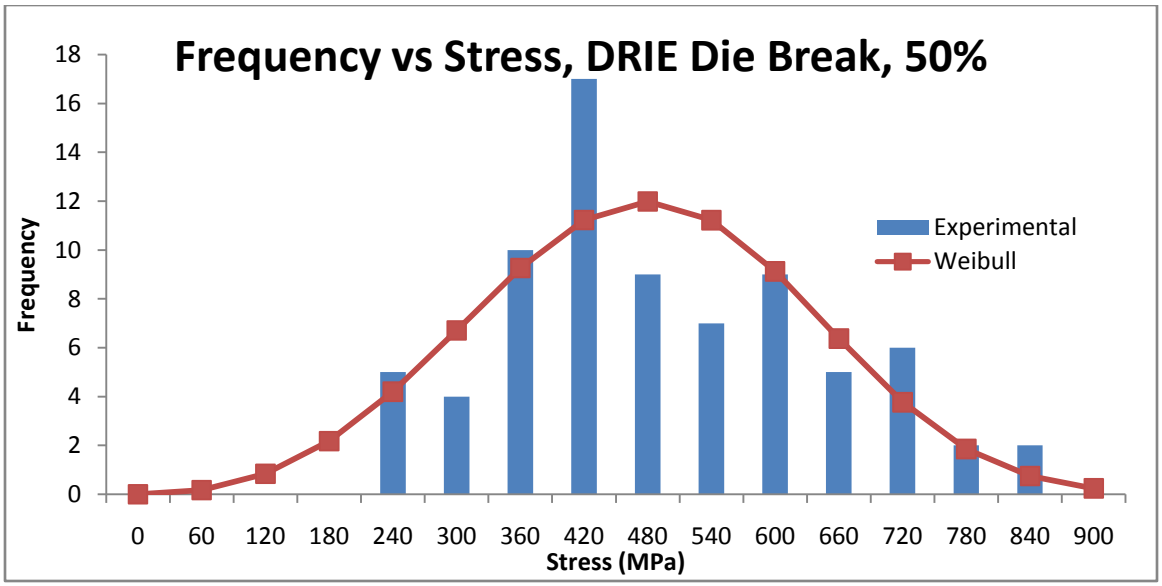

Figure 3-47. Frequency versus stress for the experimental data and the Weibull fit for the die break of the DRIE 50% samples. Total number of samples is 80.

Wafer breaking stress for all of the diced and DRIE samples are shown in Table 3-11 and Table 3-12 as well as Figure 3-48. The error bars represent one standard deviation. Note that there are slightly less samples for the 25% DRIE, this is due to many high energy fractures. The release of the high loads often caused premature failure in other notches, or damaged other die.

Diced Sep.	Stress (MPa)		
% Trench Depth	Mean	StdDev	# Samples
25	220.03	64.20	125
50	169.99	51.16	125
75	233.64	60.32	125

Table 3-11. Summary of all diced separation stresses.

DRIE Sep.	Stress (MPa)		
% Trench Depth	Mean	StdDev	# Samples
25	778	495	57
50	1119	356	115
75	1097	316	125

Table 3-12. Summary of all DRIE separation stresses.

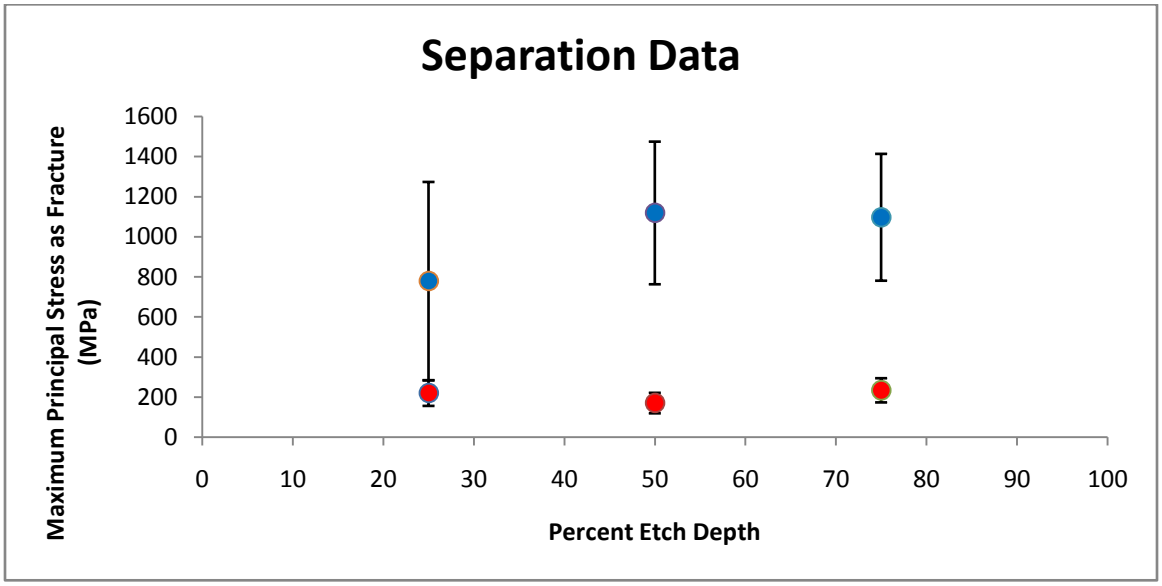

Figure 3-48. Separation data for all wafers.

Interestingly, the 50% diced wafers cleaved at slightly less stress than the stress at 75% and 25%. As the data shows, there is no conclusive dependence on trench depth versus the cleaving stress at separation. This likely indicates that the flaw density and average flaw size remain relatively constant over the trench surfaces. It can be said that with a smoother notch transition for the DRIE 50% and 75% etch that these wafers are good for handling processes. Die fracture stresses resulting from the different separation methods are shown in Table 3-13 and Table 3-14 as well as Figure 3-49 and Figure 3-50.

Diced Break	Stress (MPa)		
% Trench Depth	Mean	StdDev	# Samples
25	493.05	103.11	64
50	490.44	92.74	64
75	443.59	70.73	64
100	451.83	64.73	64

Table 3-13. Summary of all diced die break stresses.

DRIE Break	Stress (MPa)		
% Trench Depth	Mean	StdDev	# Samples
25	353.61	216.48	40
50	476.96	152.65	80
75	443.76	124.76	80
100	126.10	26.55	80

Table 3-14. Summary of all DRIE die break stresses.

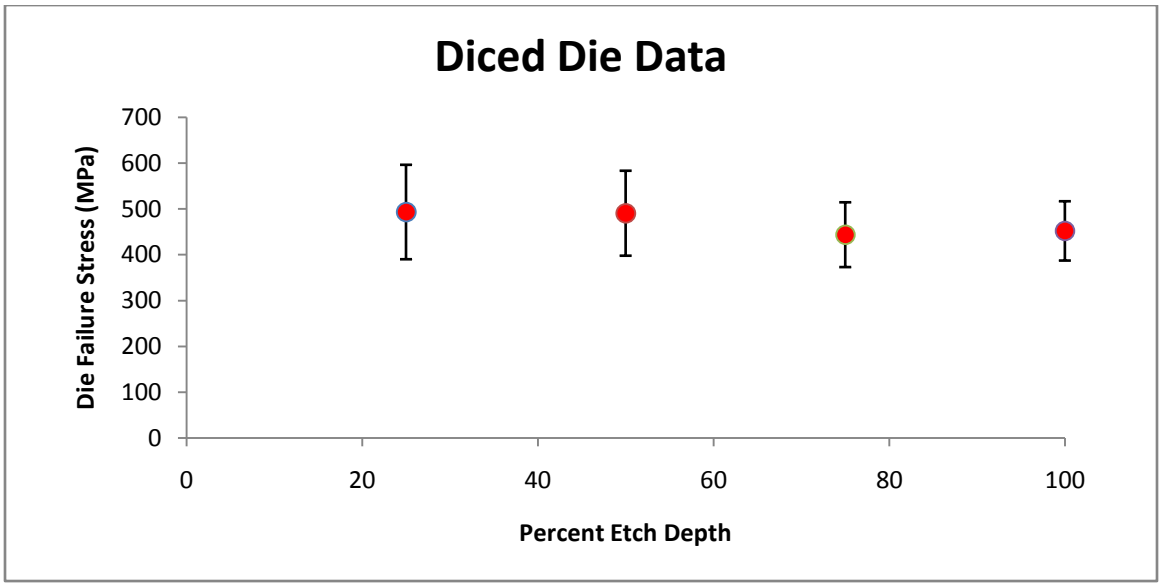

Figure 3-49. Diced die fracture stresses versus trench depth.

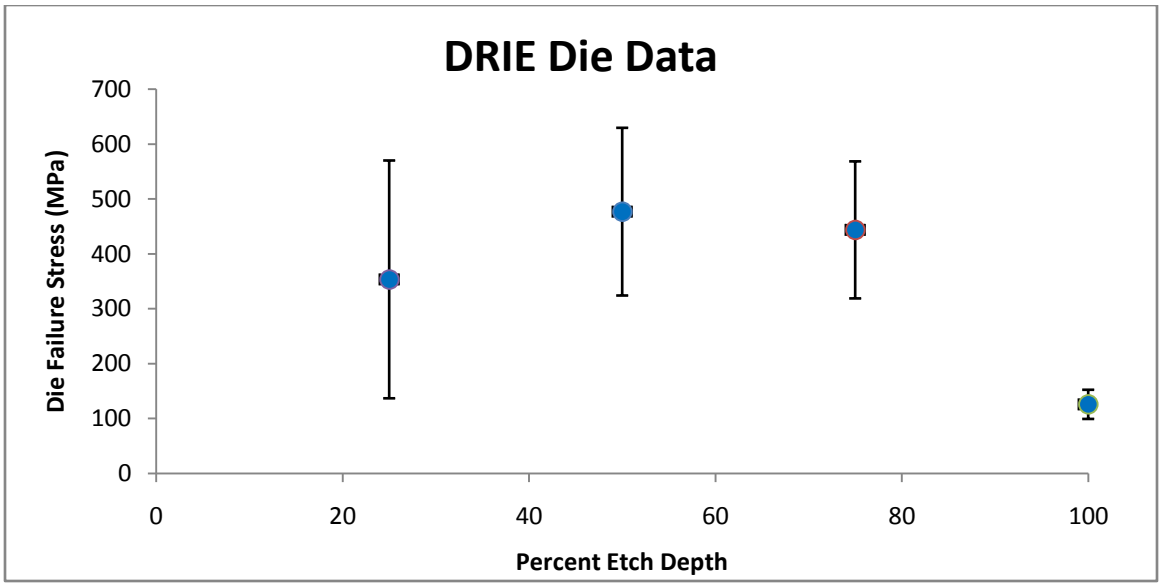

Figure 3-50. DRIE die fracture stresses versus trench depth.

In Figure 3-49 above it is evident that the stresses at which diced die fracture decrease as trench depth increases. This could be explained by a smoother sidewall surface remaining after separating the individual die. A higher percentage area of smooth shear plane shows that the strength of the die can be increased. Figure 3-2 above shows how rough of a surface dicing can produce. The stress at which the diced dies were separated is also lower than the diced die strength which would lend evidence to this theory. Therefore, die with a higher percentage of shear plane area should yield stronger die.

One issue that was observed during the 100% DRIE wafer etching occurs when the gas flow is not ultra pure, which then causes particles to deposit on the bottom of trenches and form micro-masks. Micro-masks tend to form a structure referred to as "grass" which appears like silicon stalagmites (Dixit 2006). As trenches become deeper, these particles are not easily removed. This phenomena also happens when the flow rate

of SF_6 is very high. As the DRIE trench aspect ratio increases, the side walls become more rugged and thus more flawed, which in turn can decrease the fracture stress. Figure 3-51 below shows what the formation of grass looks like (Dixit 2006). Bottom edge surface roughness like the one shown in Figure 3-52 can also become failure initiation locations if they are put under a tensile load.

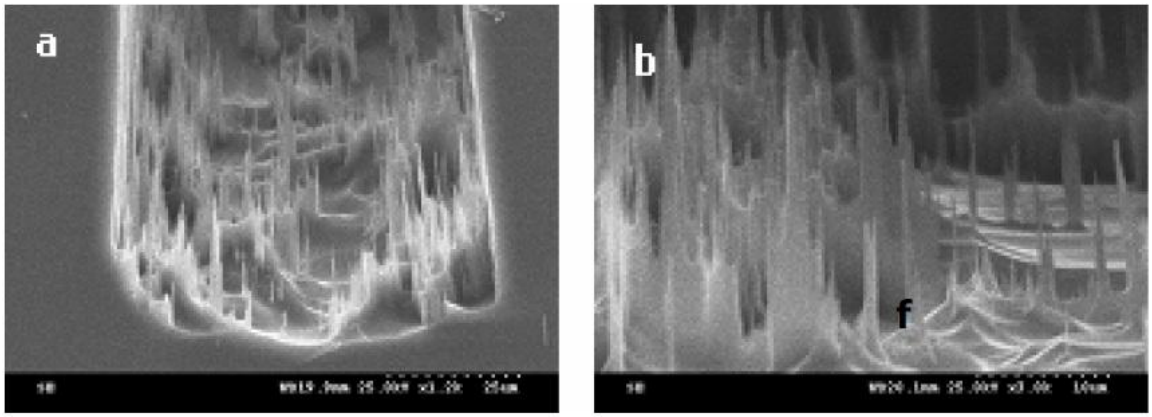

Figure 3-51. Grass formation at the bottom of DRIE trenches (Dixit 2006).

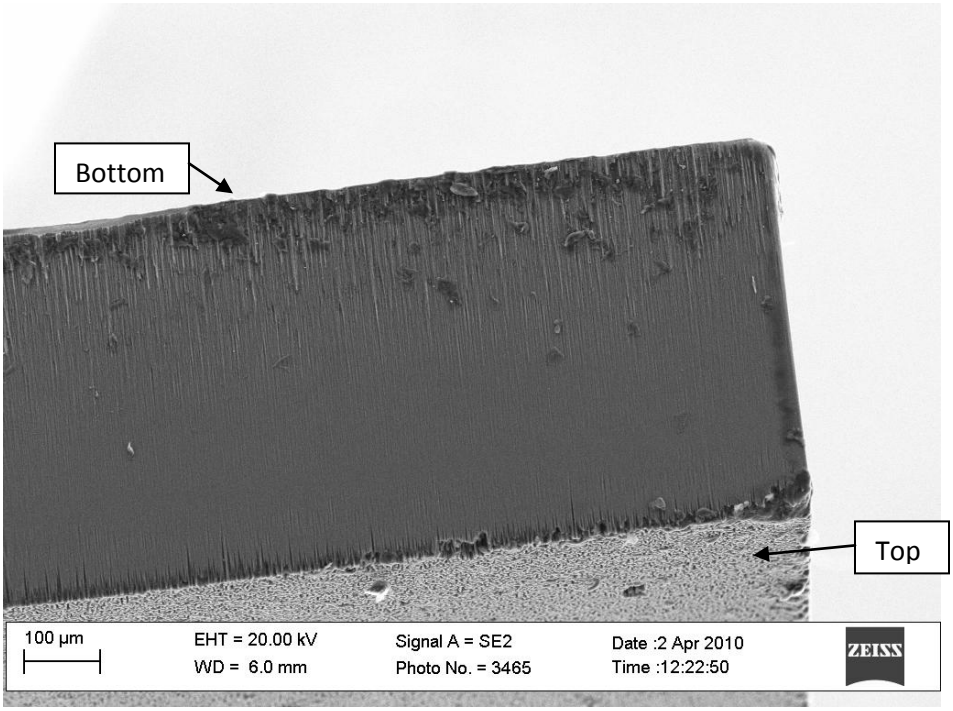

Figure 3-52. Edge surface SEM picture of a 100% DRIE sample.

The fracture stress of the 100% DRIE dies was over three times lower than the other DRIE separation depths. The surface roughness at these depths had to be extremely high with large flaw sizes. Further inspection of the 100% DRIE samples under a SEM showed that the protective photo-resist mask did not fully survive the 525µm etches. The photo-resist had failed somewhere between the 75% and 100% etch giving a deep porous structure which in turn crippled the strength of the die. This problem could have been prevented by using a more resistant photo-resist, or by spinning a thicker coating of the original photo-resist. The problem that arises with spinning a thicker coating is the formation of a steeper edge bead that would have increased the 70µm trenches geometry. For the sake of this experiment and the fact that the surface roughness of 100% DRIE samples were heavily modified, the samples that were affected by this problem cannot be used to derive a conclusion about trends. Figure 3-53 and Figure 3-54 shows surface roughness of the 100% DRIE samples.

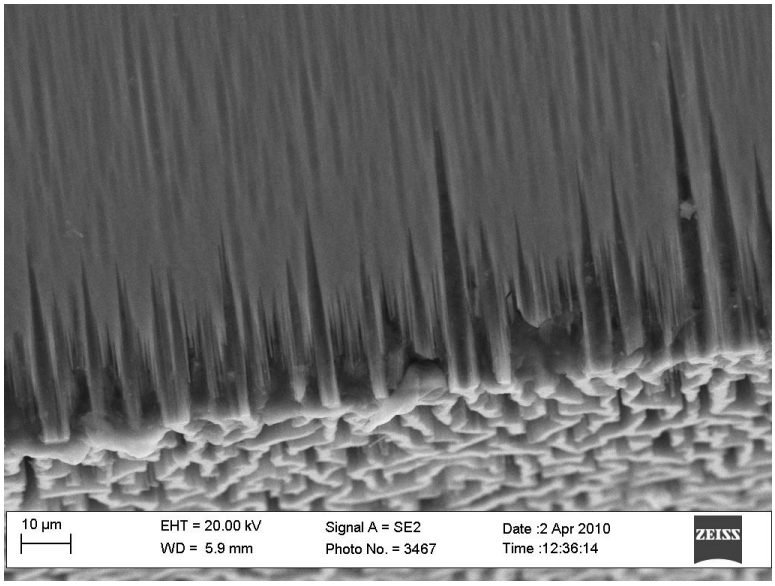

Figure 3-53. Surface roughness of 100% DRIE samples arising from the failure of the photoresist.

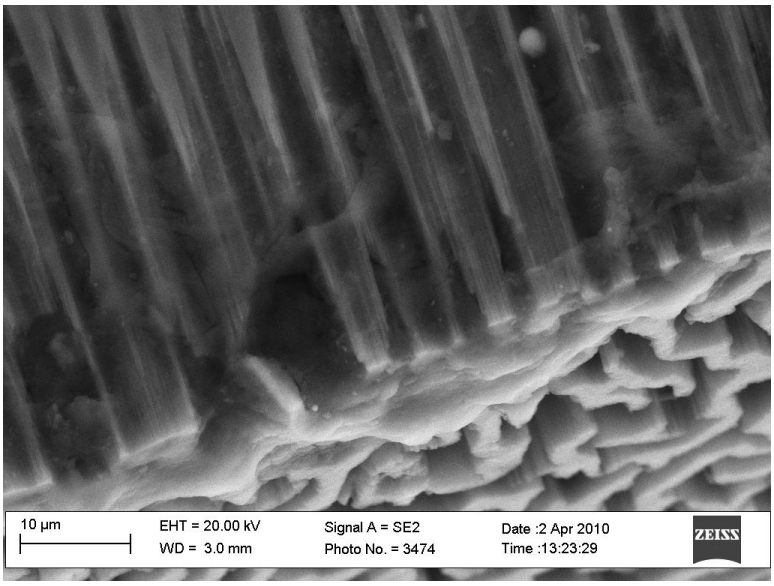

Figure 3-54. Higher magnification of the porous structure in the 100% DRIE samples.

3.5 Double-Side Notch Wafer Separation and Die Strength

The DRIE double sided wafer was separated and each individual die was tested for fracture strength just like the previous experiments. Separation and die fracture stress data had a Weibull correlation coefficient of 0.932 and 0.966 respectively. Results for the double sided wafer experiments are shown in Table 3-15 below.

Double Sided DRIE Results (MPa)	
Separation Mean	2327.27
Separation Standard Deviation	781.26
Die Fracture Mean	360.66
Die Fracture Standard Deviation	156.88

Table 3-15. DRIE double sided etch wafer results.

Shape parameters for the separation and fracture strength are 3.278 and 2.454 respectively while the scale parameters are 2595 and 406.6 respectively. When compared

to the other separation methods above, the DRIE double-sided etch had the highest separation stress but had a considerably low die fracture stress. Figure 3-55, Figure 3-56, Figure 3-57, and Figure 3-58 show the cumulative distribution and probability density function for the DRIE double sided etch.

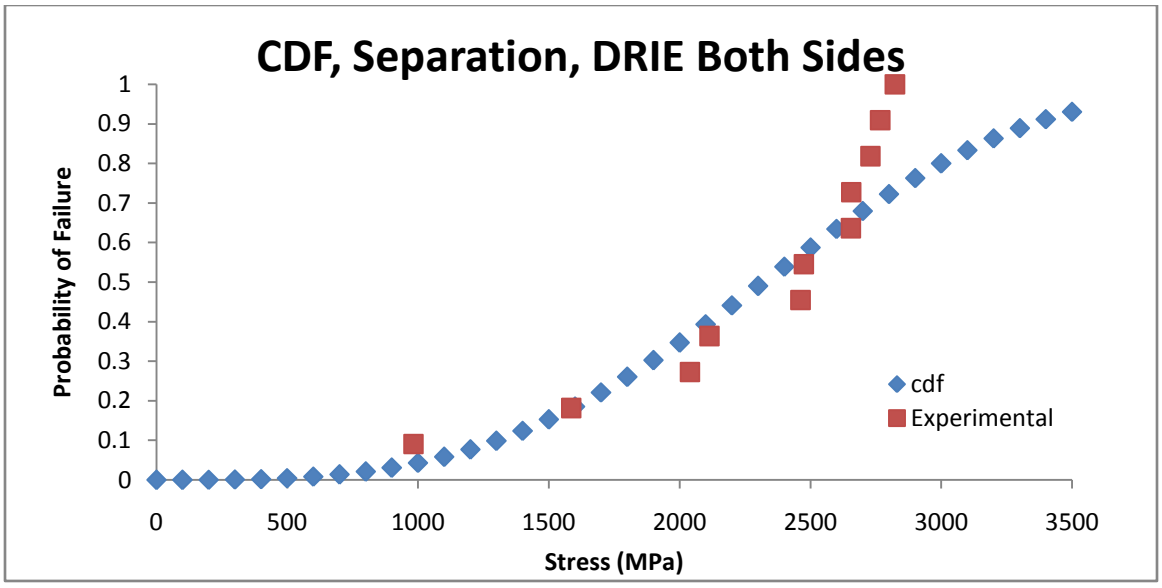

Figure 3-55. CDF separation results for the DRIE double sided wafer etch.

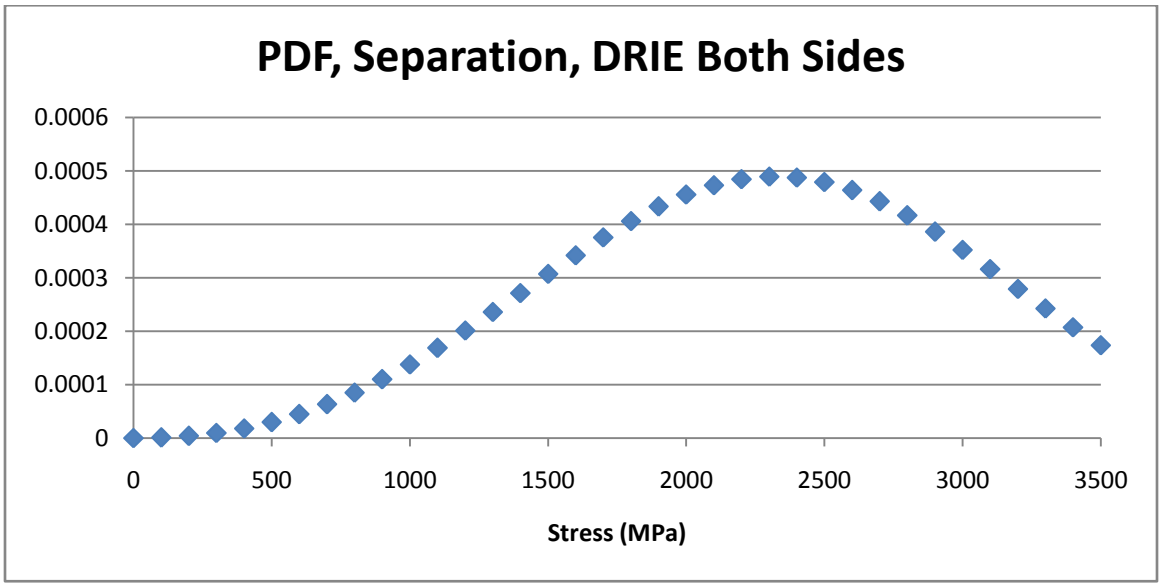

Figure 3-56. PDF separation results for the DRIE double sided wafer etch.

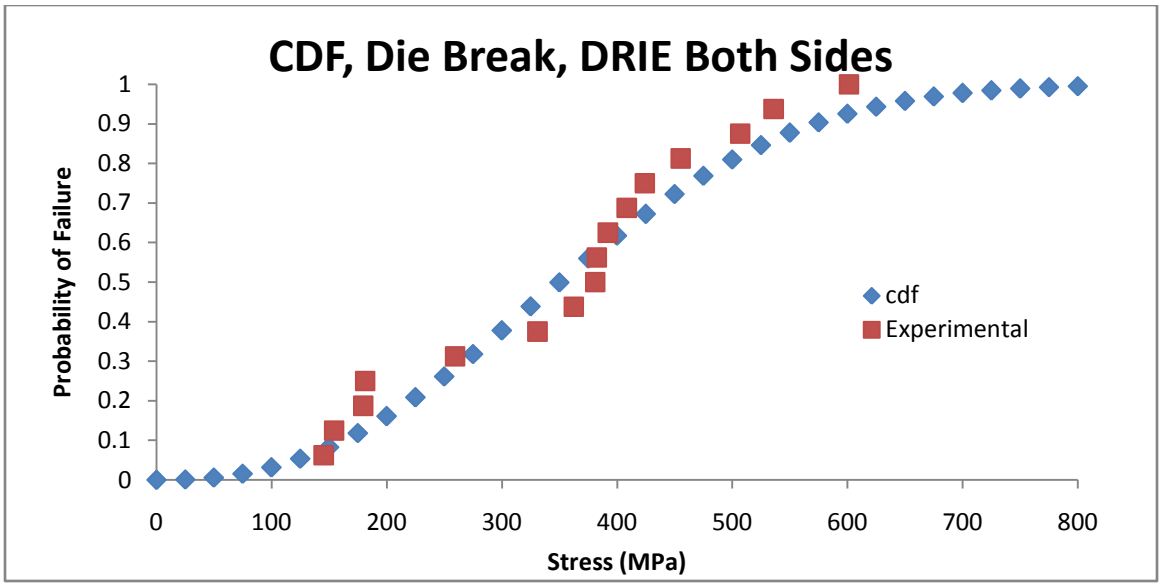

Figure 3-57. CDF for the fracture strength of DRIE double sided wafer etch.

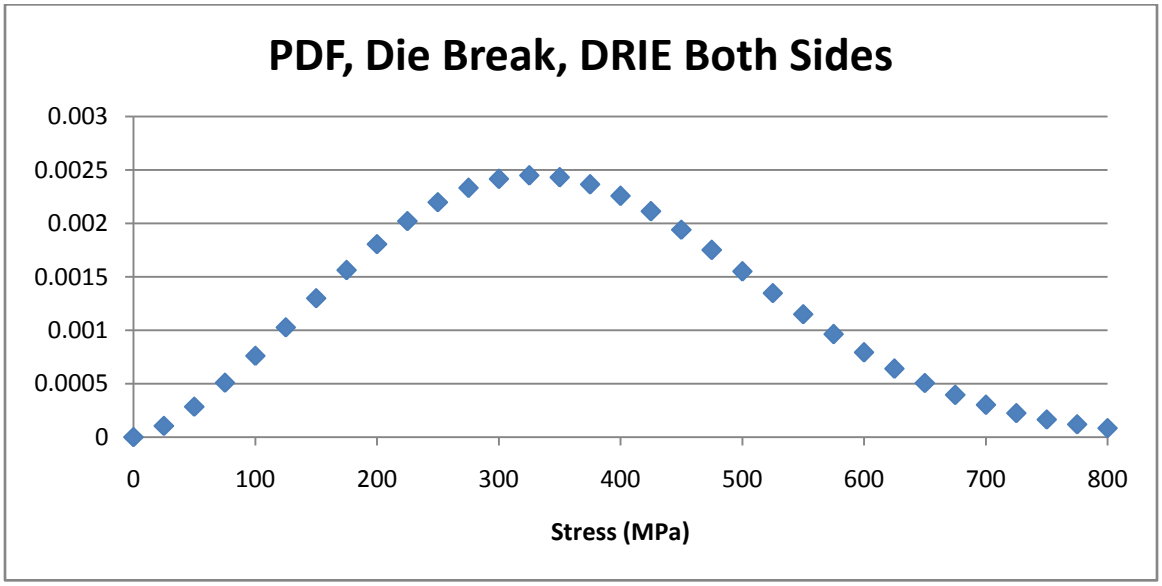

Figure 3-58. PDF for the fracture strength of DRIE double sided wafer etch.

3.6 Discussion of Results

When analyzing the Weibull fit for the die separation and die fracture, it is important to note that a higher shape factor β means a higher rate of stress transition in the cumulative distribution function as seen in the diced die separation and is an indication of better repeatability. The DRIE shape factors on the other hand are not as high as the diced and show a high variance with separation data. Whenever a probability density function skews more left or right, like shown in Figure 3-43 (50% DRIE separation), this means that there are significant outliers on either the high stress side or the low stress side. For the 50% DRIE separation data it is evident that there are a few high stress separation outliers. If the probability density function was to be integrated, the resultant function would be the cumulative distribution function.

Some trends seen in Table 3-16 and Table 3-17 below are that diced separation and die fracture samples always have a higher shape parameter meaning that the diced samples were more repeatable. The scale parameters for DRIE separation data were much higher that diced separation data. This means that the range of fracture stress for the DRIE separation samples was higher.

	Weibull Separation Parameters			
	Shape Parameter β	Scale Parameter α	Correlation Coefficient ρ	# Samples
25% Diced	3.829	243.35	0.9845	125
50% Diced	3.701	188.36	0.9229	125
75% Diced	4.384	256.41	0.9919	125
25% DRIE	1.610	868.77	0.9900	57
50% DRIE	1.524	1241.62	0.9691	115
75% DRIE	3.878	1212.43	0.9913	125

Table 3-16. Weibull separation parameters for all samples.

	Weibull Die Fracture Parameters			
	Shape Parameter β	Scale Parameter α	Correlation Coefficient ρ	# Samples
25% Diced	5.520	533.94	0.9486	64
50% Diced	6.160	527.88	0.9264	64
75% Diced	7.397	472.85	0.9940	64
100% Diced	8.304	478.92	0.9843	64
25% DRIE	1.680	395.98	0.9873	40
50% DRIE	3.456	530.45	0.9891	80
75% DRIE	4.009	489.52	0.9930	80
100% DRIE	5.482	136.62	0.9719	80

Table 3-17. Weibull die fracture parameters for all samples.

It was thought that the fracture surface after cleaving for the diced samples would weaken the dies significantly. In fact, the dies produced from a 25% and 50% diced trench depth separation had higher failure strengths than the dies resulting from a 75% and 100% diced depth separation routine. Some speculation is that the shear plane brought about by die separation is smoother and has a smaller flaw size that the original diced trench.

An important aspect of die separation to note is that the primary issue of final die strength is countered by the time and effort put into separated them. Though DRIE could lend to higher die failure stress, one has to ask if it is worth the long and tedious hours put into it (three and a half hours for a 100% sample in this case). If the cost and time of doing a DRIE process decreased significantly in the future, then maybe separation due to ion etching could compete with traditional mechanical dicing.

When separating the samples a modest balance between separation stress and resulting die failure strength must be considered. A high separation stress tends to increase the variability of die strength and even has the potential to cause catastrophic

and premature die failure as seen in the 25% DRIE etched samples. On the other hand, a very low separation stress can cause premature separation just from handling.

It has been observed numerous times that the preferred fracture plane for single crystal silicon is the <111> plane. For the notched separation process outlined in this work this has a potential to shear in areas other than the notch profile. If a component was manufactured with critical features on both sides of the wafer and near the edge of the die, then this could become a problem if separated using a notched method. Even though die strengths were slightly lower for 75% and 100% samples, it may be an acceptable trade off so that the shear plane does not incapacitate critical die components. To prevent unwanted shearing effects, some extra distance between the notch kerf and critical die components can be utilized.

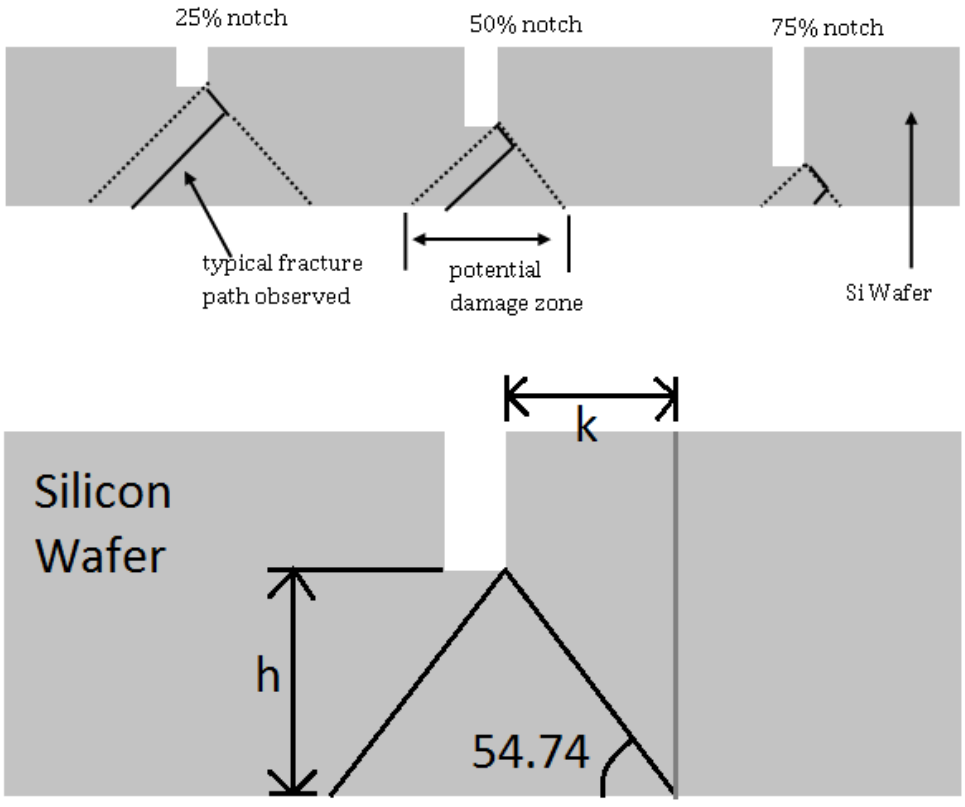

Figure 3-59. Potential damage areas resulting from <111> plane shear.

The maximum distance that a critical component should be placed, *k*, is found from

$$k = \frac{h}{tan\ 54.74^o} \qquad \text{(Eq. 3-19)}$$

where *h* is the throat area height and 54.74º is the angle that the <111> plane forms with the <100> plane.

3.7 Potential Application of Results

One potential benefit from the findings of this research is the use of shallow mechanical dicing and cleaving in the silicon ribbon pulling technique devised for photovoltaic cell manufacturing. Silicon ribbon pulling was created by D. N. Jewett of Energy Materials Corporation and creates sheets of silicon by pulling a seed ribbon out from a quartz crucible filled with molten silicon.

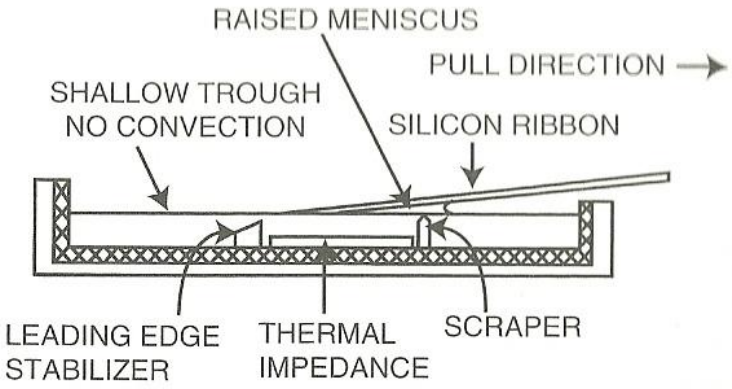

Figure 3-60. Diagram for silicon ribbon pulling (Komp 2002).

If the silicon ribbon can be processed into photovoltaic devices and then afterwards is scribed via a hard tipped tool or possibly even a dicing saw then the individual cells could be cleaved and have a higher strength than they did if they were sawn completely through. Such strength improvements may greatly increase the service lifetime of the final photovoltaic device.

IV. Conclusions

DRIE notched samples in this experiment had vertical sidewalls and a varying bottom profile that changed with depth. The side wall to bottom profile transition had fillets that were 5μm in radius on average and were where the maximum stress concentrations occurred. Dicing saw samples in this experiment had 88º sidewalls and a gradual round bottom profiles resulting in a maximum stress concentration at the very bottom of the profile.

The max stress concentrations occurred with a deeper trench in DRIE than with the dicing saw and both occurred before a 50% depth trench. Etch depths with the DRIE method were not as precise as the dicing saw method. A Weibull distribution fit the data better than a normal distribution.

The DRIE samples separated at a higher stress than the diced samples. DRIE samples separated at a 25% etch had a lower fracture stress. This is most likely from a high energy fracture that caused premature separation of samples. 100% DRIE samples failed at extremely low stress due to photoresist failure that resulted in micro pores being

formed at the surface. Formation of "grass structures" were apparent on the 100% DRIE samples. Diced sample die failure stress was higher at shallow trench separations than it was at deeper diced trenches. Variations of die failure stress decreased as the depth of the diced trench increased. The double sided DRIE etched wafer had the highest separation stress of all wafers. Though the dies resulting from this wafer had one of the lowest fracture strengths.

IV. Future Recommendations

For the next iteration of research related to the contents of this thesis it is recommended that insight into the separation stresses relating to thin wafers be tested, a successful 100% DRIE etch be performed for thick wafers, have a dynamic FEA analysis for the SCF of DRIE notches, and stress analysis using a plate stress equations that incorporate strain in the z direction.

Thinner wafers, as implied in the introduction of this thesis, are gaining popularity and an investigation of the feasibility of DRIE notch separation techniques could prove useful. Most of the time required for the DRIE samples is the actual etch process and etching notches into thin wafers should take roughly 30 minutes; a vast improvement over the three and a half hours the 525μm wafers required. Also mask failure is unlikely for shorter etches.

Etching of the 100% DRIE wafers were unsuccessful in this thesis attempt. If a thicker or a more resilient photoresist could be applied then separation and failure stresses could be derived from a 3 point bending test. It is recommended that the first

attempt be multiple applications of Shipley 1827 photoresist spun onto the wafer at 1800 rpm.

The DRIE notch profile changed with etching depth but was modeled with a consistent 90μm bottom radius and 5μm side fillets for the work of this thesis. Determining SCF with FEA models that vary with given depth to simulate an actual side profile etch given the used DRIE etching recipe would help improve the calculated SCF. The dicing saw side profile used in this work should suffice because the slope of the diced trench was constant throughout the FEA models.

With the work presented here, only one double-sided DRIE wafer was processed, separated, and each die fractured. In the future, more wafers should be fabricated with not only the original depth, but varying depths too. The more samples that are prepared, the more accurate the Weibull distribution results will be.

The standard Euler-Bernoulli theory was used in beam bending to determine separation and die failure stresses. More accurate and sophisticated theories could be used such as Kirchhoff-Love theory for thin plates or Mindlin-Reisssner theory for thick plates. The Kirchoff-Love theory assumes the out of plane stress is zero and accounts for the strain in the "width" direction. Mindlin-Reissner theory takes into account a shear angle brought about by the bending stresses and could be viable if thicker wafers are used.

REFERNECES

Acker, M. 2001. The back-end process: Step 11 –Scribe and break. *Advanced Packaging*, November.

Albalak, Ramon J. 2007. "Dicing MEMS handling with care", Advanced Packaging, 16 July, p. 20-22.

Beer, F., Johnston, E., DeWolf, J. 2006. *Mechanics of Materials, Fourth Edition*. McGraw Hill.

Bohm, C., Hauck, T., Juritza, A., Muller, W., 2004. Weibull Statistics of Silicon Die Fracture. *Electronics Packaging Technology Conference*.

Bruno De Wachter. "Poly-silicon shortage holds back PV growth." *Internet Source*, 22 June 2009, available from http://www.leonardo-energy.org/poly-silicon-shortage-holds-back-pv-growth.

Chong, D., Lee, W., Lim, J., Low, T. 2004. Mechanical Characterization in Failure Strength of Silicon Dice. *Inter Society Conference on Thermal Phenomena 2004*.

Cooke, M. 2006. Scribe and Dice. *The Advanced Semiconductor Magazine* 19 No4:20-24.

Dixit, P and Miao, J 2006. Effect of SF_6 flow rate on the etched surface profile and bottom grass formation in deep reactive ion etching process. Journal of Physics: Conference Series 34:577-582.

Dynatex International 2001. "The GST Scriber/Breaker." Internet Source, 22 June 2009, available from http://www.dynatex.com/assets/pdfs/dynDryDicingbrochure.pdf.

Greek, S., Ericson, F., Johansson, S., Schweitz, J., 1996. In Situ Tensile Strength Measurement and Weibull Analysis of Thick Film and Thin Film Micromachined Polysilicon Structures. *Thin Solid Films* v292:247-254.

Green Chip Stocks, 2010. "Solar Market Trends". Internet Source, 24 April 2010, available from http://www.greenchipstocks.com/report/solar-market-trends/419

Haftka, Raphael 2009. "Stress Concentration Power Point." Internet Source, 31 July 2009, available from http://www.mae.ufl.edu/haftka/structures/stressconc.pdf

Hamamatsu Technical Information, 2005. "Stealth Dicing Techniques and Technology" Internet Source, 11 May 2010, available from http://jp.hamamatsu.com/en/rd/technology/industry/common/image/sd_tlas9004e01.pdf

Hamamatsu, 2010. "Industry and Research" Internet Source, 11 May 2010, available from http://jp.hamamatsu.com/en/rd/technology/industry/index.html

Ikehara, T., Tsuchiya, T. 2009. Effects of Anisotropic Elasticity on Stress Concentration in Micro Mechanical Structures Fabricated on (001) Single-Crystal Silicon Films. *Journal of Applied Physics* v105 No9.

Jaeger, Richard C. 2002. *Introduction To Microelectronic Fabrication*. Second Edition. New Jersey: Prentice Hall.

Kaajakari, Ville 2008. "Silicon as an Anisotropic Mechanical Material". Internet Source, 3 February 2010, available from http://www.kaajakari.net/~ville/research/tutorials/elasticity_tutorial.pdf

Komp, Richard J.2002. *Practical Photovoltaics, Electricity from Solar Cells*. AATEC publications.

Kroninger, W., Mariani, F. 2006. *Thinning and Singulation of Silicon: Root Causes of the Damage in Thin Chips*. Electronic Components and Technology Conference.

Kumagai, M., Sakamoto, T., Ohmura, E. 2007. Laser processing of doped silicon wafer by the Stealth Dicing. *Semiconductor Manufacturing Symposium* October 2007:1-4.

Laermer, F., Schilp, A., Funk, K., Offenberg 1999. Bosch Deep Silicon Etching: Improving Uniformity and Etch Rate for Advanced MEMS Applications. *Proceedings of the IEEE Micro Electro Mechanical Systems yr1999:211-216.*

Landesberger, C., Klink, G., Schwinn, G., Aschenbrenner, R. 2001. New Dicing and Thinning Concept Improves Mechanical Reliability of Ultra Thin Silicon. *International Symposium on Advanced Packaging Materials 2001*.

Majeed, B., Paul, I., Razeeb, K., Barton, J., and O'Mathuna, S. 2006. Microstructural, mechanical, fractural and electrical characterization of thinned and singulated silicon test die. *Journal of Micromechanics and Microengineering* 16:1519-1529.

Majelac Technologies 2007. "Majelac Technologies - Integrated Circuit and Assembly Services." *Internet Source*, 22 June 2009, available from http://www.majelac.com/Wafer_Dicing.html.

Manginell, R., Adkins, D., Moorman, M., Hadizadeh, R., Copic, D., Porter, D., Anderson, J., Hietala, V., Bryan, J., Wheeler, D., Pfeifer, K., Rumpf, A. 2008. Mass-Sensitive Microfabricated Chemical Preconcentrator. Journal of Microelectromechanical Systems 17:1396-1407.

Mints, Paula 2008. "Is Booming Growth Sustainable? The Global Photovoltaic Industry". Internet Source, 10 May 2010, available from

http://www.renewableenergyworld.com/rea/news/article/2008/08/is-booming-growth-sustainable-the-global-photovoltaic-industry-53437

Open Learn. "Etching." Internet Source, 22 June 2009, available from http://openlearn.open.ac.uk/mod/resource/view.php?id=257306

Peterson, Rudolph E. 1974. *Stress Concentration Factors*. John Wiley & Sons.

Schoenfelder, S., Ebert, M., Landesberger, C., Bock, K., and Bagdahn, J. 2006. Investigations of the influence of dicing techniques on the strength properties of thin silicon. *Microelectronics Reliability* 47:168-178.

Selbrede, S., Pilloux, Y. 2009. DRIE Technology For MEMS. Tegal Corporation, Plasma Users Group February 2009.

STS, 2009. "Silicon Deep Reactive Ion Etching." Internet Source, 22 June 2009, available from http://semiconductor.firstlightera.com/EN/Microsites/1/Surface+Technology+Systems/Technologies-DeepReactiveIonEtch(DRIE)forSilicon.htm

Troyani, N., Hernandez, S.I., Villarroel, G., Pollonais, Y., Gomes, C. 2004. Theoretical Stress Concentration Factors for Short Flat Bars with Opposite U-shaped Notches Subjected to In-Plane Bending. *International Journal of Fatigue* v26 No12:1303-1310.

Tsuchiya, T., Tabata, O., Sakata, J., Taga, Y., 1998. Specimen Size Effect on Tensile Strength of Surface-Micromachined Polycrystalline Silicon Thin Films. *Journal of Microelecromechanical Systems*, v7, No1:106-113.

Venkatakrishnan, K., Tan, B. 2007. Thin silicon wafer dicing with a dual-focused laser beam. *Journal of Micromechanics and Microengineering* 17:2505-2515.

Weibull, Waloddi 1951. A Statistical Distribution Function of Wide Applicability. *American Society of Mechanical Engineers*. No 51-A-6.

Weibull.com 2010. "Estimation of the Weibull Parameters". Service of the ReliaSoft Corporation. Internet Source, 27 March 2010, available from http://www.weibull.com/LifeDataWeb/estimation_of_the_weibull_parameter.htm

Kreyszig, Erwin. 1997. *Advanced Engineering Mathematics*, 8th ed., John Wiley & Sons, Inc., New York.

Young, W., Roark, R., Budynas, R., 2002. *Roark's Formulas for Stress and Strain - 7th Edition*. McGraw-Hill.

APPENDIX I.

Weibull analysis was done in Microsoft Excel 2007. All formulas used in the separation and failure stress statistic analysis are shown in section 3.3. An example of the spreadsheet used is shown in Figure A-1 below.

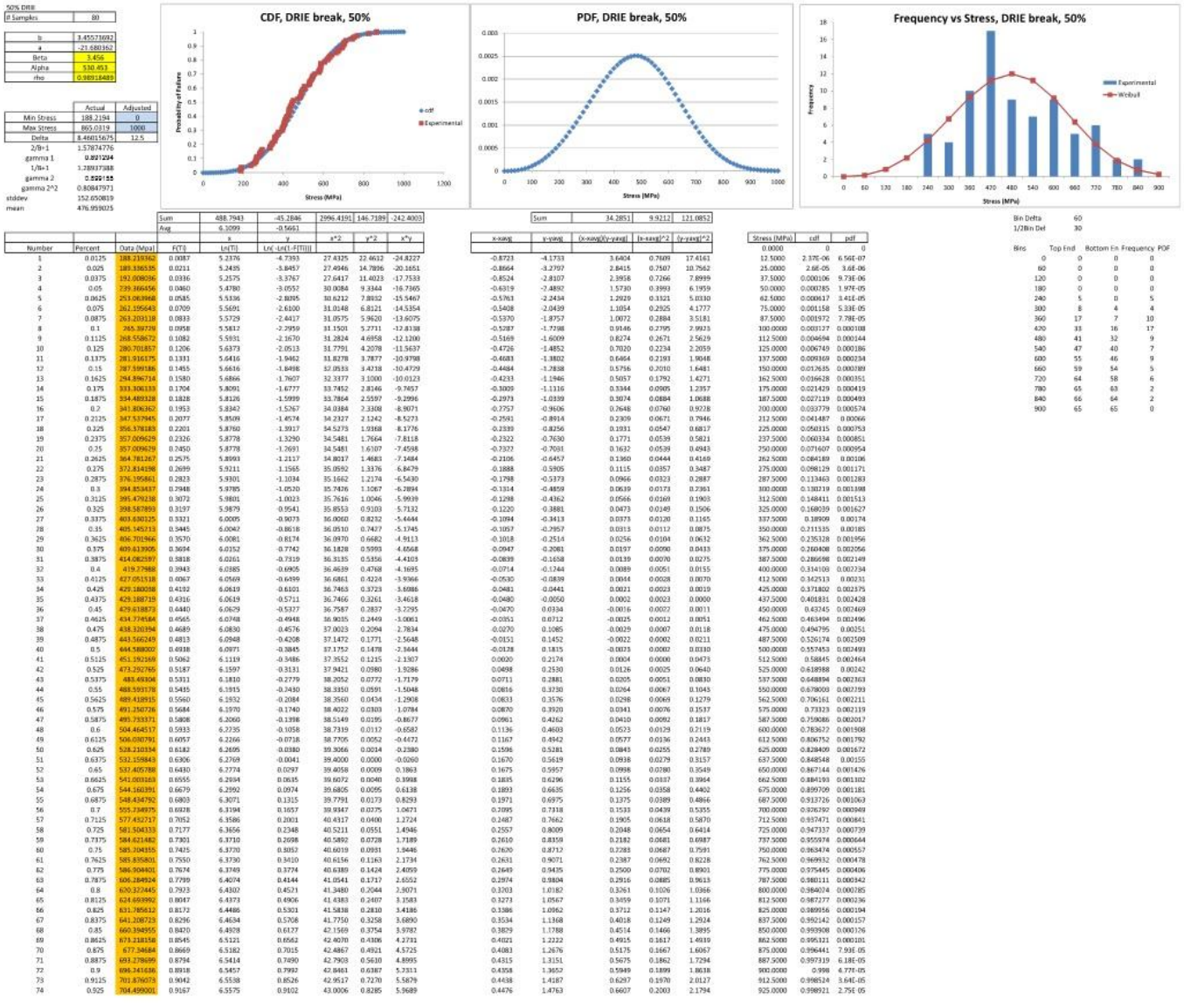

Figure A-1. Microsoft Excel 2007 spreadsheet used for Weibull analysis. All samples for DRIE 50% failure.

The LabVIEW program constructed by the student compiled two files. One file is the raw data file in which there were no averaged points. The other file was an averaged data file that also cropped the data so that it could be analyzed in a much easier manner. Data for the this thesis was taken from the averaged data file. A sample of the raw and averaged data file is shown in Figure A-2 and Figure A-3 below, respectively.

DRIE 50% #3 Break 1

12/30/2009
2:01 PM

Velocity Min (mm/s)	0
Velocity Max (mm/s)	0.025
Accel (mm/s/s)	0.1
Distance to Move (mm)	-2
Sampling Rate (Hz)	1000
Samples Per Channel	25
Time @ Max Stress (s)	34.825
Max Voltage (V)	-0.011053
Max Force (N)	-109.312783
Max 3Pt Stress (MPa)	-154058.9296
Max 4Pt Stress (MPa)	-92435.35778
Disp Start (mm)	0.875977
Disp End (mm)	1.399766
Total Disp (mm)	0.523789
Conversion Factor (N/V)	10000
Span (mm)	15
Theoretical Thickness (mm)	0.026108
Width (mm)	97.4
Stress Concentration Factor	4.1584

Normal Data

Time (s)	Disc (mm)	Voltage (V)
0	9.9999218	-0.0001266
0.001	9.9999218	-0.0001201
0.002	9.9999218	-0.0001233
0.003	9.9999218	-0.0001104
0.004	9.9999218	-0.0001168
0.005	9.9999218	-0.0001168
0.006	9.9999218	-0.0001233
0.007	9.9999218	-0.0001201
0.008	9.9999218	-0.0001168
0.009	9.9999218	-0.0001233
0.01	9.9999218	-0.0001266
0.011	9.9999218	-0.0001168
0.012	9.9999218	-0.0001233
0.013	9.9999218	-0.0001266
0.014	9.9999218	-0.0001266
0.015	9.9999218	-0.0001233
0.016	9.9999218	-0.0001201
0.017	9.9999218	-0.0001266
0.018	9.9999218	-0.0001233
0.019	9.9999218	-0.0001233
0.02	9.9999218	-0.0001201
0.021	9.9999218	-0.0001201
0.022	9.9999218	-0.0001201
0.023	9.9999218	-0.0001266
0.024	9.9999218	-0.0001233
0.025	9.9989061	-0.0001168
0.026	9.9989061	-0.0001233
0.027	9.9989061	-0.0001233
0.028	9.9989061	-0.0001201
0.029	9.9989061	-0.0001233
0.03	9.9989061	-0.0001201
0.031	9.9989061	-0.0001201
0.032	9.9989061	-0.0001266
0.033	9.9989061	-0.0001233
0.034	9.9989061	-0.0001266
0.035	9.9989061	-0.0001266

Figure A-2. Raw data file for DRIE 50%, Wafer#3, Break#1.

DRIE 50% #3 Break 1

12/30/2009 2:01 PM	
Velocity Min (mm/s)	0
Velocity Max (mm/s)	0.025
Accel (mm/s/s)	0.1
Distance to Move (mm)	-2
Sampling Rate (Hz)	1000
Samples Per Channel	25
Time @ Max Stress (s)	34.825
Max Voltage (V)	-0.011053
Max Force (N)	-109.312783
Max 3Pt Stress (MPa)	-154058.9296
Max 4Pt Stress (MPa)	-92435.35778
Disp Start (mm)	0.875977
Disp End (mm)	1.399766
Total Disp (mm)	0.523789
Conversion Factor (N/V)	10000
Span (mm)	15
Theoretical Thickness (mm)	0.026108
Width (mm)	97.4
Stress Concentration Factor	4.1584

Averaged Data						Cropped Data			
Time (s)	Disc (mm)	Voltage (V)	Force (N)	Stress 3pt (MPa)	Stress 4pt (MPa)	Disc (mm)	Force (N)	Stress 3pt (MPa)	Stress 4pt (MPa)
0.025	0	-0.0001218	-0.001946	-2.7425146	-1.6455088	0	-0.1459467	-205.6885963	-123.4131578
0.05	0.0010157	-0.0001216	-0.0006487	-0.9141715	-0.5485029	0.0009766	-0.160217	-225.8003701	-135.4802221
0.075	0.0020313	-0.0001209	0.0071352	10.0558869	6.0335322	0.0019922	-0.1913523	-269.680604	-161.8083624
0.1	0.003047	-0.000122	-0.0045406	-6.3992008	-3.8395205	0.003047	-0.1926496	-271.5089471	-162.9053682
0.125	0.0040236	-0.0001222	-0.0058379	-8.2275439	-4.9365263	0.0040236	-0.1991362	-280.6506625	-168.3903975
0.15	0.0050001	-0.0001214	0.001946	2.7425146	1.6455088	0.0050392	-0.2224876	-313.5608379	-188.1365027
0.175	0.0060158	-0.0001222	-0.0058379	-8.2275439	-4.9365263	0.0060158	-0.2328661	-328.1875825	-196.9125495
0.2	0.0070314	-0.0001226	-0.0097298	-13.7125731	-8.2275439	0.0070314	-0.2484337	-350.1276994	-210.0766196
0.225	0.008008	-0.0001215	0.0006487	0.9141715	0.5485029	0.008008	-0.2536229	-357.4410717	-214.464643
0.25	0.0090237	-0.0001223	-0.0071352	-10.0558869	-6.0335322	0.0090237	-0.266596	-375.7245025	-225.4347015
0.275	0.0100002	-0.0001218	-0.001946	-2.7425146	-1.6455088	0.0100393	-0.2678933	-377.5528456	-226.5317073
0.3	0.011055	-0.0001222	-0.0058379	-8.2275439	-4.9365263	0.0110159	-0.2834609	-399.4929625	-239.6957775
0.325	0.0120707	-0.0001219	-0.0032433	-4.5708577	-2.7425146	0.0120707	-0.3068124	-432.4031379	-259.4418827
0.35	0.0130472	-0.0001222	-0.0058379	-8.2275439	-4.9365263	0.0130863	-0.3210827	-452.5149118	-271.5089471
0.375	0.0140629	-0.000121	0.0058379	8.2275439	4.9365263	0.014101	-0.3379477	-476.2833718	-285.7700231
0.4	0.0150776	-0.0001214	0.001946	2.7425146	1.6455088	0.0151558	-0.3431369	-483.5967441	-290.1580464
0.425	0.0160542	-0.0001209	0.0071352	10.0558869	6.0335322	0.0161324	-0.3353531	-472.6266856	-283.5760114
0.45	0.0170698	-0.0001233	-0.0175136	-24.6826316	-14.8095789	0.017148	-0.3625965	-511.0218902	-306.6131341
0.475	0.0180464	-0.0001215	0.0006487	0.9141715	0.5485029	0.0181246	-0.3833533	-540.2753795	-324.1652277
0.5	0.019062	-0.0001228	-0.0123244	-17.3692592	-10.4215555	0.0191402	-0.385948	-543.9320656	-326.3592394
0.525	0.0200777	-0.0001216	-0.0006487	-0.9141715	-0.5485029	0.0201559	-0.3846506	-542.1037225	-325.2622335
0.55	0.0210543	-0.0001219	-0.0032433	-4.5708577	-2.7425146	0.0211325	-0.4002183	-564.0438395	-338.4263037
0.575	0.022109	-0.0001224	-0.0084325	-11.88423	-7.130538	0.0221481	-0.4222725	-595.1256718	-357.0754031
0.6	0.0230856	-0.0001229	-0.0136217	-19.1976023	-11.5185614	0.0231638	-0.4274617	-602.4390441	-361.4634265
0.625	0.0241013	-0.000122	-0.0045406	-6.3992008	-3.8395205	0.0241795	-0.4456239	-628.0358472	-376.8215083
0.65	0.0251169	-0.0001231	-0.014919	-21.0259454	-12.6155672	0.0251951	-0.4469212	-629.8641903	-377.9185142
0.675	0.0261326	-0.0001235	-0.0188109	-26.5109746	-15.9065848	0.0261717	-0.4482185	-631.6925333	-379.01552
0.7	0.0271482	-0.0001231	-0.014919	-21.0259454	-12.6155672	0.0271873	-0.4663808	-657.2893364	-394.3736018
0.725	0.0281248	-0.0001224	-0.0084325	-11.88423	-7.130538	0.0281639	-0.4832458	-681.0577964	-408.6346779
0.75	0.0291405	-0.0001239	-0.0227028	-31.9960039	-19.1976023	0.0291796	-0.4910296	-692.0278549	-415.2167129
0.775	0.030117	-0.0001227	-0.0110271	-15.5409162	-9.3245497	0.0301561	-0.4988134	-702.9979133	-421.798748
0.8	0.0311718	-0.0001223	-0.0071352	-10.0558869	-6.0335322	0.0312109	-0.5104891	-719.453001	-431.6718006
0.825	0.0321875	-0.0001216	-0.0006487	-0.9141715	-0.5485029	0.0322266	-0.5221649	-735.9080887	-441.5448532
0.85	0.033164	-0.0001224	-0.0084325	-11.88423	-7.130538	0.0332031	-0.5494083	-774.3032933	-464.581976
0.875	0.0341797	-0.0001227	-0.0110271	-15.5409162	-9.3245497	0.0342188	-0.5416244	-763.3332349	-457.9999409
0.9	0.0351954	-0.0001224	-0.0084325	-11.88423	-7.130538	0.0352736	-0.5494083	-774.3032933	-464.581976
0.925	0.0361719	-0.0001231	-0.014919	-21.0259454	-12.6155672	0.0362501	-0.5545975	-781.6166657	-468.9699994
0.95	0.0371876	-0.0001232	-0.0162163	-22.8542885	-13.7125731	0.0372658	-0.5805436	-818.1835272	-490.9101163
0.975	0.0381641	-0.0001228	-0.0123244	-17.3692592	-10.4215555	0.0382814	-0.5870301	-827.3252426	-496.3951455
1	0.0391798	-0.0001235	-0.0188109	-26.5109746	-15.9065848	0.0392971	-0.6013004	-847.4370164	-508.4622099
1.025	0.0401564	-0.0001228	-0.0123244	-17.3692592	-10.4215555	0.0402737	-0.6090842	-858.4070749	-515.0442449
1.05	0.041172	-0.0001226	-0.0097298	-13.7125731	-8.2275439	0.0412893	-0.62076	-874.8621626	-524.9172975
1.075	0.0422268	-0.0001235	-0.0188109	-26.5109746	-15.9065848	0.042305	-0.6363276	-896.8022795	-538.0813677
1.1	0.0432425	-0.0001223	-0.0071352	-10.0558869	-6.0335322	0.0433207	-0.6493007	-915.0857103	-549.0514262
1.125	0.0442581	-0.0001216	-0.0006487	-0.9141715	-0.5485029	0.0443363	-0.6622737	-933.369141	-560.0214846
1.15	0.0452347	-0.0001224	-0.0084325	-11.88423	-7.130538	0.0453129	-0.6661656	-938.8541703	-563.3125022
1.175	0.0462503	-0.0001223	-0.0071352	-10.0558869	-6.0335322	0.0463276	-0.6791387	-957.137601	-574.2825606
1.2	0.047266	-0.0001216	-0.0006487	-0.9141715	-0.5485029	0.0473433	-0.7011928	-988.2194333	-592.93166
1.225	0.0482426	-0.0001227	-0.0110271	-15.5409162	-9.3245497	0.0483198	-0.6985982	-984.5627472	-590.7376483
1.25	0.0492573	-0.0001222	-0.0058379	-8.2275439	-4.9365263	0.0493355	-0.706382	-995.5328056	-597.3196834
1.275	0.0502729	-0.0001222	-0.0058379	-8.2275439	-4.9365263	0.0503511	-0.7206524	-1015.64458	-609.3867477

Figure A-3. Averaged and cropped data file for 50% DRIE, Wafer#3, Break#1.

All data for the 25% diced samples are shown below. N is the number of samples.

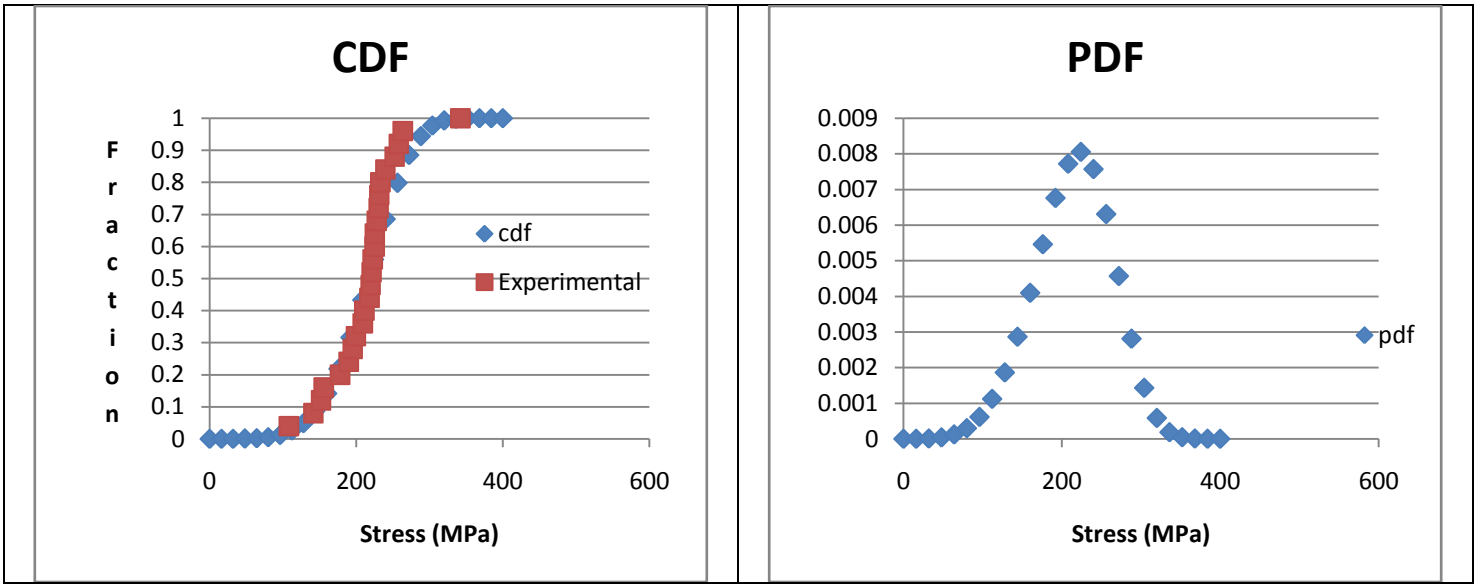

Figure A-4. 25% Diced. separation, wafer#1. β=4.992, α=233.1, ρ=0.971, N=25.

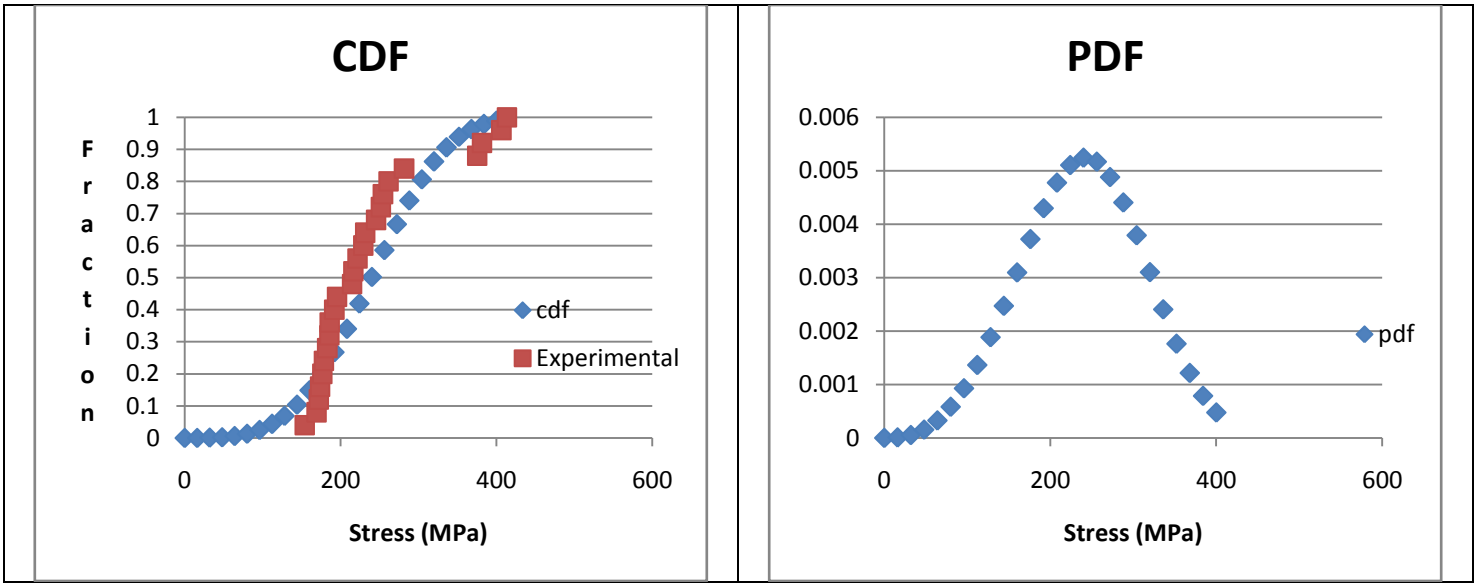

Figure A-5. 25% Diced. separation, wafer#2. β=3.623, α=265.1, ρ=0.884, N=25.

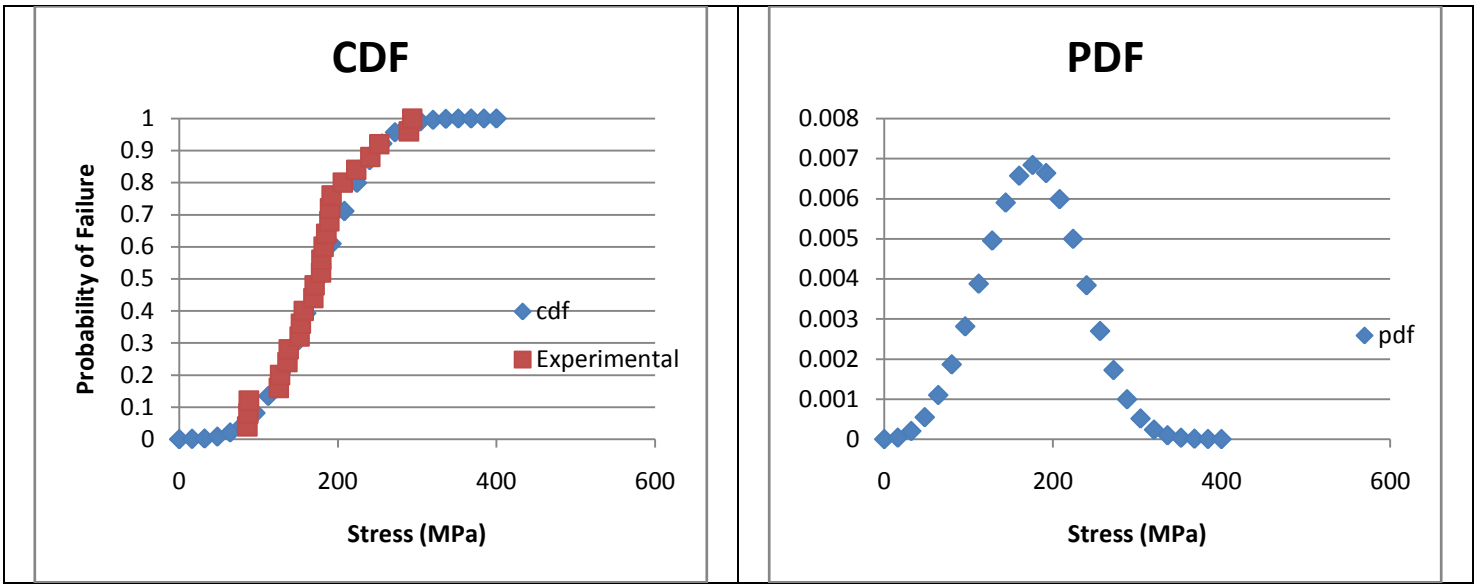

Figure A-6. 25% Diced. separation, wafer#3. β=3.472, α=195.475, ρ=0.977, N=25.

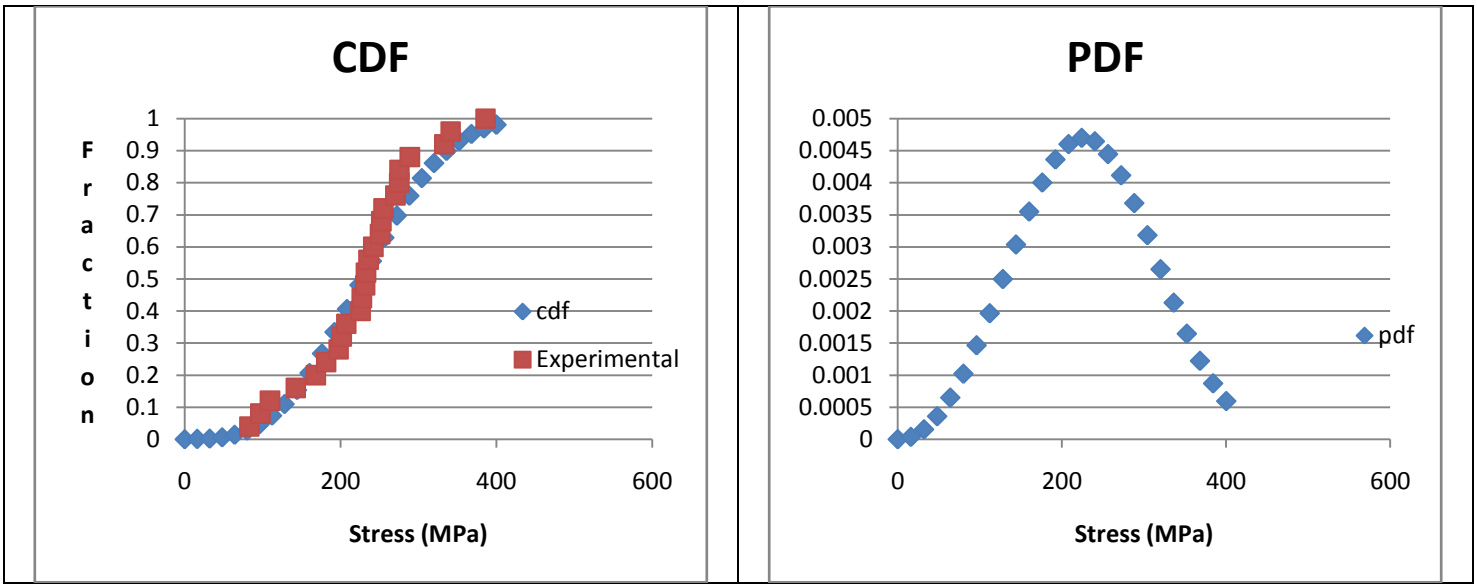

Figure A-7. 25% Diced. separation, wafer#4. β=3.093, α=256.9, ρ=0.982, N=25.

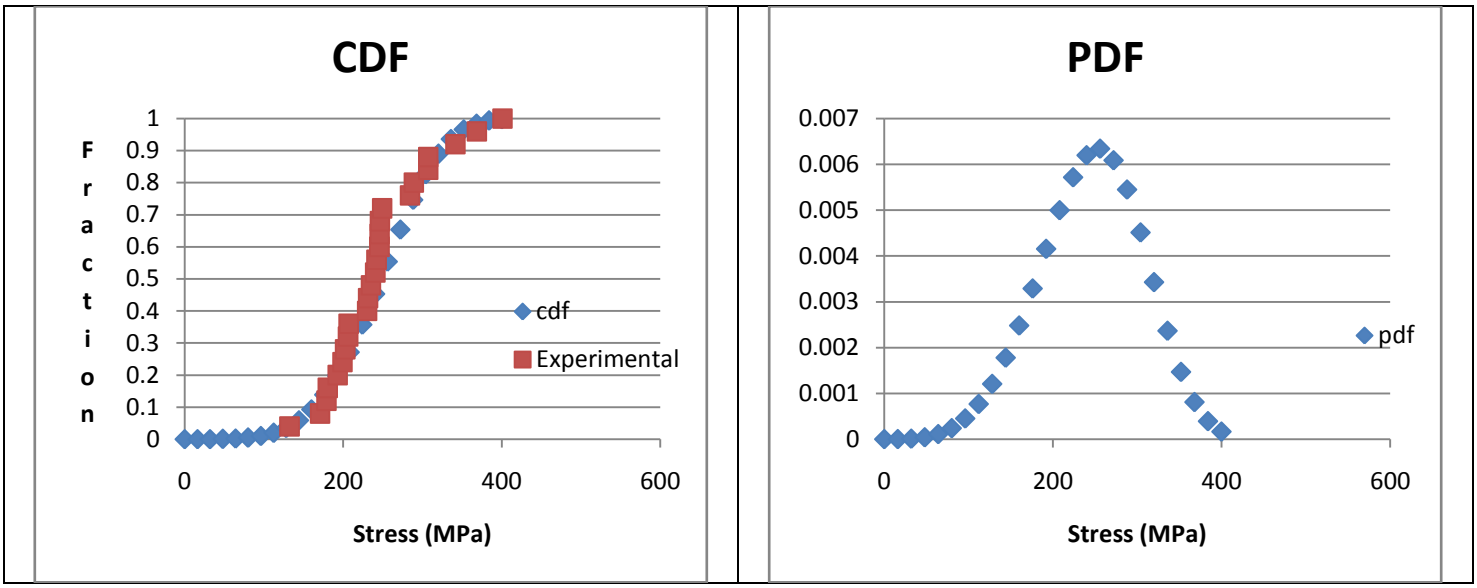

Figure A-8. 25% Diced. separation, wafer#5. β=4.506, α=268.5, ρ=0.968, N=25.

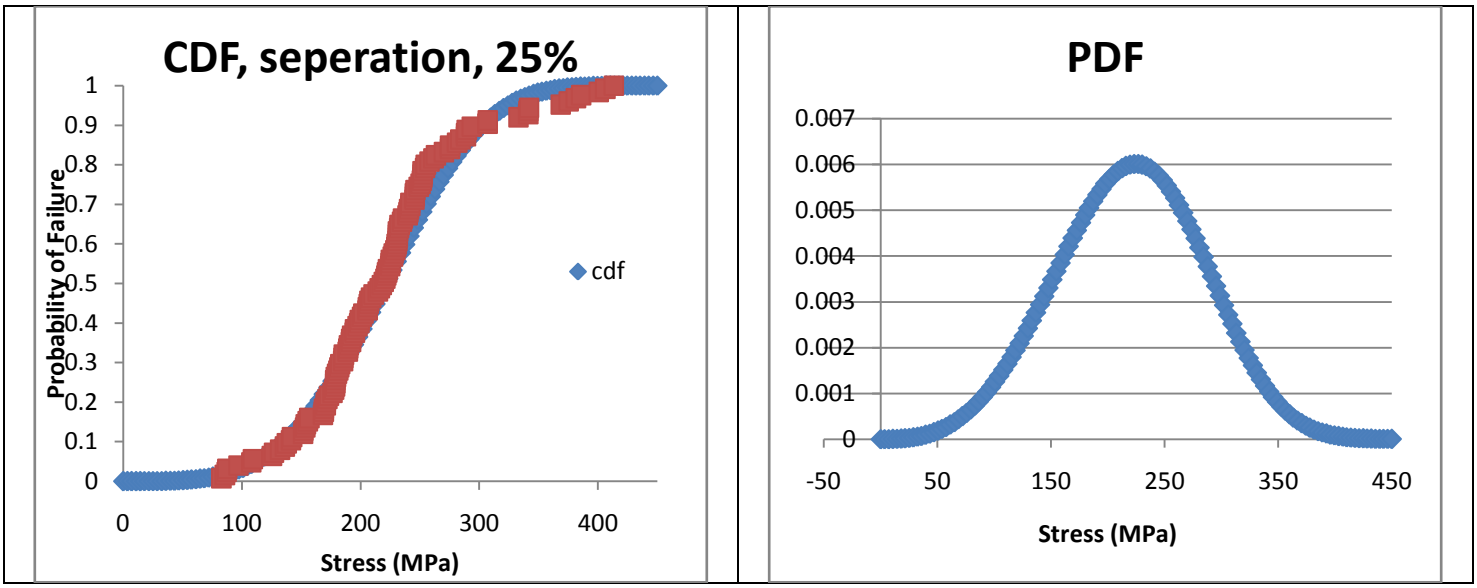

Figure A-9. 25% Diced. separation, all wafers. β=3.829, α=243.3, ρ=0.985, N=125.

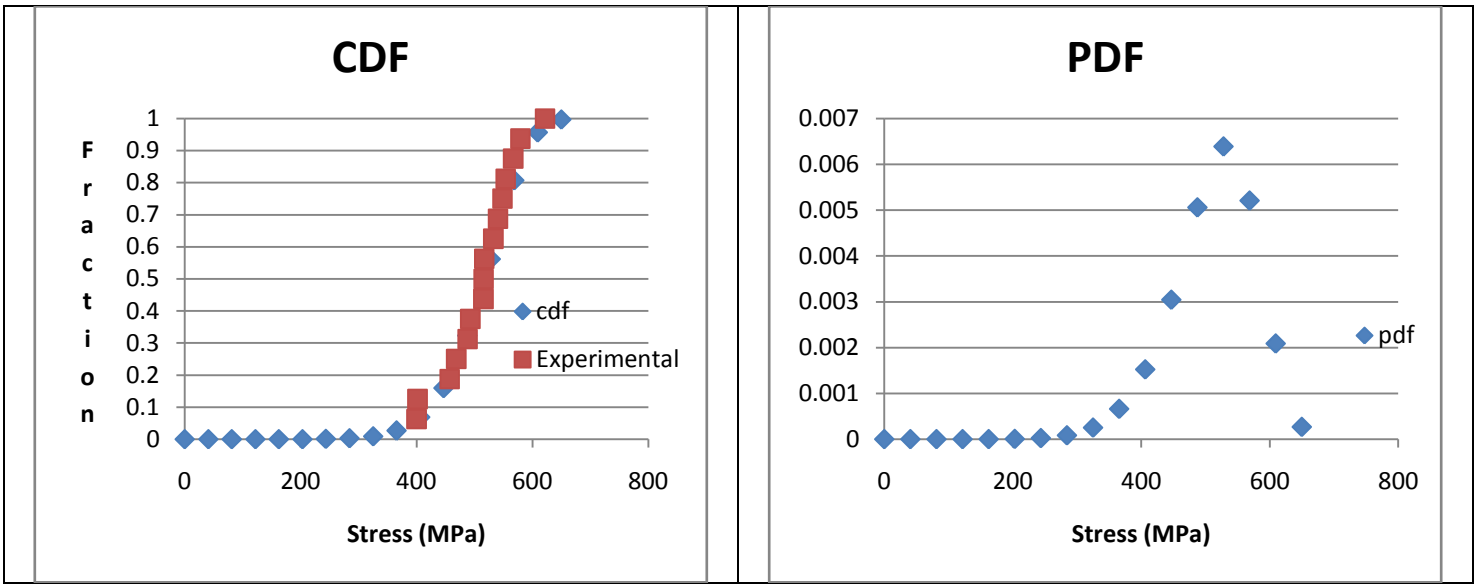

Figure A-10. 25% Diced. die fracture, wafer#1. β=9.337, α=539.2, ρ=0.984, N=16.

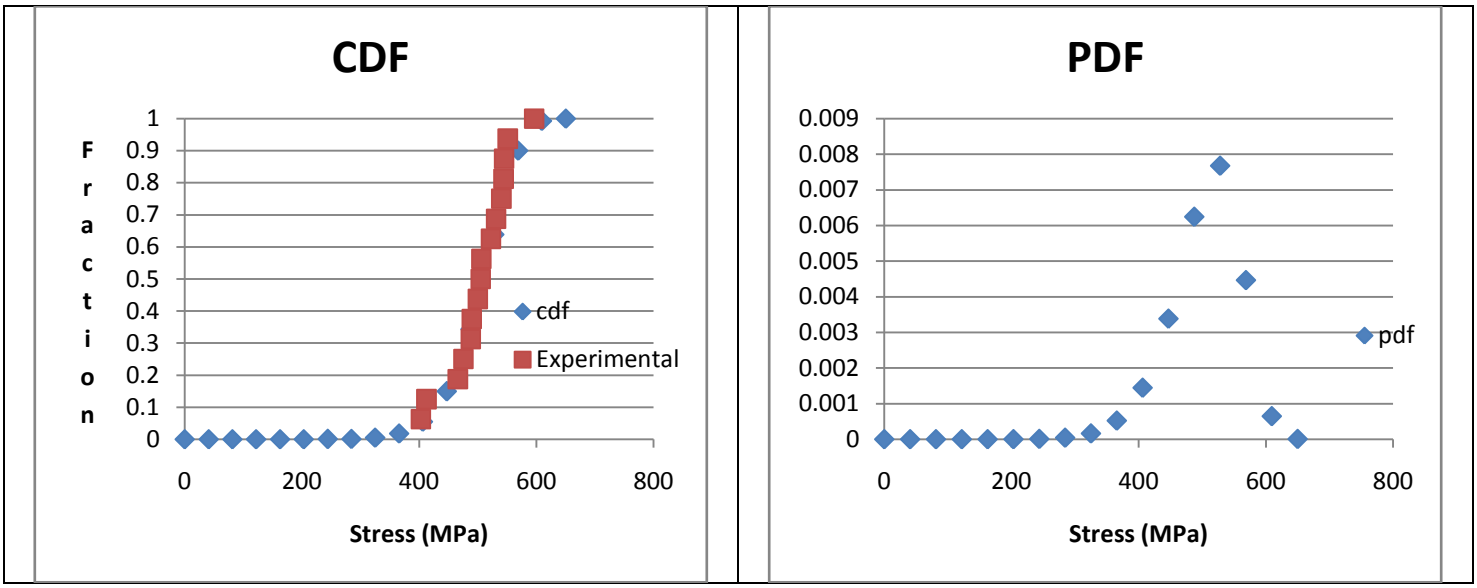

Figure A-11. 25% Diced. die fracture, wafer#2. β=11.024, α=527.3, ρ=0.981, N=16.

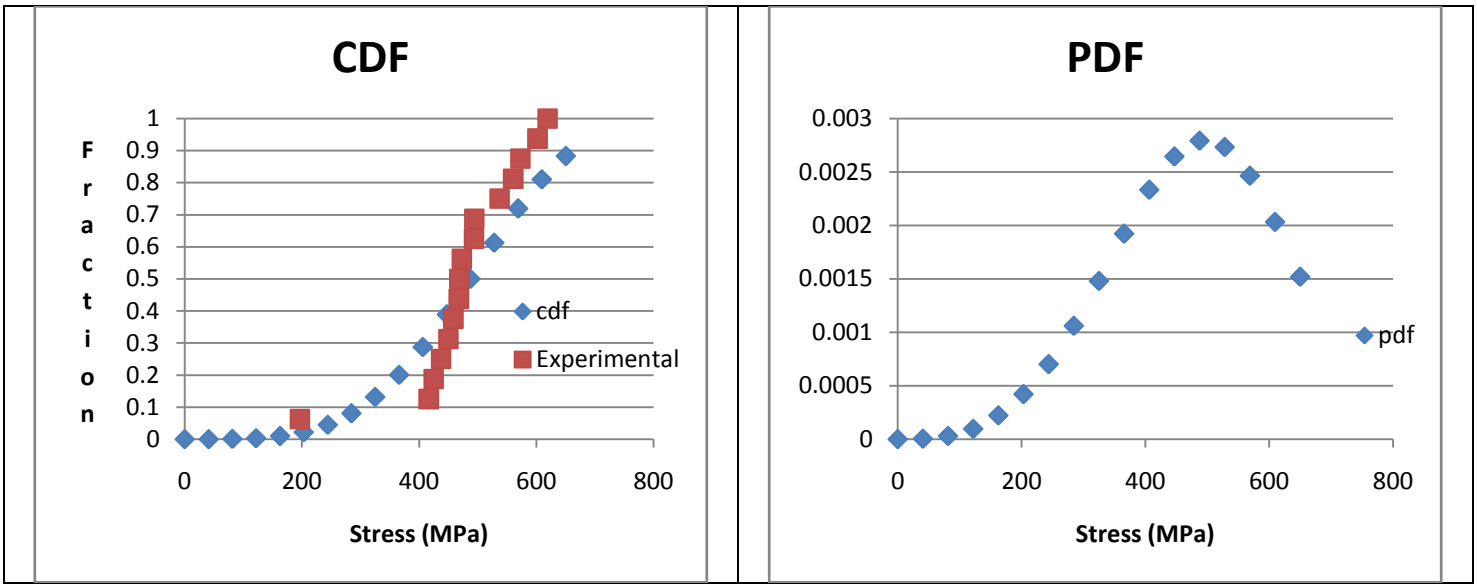

Figure A-12. 25% Diced. die fracture, wafer#3. β=3.927, α=535.3, ρ=0.888, N=16.

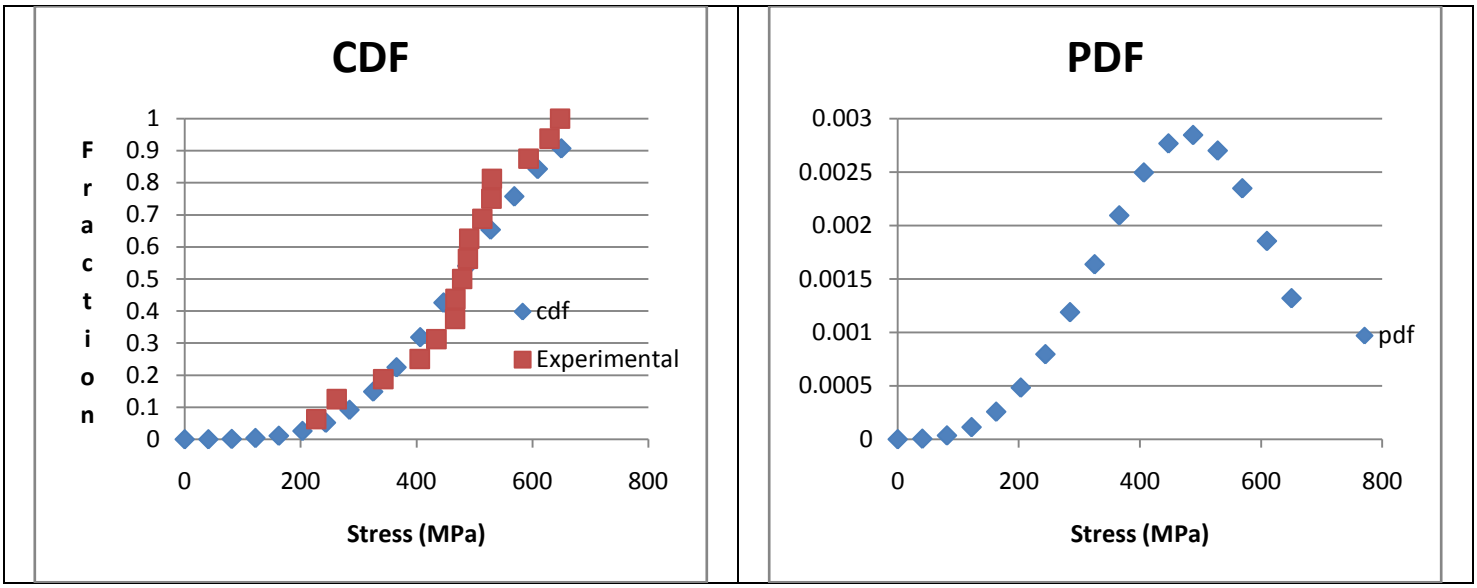

Figure A-13. 25% Diced. die fracture, wafer#4. β=3.884, α=520.2, ρ=0.974, N=16.

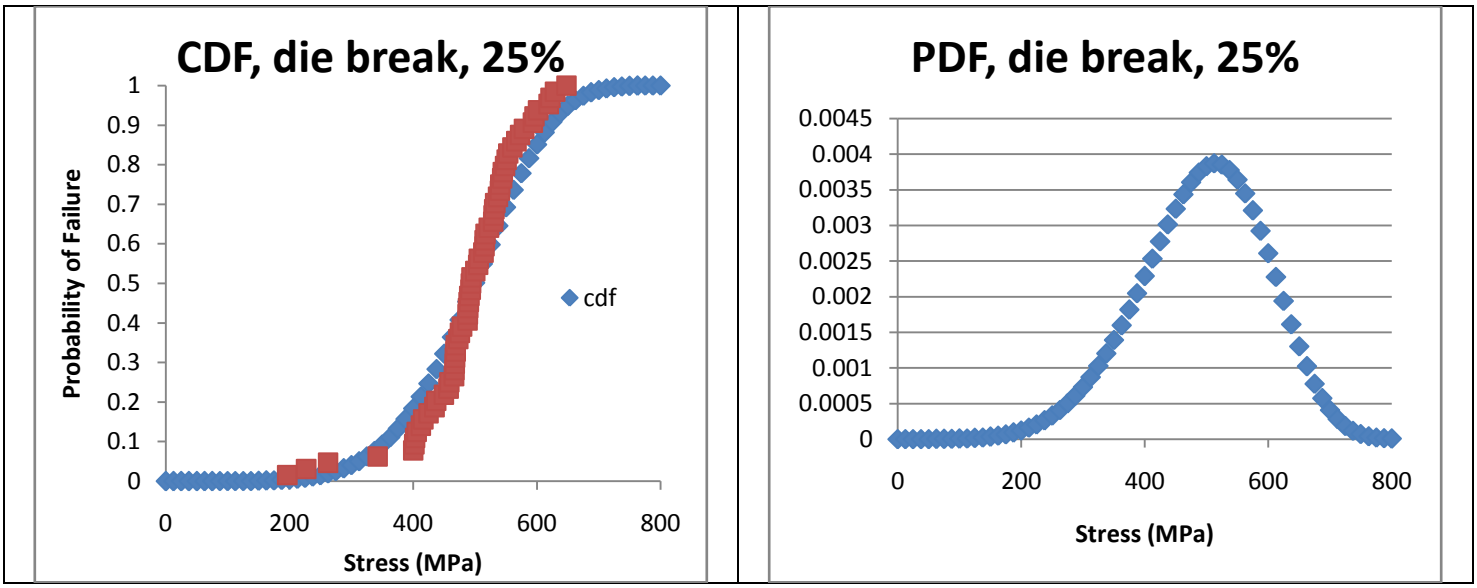

Figure A-14. 25% Diced. die fracture, all die. β=5.520, α=533.9, ρ=0.945, N=64.

All data for the 50% diced samples are shown below. N is the number of samples. Weibull analysis was only done for all of the die fracture samples together and not individually.

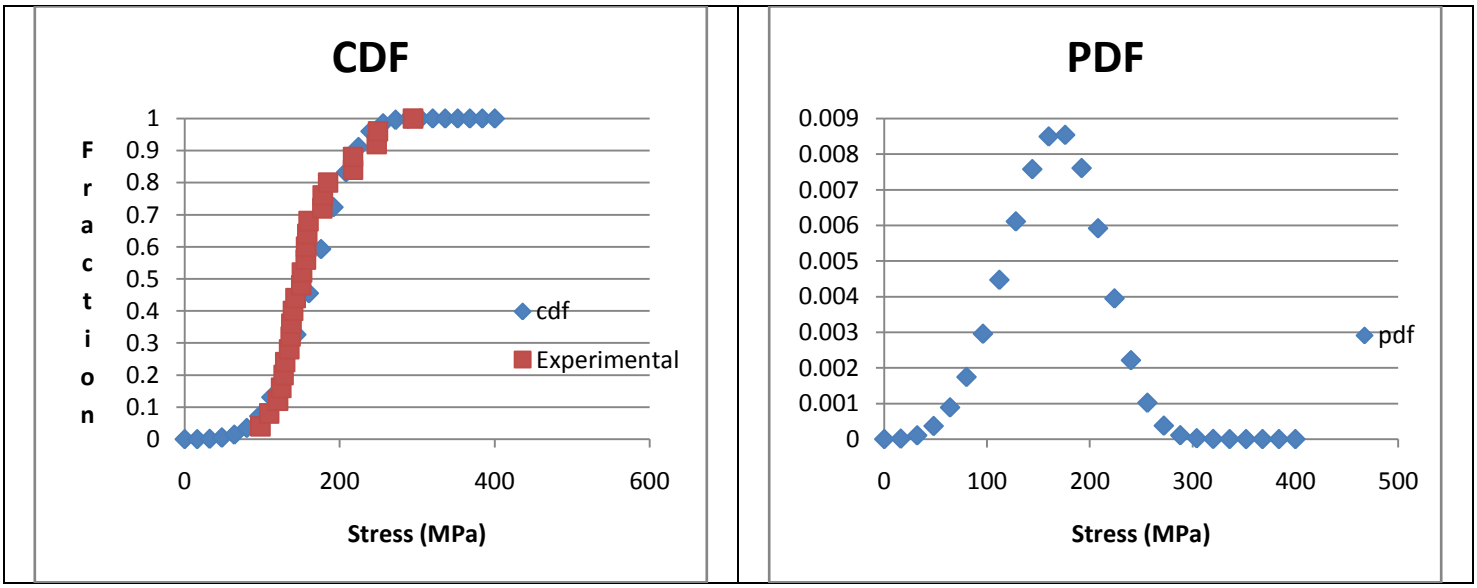

Figure A-15. 50% Diced. separation, wafer#1. β=4.109, α=180.7, ρ=0.931, N=25.

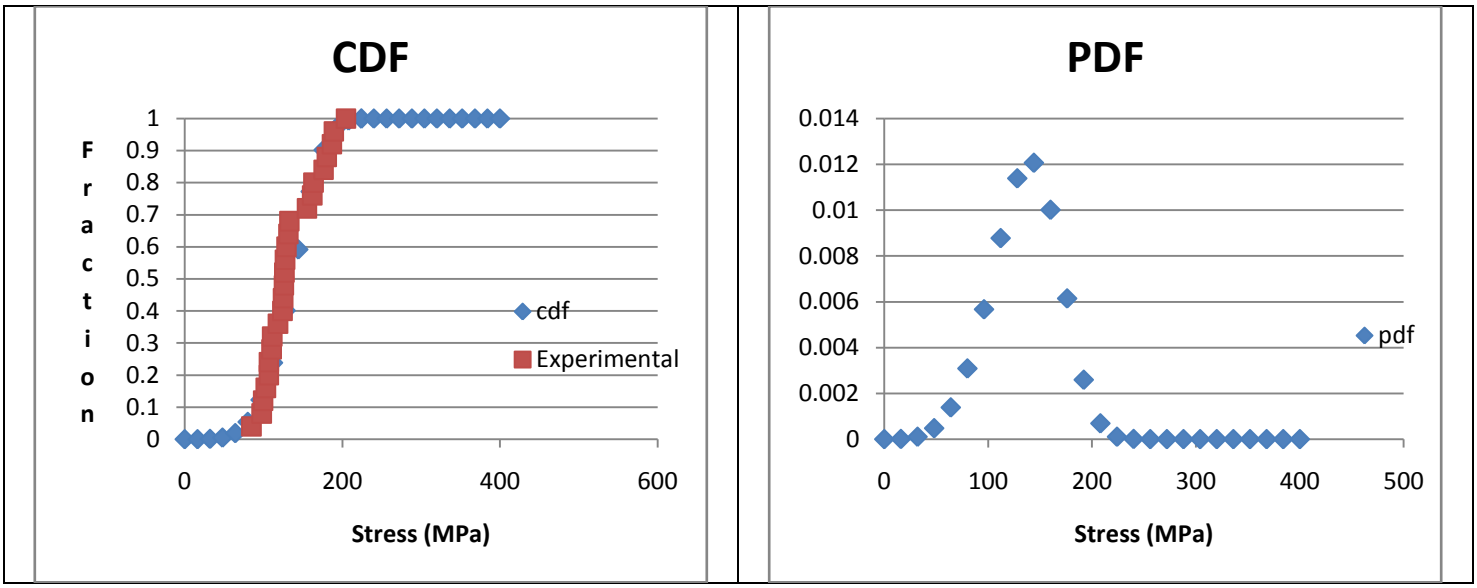

Figure A-16. 50% Diced. separation, wafer#2. β=4.750, α=147.4, ρ=0.948, N=25.

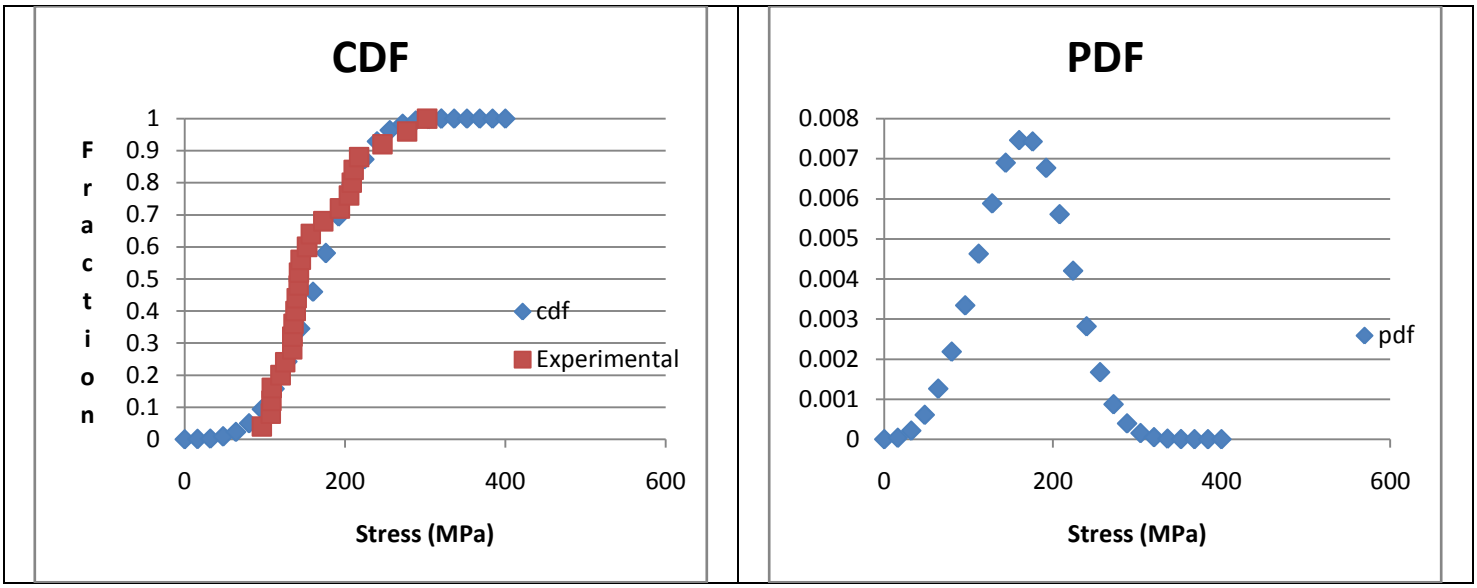

Figure A-17. 50% Diced. separation, wafer#3. β=3.587, α=183.1, ρ=0.930, N=25.

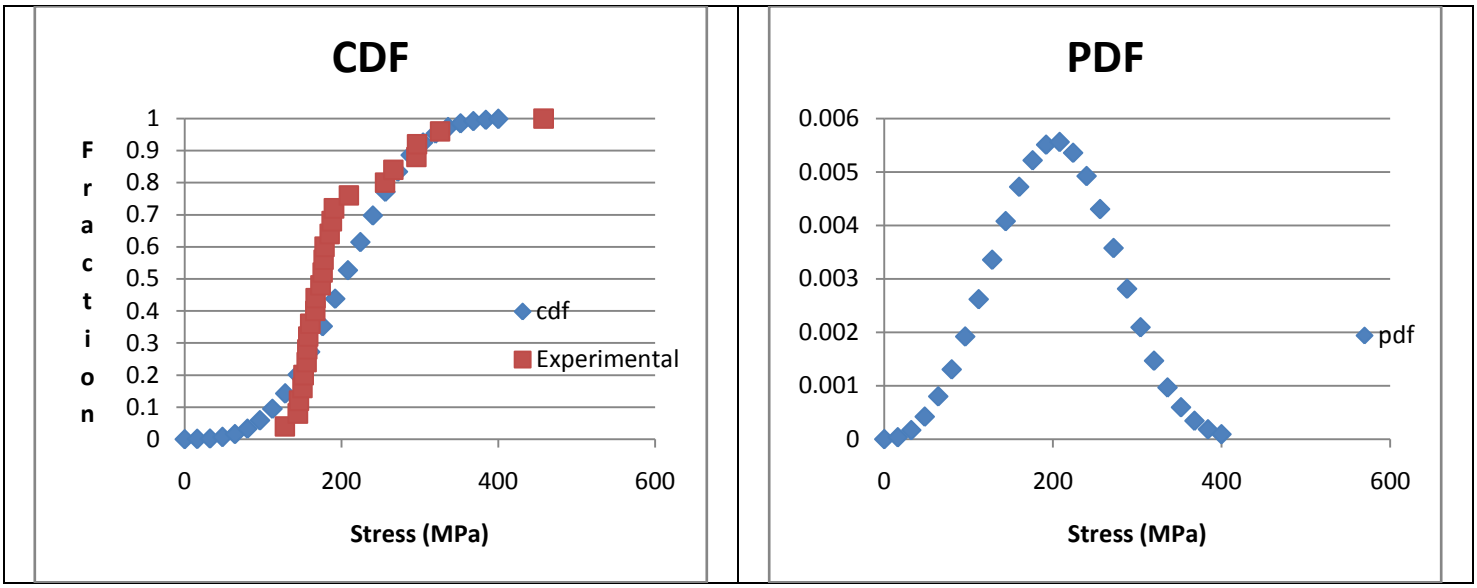

Figure A-18. 50% Diced. separation, wafer#4. β=3.266, α=227.3, ρ=0.848, N=25.

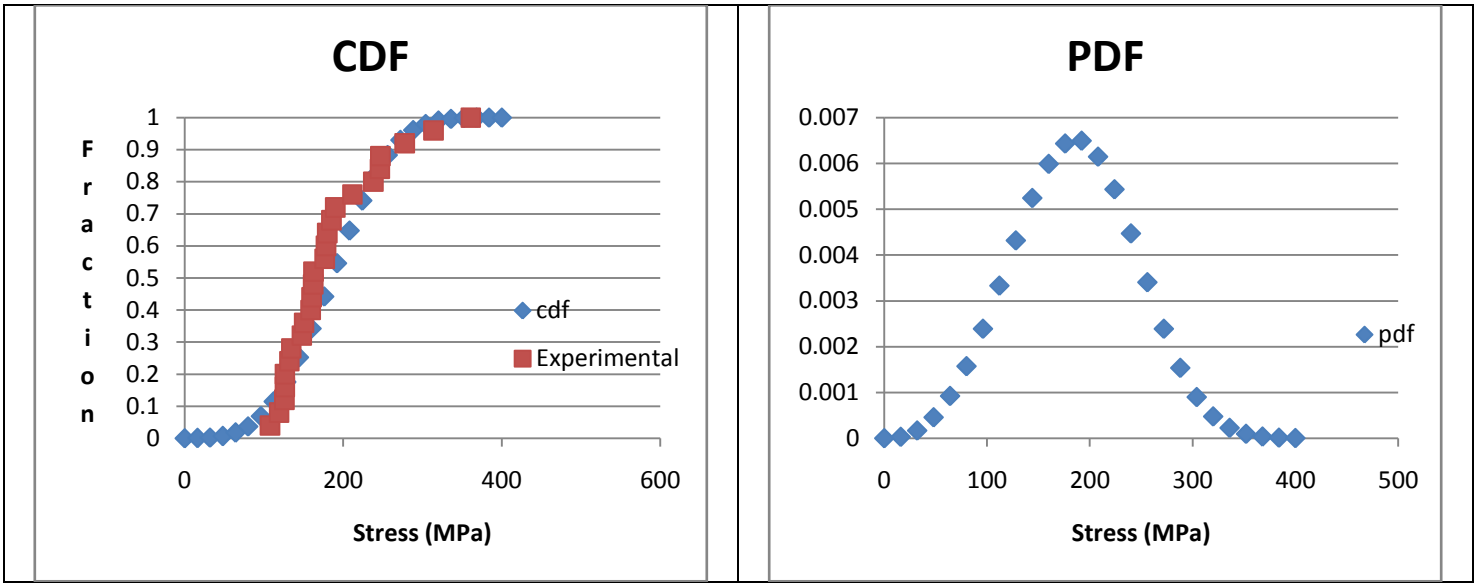

Figure A-19. 50% Diced. separation, wafer#5. β=3.479, α=205.5, ρ=0.926, N=25.

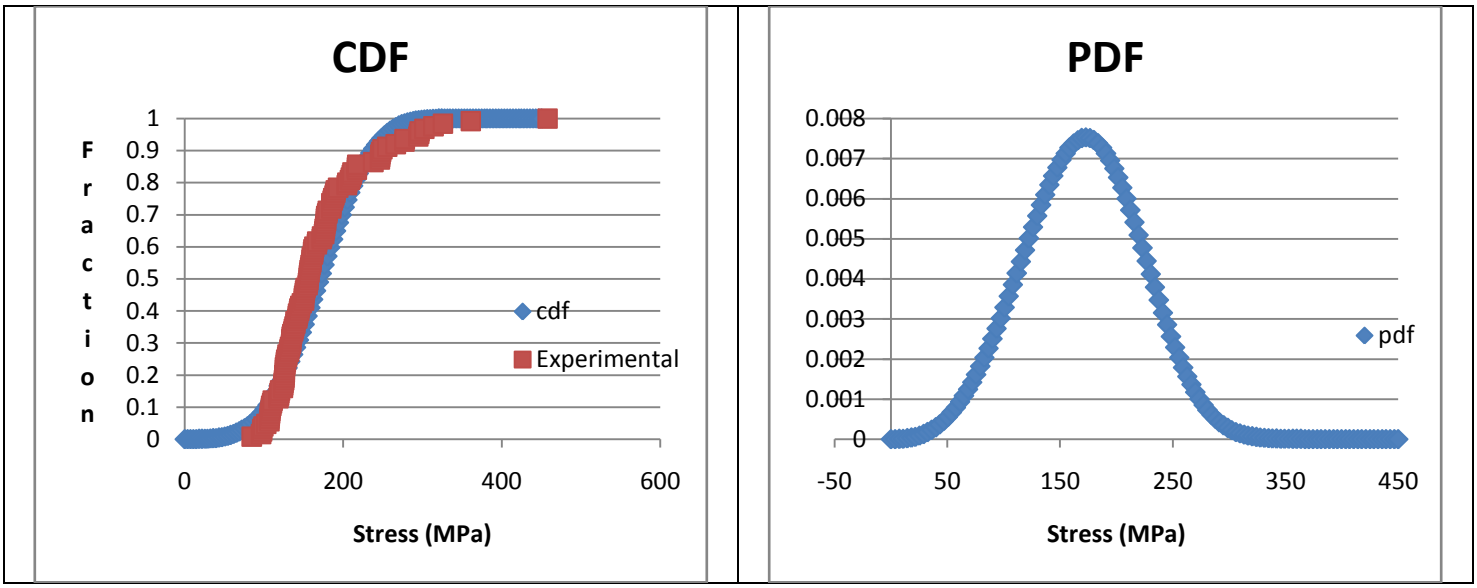

Figure A-20. 50% Diced. separation, all wafers. β=3.701, α=188.4, ρ=0.923, N=125.

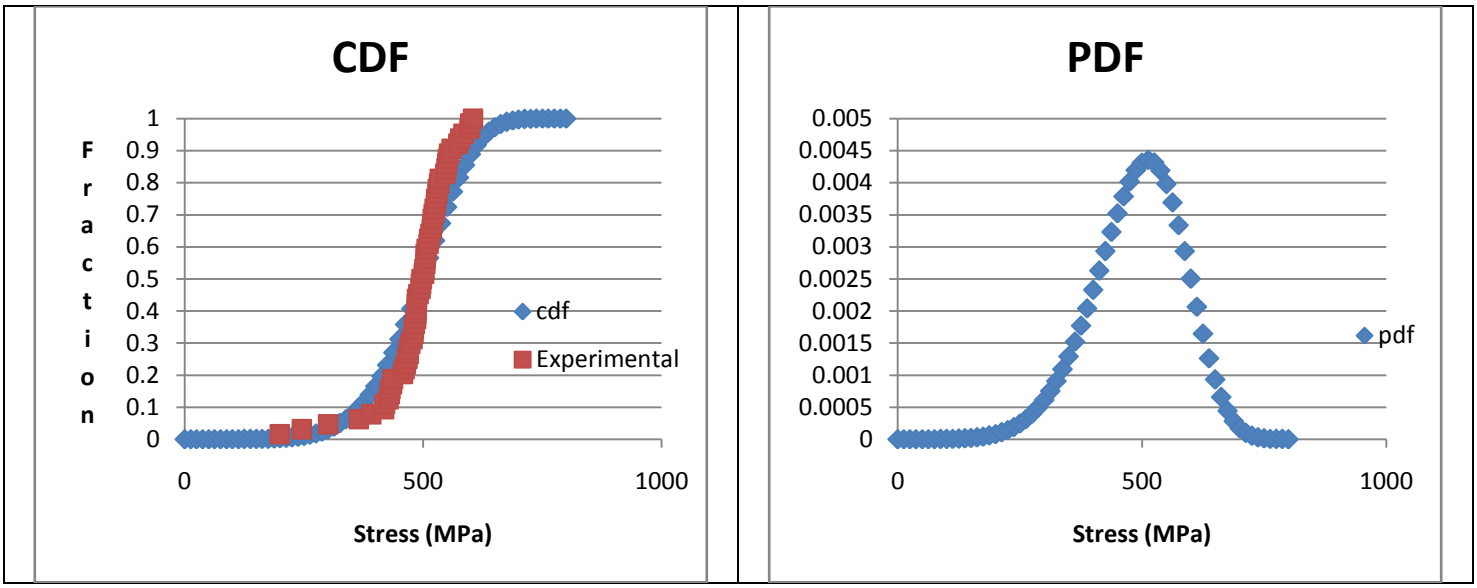

Figure A-21. 50% Diced. fracture stress, all die. β=6.160, α=527.9, ρ=0.926, N=64.

All data for the 75% diced samples are shown below. N is the number of samples. Weibull analysis was only done for all of the die fracture samples together and not individually.

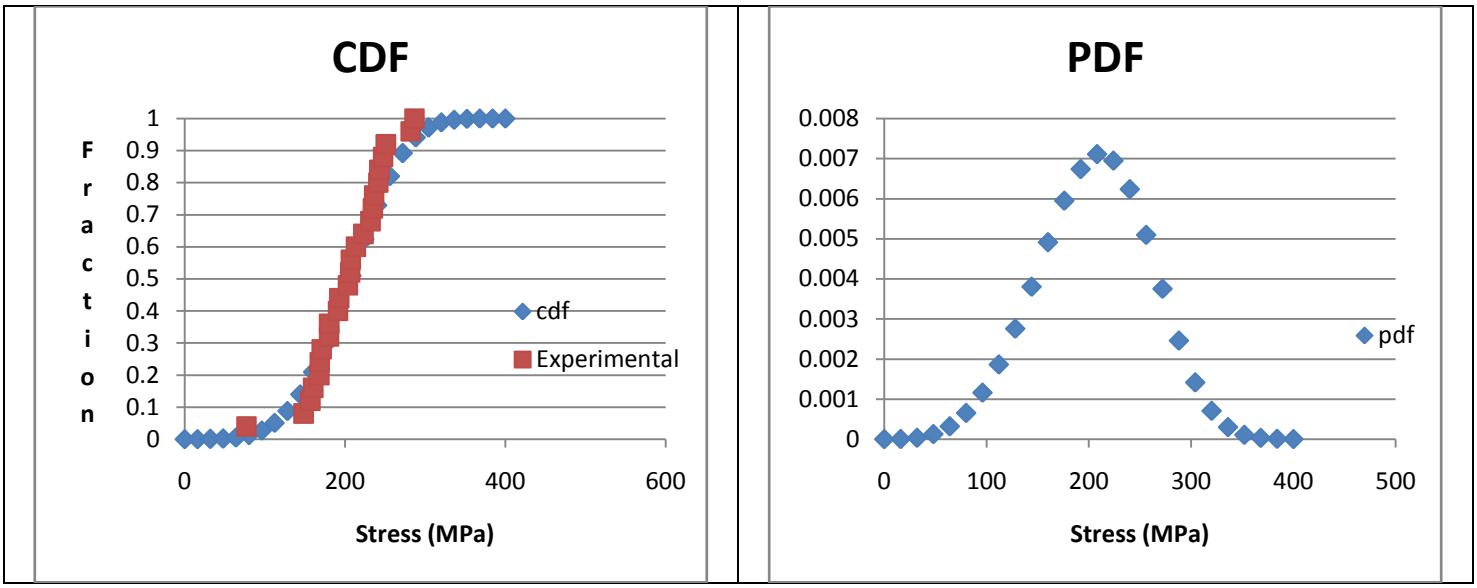

Figure A-22. 75% Diced. separation, wafer#1. β=4.232, α=225.3, ρ=0.957, N=25.

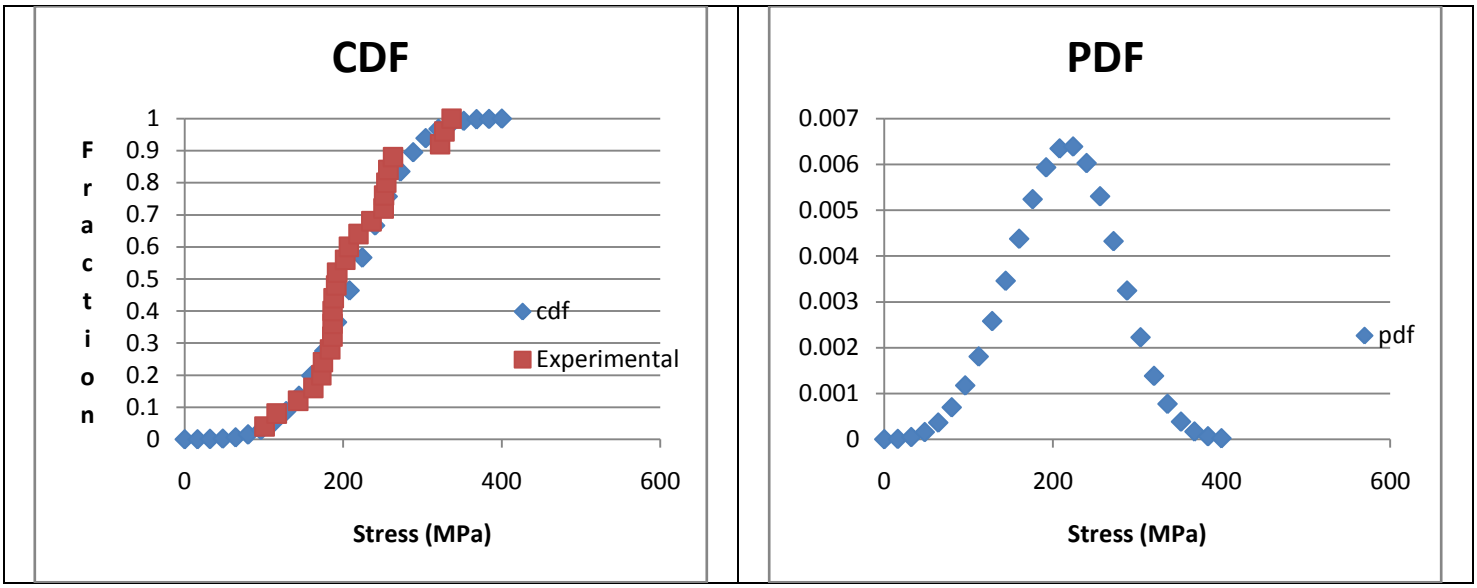

Figure A-23. 75% Diced. separation, wafer#2. β=3.950, α=234.4, ρ=0.976, N=25.

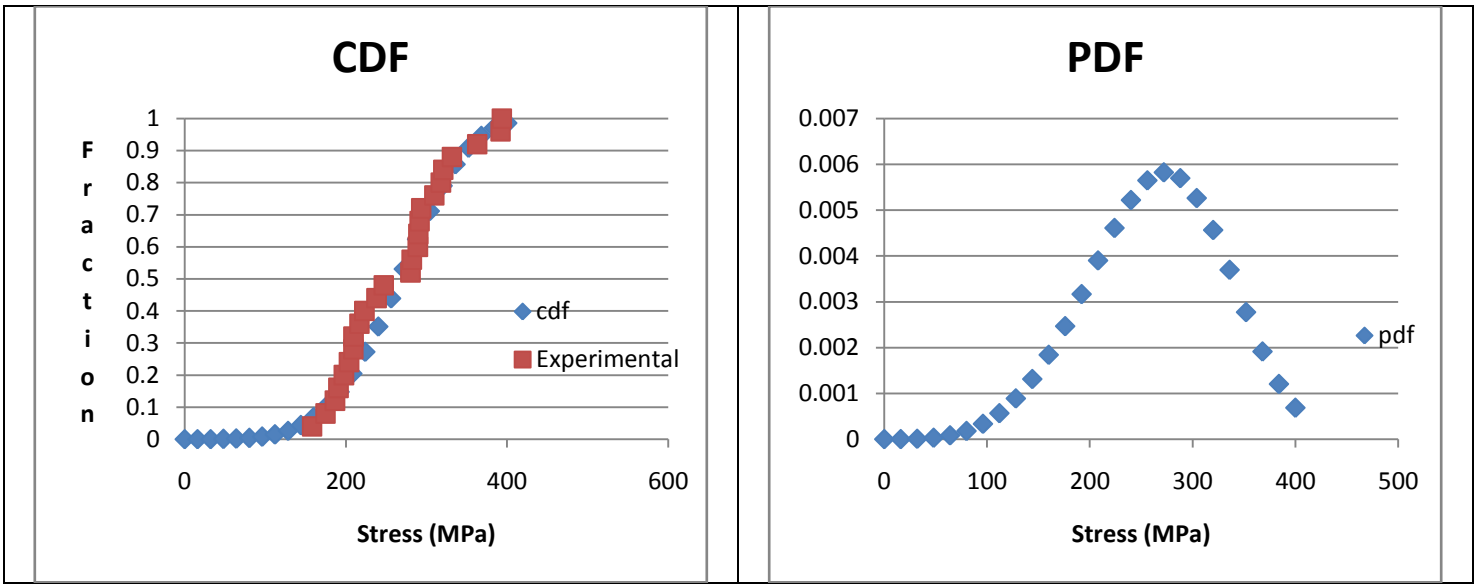

Figure A-24. 75% Diced. separation, wafer#3. β=4.463, α=289.5, ρ=0.969, N=25.

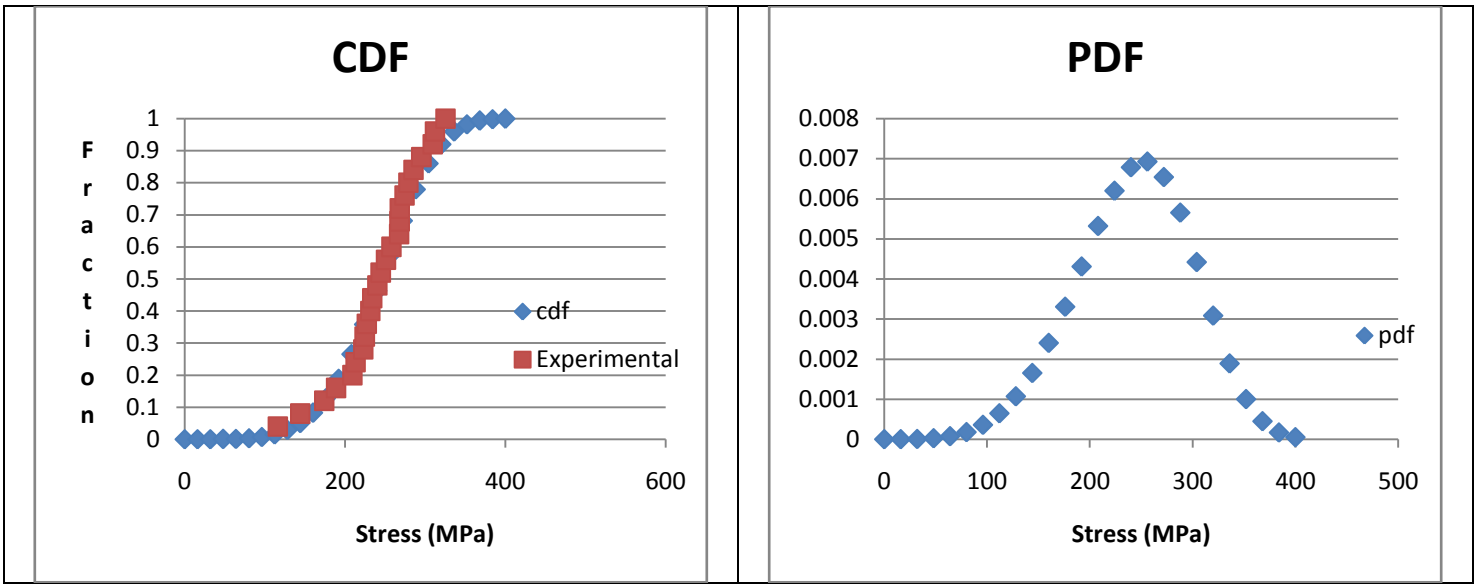

Figure A-25. 75% Diced. separation, wafer#4. β=4.879, α=264.7, ρ=0.984, N=25.

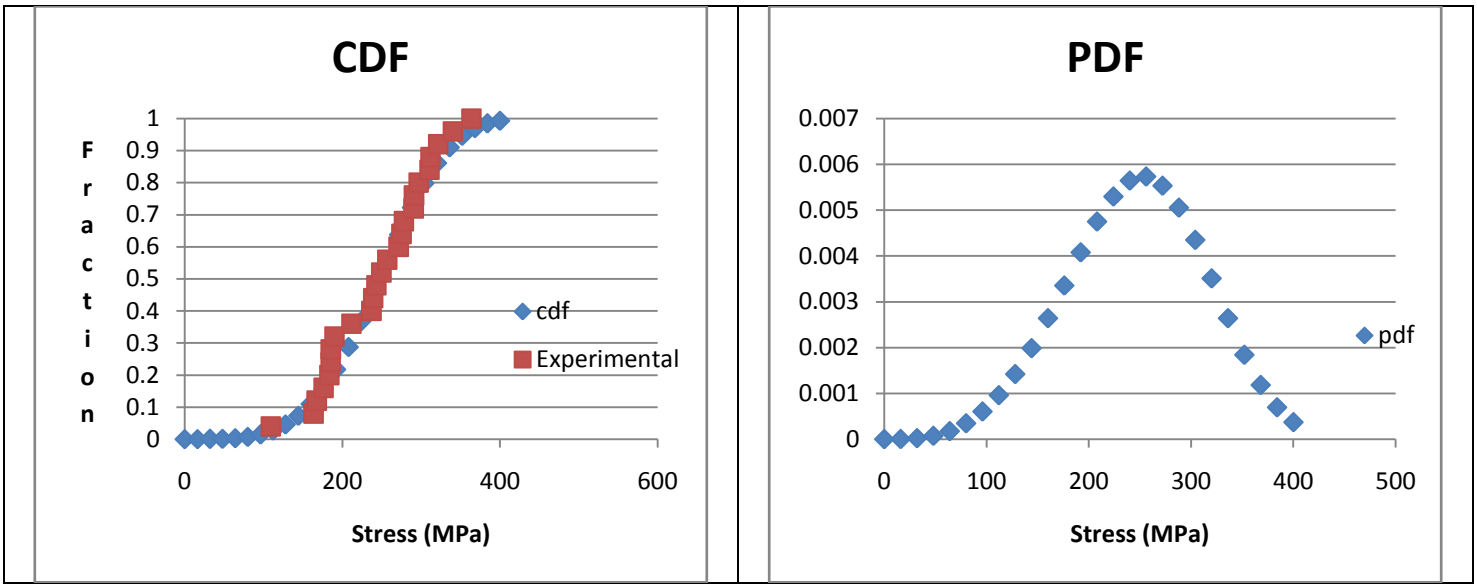

Figure A-26. 75% Diced. separation, wafer#5. β=4.088, α=271.0, ρ=0.986, N=25.

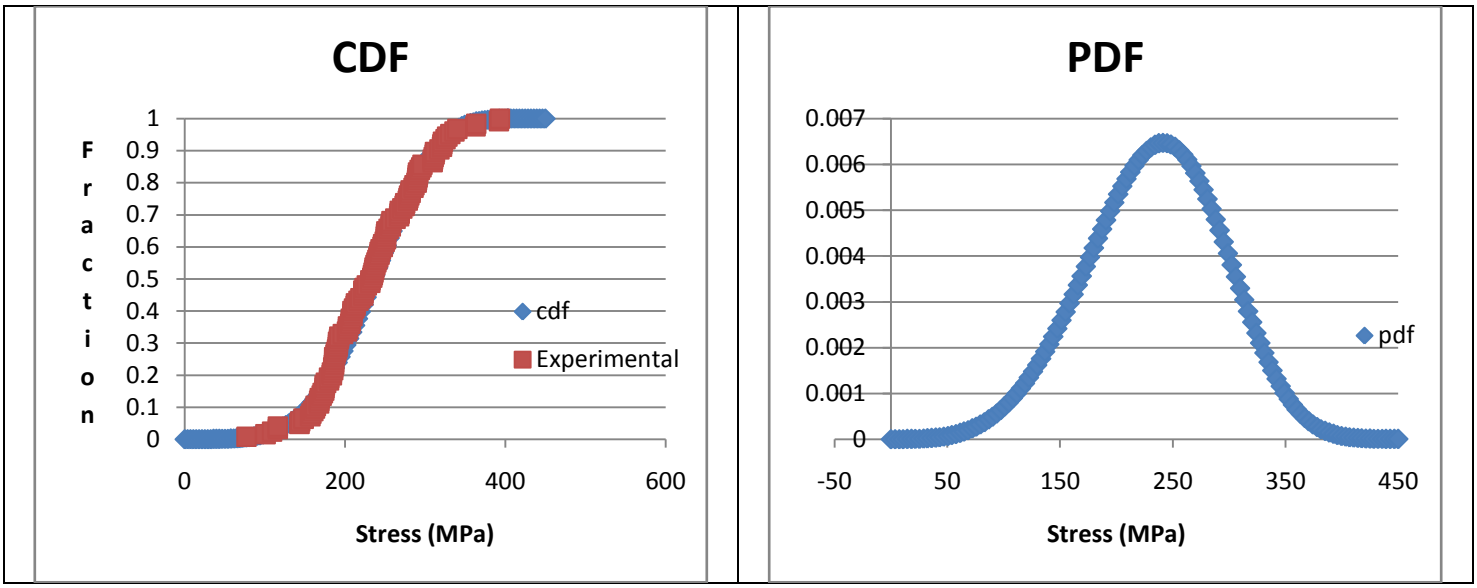

Figure A-27. 75% Diced. separation, all wafers. β=4.384, α=256.4, ρ=0.992, N=125.

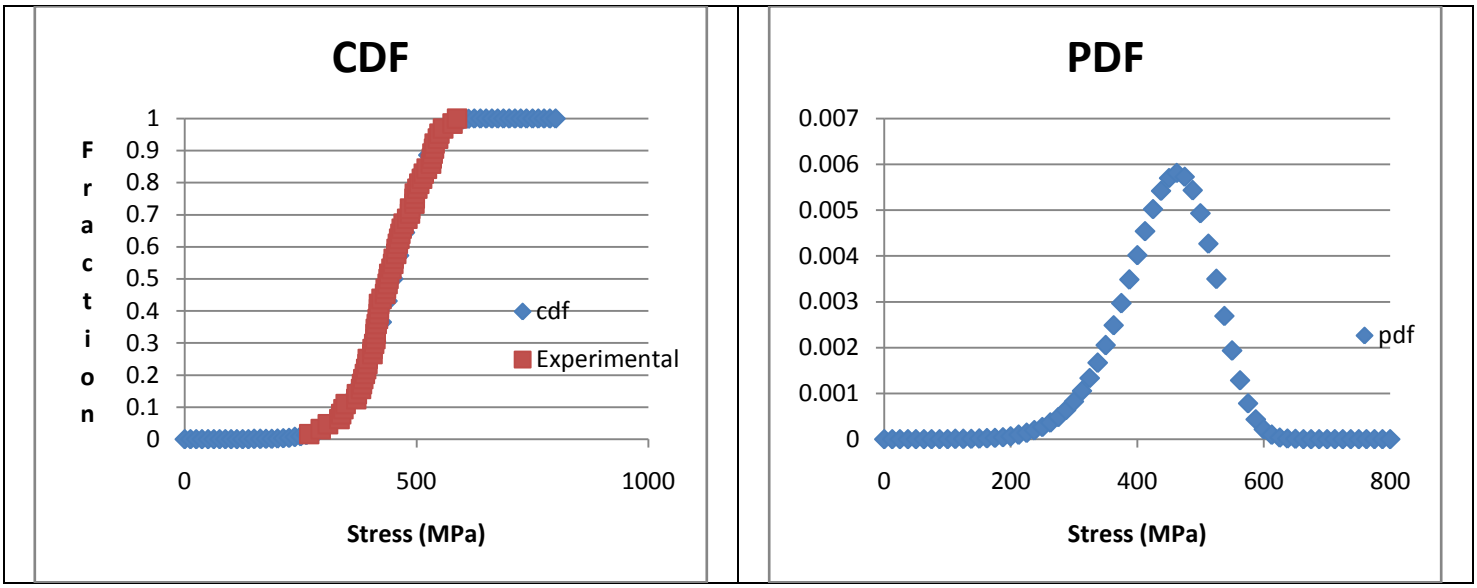

Figure A-28. 75% Diced. die fracture, all die. β=7.397, α=472.9, ρ=0.994, N=64.

All data for the 100% diced samples are shown below. N is the number of samples.

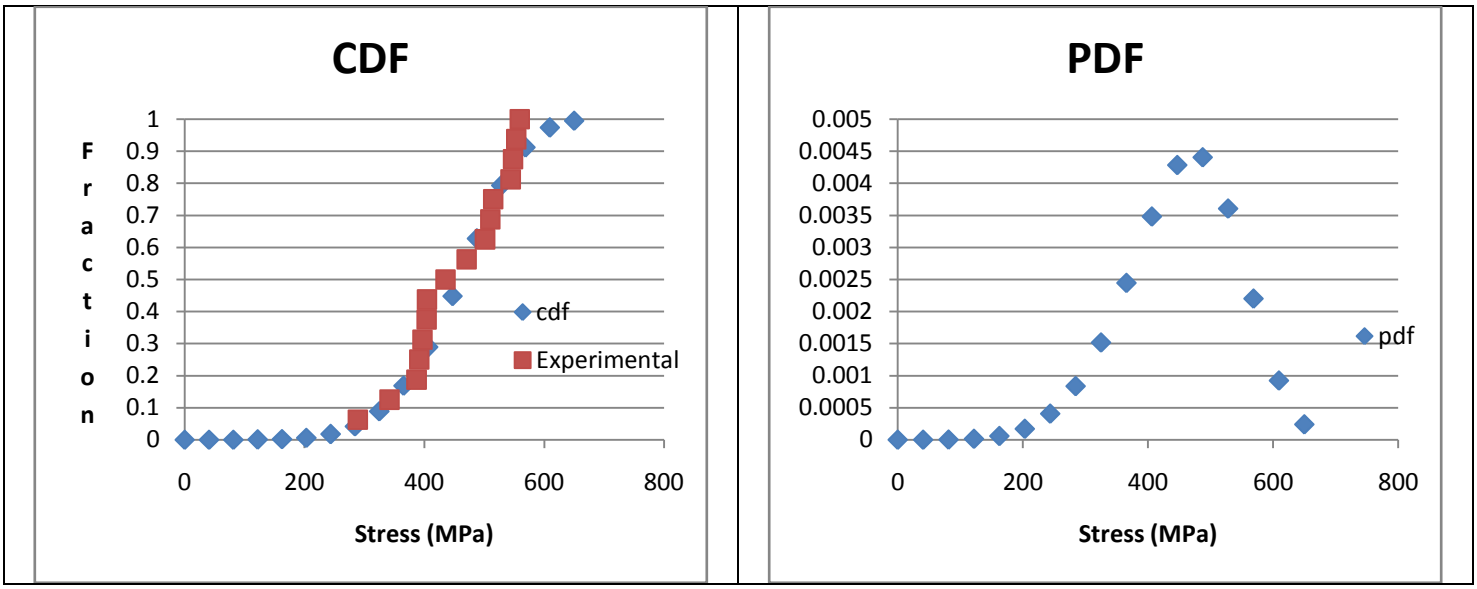

Figure A-29. 100% Diced, die fracture, wafer#1, β=5.835, α=488.6, ρ=0.980, N=16.

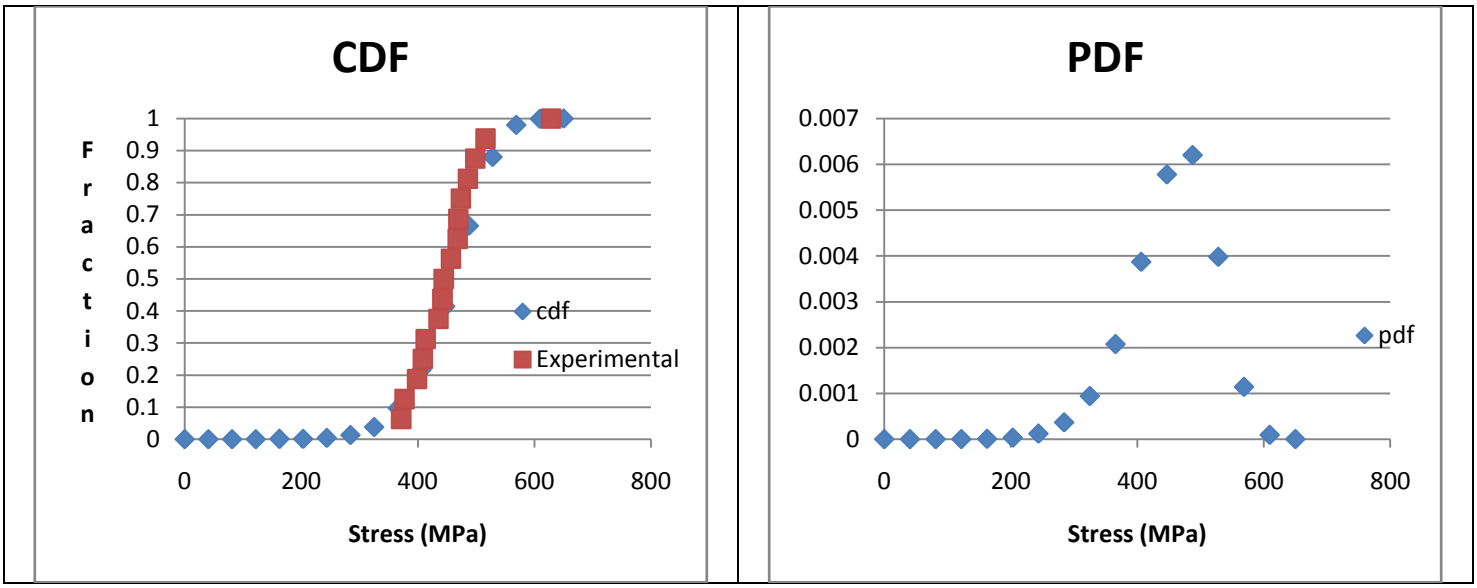

Figure A-30. 100% Diced, die fracture, wafer#2, β=8.254, α=482.2, ρ=0.930, N=16.

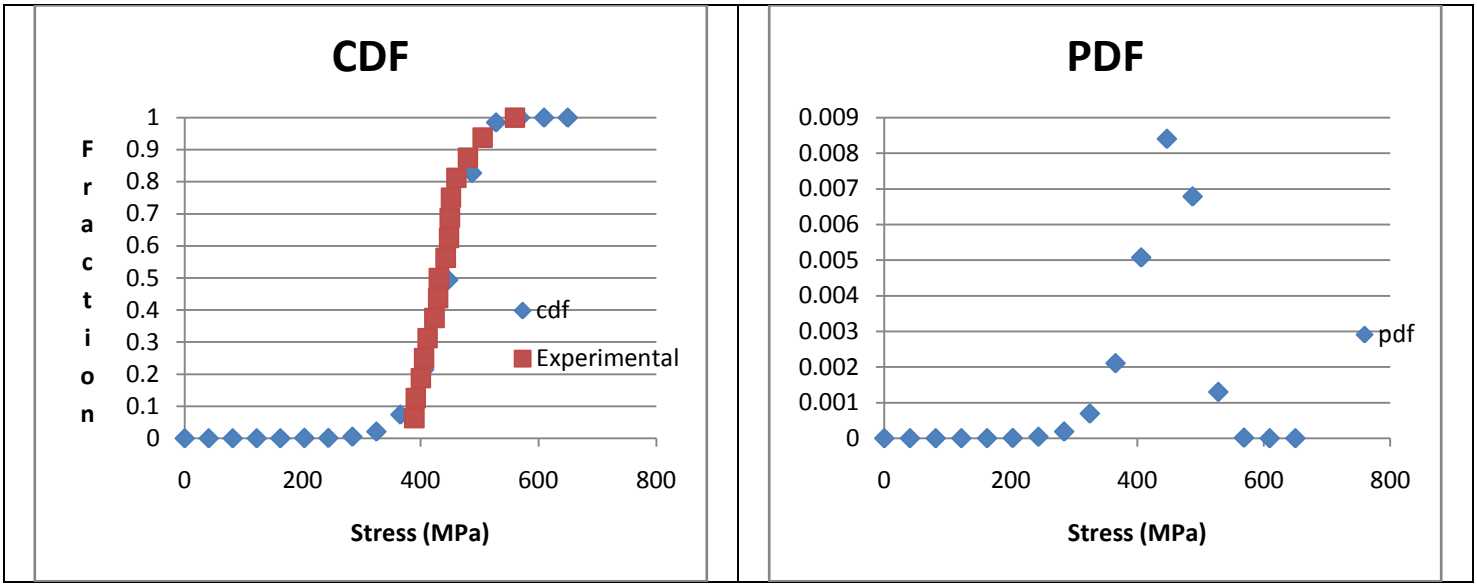

Figure A-31. 100% Diced, die fracture, wafer#3, β=10.90, α=463.0, ρ=0.908, N=16.

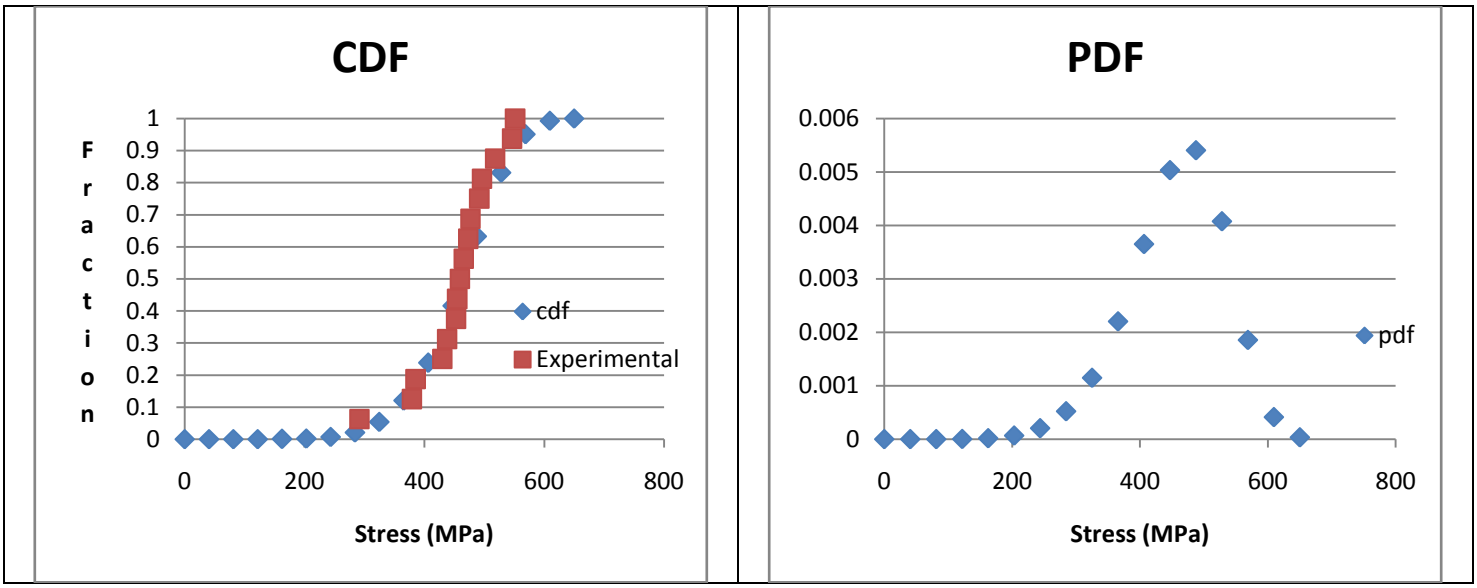

Figure A-32. 100% Diced, die fracture, wafer#4, β=7.158, α=487.4, ρ=0.970, N=16.

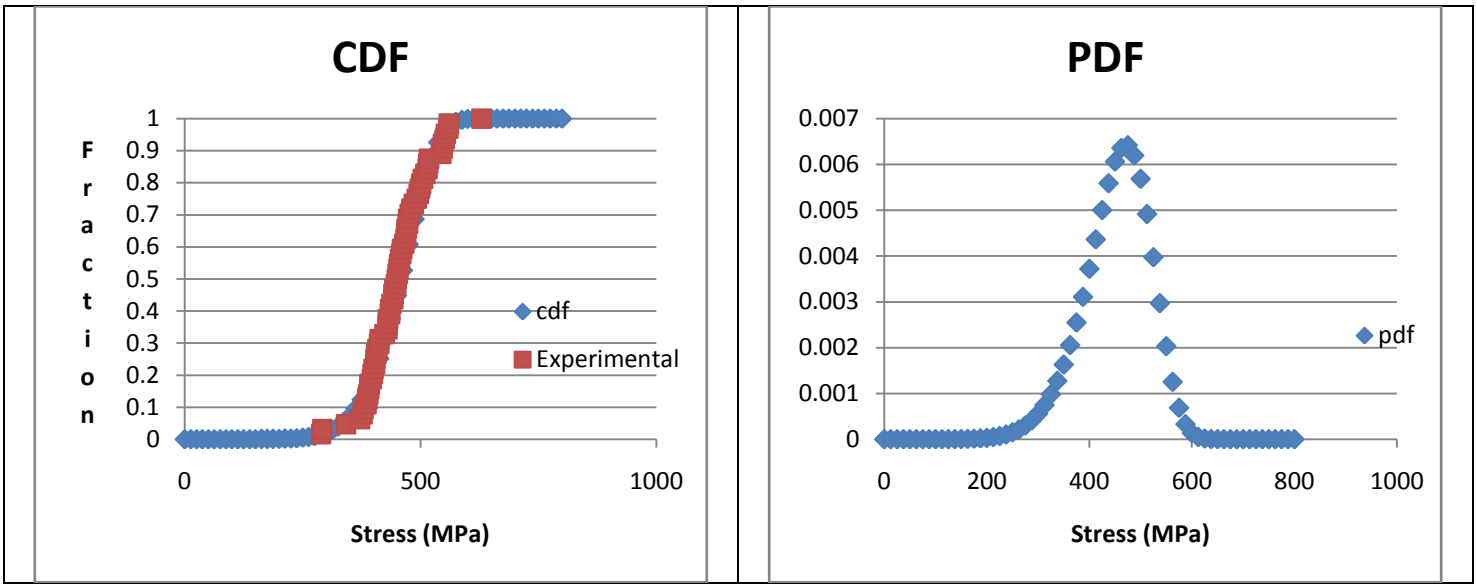

Figure A-33. 100% Diced, die fracture, all die, β=8.304, α=478.9, ρ=0.984, N=64.

All data for the 25% DRIE samples are shown below. N is the number of samples.

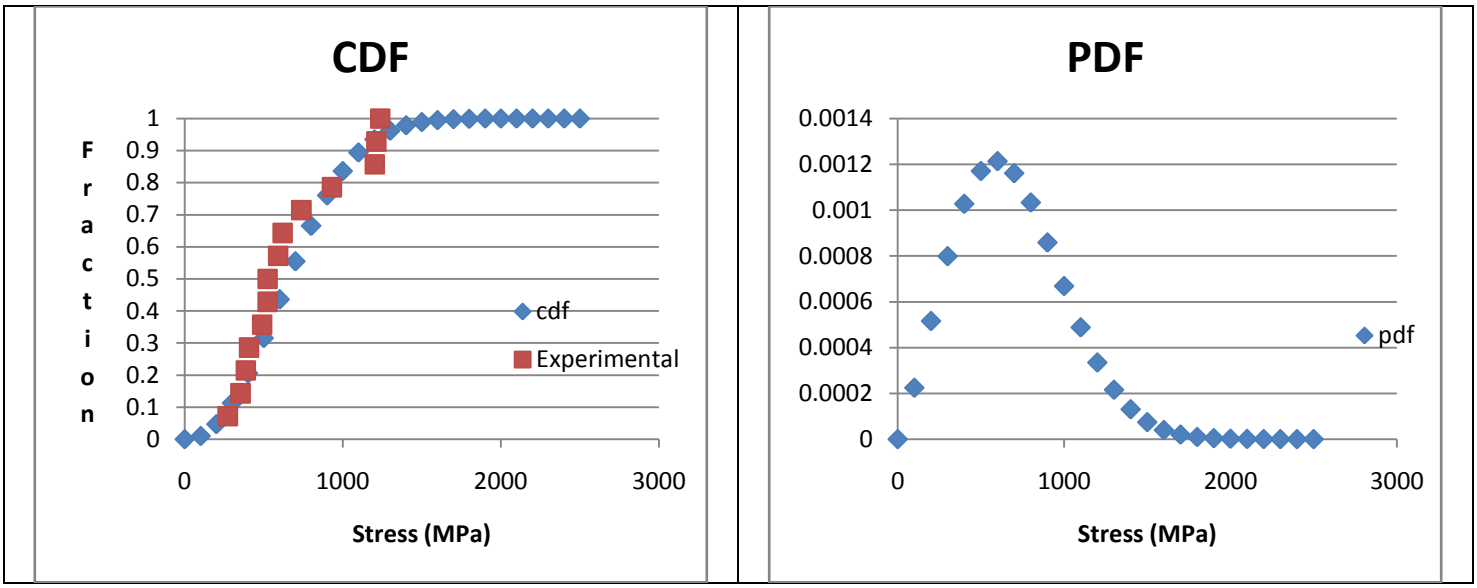

Figure A-34. 25% DRIE, separation, wafer#1, β=2.256, α=768.8, ρ=0.957, N=14.

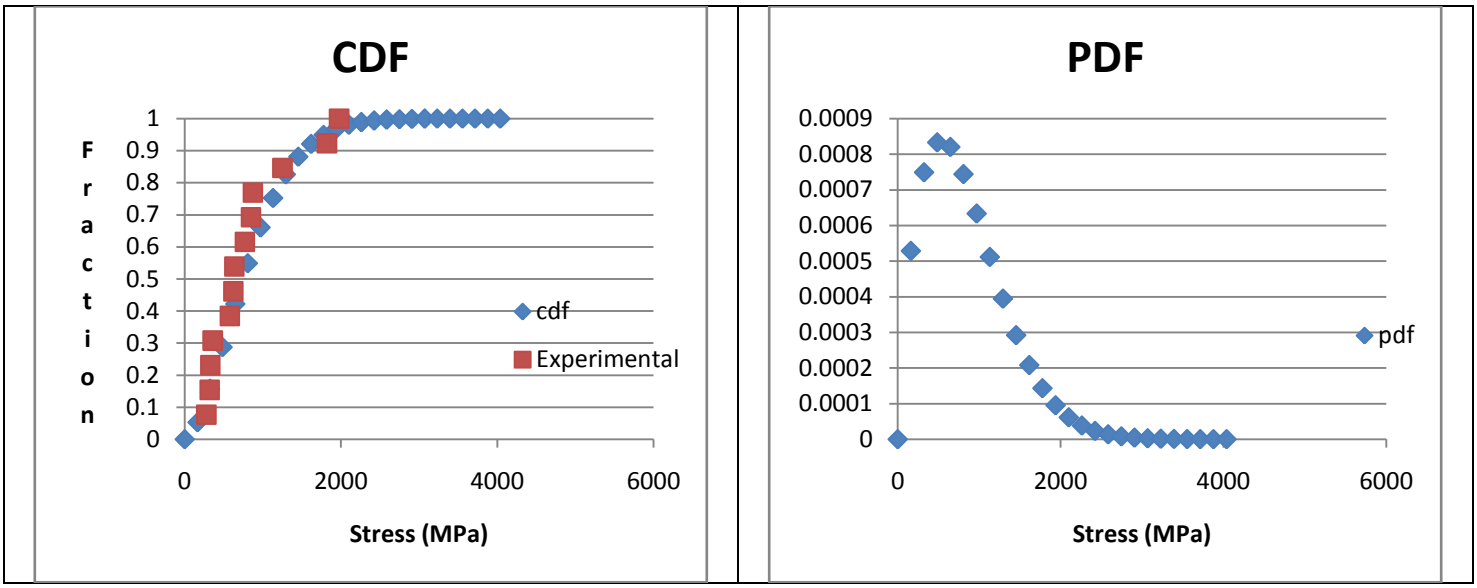

Figure A-35. 25% DRIE, separation, wafer#2, β=1.673, α=926.1, ρ=0.947, N=13.

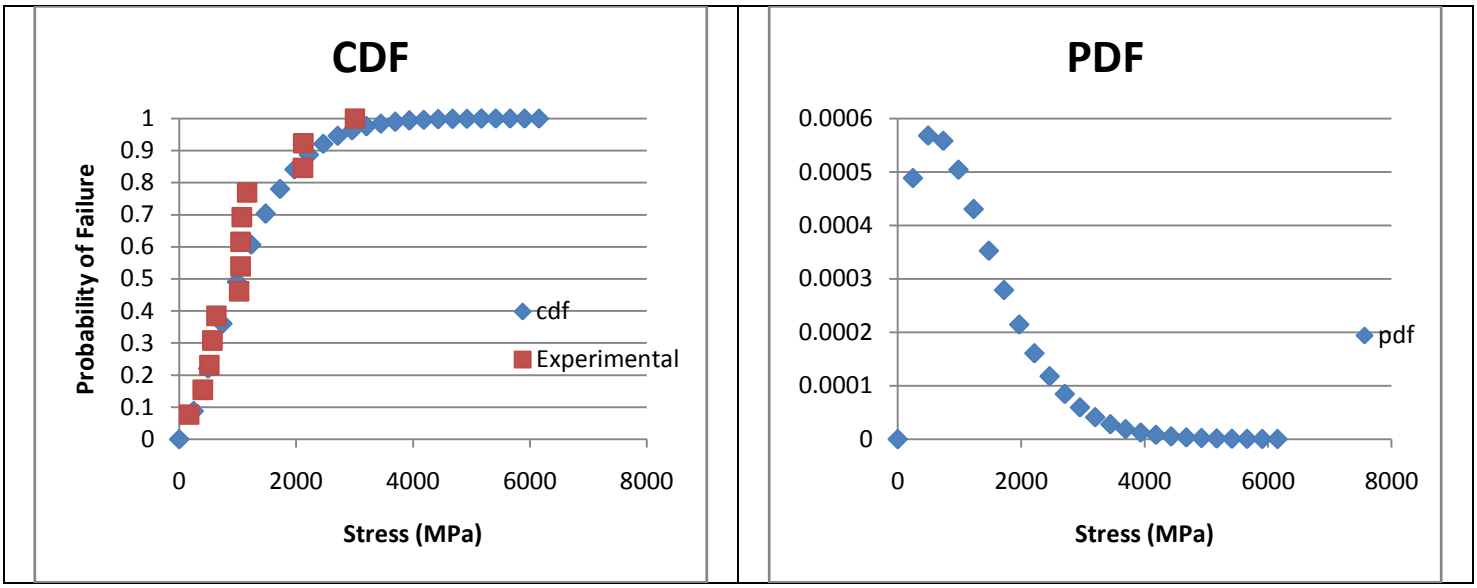

Figure A-36. 25% DRIE, separation, wafer#3, β=1.444, α=1292.0, ρ=0.981, N=13.

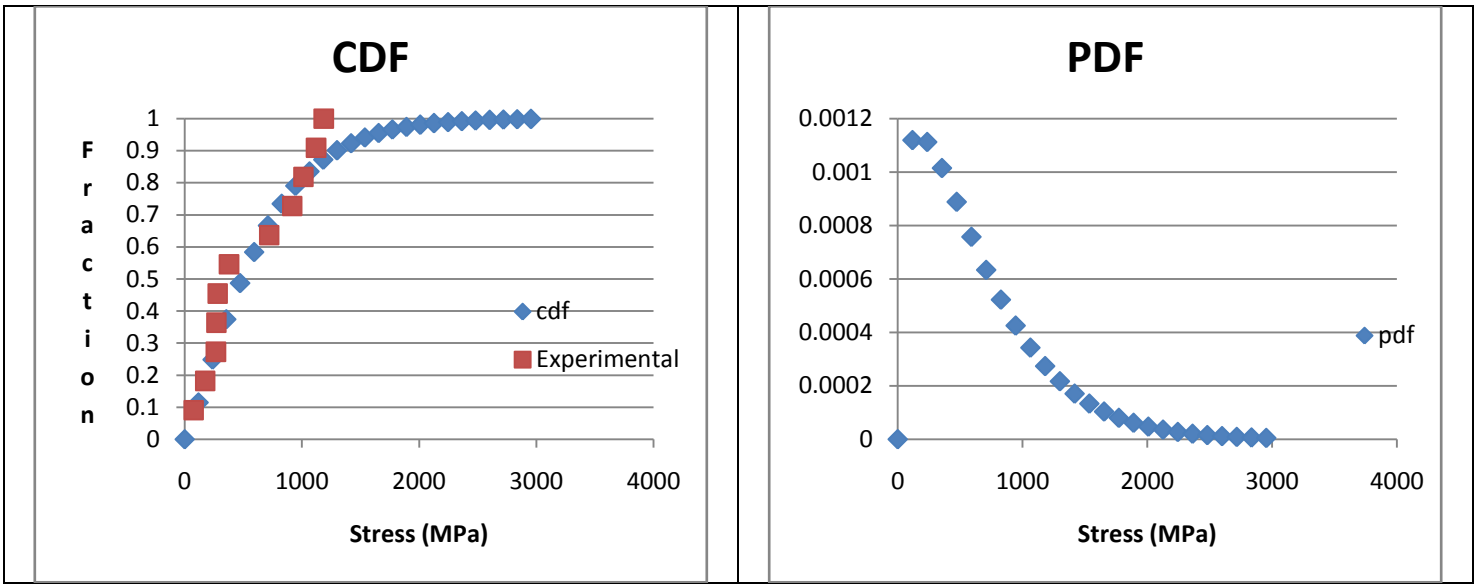

Figure A-37. 25% DRIE, separation, wafer#4, β=1.226, α=657.7, ρ=0.974, N=11.

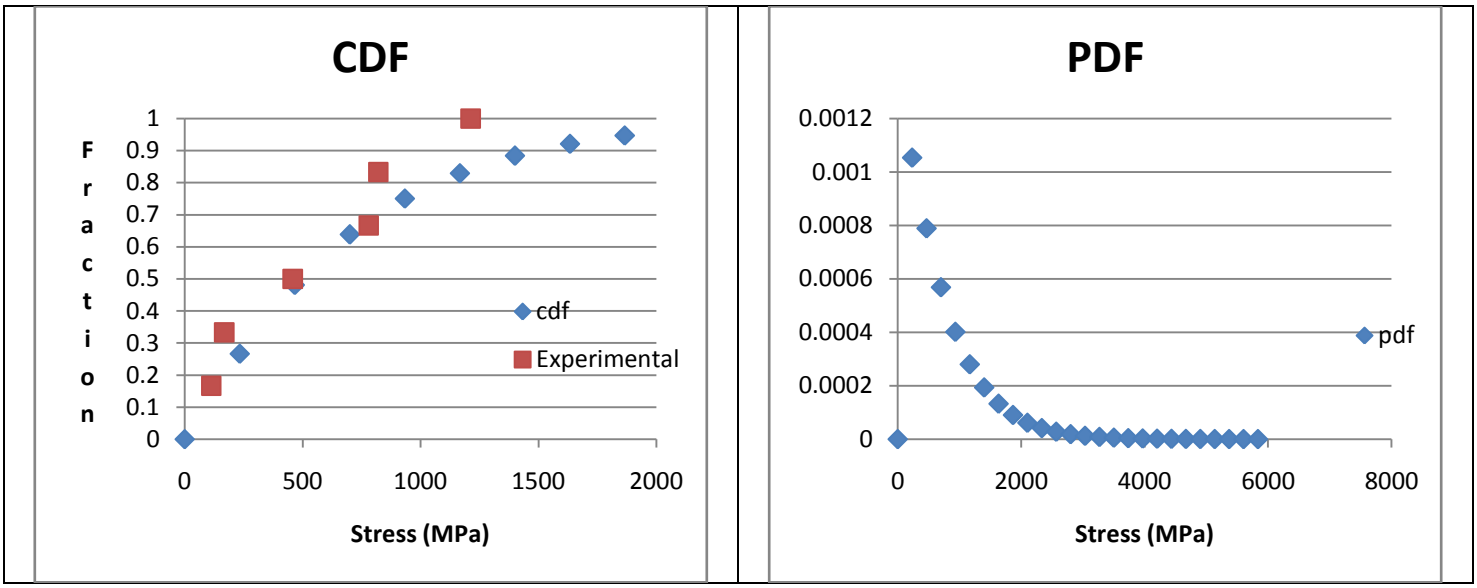

Figure A-38. 25% DRIE, separation, wafer#5, β=1.082, α=689.6, ρ=0.972, N=6.

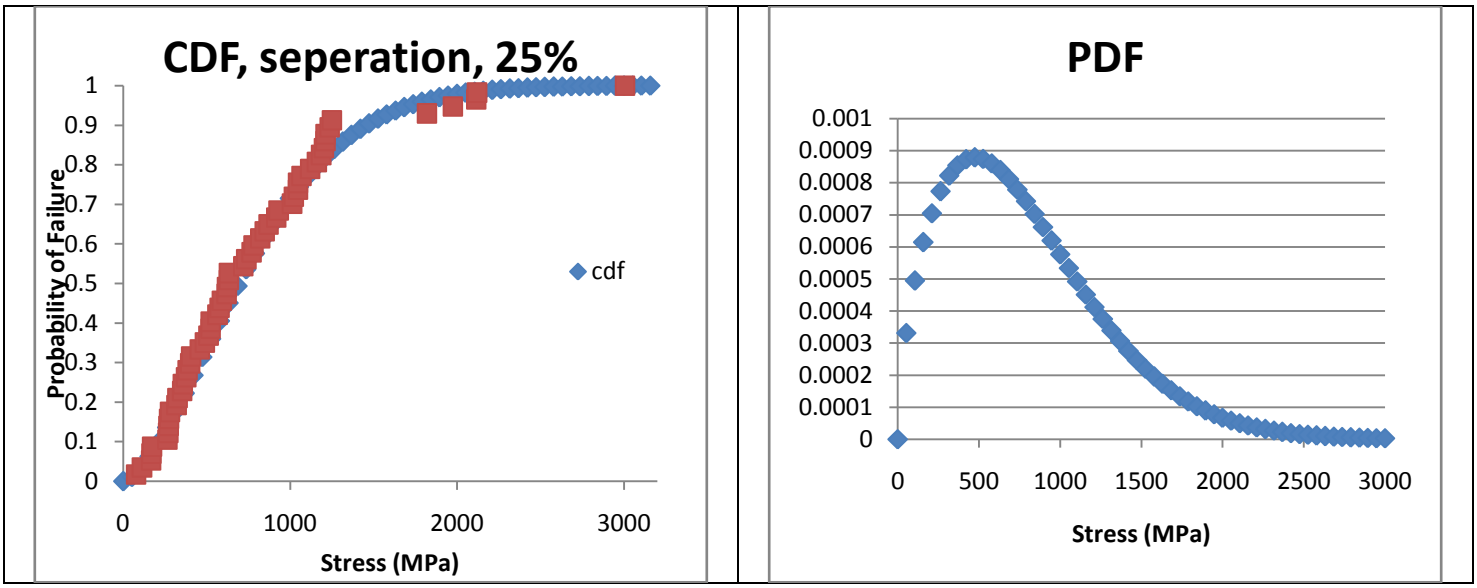

Figure A-39. 25% DRIE, separation, all wafers, β=1.61, α=868.8, ρ=0.990, N=57.

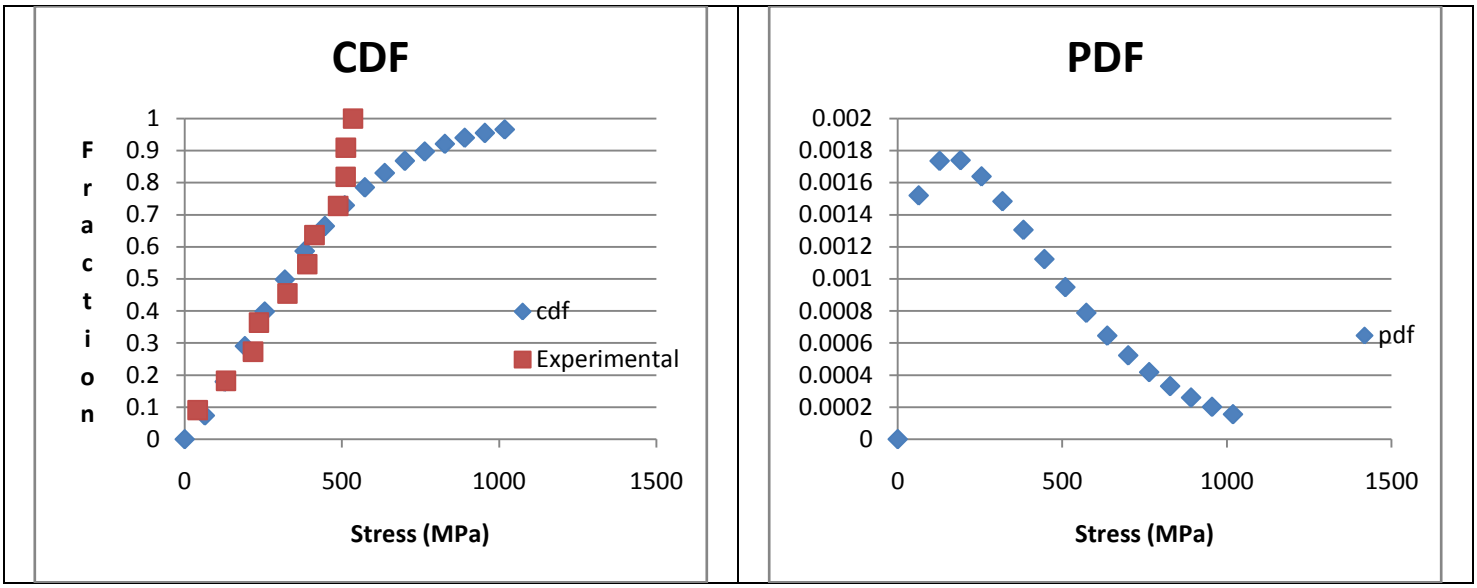

Figure A-40. 25% DRIE, die fracture, wafer#1, β=1.365, α=418.2, ρ=0.950, N=11.

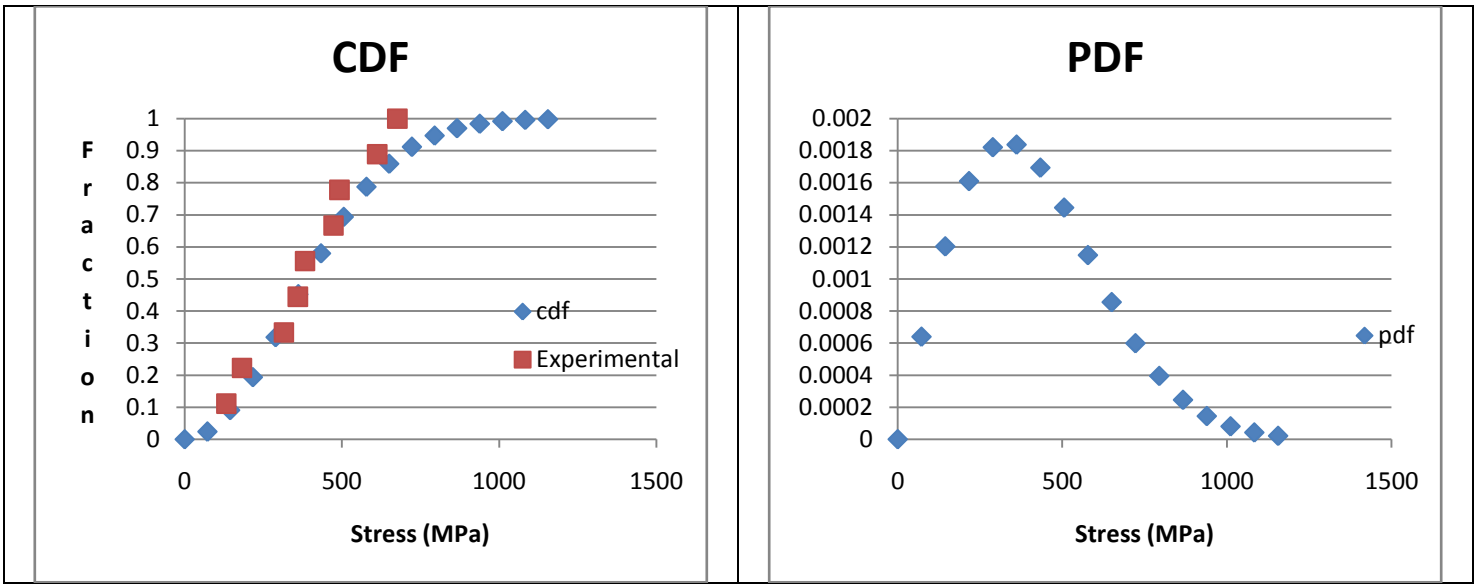

Figure A-41. 25% DRIE, die fracture, wafer#2, β=2.014, α=465.2, ρ=0.986, N=9.

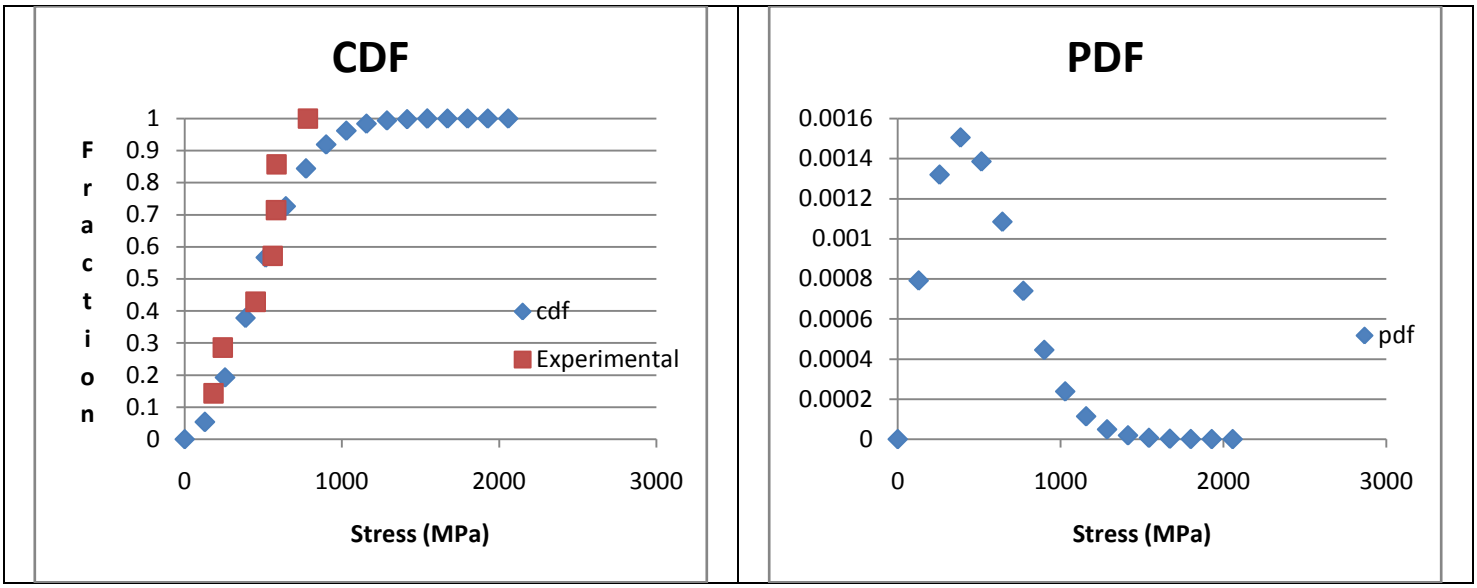

Figure A-42. 25% DRIE, die fracture, wafer#3, β=1.967, α=563.5, ρ=0.963, N=7.

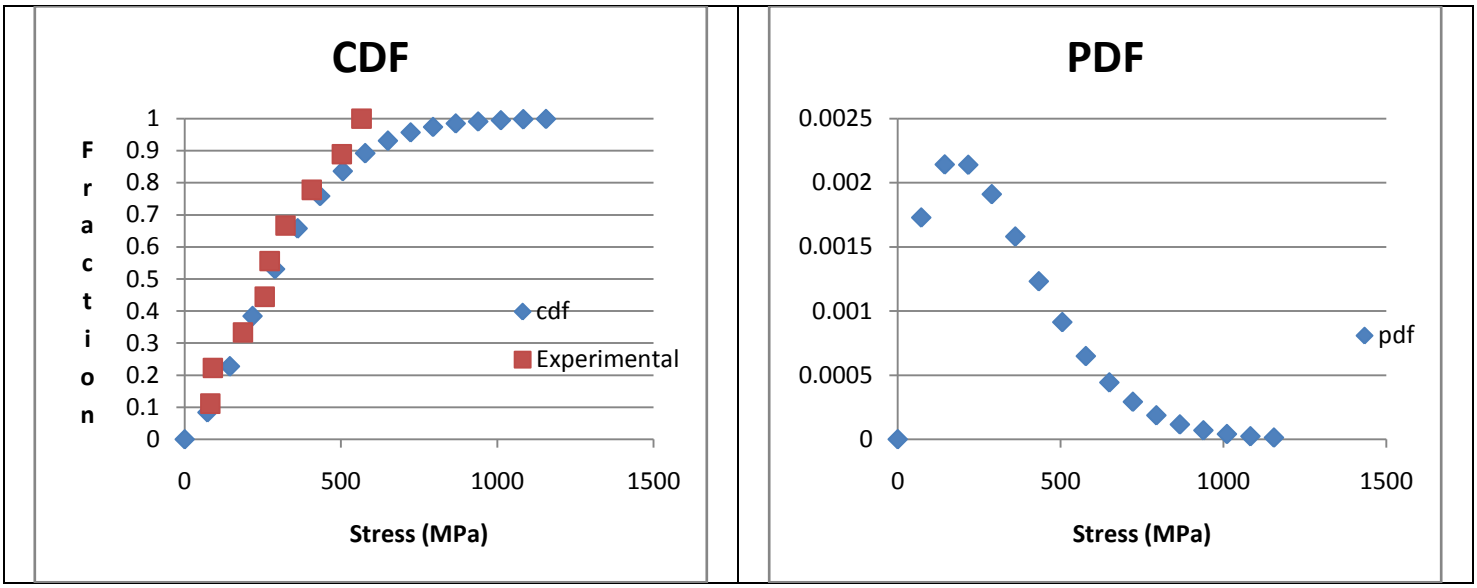

Figure A-43. 25% DRIE, die fracture, wafer#4, β=1.555, α=345.8, ρ=0.978, N=9.

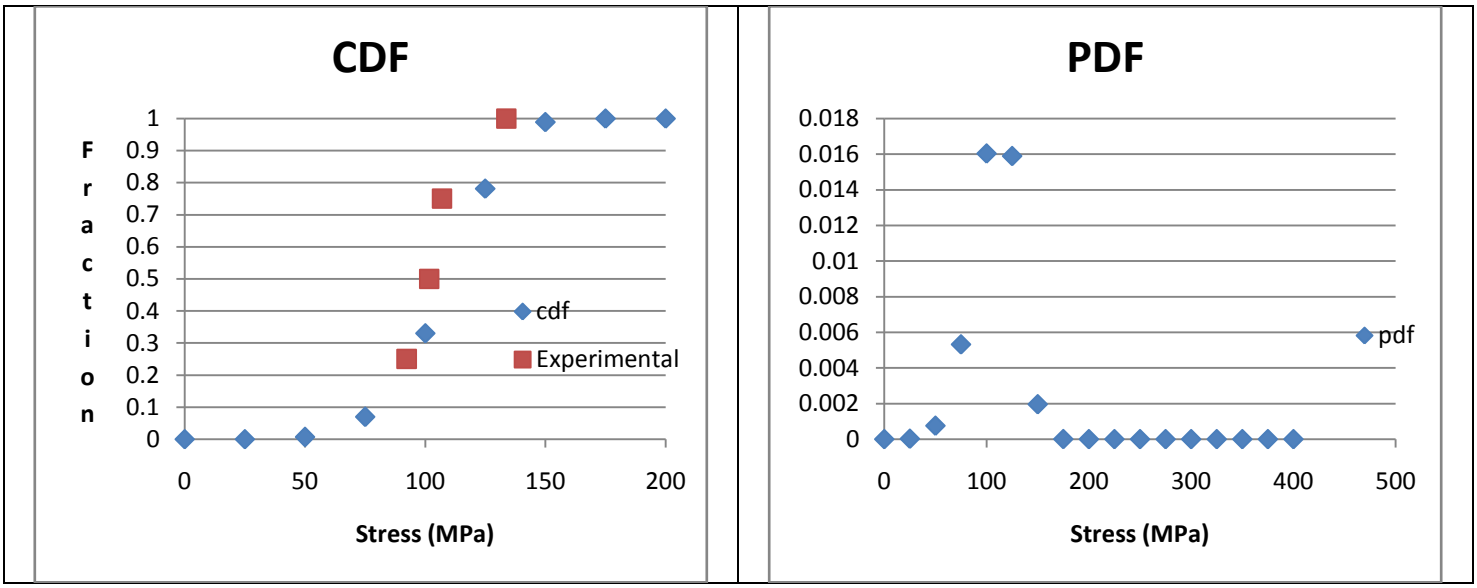

Figure A-44. 25% DRIE, die fracture, wafer#5, β=5.978, α=116.5, ρ=0.933, N=4.

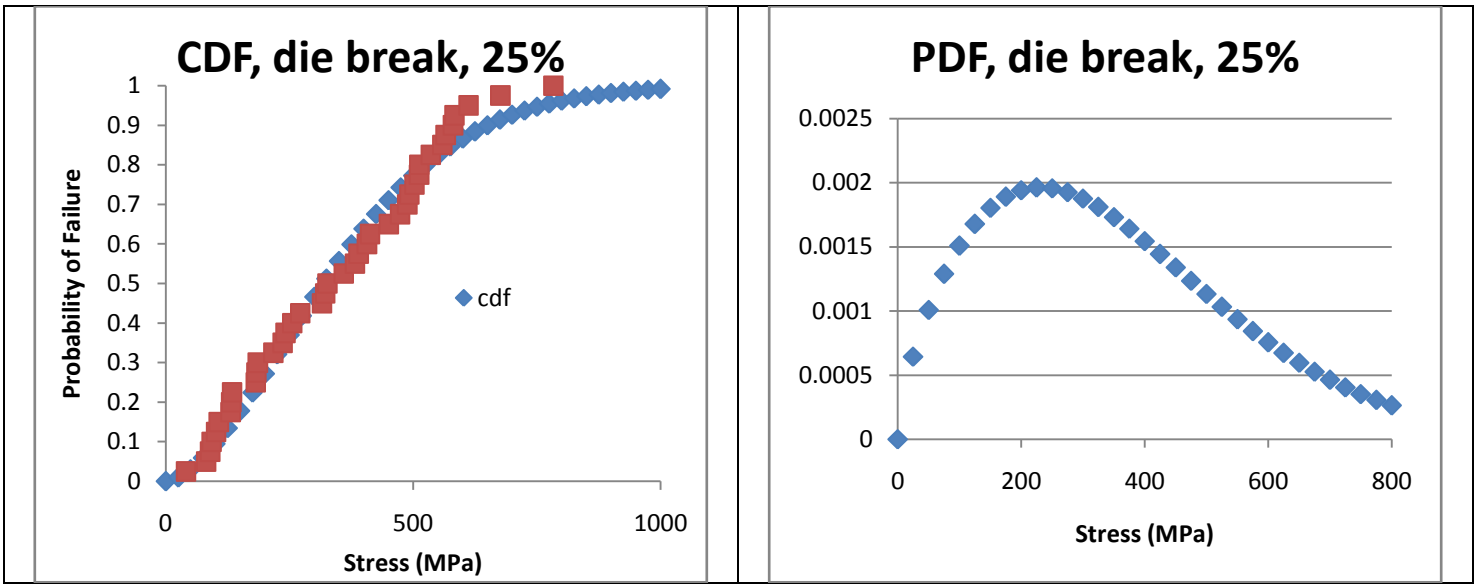

Figure A-45. 25% DRIE, die fracture, all die, β=1.680, α=396.0, ρ=0.987, N=40.

All data for the 50% DRIE samples are shown below. N is the number of samples. Weibull analysis was only done for all of the die fracture samples together and not individually.

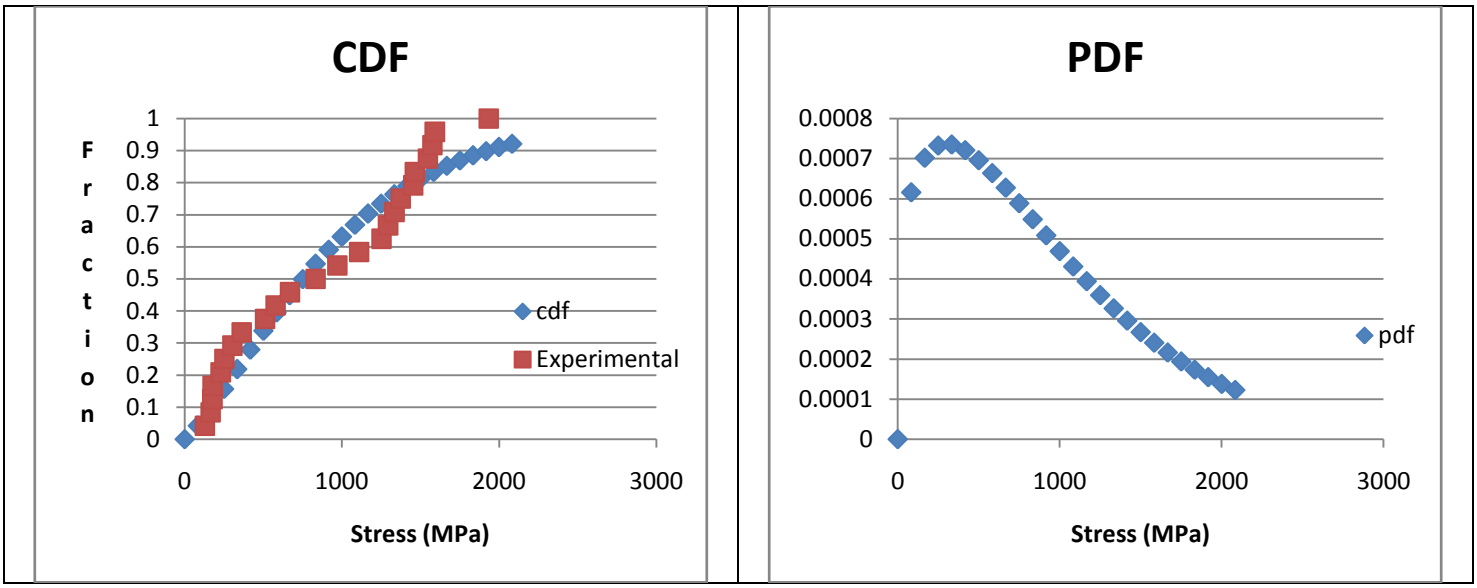

Figure A-46. 50% DRIE, separation, wafers#1, β=1.275, α=1002.3, ρ=0.960, N=24.

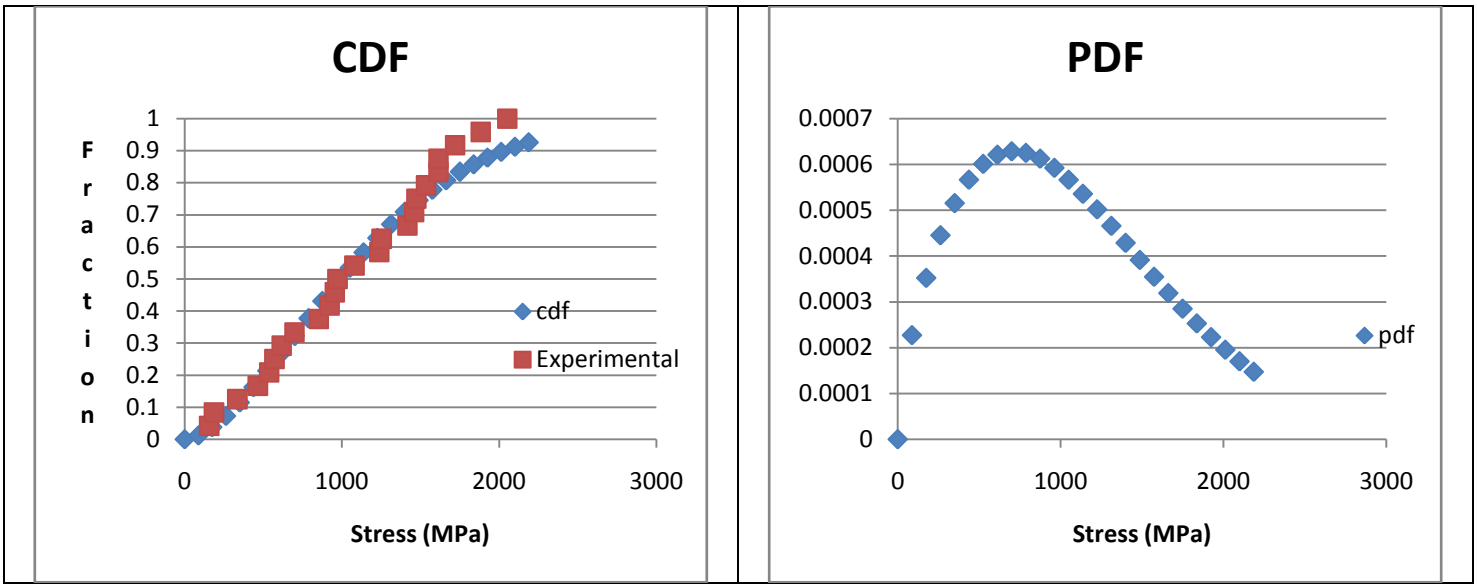

Figure A-47. 50% DRIE, separation, wafers#2, β=1.670, α=1233.5, ρ=0.986, N=24.

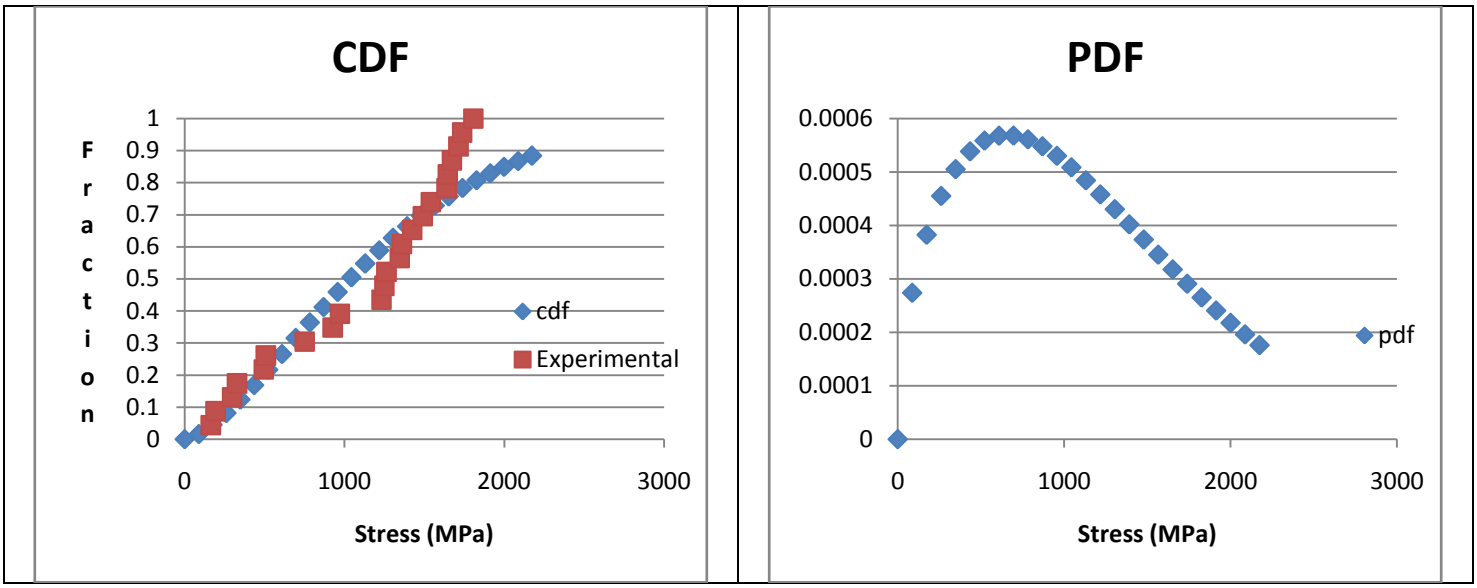

Figure A-48. 50% DRIE, separation, wafers#3, β=1.525, α=1316.5, ρ=0.959, N=23.

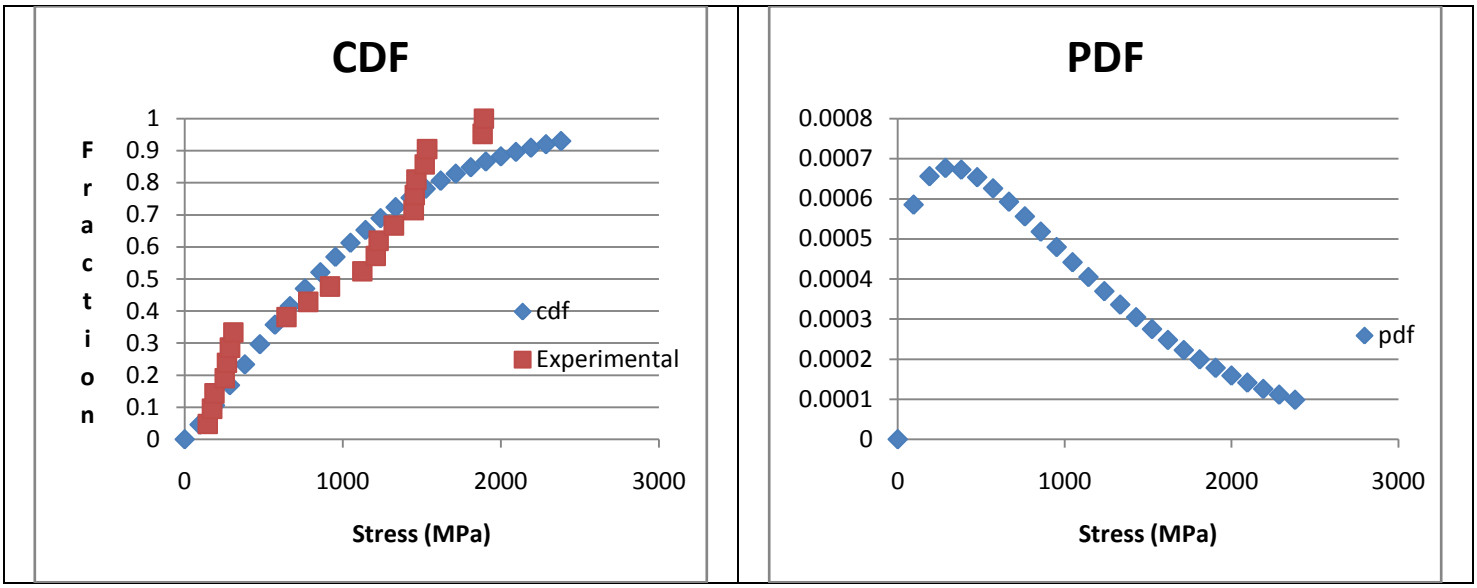

Figure A-49. 50% DRIE, separation, wafers#4, β=1.258, α=1093.6, ρ=0.949, N=21.

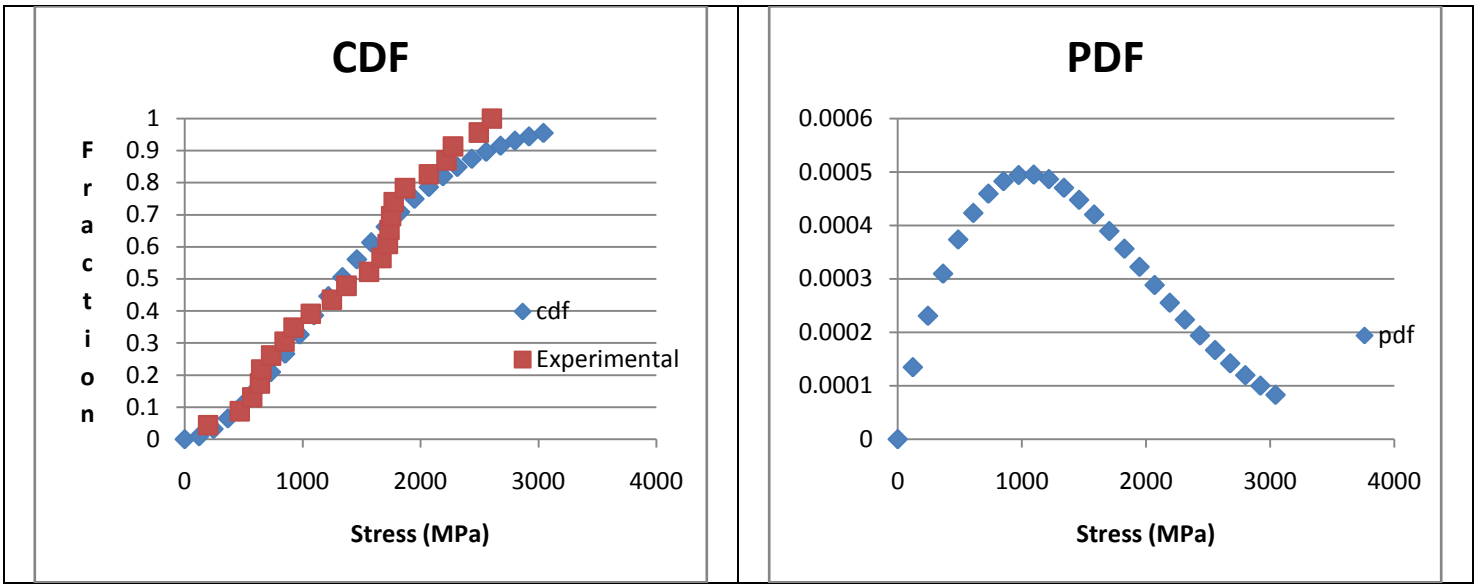

Figure A-50. 50% DRIE, separation, wafers#5, β=1.811, α=1628.1, ρ=0.986, N=23.

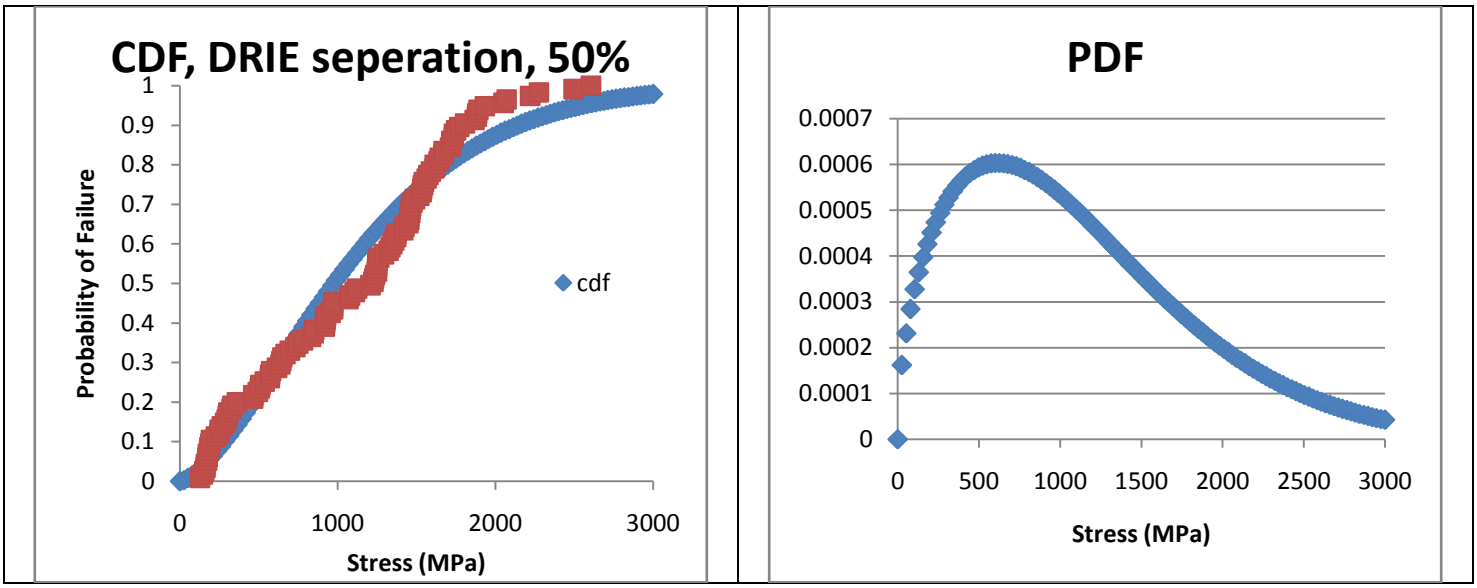

Figure A-51. 50% DRIE, separation, all wafers, β=1.524, α=1241.6, ρ=0.969, N=115.

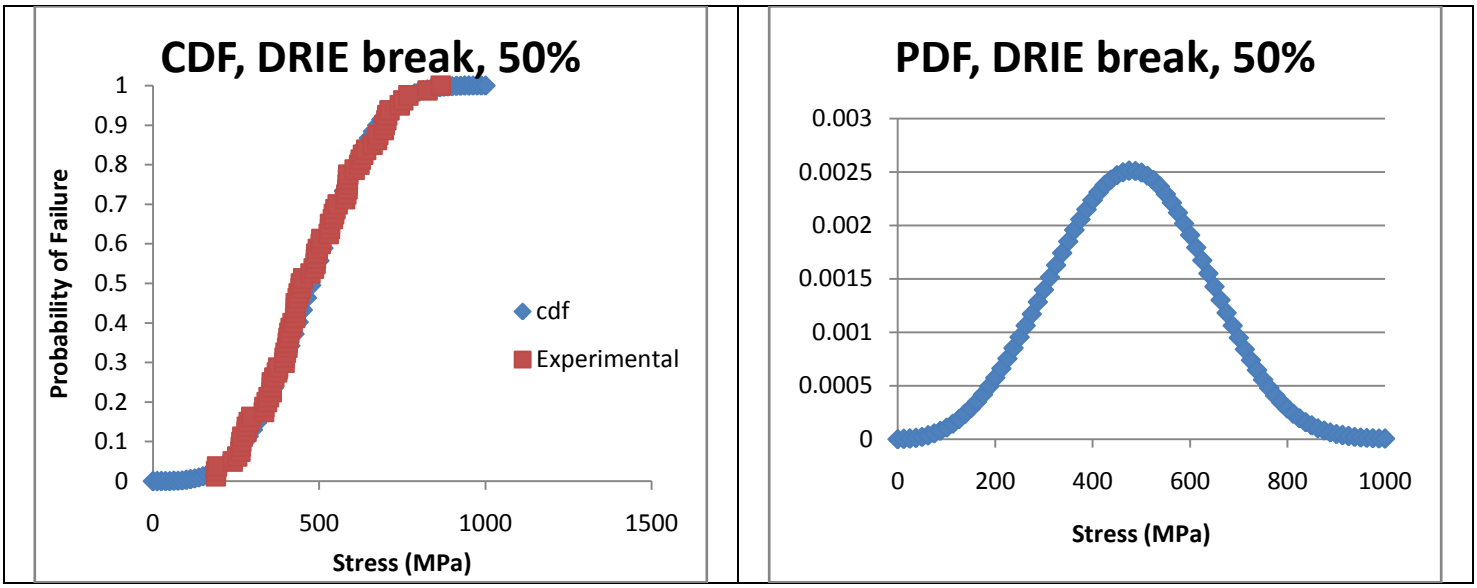

Figure A-52. 50% DRIE, die fracture, all die, β=3.456, α=530.5, ρ=0.989, N=80.

All data for the 75% DRIE samples are shown below. N is the number of samples. Weibull analysis was only done for all of the die fracture samples together and not individually.

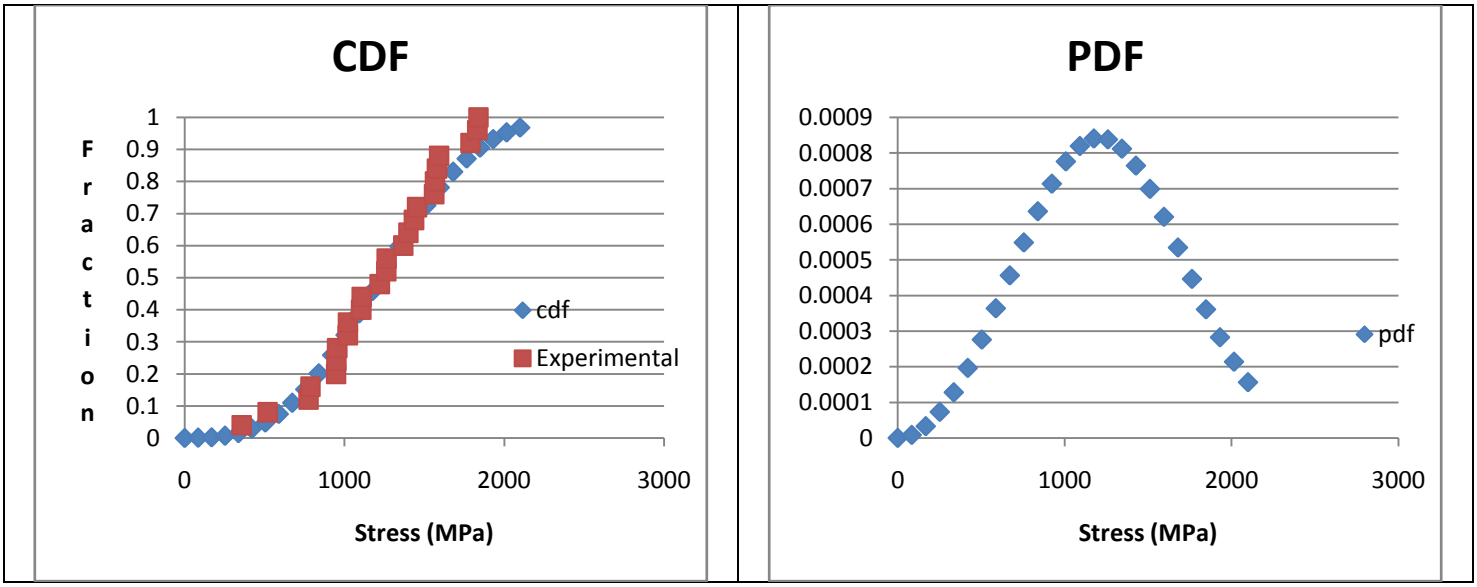

Figure A-53. 75% DRIE, separation, wafers#2, β=2.978, α=1386.9, ρ=0.983, N=25.

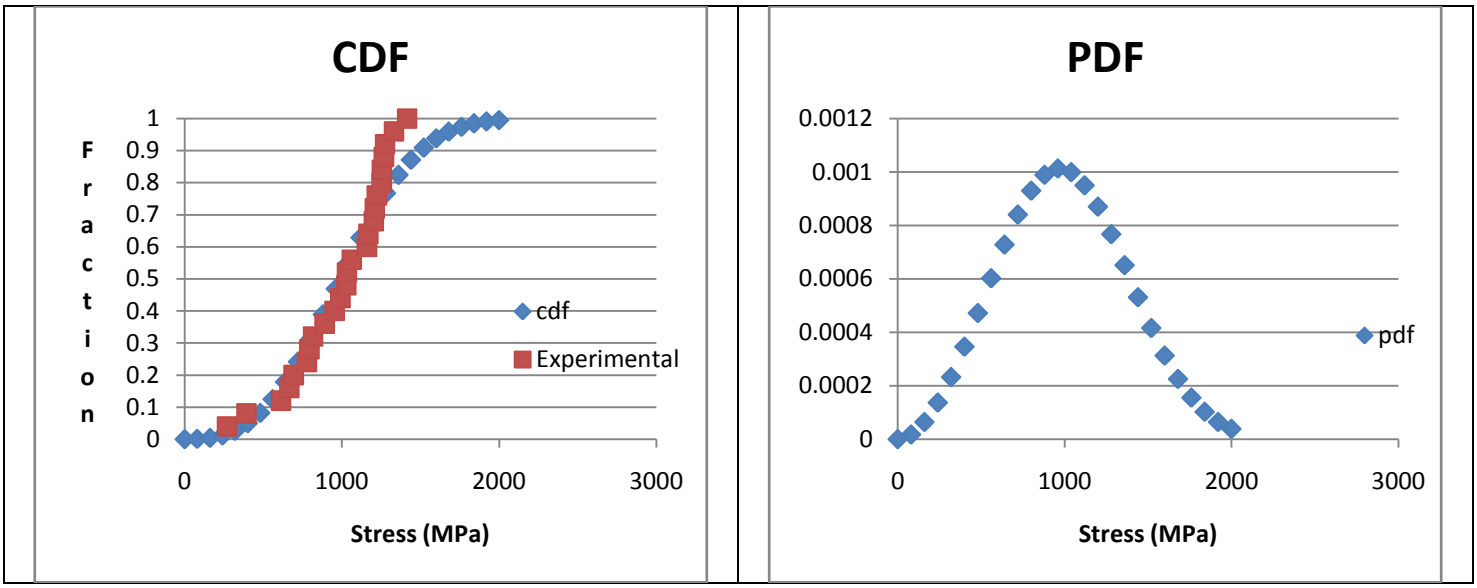

Figure A-54. 75% DRIE, separation, wafers#3, β=2.893, α=1124.2, ρ=0.967, N=25.

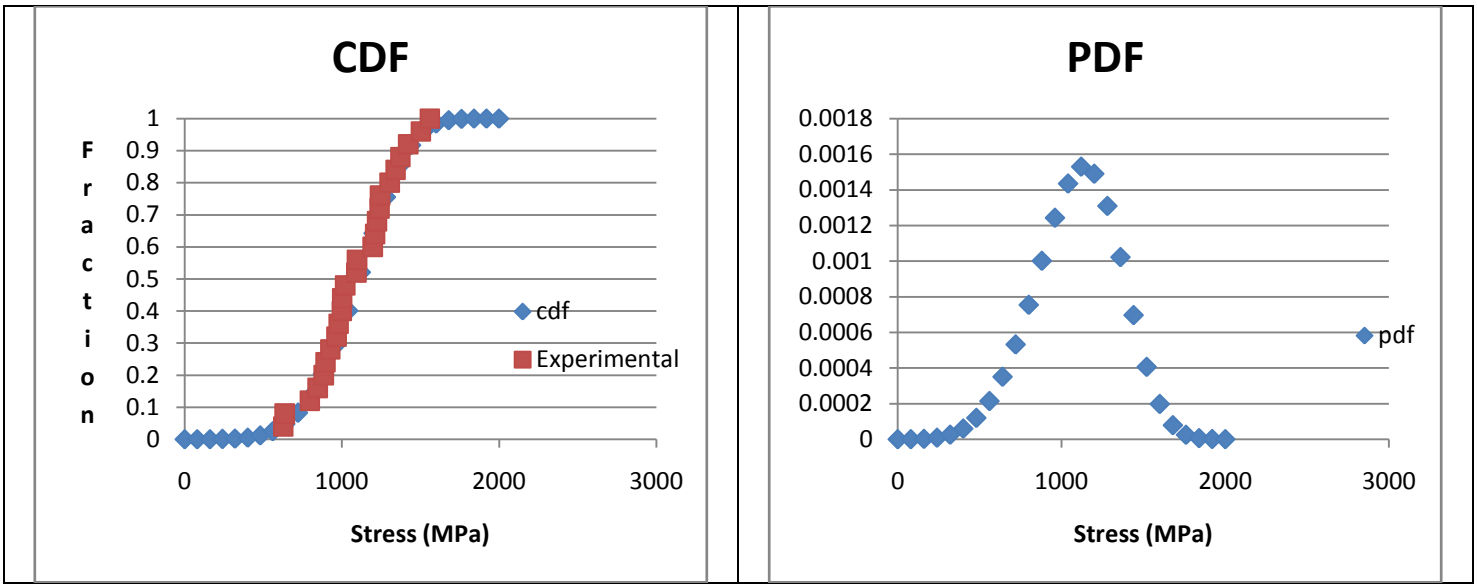

Figure A-55. 75% DRIE, separation, wafers#4, β=4.859, α=1193.4, ρ=0.989, N=25.

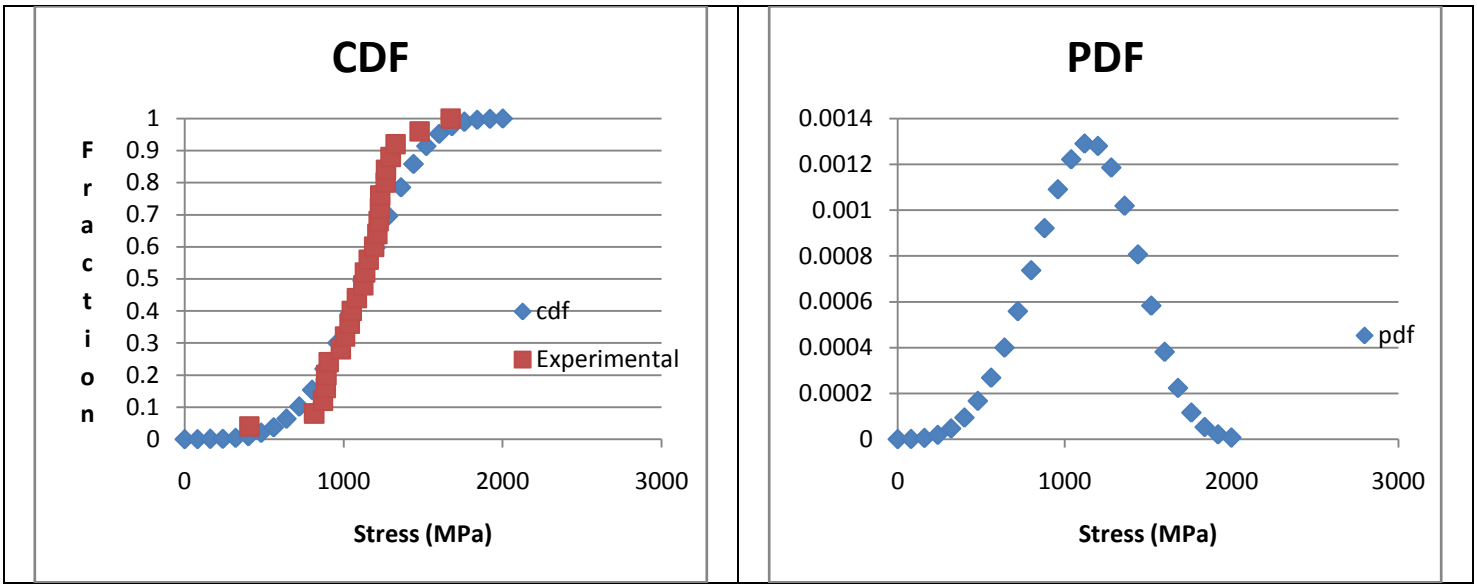

Figure A-56. 75% DRIE, separation, wafers#6, β=4.195, α=1227.5, ρ=0.941, N=25.

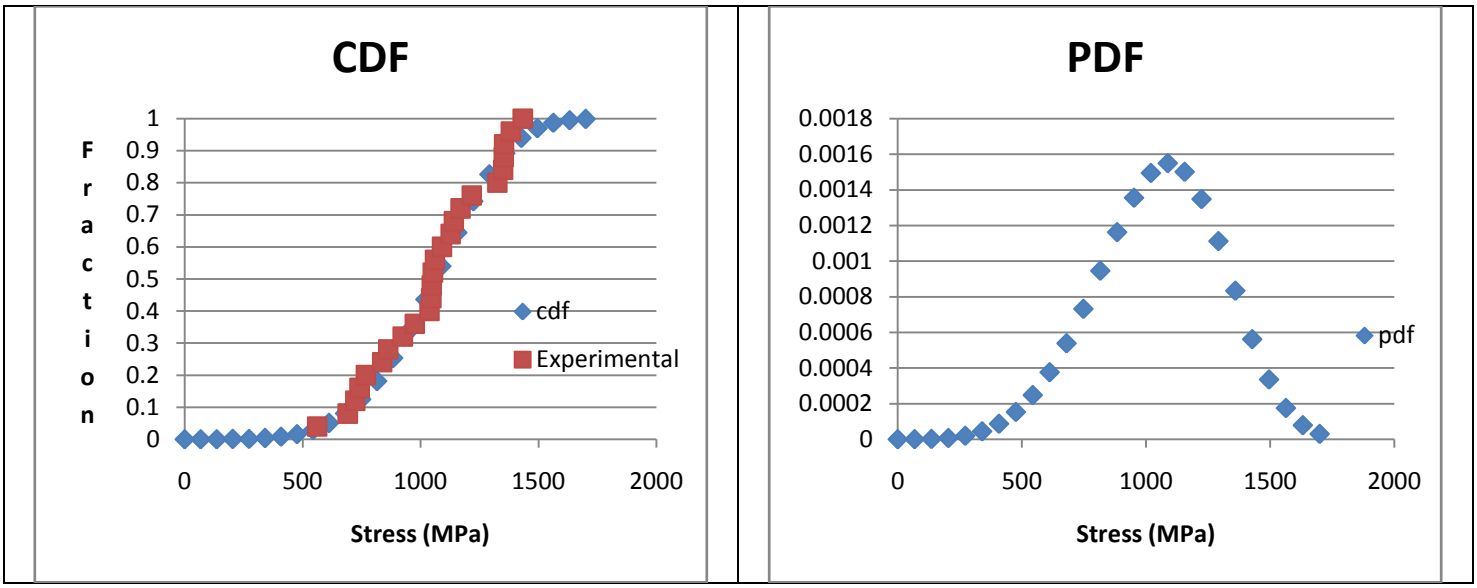

Figure A-57. 75% DRIE, separation, wafers#7, β=4.722, α=1147.9, ρ=0.990, N=25.

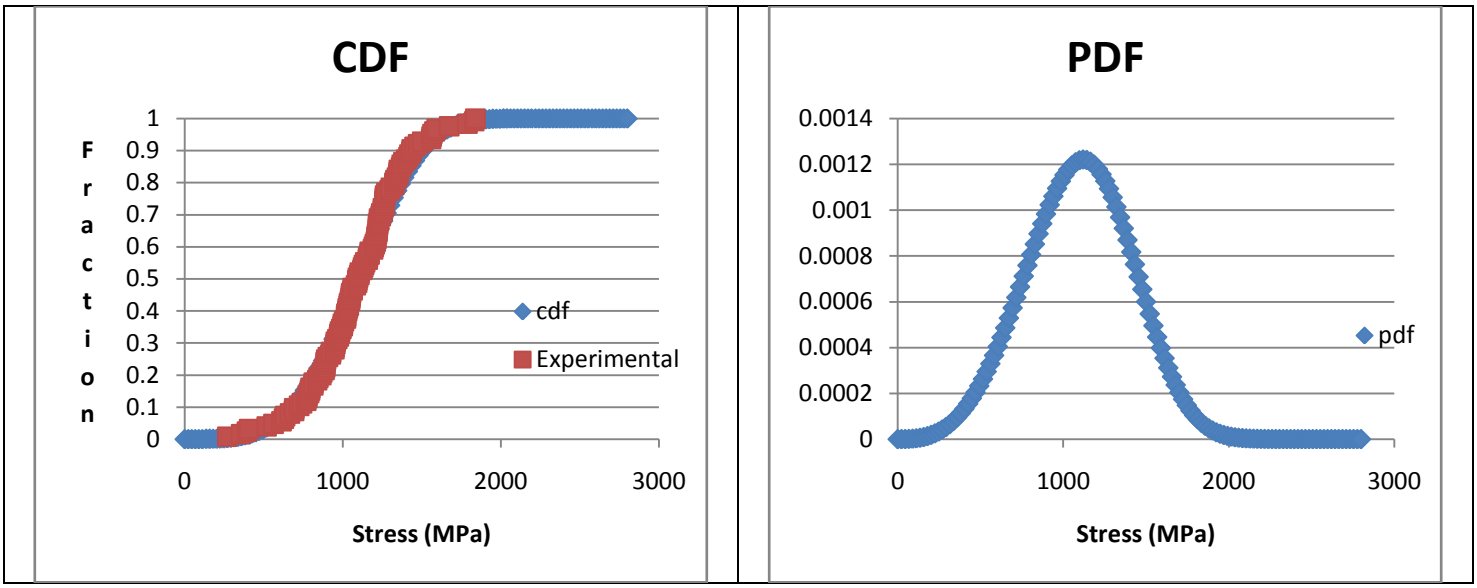

Figure A-58. 75% DRIE, separation, all wafers, β=3.878, α=1212.4, ρ=0.991, N=125.

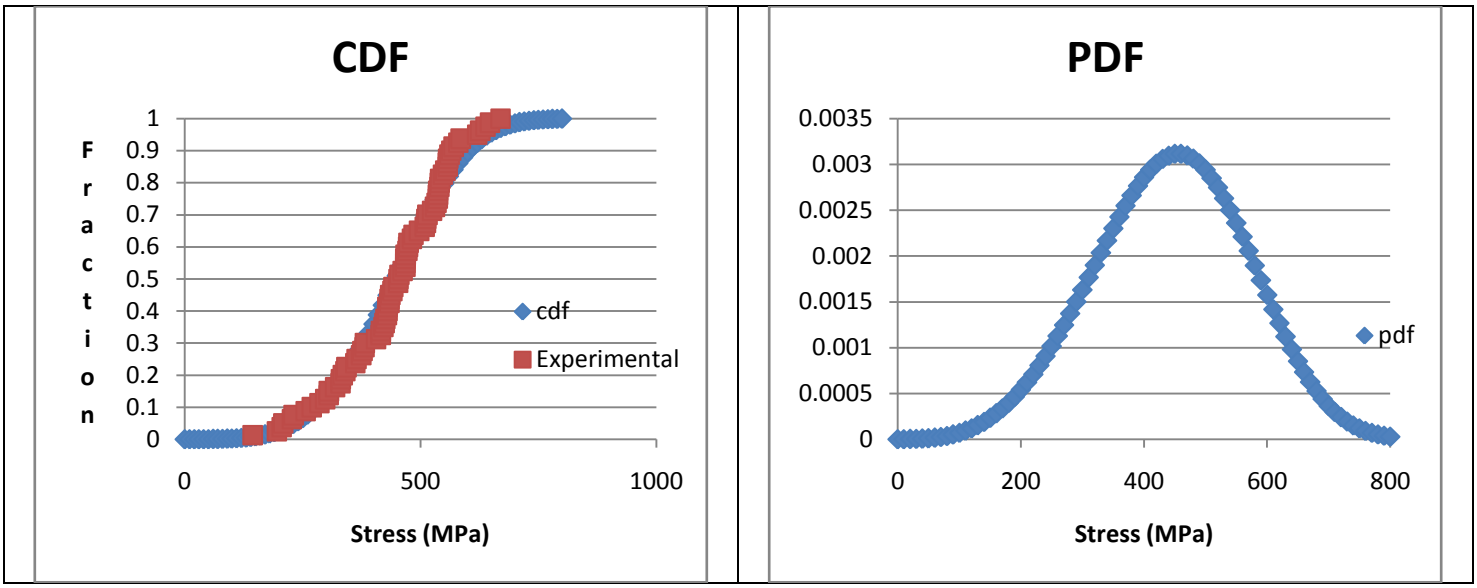

Figure A-59. 75% DRIE, die fracture, all die, β=4.009, α=489.5, ρ=0.993, N=80.

All data for the 100% DRIE samples are shown below. N is the number of samples. Weibull analysis was only done for all of the die fracture samples together and not individually.

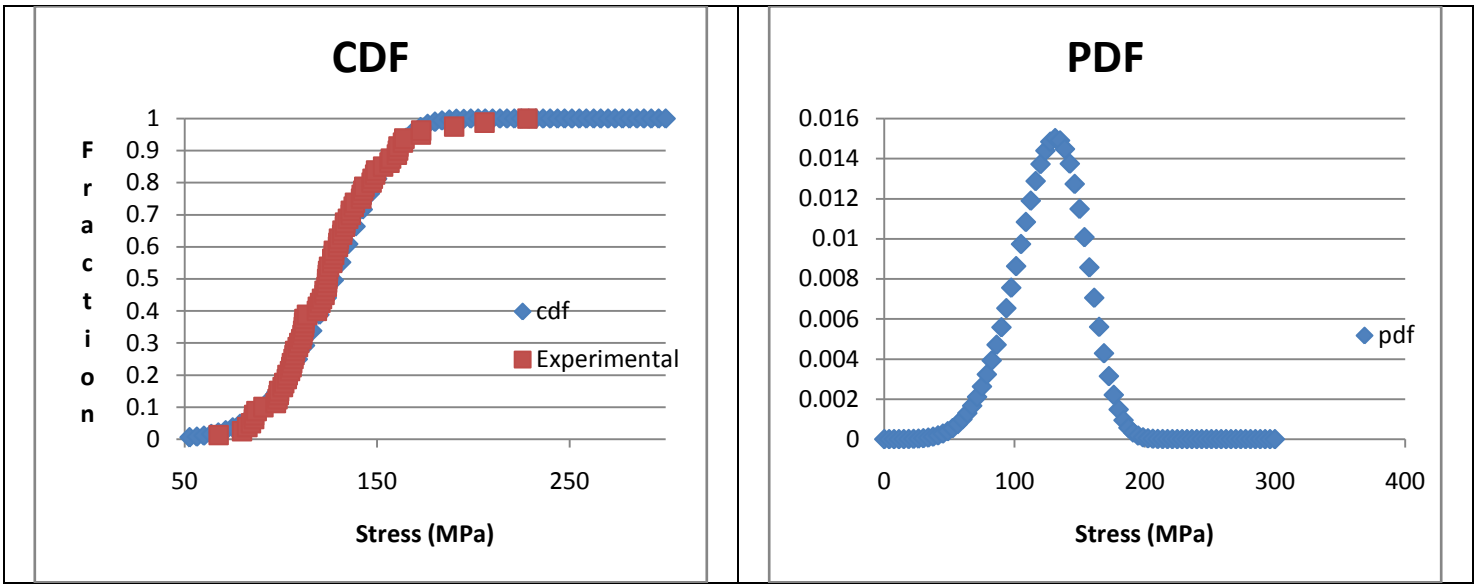

Figure A-60. 100% DRIE, die fracture, all die, β=5.482, α=136.6, ρ=0.972, N=80.

All data for the 25% DRIE double sided samples are shown below. N is the number of samples.

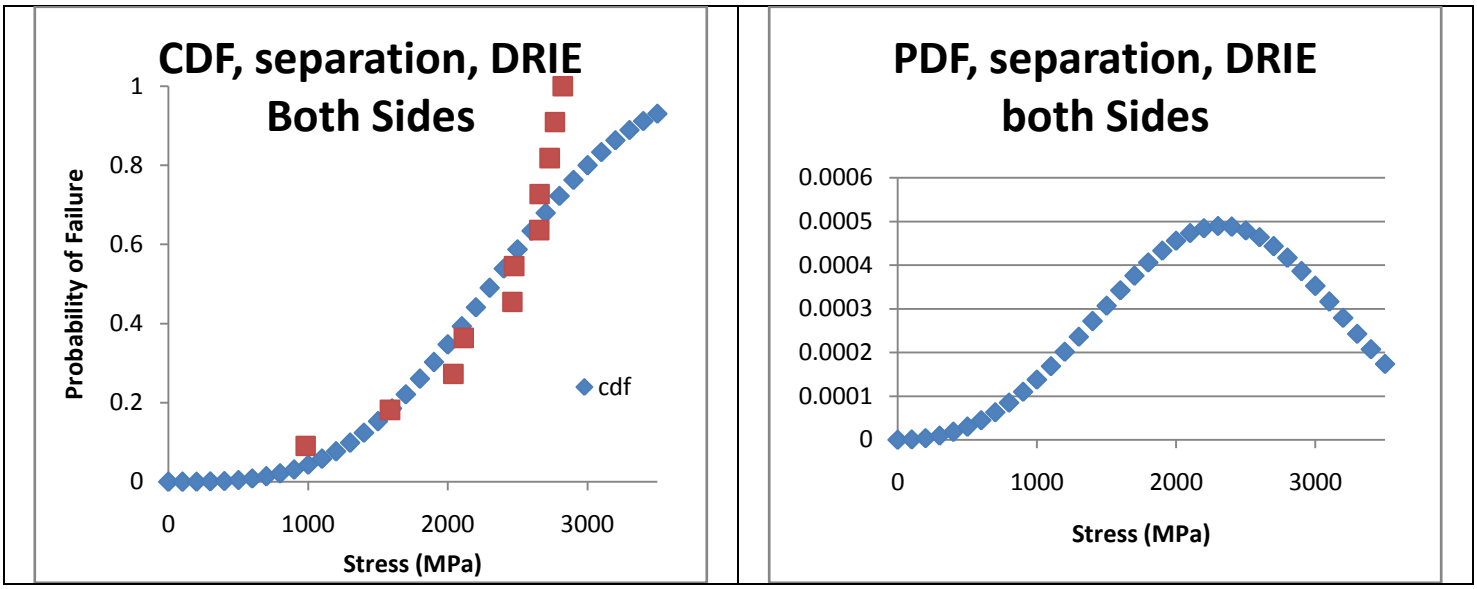

Figure A-61. 25% DRIE double sided, separation, β=3.278, α=2595.3, ρ=0.932, N=11.

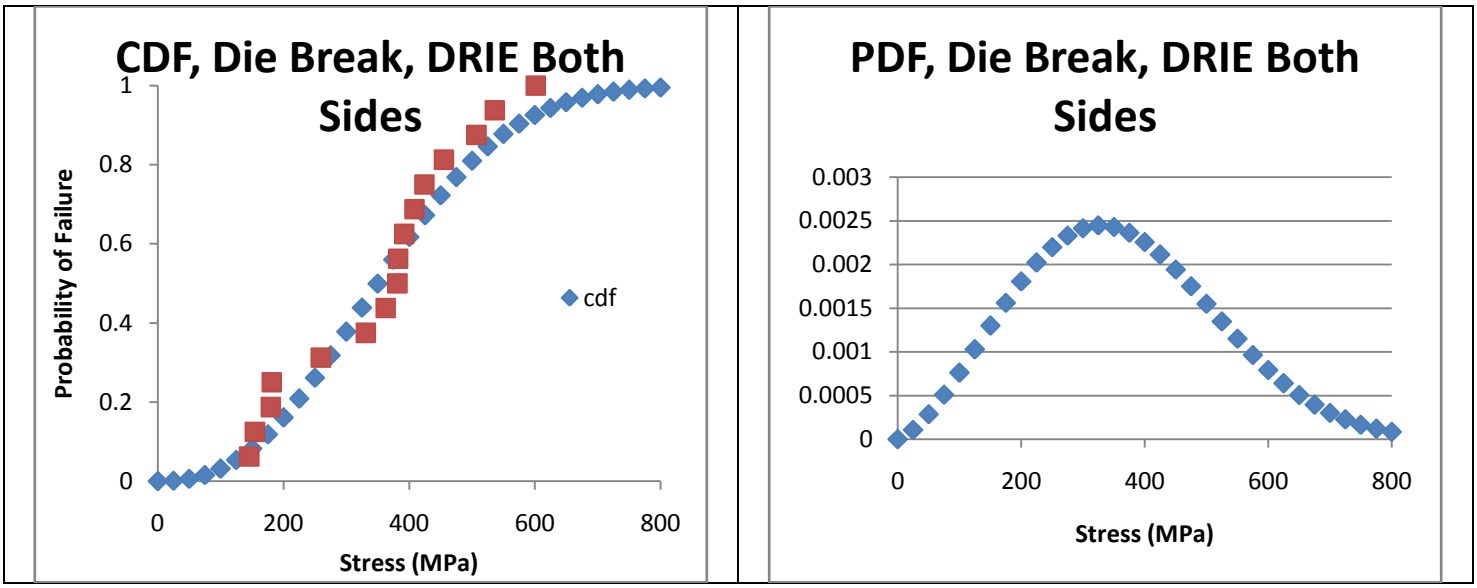

Figure A-62. 25% DRIE double sided, die fracture, β=2.454, α=406.7, ρ=0.967, N=16.